

The development of Phytocat: a biologically bound nickel catalyst for accelerated de-polymerization of plastics and hydrogenation of platform molecules

Parul Johar

Doctor of Philosophy

University of York

Chemistry

August 2022

Abstract

The goal of a carbon-neutral society can be realized by utilizing a circular carbon pathway, which combines recycling, biomass utilization, carbon capture and utilization. With mounting concerns over critical element sustainability, the conversion of phyto-extracted nickel (from contaminated lands) into an inexpensive and clean catalyst could help to reduce demand for virgin precious metals. Inspired by the potential of metal-contaminated biomass as valuable feed-stock, the development of a biologically-bound nickel catalyst (phytocat) was envisioned.

The application of the developed phytocat was explored to accelerate de-polymerization of plastics (polystyrene, polyethylene and PureFlex™ films) into high value chemicals. The synergistic effect of microwaves, together with phytocat as a microwave absorber, accelerated the catalytic de-polymerization process at low temperature (250°C). The single step process typically takes up to 70 s to transform a waste polymer into valuable liquid hydrocarbons (40-82% oil yield), hydrogen (11-30% gas yield) and filamentous carbon (25-37% solid yield), depending on varying catalyst to polymer weight ratios. The enhancement of (de) hydrogenation, de-carboxylation and cyclization, utilizing phytocat can be established as a proof of concept to advance and enable selective transformation of polymeric consumer products, paving the way to harness complete circular chemical potential of these future feed-stocks.

Furthermore, the presence of a bio-carbon matrix around the phyto-extracted Ni enabled an efficient suppression of the over-hydrogenation reaction pathway during the hydrogenation of model platform molecules containing α, β -unsaturated carbonyl groups (cinnamaldehyde, furfural and levoglucosenone). The simplicity, long-term stability and ease of handling make this catalyst an economically and environmentally attractive alternative to Raney nickel and precious metal-based catalysts.

Dedication

*To the nature and its creation
(the beautiful plants used in this study)*

List of Contents

Abstract.....	2
Dedication.....	3
List of Contents.....	4
List of Figures.....	7
List of Tables.....	16
Acknowledgements.....	18
Declaration.....	21
Chapter 1: General Introduction and Thesis Aims.....	22
1.1 A sustainable route towards phyto-mining.....	22
1.1.1. Mining critical metals for green technology.....	22
1.1.2. Spatial distribution of nickel reserves and associated serpentine flora.....	25
1.1.3. Biological pathways determining nickel accumulation rates in plants.....	29
1.1.4. Plant inspired green biomaterials.....	34
1.2 Thesis aims.....	38
1.2.1. Development of carbon supported non-noble metal catalysts.....	38
1.2.2. Catalytic hydrogenation of platform molecules.....	40
1.2.3. Catalytic de-polymerization of plastics.....	43
Chapter 2: Experimental.....	50
2.1 Preparation and characterization of phytocat.....	50
2.1.1. Hydroponic growth of nickel-dosed plant biomass.....	50
2.1.2. Microwave assisted pyrolysis of phyto-accumulated nickel rich biomass.....	51
2.1.3. Thermo-gravimetric analysis with fourier transform infrared (TGA FTIR).....	52
2.1.4. High-angle annular dark-field -scanning transmission electron microscope (HAADF-AC-STEM).....	52
2.1.5. Transmission electron microscopy (TEM).....	52
2.1.6. Field-emission scanning electron microscope (FE-SEM) equipped with an energy-dispersive X-ray (EDX) spectrometer.....	53

2.1.7. X-ray photoelectron spectroscopy (XPS).....	53
2.1.8. X-ray diffraction (XRD).....	53
2.1.9. Solid-state nuclear magnetic resonance spectroscopy.....	53
2.1.10. Microwave assisted hydrolysis of phytoaccumulated nickel-rich biomass.....	53
2.2 Application of the phytocat for hydrogenation of platform molecules.....	54
2.2.1. General procedure for hydrogenation.....	54
2.2.2. Gas chromatography coupled with mass spectrometry (GC–MS).....	55
2.2.3. GC equipped with a flame ionization detector (GC-FID).....	55
2.2.4. Nuclear magnetic resonance spectroscopy (¹ H-NMR and ¹³ C-NMR).....	55
2.2.5. Fourier transform infrared spectroscopy (FTIR).....	55
2.3 Application of the phytocat for de-polymerization of plastics.....	56
2.3.1. Microwave assisted pyrolysis at varying ratios of phytocat and plastics.....	56
2.3.2. Simultaneous thermal analyzer with gas chromatography equipped with mass spectrometry (TG-GC-MS).....	56
2.3.3. Qualitative analysis of de-polymerization products.....	56
Chapter 3: The development of phytocat: structural and molecular insights.....	58
3.1 Effect of phyto-accumulated nickel on the product distribution.....	59
3.1.1. Microwave-assisted pyrolysis.....	61
3.1.2 Microwave-assisted hydrolysis.....	75
3.2 Advanced material characterization of phytocat	82
3.3 Summary.....	92
Chapter 4 Phytocat as a sustainable catalyst for the selective hydrogenation of platform molecules.....	94
4.1 Hydrogenation of cinnamaldehyde.....	95
4.2 Hydrogenation of furfural.....	110
4.3 Hydrogenation of levoglucosenone.....	112
4.4 Summary.....	117
Chapter 5 Phytocat-accelerated de-polymerization of plastics.....	120
5.1 De-polymerization of polystyrene.....	121
5.2 De-polymerization of polyethylene.....	134

5.3 De-polymerization of PureFlex™ Film.....	152
5.4 Summary.....	161
Chapter 6 Concluding remarks and future work.....	163
6.1 Summary of key results.....	163
6.2 Recommendations for future work.....	164
Appendix.....	166
Appendix A.....	166
Appendix B.....	178
Appendix C.....	189
References.....	216

List of Figures

Figure 1.1: a) Extraction of Ni from ores, b) Processing of Ni from Sulfide ores, Processing of Ni from laterite ores: c) RKEF and d) HPAL.....	24
Figure 1.2: Spatial distribution of nickel reserves and associated serpentine flora used in this study.....	27
Figure 1.3: Biological pathways associated with nickel accumulation rates in plants.....	32
Figure 1.4: Conceptual framework of biopolymer interactions underlying the heterogeneous design of lignocellulose.....	36
Figure 1.5: Adsorption arrangements of α,β -unsaturated carbonyls on metal nanoparticles.....	41
Figure 1.6: Research overview of the thesis (Aim 2).....	43
Figure 1.7: Prospects of production of high value materials and chemicals from depolymerization of plastics.....	44
Figure 1.8: Hydrolysable and non-hydrolysable plastics.....	46
Figure 1.9: Research overview of the thesis (Aim 3).....	49
Figure 2.1: Images of willow rods at different stages of its growth pre- and post-dosing.....	51
Figure 3.1: Aeroflo system (General Hydroponics) used to grow willow rods (<i>Salix viminalis</i>) a) Pre-dosing, b) Post-dosing (3 weeks duration) c) Undosed willow for preparation of control phytocat and d) Dosed willow for preparation of phytocat-0.1.....	60
Figure 3.2: Heating rate profiles of phytocat materials at various time intervals to reach the set-point temperature in the microwave reactor.....	61
Figure 3.3: Comparison of microwave-assisted pyrolysis and conventional thermal pyrolysis: Evolution of the pyrolysis products as a function of variation in the concentration of biologically bound Ni in the plant matrix.....	64
Figure 3.4: a) Role of the biologically bound Ni to direct the microwave-assisted pyrolysis products distribution; b) Total ion chromatograms obtained by GC-MS	

analysis of the extracted bio oils and c) Major platform molecules formed during the microwave assisted pyrolysis to generate phytocat materials.....	66
Figure 3.5: Mechanistic pathway of degradation of lignocellulose utilizing the synergistic interactions between microwaves and biologically-bound Ni.....	68
Figure 3.6: Primary perspective towards the development of phytocat.....	70
Figure 3.7: a) Composition of the gas released during microwave assisted pyrolysis for the development of various phytocat materials; Real time thermo-gravimetric analysis of the gas produced during conventional pyrolysis: b) Phytocat-2.5 and c) control phytocat.....	72
Figure 3.8: Elemental composition of the biomass pre-pyrolysis and the phytocat materials developed using microwave assisted pyrolysis.....	74
Figure 3.9: a) Composition of the products formed by microwave-assisted hydrolysis, b) HPLC chromatographs of the extracted hydrolysates.....	77
Figure 3.10: Proposed mechanistic pathway of microwave assisted hydrolysis directed by phytocat	79
Figure 3.11: Cross-polarization magic angle spinning (CPMAS) ¹³ C NMR spectra of a) Pre-hydrolysis phytocat-2.5, b) post-hydrolysis phytocat-2.5, c) Pre-hydrolysis phytocat-0.1, d) post-hydrolysis phytocat-0.1, e) Pre-hydrolysis control phytocat and f) post-hydrolysis control phytocat.....	81
Figure 3.12: Cross-polarization magic angle spinning (CPMAS) ¹³ C NMR spectra of a) Pre-pyrolysis phytocat-2.5, b) Phytocat-2.5, c) Pre-pyrolysis phytocat-0.1, d) Phytocat-0.1, e) Pre-pyrolysis control phytocat and f) Control phytocat.....	83
Figure 3.13: X-ray photoelectron spectroscopy (XPS) analysis of phytocat materials a) deconvoluted high-resolution Ni 2p _{3/2} spectra, b) deconvoluted high-resolution N 1s XPS spectra, c) deconvoluted high-resolution C 1s spectra, d) X-ray diffraction (XRD) pattern of Ni-phytocat-2.5 and -0.1.....	85
Figure 3.14: a) Energy-dispersive x-ray (EDX) spectroscopy analysis of Ni-phytocat-2.5 highlighting carbon (green), nickel (blue), oxygen (red) and calcium (orange), Scanning electron microscopy (SEM) images equipped with energy-dispersive X-ray spectroscopy (EDX): b) phytocat-2.5, c) phytocat-0.1 and d) control phytocat.....	87

Figure 3.15: High-resolution transmission electron microscopy (HRTEM) image of a) Phytocat-2.5, c) Phytocat-0.1, e) control phytocat; High-angle annular dark-field scanning transmission electron microscopy (HAADF-STEM) image of b) Phytocat-2.5 d) Phytocat-0.1, f) control phytocat.....	89
Figure 3.16: Real time thermogravimetric analysis coupled with fourier transform infrared spectroscopy (TGA-FTIR) for functional groups analysis of evolved gases in real-time for (a-b) Pre-pyrolysis phytocat-2.5, (c) phytocat-2.5, (d-e) pre-pyrolysis phytocat-0.1, (f) Ni-phytocat-0.1, (g-h) pre-pyrolysis control phytocat (i) control phytocat	91
Figure 4.1: Mechanistic pathway for the hydrogenation of cinnamaldehyde.....	97
Figure 4.2: (a) Influence of reaction temperature on the catalytic conversion of cinnamaldehyde using various catalysts; FTIR spectrum of the products formed by hydrogenation of cinnamaldehyde at various temperatures using (b) phytocat-0.1 and (c) phytocat-2.5.....	99
Figure 4.3: Influence of reaction temperature on the products selectivity using (a) phytocat-0.1, (b) phytocat-2.5, (c) Raney Ni; (d) GC-MS spectra of the products formed after hydrogenation of cinnamaldehyde at 120 °C using different catalysts.....	101
Figure 4.4: Influence of concentration of catalysts on the (a) conversion of cinnamaldehyde, (b) selectivity towards HCAL (Reaction conditions: 1 mmol substrate, 0.01-0.08 mmol Ni, 24 h, 40 bar H ₂ , 120 °C).....	102
Figure 4.5: Influence of reaction time on (a) the catalytic conversion of cinnamaldehyde, (b) selectivity towards HCAL (Reaction conditions: 1 mmol substrate, 1-24 h, 40 bar H ₂ , 120 °C).....	104
Figure 4.6: Reusability of the phytocat for (a) catalytic conversion of cinnamaldehyde, (b) Reusability of phytocat-0.1 for selectivity towards HCAL, (c) Reusability of phytocat-2.5 for selectivity towards HCAL, FTIR spectra of the products formed after the catalytic hydrogenation of cinnamaldehyde using recycled catalysts (d) phytocat-0.1 and (e) phytocat-2.5 (Reaction conditions: 1 mmol substrate, 24 h, 40 bar H ₂ , 120 °C).....	105
Figure 4.7: (a, c) High-angle annular dark-field scanning transmission electron microscopy (HAADF-STEM) image of recycled Ni-phytocat-2.5 and Ni-phytocat-0.1 respectively, (b, d) high-resolution TEM (HRTEM) image of recycled Ni-phytocat-2.5 and Ni-phytocat-0.1 respectively.....	107

Figure 4.8: X-ray photoelectron spectroscopy (XPS) analysis of the pristine and recovered phytocat-2.5 and phytocat-0.1 (a) de-convoluted high-resolution Ni 2p _{3/2} spectra(b) X-ray diffraction (XRD) pattern of the recovered phytocat-2.5 and phytocat-0.1.....	109
Figure 4.9: Mechanistic pathway for the hydrogenation of furfural.....	111
Figure 4.10: (a) Conversion of furfural using phytocat-2.5 at various temperatures and its selectivity towards furfuryl alcohol, (b) GC-MS chromatograms of the products formed (Reaction conditions: 1 mmol substrate, 24 h, 40 bar H ₂ , 60-120 °C).....	112
Figure 4.11: Mechanistic pathway for the hydrogenation of Levoglucosenone.....	114
Figure 4.12: (a) Conversion of LGO using phytocat-2.5 at various temperatures and its selectivity towards Cyrene, (b) FTIR spectra of the products formed by hydrogenation of LGO using phytocat-2.5 (Reaction conditions: 1 mmol substrate, 24 h, 40 bar H ₂ , 60-120 °C).....	115
Figure 4.13: (a) Conversion of LGO using various catalysts, (b) GC-MS analysis of the products formed by hydrogenation of LGO at 120 °C using various catalysts.....	117
Figure 4.14: Comprehensive outlook of the selective hydrogenation using phytocat at various temperatures	119
Figure 5.1: (a) Comparison of efficiency of various catalysts for rapid de-polymerization of PS, (b) graphical illustration of the accelerated de-polymerization process of PS to produce monomer units.....	122
Figure 5.2: (a) Gas chromatography-mass spectrometry (GC-MS) characterization of oils formed by MAP of PS using various catalysts (1:10 catalyst to polymer ratio, by weight); (b) Product selectivity and (c) chemical structures of the major compounds formed during the de-polymerization process	124
Figure 5.3: Product distribution and composition on de-polymerization of PS using microwaves (200W and 250°C) (a, b) phytocat-1.5; (c, d) phytocat-0.1; (e, f) control phytocat and (g, h) activated carbon using various mixing ratios with polystyrene.....	126
Figure 5.4: Conventional pyrolysis (400-900 °C, TG-FTIR analysis) (a) PS, (b) control phytocat and polystyrene mixture (1:10 by weight) (c) phytocat-1.5 and	

polystyrene mixture (1:10 by weight); (d) Characterization of the gas evolved during MAP (250 °C) of PS using GC-TCD analysis.....	128
Figure 5.5: Possible reaction mechanism of de-polymerization of PS using phytocat.....	130
Figure 5.6: Characterization of phytocat post microwave-assisted de-polymerization of PS a) Field emission scanning electron microscopy (FESEM) image, b) High resolution transmission electron microscopy (HR-TEM) image, c) X-ray diffraction and d) X-ray photoelectron spectroscopy (XPS) analysis (C 1s XPS spectra).....	132
Figure 5.7: Comparison of experimental results of microwave assisted de-polymerization of LDPE using varying catalyst to polymer ratio: (a-b) phytocat-2.5, (c-d) phytocat-0.1, (e-f) control phytocat and (g-h) activated carbon.....	136
Figure 5.8: Gas chromatography-mass spectrometry (GC-MS) characterization of oils formed on microwave –assisted pyrolysis of LDPE using (a) activated carbon, (b) control phytocat, (c) phytocat-0.1 and (d) phytocat-2.5; Product yields (e) and selectivity (f) using various catalysts (1:10 catalyst to polymer ratio, by weight).....	138
Figure 5.9: (a) Comparison of efficiency of various catalysts for accelerated de-polymerization of LDPE, (b) Relative amounts of the gaseous molecules formed during microwave-assisted accelerated de-polymerization of LDPE using various catalysts, Depth of cracking of various hydrocarbons formed during microwave-assisted accelerated de-polymerization of LDPE on the surface of (c) control phytocat or activated carbon and (d) Ni-phytocat.....	141
Figure 5.10: Comparison of experimental results of the microwave-assisted (for 3 successive cycles to reach the set-point of 250°C) and conventional thermal (500°C) de-polymerization of polyethylene (Low density polyethylene, LDPE) using (a-b) Ni-Phytocat-2.5, (c-d) Ni-Phytocat-0.1, (e-f) Control phytocat and (g-h) activated carbon (1:10, catalyst: LDPE by weight).....	143
Figure 5.11: Mechanistic pathway for accelerated de-polymerization of low-density polyethylene utilizing synergistic interactions of microwave and Ni-phytocat.....	146
Figure 5.12: Characterization of phytocat post MW assisted de-polymerization of LDPE: HR-TEM images of a) phytocat-1.5, b) phytocat-0.1, c) control phytocat; d) XRD analysis; e) TPO profiles.....	148

Figure 5.13: (a) Schematic illustration of the processes to generate high value chemicals, (b) Microwave energy consumption for accelerated de-polymerization of PE (to reach the set point of 250°C) using varying catalyst to polymer ratio.....	150
Figure 5.14: a) Layers of PureFlex™ film243; b) visual appearance of PureFlex™ film and c) structural formulae of the polymeric units of PureFlex™ film.....	152
Figure 5.15: Visual appearance of the samples post MW irradiation (cycle 1): (a, e) PF, mixtures of (b, f) Phytocat-2.5 and PF (1:10 by weight), (c, g) control phytocat and PF (1:10 by weight) and (d, h) activated carbon and PF (1:10 by weight); (i) Comparison of efficiency of various catalysts for rapid de-polymerization of PF	154
Figure 5.16: Products distribution post microwave-assisted de-polymerization of PF (for 3 successive cycles at 200W to reach the set point of 250°C) using (a) phytocat-2.5, (b) phytocat-0.1, (c) activated carbon and (d) control phytocat (1:10, catalyst: PF by weight)	155
Figure 5.17: Visual appearance of PF in the microwave reactor (a) pre-pyrolysis, (b) post-pyrolysis using phytocat-2.5, (c) post MW cycle 3 (before and after the extraction of oil and gas); (d) FTIR spectra of PF pre-pyrolysis, mixtures of PF and phytocat-2.5 (1:10, by weight) post MW cycle 1 and 3 respectively.....	157
Figure 5.18: Product yields and selectivity using various catalysts (1:10 catalyst to polymer ratio, by weight) of (a) liquid fraction and (b) gaseous fraction formed on MAP of PF	159
Figure 5.19: Gas chromatography-mass spectrometry (GC-MS) characterization of oils produced by MAP of PF (1:10 catalyst to polymer ratio, by weight) using (a) phytocat-2.5, (b) control phytocat, (c) activated carbon and (d) without catalyst; alongside structural formulae of the major compounds formed (highlighted in various colors).....	161
Figure A.1: ¹ H NMR spectra of the MAP oil extracted during the formation of phytocat-2.5	166
Figure A.2: ¹ H NMR spectra of the MAP oil extracted during the formation of phytocat-1.5.....	167
Figure A.3: ¹ H NMR spectra of the MAP oil extracted during the formation of phytocat-0.1	168

Figure A.4: ^1H NMR spectra of the MAP oil extracted during the formation of control phytocat	169
Figure A.5: ^{13}C NMR spectra of the MAP oil extracted during the formation of phytocat-2.5	170
Figure A.6: ^{13}C NMR spectra of the MAP oil extracted during the formation of phytocat-1.5	171
Figure A.7: ^{13}C NMR spectra of the MAP oil extracted during the formation of control phytocat	172
Figure A.8: (a) Scanning electron microscopy (SEM) images equipped with energy-dispersive X-ray spectroscopy (EDX) analysis of control phytocat, (b) Elemental mapping of control phytocat highlighting carbon, calcium, sulfur, potassium, oxygen and magnesium, (c) Energy-dispersive x-ray (EDX) spectroscopy analysis of control phytocat.	173
Figure A9: High-resolution TEM (HRTEM) image of Ni-phytocat-2.5 showing lattice fringes corresponding to (111) and (200) crystal planes, respectively, of cubic Ni phase.	173
Figure A10: Plots of lattice spacing corresponding to the fast fourier transform (FFT) pattern of the high-resolution TEM (HRTEM) image of Ni-phytocat-2.5.....	175
Figure B1: Gas-chromatography equipped with flame ionization detector (GC-FID) analysis of the products formed by hydrogenation of CAL using (a) phytocat-2.5, (b) Raney Ni and (c) control phytocat	178
Figure B2: ^1H NMR analysis of the products formed after catalytic hydrogenation of cinnamaldehyde using phytocat-2.5 at 120 °C.....	179
Figure B3: ^{13}C NMR analysis of the products formed after catalytic hydrogenation of cinnamaldehyde using phytocat-2.5 at 120 °C.....	180
Figure B4: ^1H NMR analysis of the products formed after catalytic hydrogenation of cinnamaldehyde using phytocat-0.1 at 120 °C.....	181
Figure B5: ^{13}C NMR analysis of the products formed after catalytic hydrogenation of cinnamaldehyde using phytocat-0.1 at 120 °C.....	182
Figure B6: ^1H NMR analysis of the products formed after catalytic hydrogenation of levoglucosenone (LGO) using phytocat-2.5 at 120 °C.....	183

Figure B7: ^{13}C NMR analysis of the products formed after catalytic hydrogenation of levoglucosenone (LGO) using phytocat-2.5 at 120 °C.....	184
Figure C1: Time (a) and energy consumption (b) under microwave irradiation to reach the set point of 250 °C for de-polymerization of polystyrene using various mixing ratios with phytocat and activated carbon.....	189
Figure C2: FTIR analysis of pyrolysis oil produced by microwave assisted de-polymerization of Polystyrene using (a) phytocat-0.1 and (b) control phytocat.....	190
Figure C3: ^1H NMR spectrum of pyrolysis oil produced by microwave assisted de-polymerization of Polystyrene using (a) phytocat-0.1 and (b) control phytocat.....	191
Figure C4: ^{13}C NMR spectrum of pyrolysis oil produced by microwave assisted de-polymerization of Polystyrene using (a) phytocat-0.1 and (b) control phytocat.....	192
Figure C5: Conventional TGA profiles of (a) polystyrene (PS), (b) <i>S. tryonii</i> (pre-pyrolysis phytocat-1.5), (c) <i>S. viminalis</i> (pre-pyrolysis phytocat-0.1), (d) <i>S. viminalis</i> (<0.01 wt% Ni; pre-pyrolysis control phytocat), (e) activated carbon: PS (1:10), (f) phytocat-1.5: PS (1:10), (g) phytocat-01: PS (1:10) and (h) control phytocat: PS (1:10) with a heating rate of 10°C min ⁻¹ under nitrogen atmosphere of 100 ml min ⁻¹ flow rate.....	193
Figure C6: Gas chromatograms of the pyrolysis oils produced using conventional pyrolysis of (a) low density polyethylene (LDPE), (b) activated carbon: LDPE, (c) control phytocat: LDPE, (d) phytocat-0.1: LDPE and (e) phytocat-2.5: LDPE (1:10 by weight)	194
Figure C6: ^1H NMR analysis of the oil formed after microwave-assisted de-polymerization of LDPE using phytocat-2.5.....	195
Figure C7: ^1H NMR analysis of the oil formed after microwave-assisted de-polymerization of LDPE using phytocat-0.1.....	196
Figure C8: ^1H NMR analysis of the oil formed after microwave assisted de-polymerization of LDPE using control phytocat.....	197
Figure C9: ^1H NMR analysis of the oil formed after microwave-assisted de-polymerization of LDPE using activated carbon.....	198
Figure C10: ^{13}C NMR spectrum of pyrolysis oil produced by microwave assisted de-polymerization of LDPE using phytocat-2.5	199

Figure C11: ^{13}C NMR spectrum of pyrolysis oil produced by microwave assisted de-polymerization of LDPE using phytocat-0.1.....	200
Figure C12: ^{13}C NMR spectrum of pyrolysis oil produced by microwave-assisted de-polymerization of LDPE using activated carbon.....	201
Figure C13: Conventional TGA profiles of PF (a) with phytocat-2.5 (1:10 by weight) and (b) without phytocat-2.5	202
Figure C14: Microwave energy consumption for accelerated de-polymerization of PF (to reach the set point of 250°C) using various catalysts.....	203

List of Tables

Table A1: Detailed elemental distribution of phytocat precursors and phytocat using ICP-MS analysis.....	176
Table A2: List of major compounds identified in the MAP oils of phytocat-2.5 based on the GC-MS data.....	177
Table B1: Comparison of this work with the literature reports on catalytic hydrogenation of cinnamaldehyde using Ni based catalysts.....	185
Table B2: Comparison of turn over numbers (TON) for hydrogenation of cinnamaldehyde at various temperatures and concentration of catalysts.....	187
Table C1: List of compounds identified using total ion chromatograms of pyrolysis oil of Phytocat-1.5/PS (1:10 by weight).....	204
Table C2: List of compounds identified using total ion chromatograms of pyrolysis oil of control phytocat/PS (1:10 by weight).....	205
Table C3: Experimental results of the microwave-assisted de-polymerization of polyethylene (Low density polyethylene, LDPE) using Phytocat-2.5 (varying catalyst: LDPE ratio by weight) at 250°C	206
Table C4: Experimental results of the microwave-assisted de-polymerization of polyethylene (Low density polyethylene, LDPE) using Phytocat-2.5 (1:10, catalyst: LDPE by weight) for 3 successive cycles (each cycle takes $t < 70$ s to reach the set-point of 250°C)	208
Table C5: Comparison of experimental results of the microwave-assisted (250°C, up to 2 min) and conventional thermal (500°C, up to 2 h) de-polymerization of polyethylene (Low density polyethylene, LDPE) using Phytocat-2.5 (1:10, catalyst: LDPE by weight)	209
Table C6: Experimental results of the microwave-assisted de-polymerization of low density polyethylene (LDPE) using phytocat-0.1 (1:10, catalyst: LDPE by weight) for 3 successive cycles (each cycle took $t < 70$ s to reach the set-point of 250°C).....	210
Table C7: Experimental results of the microwave-assisted de-polymerization of low density polyethylene (LDPE) using control phytocat (1:10, catalyst: LDPE by weight)	

for 3 successive cycles (each cycle took $t < 70$ s to reach the set-point of 250°C)
.....211

Table C8: Experimental results of the microwave-assisted de-polymerization of low density polyethylene (LDPE) using activated carbon (1:10, catalyst: LDPE by weight) for 3 successive cycles (each cycle takes $t < 70$ s to reach the set-point of 250°C).....212

Table C9: Comparison between literature reports on catalytic microwave assisted pyrolysis of plastics and this research213

Acknowledgements

I am, and will remain, incredibly grateful to my supervisor Professor James Clark- not least for initially selecting me to undertake this wonderful work, and in doing so to become and grow as an independent researcher. I am full of gratitude for everything he has done for me, and for encouraging me to attempt any experiment that raised my curiosity.

I would like to express my gratitude to my co-supervisors Dr. Rob McElroy, Prof. Avtar Matharu and my independent panel member, Dr. Liz Rylott (Department of Biology, University of York). Thank you Rob for your joyful laughter and cheerful expressions. You have been highly encouraging throughout. Thank-you for giving me a wonderful opportunity to work on this fascinating research funded by Merck KGaA. I would also like to thank Jaqueline Hollands (Merck KGaA) for kindly providing the required materials for this work. I would also like to acknowledge Prof. Seth Davis (Department of Biology, University of York) for this valuable collaboration and insightful discussions.

Thank you Liz for fulfilling the role of the independent panel member to this research and my life as a PhD student. Your guidance, expertise and attention to detail are very much appreciated. Thank you for all your kindness and compassion that goes beyond the work. You are totally inspirational!

Thank you Prof. Avtar for your incredible motivation throughout. Your professional standards, ability to couple work and life, have been and will remain inspirational. You have played an influential role in my life, which showed me how to act in a polished and professional manner. Thank you for everything. Special thanks must go to Mrs. Sukhvinder Kaur Matharu (Prof. Avtar's wife) for being so compassionate and helpful. I am grateful to have been blessed to receive the support specifically when I was diagnosed with Neuromyelitis optica. Thank you for being with me during difficult times and all the care and support.

My sincere thanks must go to Dr. Tony Wild for his generous support in the form of Wild Fund Platinum Scholarship, which led me to initiate my doctoral studies and re-discover such fascinating work. Special thanks goes to the Association of Commonwealth Universities (ACU) for selecting me as one of a cohort of 35 successful applicants around the world to be awarded the prestigious Blue Charter fellowship. This fellowship led me to conduct research work themed around addressing the critical global issue of marine plastics, which are drastically affecting the health of our oceans and marine life. This wouldn't have been possible without the support of Professor Amanda Ellis (University of Melbourne, Australia), who hosted me in her lab to initiate this essential work.

My own individual work has been complemented by a number of valuable technical assistance. I would like to thank Dr Jon Barnard and Dr. Leonardo Lari (Jeol nanocentre, University of York) for sharing their expertise and training me on the state-of-art instruments for advanced material characterization, Dr Adrian Whitwood for training me on powder XRD analysis, Dr. Heather Fish for training me on the solid state NMR, Mr. Karl Heaton, Dr. Florent Bouxin, Mr. Paul Elliot, Dr. Hannah Briers, Dr. Tabitha Petchey, and Dr. Richard Gammons. Thanks must also go to the various technical staff for either provided training and analysis, both within the GCCE and wider Department of Chemistry within the University of York. I would also like to acknowledge Dr. David Morgan (University of Cardiff) for providing the XPS analysis.

I would also like to thank my examiners, Prof. Helen Sneddon and Prof. Philip Longhurst for their time and insightful discussion during my viva examination.

There are a large number of people working behind the scenes in order for the institution to run as seamlessly as possible. To this end, I would like to thank the incredible, all-knowing Rachel Crooks, Sharon Stewart and Alice Duckett (Chemistry graduate office) and Katy Brooke (Green Chemistry Administrator). The many cleaners and facilitators who have not been named have been none-the-less incredibly valued, and their efforts through the years much appreciated!

Most importantly, I am grateful to my mother (Mrs. Taruna Johar) for being my real guru. You are forever my inspiration to be all I can, my supreme leader, and my love. Words can never be enough to express my gratitude for everything you have done for me. Enormous thanks goes to my father (Mr. Manish Johar) for all the invaluable lessons, my sister and brothers as well for all the motivation, laughter and support. My Pathakji, thank you for being my biggest cheerleader. Finally, huge thanks to my huge family and my friends for being there throughout!

To my master's thesis supervisors, Professor Arun Kumar (Department of Environmental Engineering, Indian Institute of Technology, IIT Delhi) and Professor Sudhanshu Mallick (Department of Metallurgical Engineering and Material Science, Indian Institute of Technology, IIT Bombay), thank you for your mentorship and for encouraging me in all aspects of my work. This wouldn't have been possible without your support as well. Thank you for the motivation and introducing me to such diverse fields of research.

For the god, who is limitless and through whom everything is possible!!!

Declaration

I declare that this thesis is a presentation of original work and I am the sole author. This work has not previously been presented for an award at this, or any other, University. All sources are acknowledged as References.

Parts of the work reported in this thesis have been published as the following peer-reviewed journal articles:

- a) **Johar P**, Rylott EL, McElroy CR, Matharu AS, Clark JH. Phytocat—a bio-derived Ni catalyst for rapid de-polymerization of polystyrene using a synergistic approach. *Green Chemistry*. 2021;23(2):808-14.
- b) **Johar P**, McElroy CR, Rylott EL, Matharu AS, Clark JH. Biologically Bound Nickel as a Sustainable Catalyst for the Selective Hydrogenation of Cinnamaldehyde. *Applied Catalysis B: Environmental*. 2022; 121105.
- c) **Johar P**, Rylott EL, McElroy CR, Matharu AS, Clark JH. Biologically bound nickel accelerated de-polymerization of polyethylene to high value hydrocarbons and hydrogen. *RSC Sustainability*. (Revised manuscript under review)

The author would like to declare the individual contributions made in the above-mentioned research articles:

PJ conceptualized the research, planned and performed all the experiments and subsequent data analyses, wrote the manuscript and responded to reviewers. CRM, ELR, ASM and JHC contributed to reviewing and editing.

All other collaborators (particularly those involved in technical assistance) are duly declared where appropriate.

Chapter 1 General Introduction and Thesis Aims

1.1. A sustainable route towards phyto-mining

1.1.1. Mining critical metals for green technology

Climate change is remodeling the mineral resource stock landscape.¹ There has been a major shift in investment from thermal coal towards the low-carbon energy technologies (~30% of global energy investments).² These low-carbon energy technologies need more metal to produce the same power output as their fossil fuel equivalents. Due to escalation of these green technologies, more than 20 energy transition metals (ETMs), including nickel, lithium, cobalt, platinum and rare earth elements (REEs), are predicted to face market pressure.^{2,3} A rising concern is whether continued technological advance can be sustained with a diminishing known reserves of these accessible mineral resources. This concern is particularly evident for the resources known as critical elements, defined as the resources vulnerable to supply chain risks that nonetheless play an important role in modern society.⁴

Over the years since the concept of criticality was formalized (initiated in 2008 by the commission of United States National Academies)⁵, a number of assessments of risks associated with critical elements have followed.^{4,6-8} Current methodologies have also validated that environmental implications of procuring a material and the availability of comparably functioning substitutes should be considered in determining criticality.⁶ Despite differences in methodology and in local resource availability, all lists of critical metals that have been compiled globally are largely similar.⁶ While these findings project that the annual demand for most critical metals will continue to grow, there has been limited realization in supplementing the supply of said materials through recycling.⁹ Moreover, recycling and enhancements in material efficiency alone is not enough to meet the increasing demand for ETM.^{1,3} This enormous demand can only be met through substantial advances in resource extraction. The environmental and social implications associated with projected growth in ETM extraction are seldom acknowledged in energy transition scenarios.^{1,10,11} Mining

activities alter the host environment, leading to aggravation of pre-existing vulnerabilities.¹⁰ The potential increase in land disturbance for the extraction of nickel is significantly higher than for lithium and cobalt.¹² For nickel, which has a uniform coverage of projects in low-risk and high-risk settings, innovation in the management and mitigation of environmental and social governance (ESG) risks is critical.¹³ The mining industry demands high-energy consumption, alongside being a significant greenhouse gas (GHG) emitter (7.64 kg CO₂-eq/kg) and is perceived as a dirty activity that has caused adverse social and environmental impacts.¹⁴ Globally, mining influences 5,000 Mha of land surface, with 7% overlapping with key biodiversity areas and 8 % with protected areas.¹ Most mining regions (~81%) target metals such as copper, nickel, and lithium needed for renewable energy production.¹ Over recent years, the impact on biodiversity caused by nickel mining has received specific consideration, due to removal of native vegetation and its destruction by the deposition of mine tailings.^{15-17,18} Mudd *et al.* showed the potential conflict between nickel mining and biodiversity in Indonesia.¹⁵ Pascal *et al.* projected biodiversity risks associated with an increase in nickel mining activities.¹⁶ In the case of New Caledonia, Jaffre *et al.* showed the impact of habitat reduction and fragmentation by nickel mining activities.¹⁷ These countries and regions are known as biodiversity hotspots, although the implications of nickel mining and correlation between biodiversity impact and land-use amendment is not universal.¹³ Identified land-based resources contain at least 0.3 billion tons of nickel (Ni), with about 60% in laterites and 40% in sulfide deposits.¹⁹

Historically, most Ni production has been derived from sulfide ores due to ease of processing as compared to Ni laterites (**Figure 1.1a**).²⁰ Laterite ores require relatively complex treatment to extract Ni, and have thus historically been more expensive than sulfide ores.²⁰ Broadly, production from sulfide ores involves either open cut or underground mining, followed by concentration *via* flotation, smelting of concentrates, then refining to produce a pure metal (**Figure 1.1b**). Pyro-metallurgical processing of sulfide ores is very similar to the processing required for other base metals, with Cu as an important by-product or co-product (depending on ore grades).¹⁵ Laterite mines are mostly open cut, due to the shallow nature of the ores, and apply a basic ore beneficiation before processing (since flotation is not feasible). The high moisture content of laterite ores also needs to be addressed through

calcination. After this stage, there are three major process designs—rotary kiln electric furnaces (RKEF), the Caron ammonia leach process or high pressure acid leaching (HPAL).¹⁵ Most laterite projects around the world use RKEF plants, commonly producing ferronickel (**Figure 1.1c**). The Caron process is based on high temperature ammonia leaching, with metal-rich solutions then fed to a solvent extraction (hydrometallurgical) facility.¹⁵ At HPAL plants, the ore is leached with sulfuric acid at high pressures (up to 5.4 MPa) and temperatures (245 to 270 °C) in a titanium-clad autoclave.¹⁵ At this stage, HPAL projects vary, few operating a Ni refinery to produce pure metal, while most produce an intermediate Ni hydroxide product (**Figure 1.1d**).¹⁵

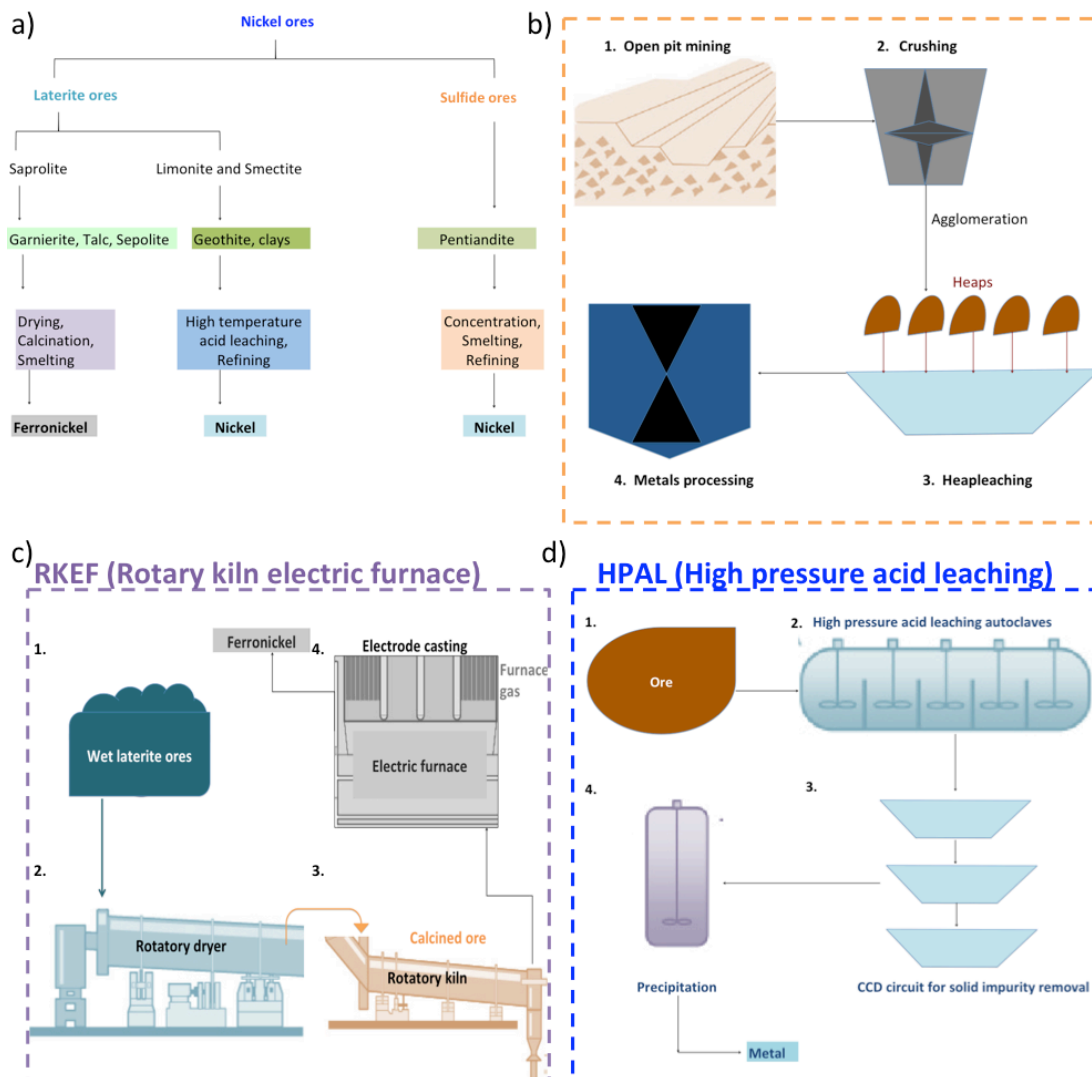


Figure 1.1: a) Extraction of Ni from ores, b) Processing of Ni from Sulfide ores, Processing of Ni from laterite ores: c) RKEF and d) HPAL

The final strategic theme associated with the global Ni industry is the extent of its environmental impacts. In particular, the historic impacts of Ni sulfide smelting and refining has created a lasting legacy of pervasive pollution in Canada and Russia.^{13,15} Canada has evidently improved its practices and is continuing to lower net environmental impacts, leading to the ongoing recovery of ecosystems.¹³ Conversely, very little is known about Russian impacts and their management.¹⁵ The higher GHG intensity of laterite (25 to 46 t CO_{2-e}/t metal) over sulfide (<10 t CO_{2-e}/t metal) is evident, with energy costs associated with sulfide being less than 100 GJ/t metal, compared to laterite projects with unit energy costs between 252 to 572 GJ/t metal.¹⁵ These environmental aspects are critical to understand given the existing global concerns over climate change and energy production and consumption. Technology and process innovation will continue to evolve and remain pivotal to the global Ni industry; but now, technology must explicitly address environmental as well as economic and process factors in order to ensure viability. This environmental aspect remains an intimidating challenge to the global Ni industry.²¹

Because of its widespread usage and tendency to accumulate, Ni contamination has exceeded its ecological threshold, now accounting for approximately 5 % (8.75 Mha) of E.U. agricultural land area.²² Reactive substances within the extracted material are exposed to wind, rain and oxygen, which favor their reaction and diffusion through either dust or acid drainage. Metal contamination in agricultural soils is an obstruction to achieving global food safety and security and will worsen as climate change reduces crop yields. There is a need to have a plan for long-term containment and ensure the mechanical reliability of waste facilities.

1.1.2. Spatial distribution of nickel reserves and associated serpentine flora

In the early phase of the 20th Century, the location of economic Ni resources was confined almost entirely to Canada and New Caledonia.¹⁵ By the mid-century, there was an observed expansion of laterite resources around the world, with growing

sulfide production from Russia and Australia.¹⁵ As discussed in the previous section 1.1.1, Ni is commonly present in two primary ore types- sulfide or laterite. Sulfide ores are typically derived from volcanic or hydrothermal processes and usually include Cu and/or Co, and precious metals such as Au or Pt and Pd.²¹ Laterite ores are formed near the surface following extensive weathering of ultramafic rocks, and occur abundantly in tropical climates around the equator, the arid regions of central Western Australia or humid areas of Eastern Europe (**Figure 1.2**).²³ In 2019, around 55% of global nickel ore extraction took place in the species-richest tropical biome.¹¹ Such areas suffered from massive deforestation in recent decades, with nickel mining a significant driver. Growing demand for essential minerals and declining quality of ores led to larger volumes of unused material extracted and disposed, increasing appropriation of land.^{24,25,26} There is likely enough economically-exploitable primary Ni to meet increased demand; however, mining, purifying, and refining Ni metal release greenhouse gases (7.64 kg CO₂-eq/kg), degrade the environment (including soil contamination with heavy metals and acidification of local wetlands), and present human health concerns in nickel mining and refining factories.^{3,27} An alternative method of primary Ni production which could complement mining is phytomining.¹² The key steps in developing sustainable phytomining are: (i) identifying potential metal-rich soils, (ii) selecting suitable plant species, and (iii) developing valuable product recovery processes.²⁸ The target metal-rich soils include smelter contaminated areas, ore beneficiation tailings and naturally occurring ultramafic (also referred to as serpentine) soils. Ultramafic rocks are hydrothermally altered (a process called serpentinization), typically on the ocean floor, and can emerge due to the subduction of tectonic plates.²³ Variation in the composition of ultramafic rocks due to processes occurring during their formation and weathering results in variation in the composition of soils derived from them which, in turn, influences the ecology of ultramafic plant communities.²⁹

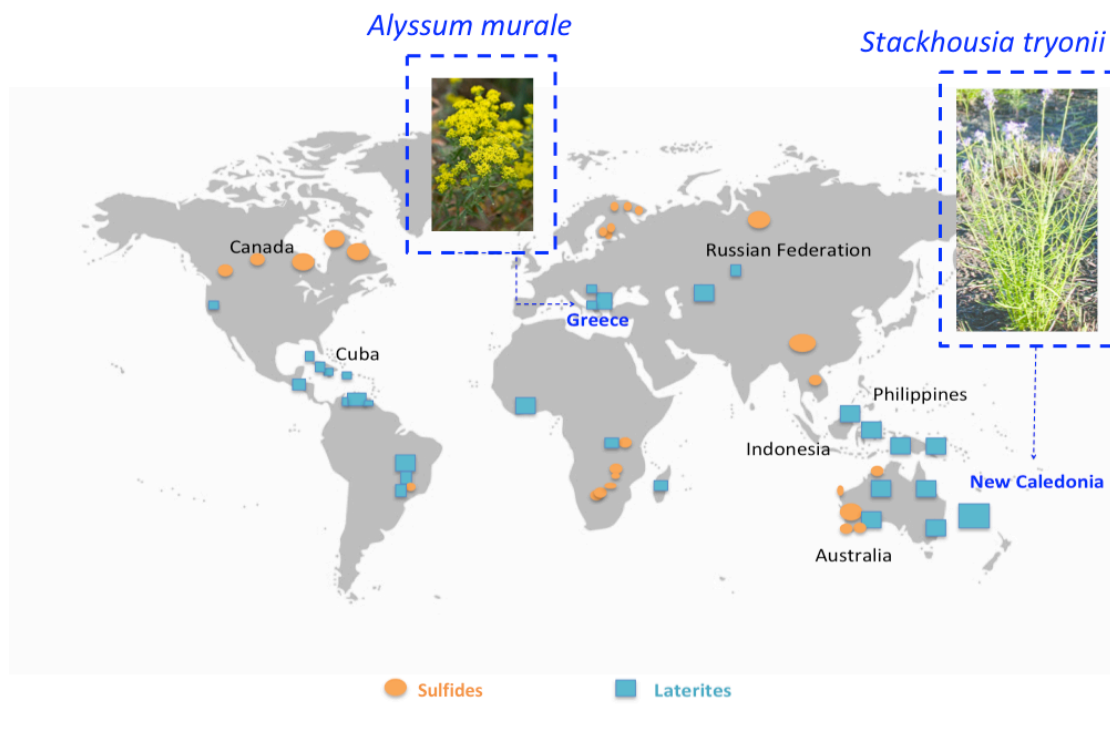


Figure 1.2: Spatial distribution of nickel reserves and associated serpentine flora used in this study^{12,13,18,23}

In many parts of the world, serpentine flora are notable for a high degree of endemism (native to a specific geographical area), as the evolutionary adaptation required for tolerance of the unusual soil characteristics results in substantial morphological and genetic changes.²³ One particular adaptation that has occurred in a small proportion of serpentine species worldwide is that of Ni hyperaccumulation, defined as the presence of this element at a concentration exceeding 1,000 mg/kg in some part of the above-ground dry matter.³⁰ At the present time, more than 500 species have been recorded as hyper-accumulators.³⁰

Knowing the chemical species of trace metals is important for rehabilitation of lateritic Ni mining spoils, which can potentially contaminate the environment. For example, Ni in garnierite material was associated with smectite and talc, and Ni in this phase was more exchangeable and thus more mobile than in limonitic ores where Ni was contained in the goethite lattice.³¹

The majority of hyperaccumulator species are Ni hyperaccumulators (>75% in 532 different species), which are found in a large number of naturally Ni-enriched serpentine soils worldwide.^{30,32} The main areas of distribution of Ni hyperaccumulator plants include the Mediterranean region, especially with species in the genus *Alyssum*.²⁸ The tropical serpentine soils in Cuba, where the Ni hyperaccumulator, *Phyllanthus pallidus*, was discovered.³³ In New Caledonia, *Pycnantha acuminata*, an endemic tree that accumulates 25% Ni in its latex.³⁴ Also, in Malaysia, 17% Ni was found in the phloem sap exudates of *Phyllanthus balgooyi*.³⁵ It is essential to characterize these naturally occurring Ni-rich reserves to understand the relationship between serpentine soils, metal hyper-accumulating plants, trace metal mobility, and environmental risk.

1.1.3. Biological pathways directing nickel accumulation rates in plants

The first description of a plant able to gather extremely high levels of metals dates back to 1948, when *Alyssum bertolonii* (growing in the Tuscan region of Italy), was reported to accumulate a Ni content of more than 1 mg/g of dry weight in the shoot.³⁶ Formally, in 1976, the term ‘hyperaccumulator’ was coined to indicate plants able to accumulate high metal concentrations in the shoot without showing symptoms of toxicity, demonstrating association between metal hypertolerance and the ability to detoxify the metals stored.³⁴ Metal-hyperaccumulating plants uptake metal through low-selectivity cation transporters in the roots and, rather than pumping it out, store these metals from the soil inside the plant biomass at concentrations higher than some commercially mined ores.³²

Insights into the mechanism of hyper-accumulation have been attributed to hyperactive metal transporters and diverse detoxification pathways, which include glutathione synthesis and metal compartmentalization in vacuoles and other organelles.^{32,37,38} Several fundamental metal transferring components are essential for the survival of Ni hyper-accumulating plants, including cell membrane transporters, organelle storage systems, and chelator molecules.³⁷ Once transported, the metal ions are primarily enriched in the vacuole, with a small amount also absorbed on the cell wall and cytoplasm.³⁹ Cell wall, an ion exchanger of relatively low affinity, is the first barrier for metal ions to enter the cytoplasm. It blocks the metals reaching into the interior of cell by adsorption, and complexation, leading to the immobilization of metal ions in the cell wall.³⁷ After the quantity of metal ion in cell wall reaches the maximum level, the remaining metal ions can transfer to the plasmogen through cytomembrane.³⁹ Then majority of metal ions are sequestered and accumulated in cell vacuoles.^{37,38} Vacuole has abundant organic acid, protein and alkaloid that can coordinate with metal ions to form complexes and decrease their impact on cell activity.³⁷ Complex interactions of transport and chelating activities control the rates of metal ion intake and accumulation in different parts of the plant. Meanwhile, the cells pump out the excessive metal ions, transfer them into intercellular space, and accumulate in epidermis passing through cortex.³²

Metal ions enter *via* highly active membrane transporters, and are compartmentalized into organelles such as the vacuole.³⁸ To limit cellular toxicity, chelators such as glutathione, metallothionein, and phytochelatins bind and remove metals from sensitive metabolic functions.⁴⁰ The hyper-accumulation mechanisms generally include stimulated metal absorption in roots, reduced metal sequestration in root vacuoles, efficient xylem loading and xylem transport, strong metal sequestration and compartmentation in leaves.³⁸ The hyper-accumulator plants absorb Ni mainly as Ni²⁺, which is the same as non-hyperaccumulators. Nickel uptake has been suggested to be a kinetic process, which fits the Michaelis-Menten kinetics, with Michaelis-Menten constant values (K_m) ranging from 0.51–379 μM , which suggests that Ni uptake may be involved with low-affinity transporters.^{31,37} No high-affinity Ni influx transporter(s) have been identified in hyper-accumulators, or in other higher plants. Histidine acts as a Ni transport facilitator in the cytoplasmic matrix of root cells.^{37,40} However, carboxylic acids may still be the main chelators for Ni in roots, in particular when relatively high concentration of Ni is sequestered into root vacuoles after long cultivation periods.⁴⁰

On reaching xylem parenchyma, Ni is loaded from root symplast to xylem vessels.⁴⁰ Both hyperaccumulator and non-hyperaccumulators may possess similar efflux transporter(s) during the xylem loading processes, as the root to shoot Ni translocation rates are the same in both species.^{32,37} It is demonstrated that the concentrations of organic ligands are too low to account for complete Ni chelation in xylem sap, suggesting that most of the Ni in xylem sap remains as hydrated cation.⁴¹ This is a reasonable finding as Ni²⁺ is quite stable in acidic xylem sap (pH 5–6), and xylem vessels are non-living cells and should not be affected by high concentrations of Ni²⁺.^{39,40}

On reaching leaves, the main storage organ, Ni is then transferred across the whole apoplastic space *via* leaf veins.⁴⁰ At the subcellular level, Ni is mainly accumulated in leaf vacuoles.^{37–39} Ni in leaf cells is mostly complexed by carboxylic acids. For example, citric acid is the main ligand for Ni in several woody hyperaccumulators from New Caledonia.^{37,42} While in the herbaceous *Alyssum* species, Ni is principally associated with malic and malonic acids.^{40,41}

The phloem translocation process in hyperaccumulator plants has long been overlooked, due to strongly sequestered heavy metals in leaves. However, field evaluations have already shown that flowers of hyperaccumulator plants can

accumulate Ni as high as in leaves. These findings suggest that upward motion is the dominant direction for phloem translocation, and young leaves and reproductive organs are the main sink for phloem-based Ni.^{23,39}

A theoretical model for Ni hyperaccumulation mechanisms is proposed in **Figure 1.3** and comprises nine biological processes, summarized as follows:

(i) Low-affinity transport systems (mainly associated with Zn and Fe transporters, ZIP family) facilitate uptake of rhizospheric Ni^{2+} into the cytoplasm of the epidermal root cells.^{23,40}

(ii) In the cytoplasm, the transported Ni ions form complexes with chelator molecules (e.g. histidine). In the aerial tissues, these Ni-chelates would be stored in the vacuole, but due to the weak sequestration capacity of root vacuoles, the majority of Ni is transferred radially from the epidermal cells *via* a symplastic route (i.e. *via* plasmodesmata connecting the cytoplasm of the cells) to the pericycle.^{37,40}

(iii) Elevated expression of Ni efflux transporters at the pericycle, efficiently load the Ni, in the form of free hydrated cations, into the xylem vessels.³⁷

(iv) Once in the xylem, the Ni is translocated to the aerial tissues. Due to the strong transpiration in these tissues the majority of Ni accumulates in the mature leaves.³⁷

(v) As xylem flow fills in the apoplastic space in leaves and reaches minor veins, Ni is then transported into the leaf symplast, or remains in apoplast.³⁷

(vi) Ni is pumped into vacuoles, particularly in epidermis cells by transporters on the vacuolar membrane, then primarily chelated by carboxylic acids.^{32,37}

(vii) Phloem companion cells saturated in Ni-rich apoplastic fluid absorb large quantities of Ni^{2+} into the cytosols. The incorporated Ni^{2+} is chelated by a selection of carboxylic acids, e.g. malate or citrate to form Ni-ligand complexes.³⁷

(viii) From companion cells, Ni-ligand complexes are then transferred to phloem sieve elements *via* plasmodesmata, following the phloem flow, which is mostly driven

by osmotic pressure generated by photosynthate (mainly sucrose) concentration gradients between sources and sinks.³⁷

(ix) Again Ni may be transferred from phloem tissues to the apoplast on reaching sink organs (young growing tissues).³⁷

Figure 1.3 illustrates the processes influencing metal accumulation rates in plants: mobilization and uptake from the medium, compartmentation and sequestration within the root, efficiency of xylem loading and transport, distribution between metal sinks in the aerial parts, sequestration and storage in leaf cells.³⁷ At every level, concentration and affinities of chelating molecules, as well as the presence and selectivity of transport activities, affect metal accumulation rates.³⁷

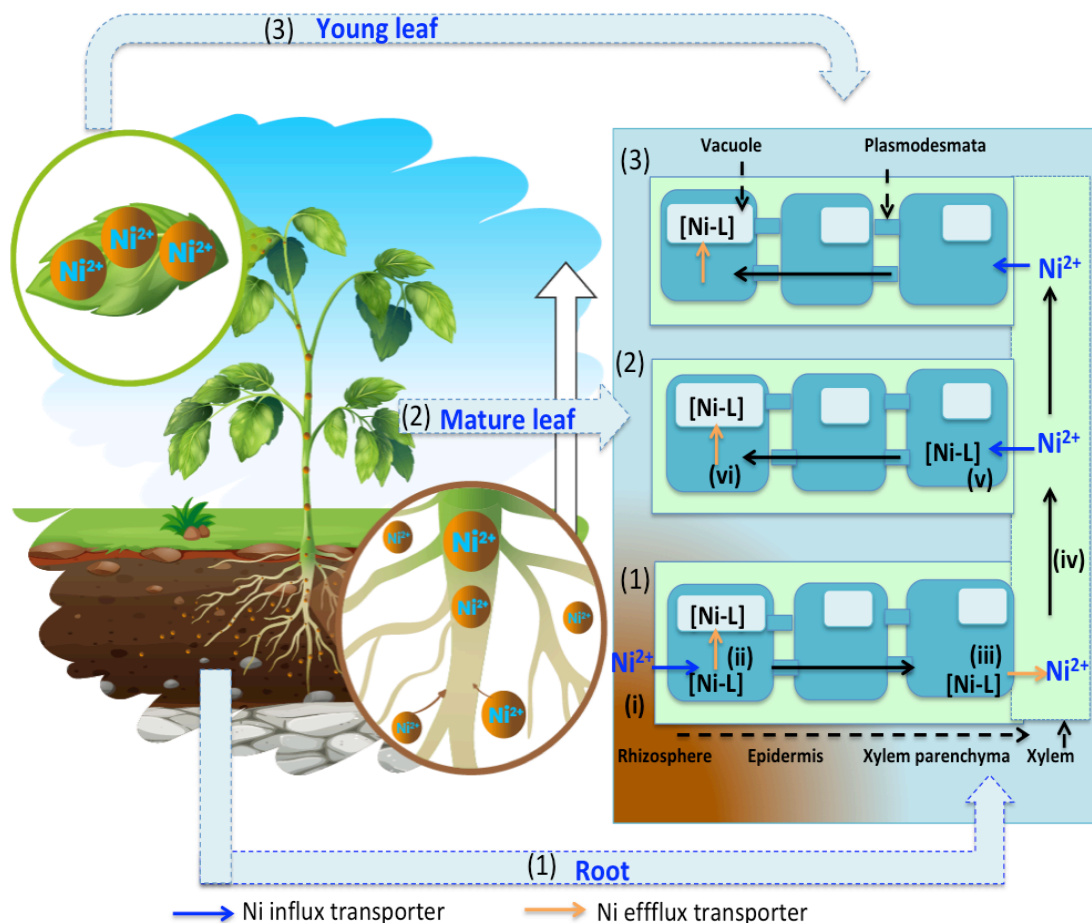


Figure 1.3: Biological pathways associated with nickel accumulation rates in plants

Although hyper-accumulators are able to extract relatively large amounts of Ni from contaminated land (up to 1,000 mg/kg dry tissue), they might not be suitable for soils with multiple contaminants.^{43,44} In such cases, fast-growing and high-biomass yielding plants including willow (*Salix* spp) or poplar (*Populus* spp) trees can be used to extract a wide range of metals from soil.⁴⁵ Harvested biomass can be used as a feedstock for production of bio-energy or bio-materials.^{46,47-49} but recovery of metals from ashed biomass waste is an inefficient, and prohibitively costly process that still needs technological development.

A significant added advantage of using phytomining is that it can help remediate contaminated land thus making it suitable for growing crops. Understanding how plants are able to selectively accumulate, or exclude, metals is fundamental for selecting and developing species that could then be applied for phytomanagement or phytomining.

Alternatively, the hyperaccumulation of metal ions in biological structures could offer an attractive pathway to engineer bio-composite materials. Various plant structures have been explored for the creation of hierarchical porous carbon structures, but not encapsulated metal bio-composites to date due to rather low mass loading of elements other than carbon in typical plant tissues.⁵⁰⁻⁵²

1.1.4. Plants inspired green biomaterials

Nature has been a source of bio-inspiration for scientists in the design of high-performance functional materials. Inexpensive and sustainable deconstruction or fractionation of lignocellulose into functional building blocks or platform molecules is key to achieving a green bio-based economy.⁴⁷ Biomimetic engineering involves synthesis of materials and systems utilizing principles of chemistry, biology and engineering, to mimic the biological processes and functions.⁵³ This offers a prevailing pathway to complex material architectures and enables exciting technology prospects beyond the reach of conventional synthetic chemistry. Biological structures that result from millions of years of natural evolution and selection have provided many essential materials for human civilization and have consistently inspired scientists to design and engineer materials for diverse technologies.^{46,50,54–58} Through photosynthesis, plants use sunlight energy to convert carbon dioxide, water, other nutrients and minerals from the soil into organic matter, with exquisite hierarchical structures that are not readily accessible in synthetic materials.^{57,58} Plant cell walls constitute the majority of lignocellulose biomass and serve as a renewable resource of biomaterials, biochemical and biofuel (Fig.2).⁵⁴ Lignocellulose biomass is the most abundant form of land-bound biomass and, as such, is a massive source of renewable reduced carbon.^{46,54,55} More than 80% of the mass of lignocellulose comes from three of its constituent biopolymers: lignin (15–30% (wt/wt), dry basis), cellulose (35–55% (wt/wt), dry basis), and hemicellulose (10–35% (wt/wt), dry basis) (Fig.2).^{54,55}

The monomers of these biopolymers represent potential feed-stocks for our green chemical industry and include glucose from cellulose, predominantly xylose from hemicellulose, and aromatic molecules from lignin (**Figure 1.4**).⁵⁵ To acquire these feedstocks, the biomass is usually, firstly separated to its individual biopolymers (cellulose, hemicellulose, and lignin) through pretreatment and then catalytically upgraded to value-added chemicals and fuels.^{54,56,58,59} However, this process is associated with several disadvantages, including complex separation, loss of biomass functionality, and high-energy consumption.⁵⁹ Therefore, the total or direct

transformation of lignocellulose biomass into valuable materials and chemicals in a single step process has drawn immense attention.⁵⁹

Lignification physically strengthens secondary walls; however, the presence of these inflexible polyphenols and their connection with carbohydrate components contributes to the biomass recalcitrance that renders the feedstock resistant to enzymatic hydrolysis during its conversion to biofuel.⁶⁰ Lignin primarily packs with xylan in a non-flat conformation *via* non-covalent bonds and partly binds the junction of the flat-ribbon xylan and cellulose surface as a secondary site.⁵⁴ All fragments are uniformly mixed in softwoods; enabling water retention even around the hydrophobic aromatics.⁵⁴

The secondary cell wall is assembled by carbohydrate and aromatic constituents, with remarkable complexity and variability. Each elementary cellulose microfibril contains eighteen 1,4- β -glucan chains, which are held together by a hydrogen-bonding network.⁶¹ Hemicellulose, comprising xylan, glucuronoxylan, arabinoxylan, and glucomannan, are highly variable in their monosaccharide composition and linkage pattern.^{56,57} Xylan is among the most common hemicelluloses, and its backbone comprises β -1,4-xylose units in a wide range of conformations, with substitutions by arabinose (Ara) or glucuronic acid (GlcA), and modifications by acetyl (Ac) groups.⁵⁴ Lignin contains guaiacyl (G), syringyl (S), and *p*-hydroxyphenyl (H) phenolic residues, which are interconnected by different types of covalent linkers such as β -O-4 ether-O-aryl, β - β' resinol, and β -5' phenylcoumaran.^{54,62} Conceptually, the mechanical framework of crystalline cellulose is dispersed in a matrix formed by hemicellulose and lignin, as shown in **Figure 1.4**. These findings show the principles of polymer interactions underlying the heterogeneous nature of lignocellulose, which may direct the realistic design of more efficient biomass-conversion pathways. However, current conversion strategies rely on high-temperature hydrogenolysis by synthetically supported metal catalysts, leading to products.⁵⁶

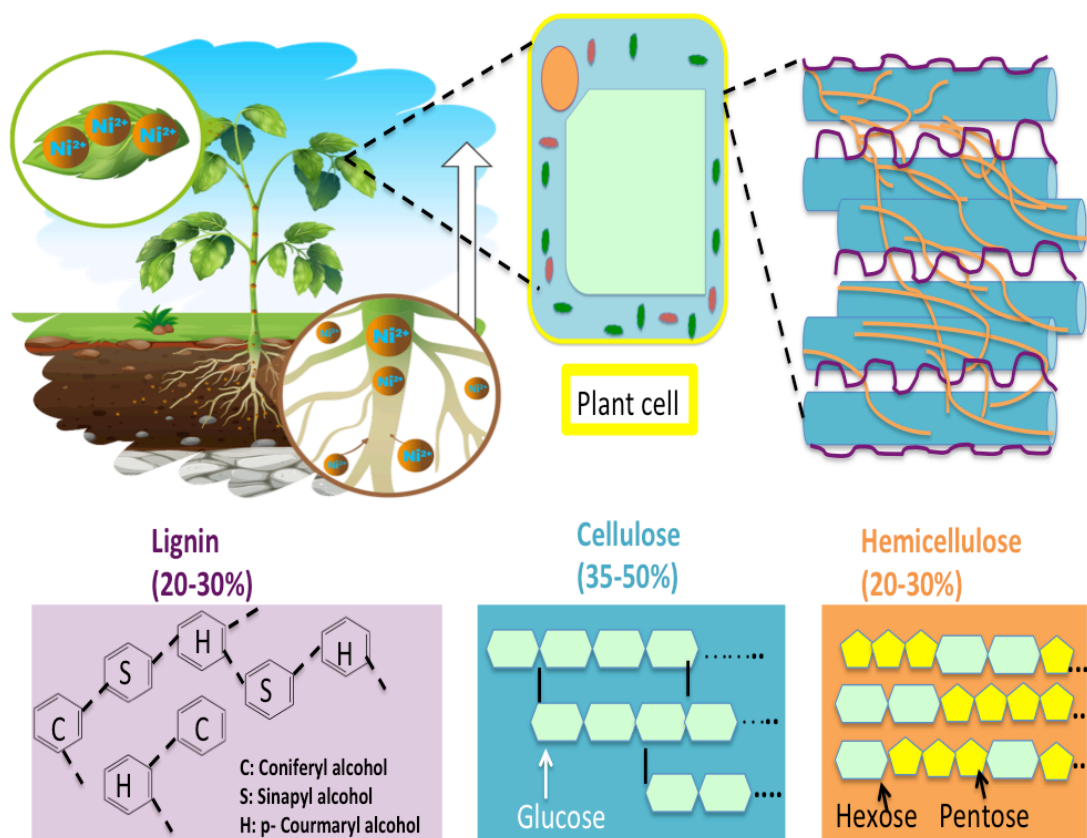


Figure 1.4: Conceptual framework of biopolymer interactions underlying the heterogeneous nature of lignocellulose

Nature has long developed the ability to combine brittle minerals and organic molecules into hybrid composites with exceptional functional capabilities.^{50,54} Recently, various lignocellulose derived chemicals and composite materials with remarkable performances fabricated by modifying the microstructure of the natural woods such as combining wood-derived cellulose with synthetic materials or conversion of wood-derived chemicals for ink production.^{53,57,58} The lignocellulose derived chemicals and materials have inherent exceptional advantages, such as renewability, biodegradability, exceptional toughness, and the prospect for novel functionalities.⁵³ The low-cost and abundant raw materials also provide an ample source for the high-performance lignocellulose derived materials with promising applications. For instance, researchers fabricated a carbon sponge directly from natural balsa (*Ochroma pyramidale*) wood for applications including batteries, flexible electronics and catalyst supports.⁵⁷ While this study is of huge significance,

a massive challenge to develop high-performance, all-green bulk materials from renewable and sustainable building blocks still remains.

As discussed in **section 1.1.2**, although metal-rich biomass can be used as a feedstock for production of bio-energy or bio-materials there are significant issues regarding recovery of metals from the metal-concentrated bottom ash, which is currently usually disposed of in landfills.^{46,47-49}

Over the past few years, the development of catalytically active materials derived from biomass has attracted huge attention, owing to their unique qualities of widespread availability, natural abundance and renewability, and relatively low-cost.^{47,48,59,63,64} To date, several synthetic procedures have been reported for fabricating bio-catalysts that contain metals including wet impregnation, ion-exchange, co-precipitation, reduction, high-temperature pyrolysis and atomic layer deposition.^{65,66} However, these protocols focus on artificial incorporation of noble and non-noble metallic species onto bio-derived carbon materials.^{63,67} This study focuses on developing metal-containing biocatalysts from plants that have taken up nickel through natural, biological processes. This process allows both the recapturing of a limited, natural resource, remediation of land, and once the catalyst is used-up, the metal can be reused, presenting a sustainable, circularity. In this context, it is envisioned the development of phytocat materials, prepared using a simple, one-step protocol using plant biomass rich in nickel accumulated by the plant during growth on nickel contaminated wastelands.

1.2 Thesis aims

1.2.1. Development of carbon supported non-noble metal catalysts

Carbon based materials have been extensively applied in the interdisciplinary fields covering catalysis, metallurgy, environmental remediation, energy storage and conversion, and drug delivery due to its tunable physicochemical properties.^{27,68–72} The development of metal impregnated carbon was first accomplished in order to increase the catalytic activity of the carbon itself, thereafter carbon materials have been used industrially as catalyst or catalyst support.^{73,74} In addition to a tunable surface chemistry, carbon based materials present several advantages to be used as catalyst support, such as (i) an easy reduction of the metallic phase; (ii) a good resistance to acids and bases; (iii) a stable structure to high temperatures; (iv) lower cost than that of other conventional supports, such as alumina and silica.^{74,75}

The first works on the understanding of the surface chemistry of carbonaceous materials and its involvement in catalyst preparation and even catalysis appeared in the 1980s. Some pioneering papers were published during this period, related to the influence of surface functionality on the preparation and their activity.^{76–78} The field of carbon nanomaterials for catalysis has been rapidly expanding. This is mainly due to the (re) discovery of innovative carbon materials and the emergence of different demanding applications, particularly in the field of energy, environment, and biomass conversion.^{70,71,79} In most applications, the metal nanoparticles are the active centers; however, in some cases both the supported metal and the support itself function as a catalyst. The support effects on the catalytic properties of metallic particles are related to (i) changes due to metal particle charge, (ii) effects related to variations in particle shape and crystallographic structure and, (iii) appearance of specific active sites at the metal–support boundary.⁸⁰

Because of the limited abundance of noble metals and their instability, there is an emergent effort to explore new types of non-noble metal catalysts. In nature, many enzymes contain redox-rich 3d transition metal centers with ligand coordination, such as Fe, Cu, Ni, and Co, which enable high turnover rates and superior selectivity in

several biochemistry reactions.^{81,82} To mimic the enzyme activity, organometallic complexes based on non-noble metals have been extensively explored as catalysts for quite some time.^{83,84} Despite many successes, the organometallic complexes have the intrinsic problem of poor recyclability and limited stability under harsh chemical conditions.^{82,85} Carbon-supported non-noble metals have recently attracted significant attention for the promotion of various reactions owing to their low cost and potentially high activity and stability.^{68,70,75,86}

Pyrolysis is one of the most popular methods for preparing carbon-based catalysts.^{46,87,88} Factors including pyrolysis temperature, temperature ramping rate, and reaction time play major roles in determining the particle size, surface area, and dopant content of the catalysts.^{75,87,89–91} For example, a high pyrolysis temperature usually improves the graphitization degree of carbons, which is advantageous for electrical conductivity, whereas an excessively high pyrolysis temperature results in the loss of unstable heteroatom dopants and degeneration of surface areas.^{50,92} Therefore, it is necessary to adjust the pyrolysis conditions to optimize the physicochemical properties of carbons. Although pyrolysis is a scalable and simple method for preparing carbons, its reaction time is relatively long, which potentially leads to the aggregation of transition metal species.^{89,93,94} Fast heating technologies, such as microwave heating has gained considerable attention to resolve this problem because of its advantages such as a fast reaction time and high heating efficiency.^{89,95,96}

A promising route towards achieving sustainable catalysis could be realized by the use of abundant materials (including non-noble metals), novel production strategies involving energy efficient processes (such as microwave heating), and biological design that includes biodegradation at end of life (biocarbon extracted from biomass feedstock), which is one of the aims of this thesis (**Aim 1**). Biocarbon, also known as biochar, has emerged as a new sustainable material for multiple applications, including the development of next-generation functional carbon materials for potential applications in energy storage, catalysis and filtration devices.^{71,97,98} Innovative sustainable resources such as bio sourced materials can be utilized as the matrix and support in bio-composites to minimize the use of non-renewable resources and to make better use of waste streams.⁹⁸ Modern advancements in bio refinery

concepts create new opportunities with such waste streams that can be valorized in the fabrication of a diverse range of biocomposites.⁹⁸

1.2.2. Catalytic hydrogenation of platform molecules

Interestingly, to alter the activity and stability of non-noble metal-based catalysts, sets of such nanocomposites have been developed by pyrolysis of a mixture of biomass and metal precursors at high temperature (>600 °C).^{64,65,98,99} Surprisingly, many examples showcase that these non-noble metal-based catalysts exhibited extraordinary catalytic performance in terms of activity, selectivity, and stability for various organic transformations in a green and sustainable approach.^{86,91,100,101} Among these organic transformations, catalytic hydrogenation has attracted remarkable attention and made great achievements.^{65,102–104} Selective catalytic hydrogenation has wide applications in both petroleum refining and processing and fine chemical industries.^{105–107} While most catalytic hydrogenations rely on noble metals such as Pd and Pt, the high cost and low availability of these metals have caused scientific interest to shift towards non-noble metals for hydrogenation catalysts.^{65,67,105,108,109}

Earth-abundant first-row transition metals such as Fe, Co, and Ni have received considerable attention due to their low price, low toxicity, and unique catalytic properties.¹⁰⁵ In the field of catalysis, Ni has a long history with its first application for hydrogenation, which led P. Sabatier to earn the Nobel Prize in chemistry in 1912.^{110,111} However, the selective hydrogenation of a target functional group in the presence of other reactive functional groups in a molecule is difficult to achieve because most transition metal catalysts cannot recognize and preferentially interact with the target group.^{105,112} For this reason, great efforts have been made to achieve heterogeneous Ni-based catalysts with high activity for chemoselective hydrogenation reactions.^{65,68,113–115}

Chemoselective hydrogenation is defined as preferential transformation of one of the functional groups (or substrate) when two or more functional groups coexist in one substrate, or different unsaturated substrates are present in the catalytic system.¹¹²

One of the challenging substrates for chemoselective hydrogenation reactions are α,β -unsaturated carbonyls, where both C=O and C=C groups coexist in one molecule.¹¹² Generally, the C=C bond is more sensitive and prone to reduce based on both thermodynamic (the bond energy is 715 kJ/mol for C=O and 615 kJ/mol for C=C) and kinetic considerations, including the mode of adsorption and desorption of the substrate onto the metallic surface.¹¹² Industrially, metal hydrides (e.g., NaBH₄) or Cu–Cr based catalysts are employed in this transformation, which, however, suffered from environmental issues.¹⁰⁵ From the technical and economic point of view, the chemoselective hydrogenation of α,β -unsaturated carbonyls over supported metal catalysts is a mild, efficient, and straightforward approach. The key to the selective hydrogenation relies on the fabrication of efficient and selective catalysts.¹¹⁶ Usually, α, β -unsaturated carbonyls can be adsorbed on the catalysts *via* different configurations depending on the type of the active metals and the size of the metal ensembles.^{105,117} For example, on an extensive Pt(111) surface, either C=C or C=O bonds can be adsorbed *via* di- σ or π mode, respectively (**Figure 1.5a-c**).¹¹⁷ The C=O bond can also be solely adsorbed *via* the end-on mode (**Figure 1.5d**).^{105,117} In addition, because C=C and C=O groups are conjugated in one molecule, they can be co-adsorbed adopting the 1,4-di- σ modes (**Figure 1.5e**).¹¹⁷ Among these adsorption patterns, the C=C di- σ mode and the 1,4-di- σ mode both lead to the saturation of C=C group, while the end-on mode can facilitate the preferential hydrogenation of C=O bond.¹¹⁷

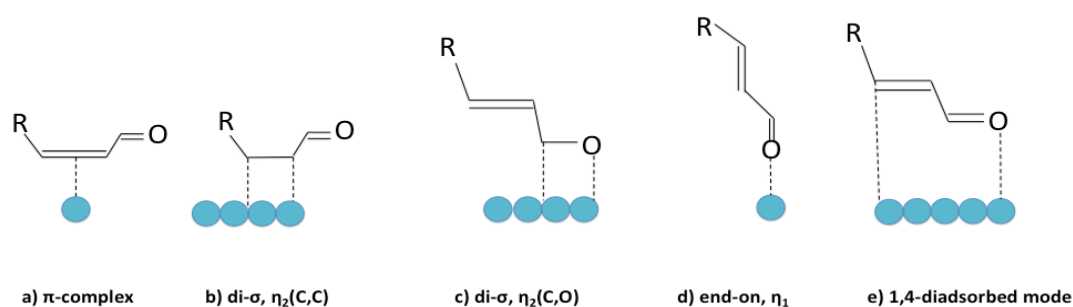


Figure 1.5: Adsorption arrangements of α,β -unsaturated carbonyls on metal nanoparticles. Adapted from references.^{105,117}

In this study, catalytic hydrogenation of α , β -unsaturated carbonyl group were performed on the model platform molecules derived from lignocellulose, which is another aim of this thesis (**Aim 2, Figure 1.6**). Lignocellulose derived chemicals can serve as platform molecules for the production of a wide range of value-added chemicals, with implementation motivating the transformation towards a sustainable chemical industry.^{55,118,119} Among these, cinnamaldehyde (CAL) which represents a typical model compound of the coniferyl aldehydes derived from lignin was tested (**Section 4.1, Chapter 4**).¹⁰⁸ Furfural also deserves attention as a potential platform as it offers a rich source of derivatives that are potential biofuel components and hence was considered (**Section 4.2, Chapter 4**).^{52,118} Furthermore, the high potential of Levoglucosenone (LGO) as both a platform molecule and a precursor of CyreneTM, a green aprotic polar solvent, have caught the attention of several research groups as well as industries.^{109,120,121} An enduring interest in exploration and expansion of the chemical utility of LGO formed the basis of this study as well and was therefore tested further for catalytic hydrogenation reaction (details **in section 4.3, Chapter 4**).

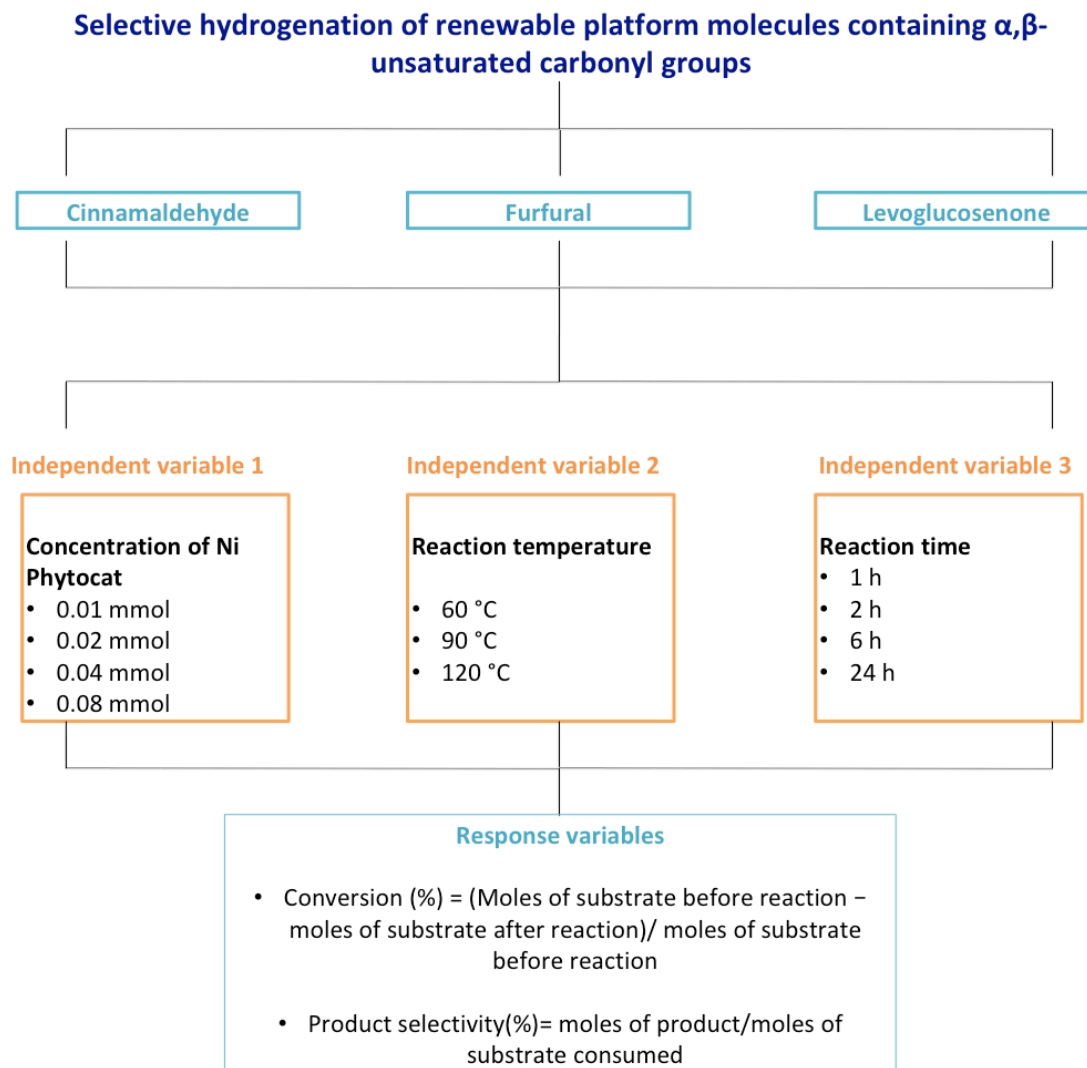


Figure 1.6: Research overview of the thesis (Aim 2)

1.2.3. Catalytic de-polymerization of plastics

The production of plastics is an energy intensive process, accounting for 62–108 MJ kg⁻¹ of feed-stocks energy.^{122,123} Around 4% of fossil-fuel extracted annually (natural gas liquid fraction or low-value gaseous fraction from petroleum refining) is presently used as raw materials for plastics.¹²² By 2050, the global production of plastics is expected to account for 20% of petroleum consumed globally and 15% of the annual carbon emissions.¹²² Currently, less than 10% of the total plastic waste generated (>6300 Mt) is recycled, yet even if increased, this is not a long-term solution.^{124–126} Furthermore, repeated recycling results in decreased

mechanical quality, alongside issues of mixing of different plastic types and contamination with additives (plasticizers such as phthalate esters, flame retardants such as polybrominated diphenyl ethers and stabilizers such as phenolic antioxidants), which reduces product quality.^{127,128} Current recycling processes also add substantially to the energy burden of using plastics.^{127,129–131} New strategies are needed for the selective de-polymerization of plastics, either to their constituent monomers for recycling into virgin plastics, or as feedstocks for other chemical processes (**Figure 1.7**).^{127,129,130,132–134}

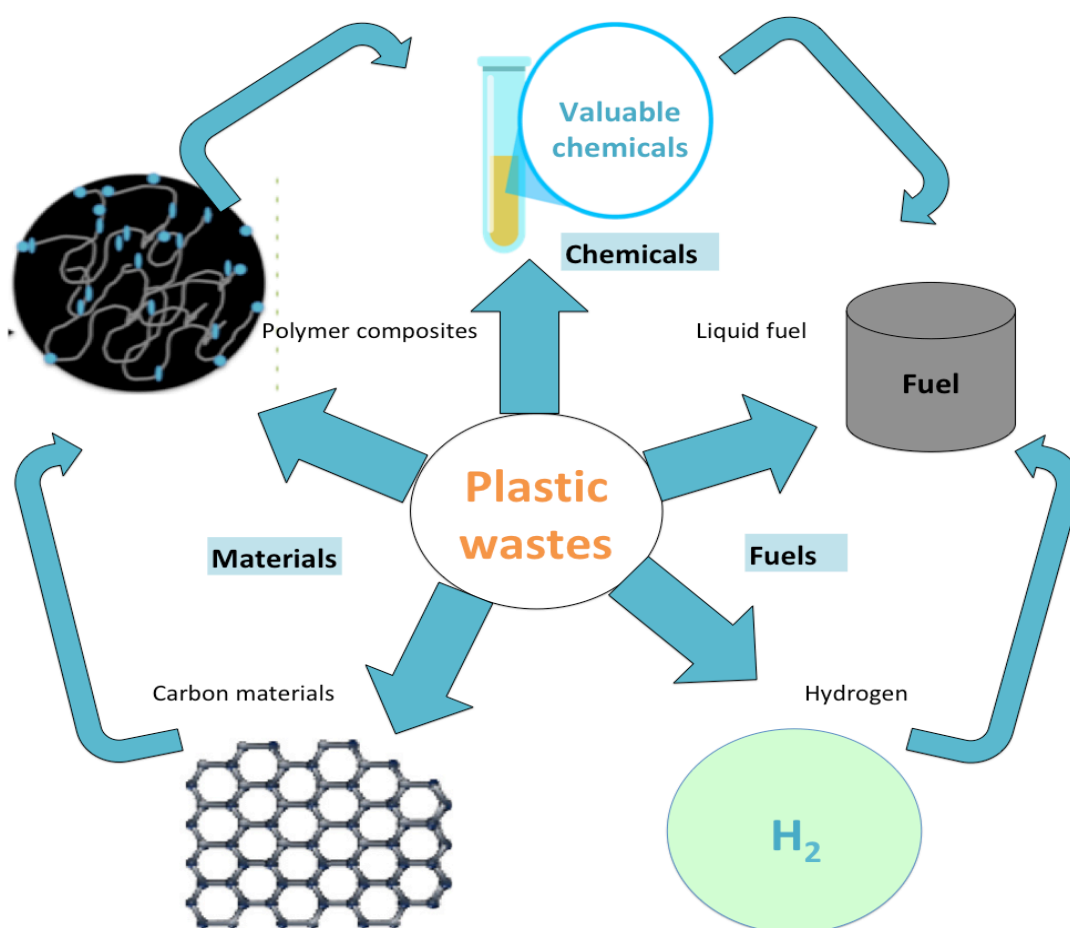


Figure 1.7: Prospects of production of high value materials and chemicals from de-polymerization of plastics

To this end, the microbial degradation of hydrolysable plastics; for example, polyethylene terephthalate (PET), polycarbonate and polyurethane is more likely in the environment than for non-hydrolysable polymers (polystyrene (PS), polyethylene (PE) and polypropylene) that are predominantly found as pollutants in marine environment (**Figure 1.8**).^{135,136} Functional groups, such as esters, carbonates, and urethanes, allow much faster degradation *via* hydrolysis than plastics without functional groups, such as PS, even though they contain tertiary C–H bonds.^{135,137} Moreover, due to inadequate recycling, most of the polystyrene waste generated ends up in oceans.^{138–140} Recent studies revealed that styrene oligomers (SOs) were leached from PS plastic weathering in marine environments even at low temperatures.^{139,141} A large variation in global SOs concentration was observed (10 - 31,400 $\mu\text{g kg}^{-1}$), with a global average value of 3679 $\mu\text{g kg}^{-1}$ in coastal beach sand samples.^{142,143} Currently, 1.2×10^7 MT of PS debris is drifting in the oceans of which 20% degraded to SOs.¹⁴⁴ These non-hydrolysable plastics such as PE and PS which are inert towards degradation by chemical solvolysis or enzymatic methods, unlike the carbonyl-containing bonds of hydrolysable plastics like polyesters, comprise more than half of the plastics produced globally (> 360 million tonnes in 2019).¹³⁷ Therefore, depolymerization of PE and PS will be studied in detail in this research.

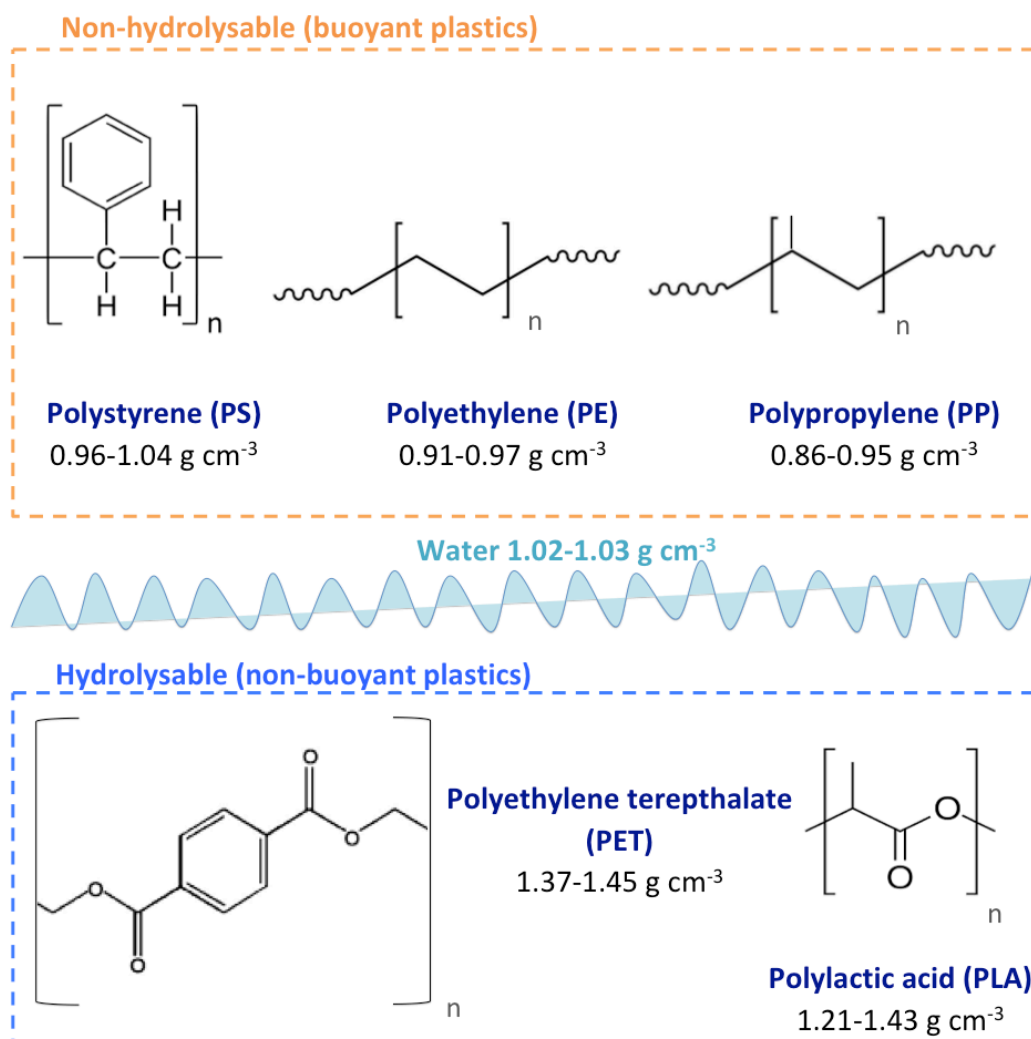


Figure 1.8: Hydrolysable and non-hydrolysable plastics. Material densities of plastics are indicated in g cm⁻³.

Despite these challenges, the concept of creating high value products from these plastics has gained huge attention.¹⁴⁵⁻¹⁴⁹ Pyrolysis is currently the most established technology for upcycling plastic waste and it possesses several advantages over other methods.^{126,130,150-152} Apart from being flexible to low quality waste plastic upcycling, this technology is also tolerant toward mixed plastic streams.^{92,126,153,154}

Madorsky and Straus were one of the first to perform PS pyrolysis in a laboratory-scale batch reactor (340-420 °C) and reported a maximum styrene recovery of 42 wt.% at 420 °C.¹⁵⁵ The earliest works by Kim *et al.* using laboratory-scale reactors proved the concept of monomer recovery through pyrolysis of PS.¹⁵⁶ Later, a

microwave laboratory-scale reactor was used to pyrolyze PS (464-678 °C), and reported a styrene yield of 66 wt.%.¹⁵⁷ Similarly, Bartoli *et al.* used a microwave laboratory-scale reactor at a temperature range of 301–536 °C and reported a styrene yield of 60.6 wt.%.¹⁵⁸ Even though data is limited, advancements in PS pyrolysis on an industrial scale with several demonstration projects have been announced.^{159,149, 154} Mostly reactors such as a twin-screw and a microwave reactor have been used to process PS, subject of this study.^{160–162}

The linear approach to resource utilization has led to the accumulation of waste plastic (around 200 million metric tons generated annually) in the environment over decades.¹⁴⁰ Thus to realize the goal of a carbon-neutral society, closing of carbon and hydrogen cycles in plastics would be extremely important.¹³² There exists an imbalance between the production and end-of-life treatment of plastic wastes.¹⁶³ Among many plastic materials that are commercially manufactured, polyolefins (>90% of packaging materials) account for nearly half of world plastic demand, with 36 % of all plastics being polyethylene (PE), subject of this study.¹⁶⁴ Polyethylene is designed to resist the tough conditions of high temperature and pressure, mechanical forces, and chemical corrosion, and to maintain these properties throughout their consumption. This physical and chemical stability makes PE recycling an ambitious challenge.¹³⁵ The global spread of COVID-19 has further worsened the problem by increasing the use of single-use personal protective equipment (PPE) and food packaging.¹⁶⁵ Chemo-catalytic strategies to produce high value chemicals, fuels, and monomers hold the promise of positively transforming waste plastic, which is barely addressed by mechanical recycling and incineration, into an opportunity.^{125,128,145,164}

Both de-polymerization of plastics into value-added chemicals and carbonization to high value carbon materials will relieve environmental pollution and reduce demand for virgin resources.^{166,167} However, these methods are often cost prohibitive, energy intensive and require high operating temperatures, often leading to uncontrollable product distribution with little product value other than as a low-grade fuel.^{129,168} For instance, noble metal-catalyzed hydrogenolysis of polyethylene normally requires high reaction temperatures and durations. Bifunctional metal/acid catalysts are an attractive option because the acid catalyst can activate C–C bonds, while the metal

catalysts possess high hydrogenation ability and can inhibit catalyst coking. For example, Liu and coworkers reported a Pt/WO₃/ZrO₂+HY(30) zeolite catalytic system for mild hydrocracking in low density polyethylene (LDPE) melts to produce a mixture of gasoline, diesel, and jet fuel range hydrocarbons.¹⁶⁸ When using Pt/WO₃/ZrO₂ or HY(30) alone as catalyst, the conversion of LDPE is relatively low even at 250 °C. Edwards and co-workers used microwaves, together with inexpensive iron-based catalysts (FeAlO_x) as microwave absorbers to convert a mixture of mechanically pulverized, real-world plastic waste into hydrogen and multi-walled carbon nanotubes.¹⁶⁹ However, these bifunctional metal/acid catalyst-based protocols focus on the use of either additional H₂ or artificial synthesis of noble and non-noble metallic species onto different supports.

Therefore, the aim of this study is to develop a protocol to accelerate depolymerization of the non-hydrolysable and some of the least recycled polymers (PS and LDPE) into high value hydrocarbons without the need of molecular hydrogen or artificially fabricated metal catalysts (**Aim 3, Figure 1.9**).

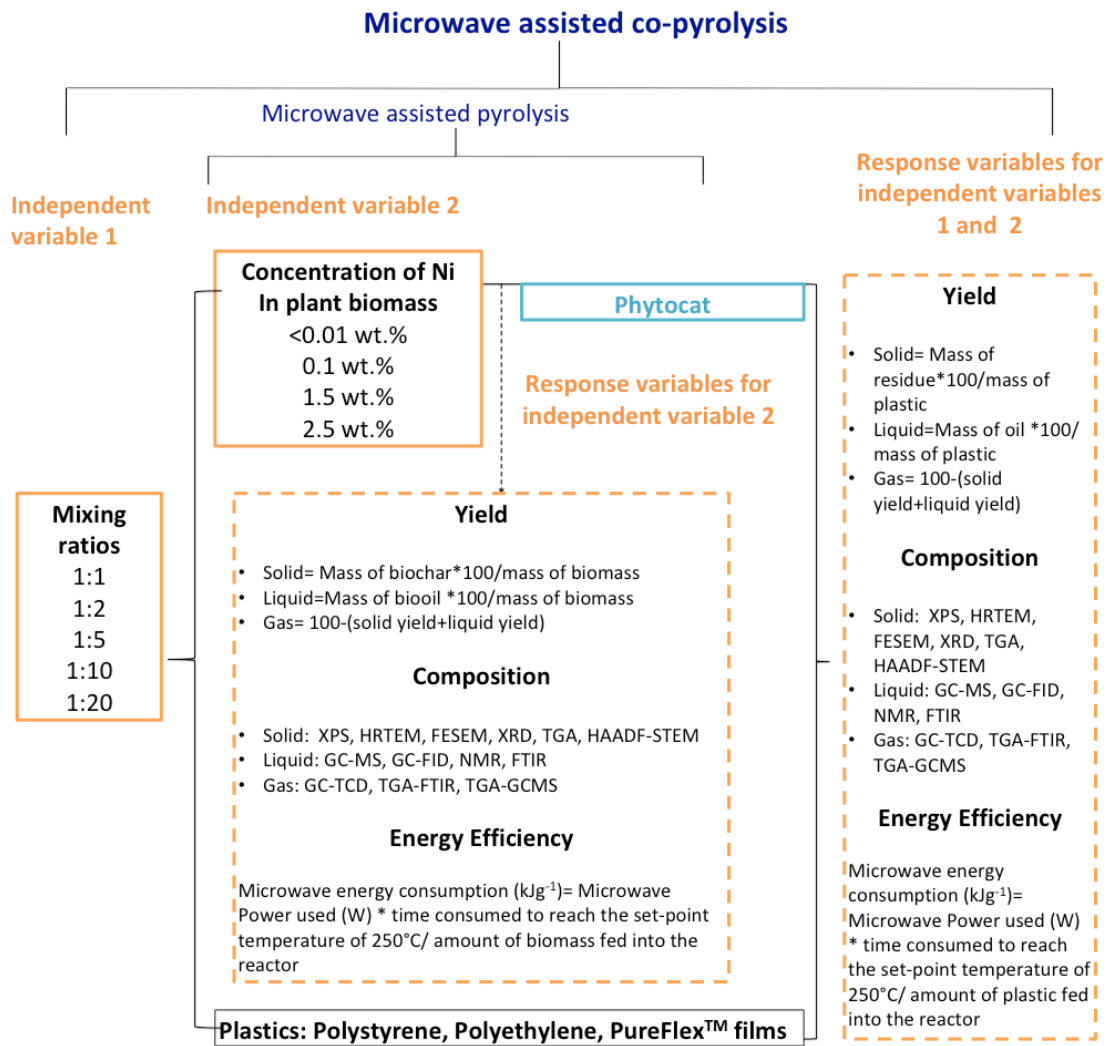


Figure 1.9: Research overview of the thesis (Aim 3)

Chapter 2 Experimental

2.1 Preparation and characterization of phytocat

Two varieties of biomass were used in the experiments; one was the Ni hyperaccumulator plant species (*Alyssum murale* and *Stackhousia tryonii*, collected from field on nickel-rich soils in Greece and New Caledonia, respectively). These hyperaccumulator plant species were procured with the assistance of Dr Antony Van der Ent of the University of Queensland, Australia, Dr Chris Anderson of Massey University, New Zealand, Dr. Baptiste Laubie and Dr. Guillaume Echevarria from University of Lorraine by their kind assistance in the field collection of the hyperaccumulator species. Another was the hydroponically grown willow plant species (*Salix viminalis* procured from Yorkshire willow, UK) for the preparation of Ni based phytocat and Ni free controls (<0.01 wt% Ni). All Ni hyper-accumulators need trace quantities of Ni for growth; therefore, non-hyper-accumulator species were used as controls.¹⁷⁰

2.1.1. Hydroponic growth of nickel dosed plant biomass

Willow rods (*Salix viminalis*) were grown hydroponically for six weeks using the Aeroflo system (General Hydroponics) then dosed with 100 mg kg⁻¹ of NiNO₃.6H₂O (Sigma Aldrich) solution for two weeks (**Figure 2.1**).¹⁷⁰ Metal accumulation was determined in leaves and stems using an inductively coupled plasma optical emission spectrometer (ICP-OES, Agilent 700 series) (**Appendix A, Table A1**). All other chemicals were purchased from Sigma-Aldrich and were used as received unless otherwise stated.

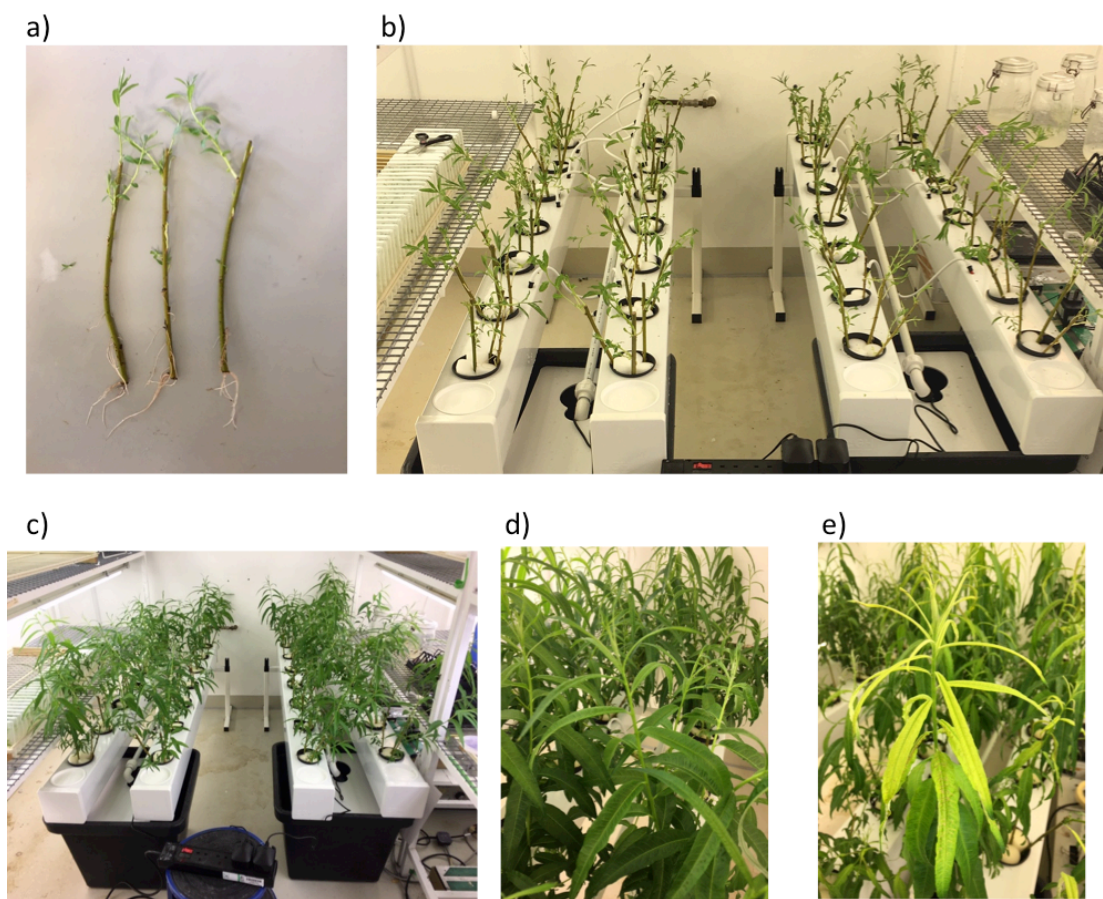


Figure 2.1: Images of willow rods at different stages of its growth pre- and post-dosing

2.1.2. Microwave assisted pyrolysis of phyto-accumulated nickel rich biomass

Firstly, microwave-assisted pyrolysis of air-dried, ground leaf tissues of the above mentioned plant species was performed on a CEM Discover, equipped with 35 ml quartz vial under N_2 at 250 °C and 200 W to produce biochar with different Ni loadings (termed as phytocat). The feedstock was converted into vapors, which were passed through a condenser and collected as liquid oil. The mass yield of biochar and biooil produced were measured and the gas yield calculated as the mass balance of the original sample. The total conversion was evaluated based on the sum total of liquid and gas yields. After the successful extraction of biooil and biogas, the bio-char containing biologically bound nickel with different metallic loadings was used as catalyst for further experiments.

2.1.3. Thermo-gravimetric analysis with fourier transform infrared (TGA-FTIR)

The thermal decomposition profiles were monitored using the thermo-gravimetric analysis with fourier transform infrared (TGA-FTIR) analysis in the temperature range of 30 °C to 700 °C at a heating rate of 10 °C min⁻¹ under nitrogen atmosphere of 100 ml min⁻¹ flow rate. The analysis was done using the plant biomass (with and without Ni). TG-IR was carried out using Netsch STA409 linked to a gas cell in a Bruker Equinox 55 infra-red spectrometer by a heated gas line. The volatiles released during pyrolysis were immediately transferred to the FTIR gas cell and analyzed using a FTIR equipped with an MCT detector within the range of 500–4000 cm⁻¹ at a resolution of 4 cm⁻¹.

2.1.4. High-angle annular dark-field -scanning transmission electron microscope (HAADF-AC-STEM)

High-angle annular dark-field -scanning transmission electron microscope (HAADF-AC-STEM) images were acquired using a 200 keV JEOL 2200FS scanning transmission electron microscope with a field emission gun. Sample preparation for TEM analysis was done by crushing a few grains of the sample between two microscope glass slides and dusting with powder holey carbon films supported by 300 mesh TEM Cu grids (Agar scientific, S147-3). Excess powder was then removed by flicking the grids onto the edges of the glass slides under a fume hood before transfer to single tilt TEM sample holders.

2.1.5. Transmission electron microscopy (TEM)

Transmission electron microscopy (TEM, JEOL 2010) was used under the accelerating voltage of 200 kV to investigate the microstructure of phytocat material. The TEM samples were prepared by suspending in methanol, followed by sonication

for 10 minutes. A uniform thin layer of the sample was deposited on a carbon grid support followed by air-drying.

2.1.6. Field-emission scanning electron microscope (FE-SEM) equipped with an energy-dispersive X-ray (EDX) spectrometer

Microstructural and chemical information of phytocat was obtained by using a field-emission scanning electron microscope (FE-SEM) equipped with an energy-dispersive X-ray (EDX) spectrometer (JSM-7800F PRIME, JEOL Ltd.).

2.1.7. X-ray photoelectron spectroscopy (XPS)

Elemental composition and valence near the surface were measured using XPS (AXIS Ultra DLD, Kratos. Inc.), and the data were analyzed using CASA XPS software. Dr. David Morgan, University of Cardiff, UK, conducted the analysis.

2.1.8. X-ray diffraction (XRD)

XRD was performed at operating voltage of 40 kV, current, 40 mA, scan speed of 0.1 sec/step and the scan scope from 10 Θ to 90 Θ using a Bruker AXS D8 Advance.

2.1.9. Solid-state nuclear magnetic resonance spectroscopy

Solid state ^{13}C cross-polarization magic angle spinning (CPMAS) NMR was performed on the 400 MHz solid state magic angle spinning spectrometer.

2.1.10. Microwave assisted hydrolysis of phyto-accumulated nickel rich biomass

Microwave assisted hydrolysis on air-dried, ground leaf tissues of the above-mentioned plant species was performed on a CEM Discover, equipped with 35 ml quartz vial. Briefly, 100 mg of biomass was hydrolyzed in water (10 mL) at 100 W and 120°C for 10 min. The produced hydrochars and hydrolysates were collected for further characterization using the above mentioned material characterization techniques and HPLC analysis respectively.

For HPLC analysis, samples were initially syringe filtered (< 0.45 μm) before being injected into an Agilent Hi-Plex H column (internal diameter and length of 7.7 and 300 mm respectively, particle size = 8 μm) running at 60 $^{\circ}\text{C}$ in isocratic mode with pure water (0.400 mL min^{-1}) as the eluent. Detection was achieved using an Agilent 1260 Infinity II Series Refractive Index Detector operating at 55 $^{\circ}\text{C}$. Dr. Richard Gammons (Green Chemistry Centre of Excellence, University of York) conducted the HPLC analyses.

2.2 Application of the phytocat for hydrogenation of platform molecules

2.2.1. General procedure for hydrogenation

The liquid phase hydrogenation was tested in a stainless steel multipoint (6 \times 10 mL pots) reactor (manufactured at chemistry workshops, University of York). For a typical test, substrate (cinnamaldehyde or furfural or levoglucosenone) (1 mmol), anisole (internal standard, 0.5 mmol), 10-50 mg of catalyst (0.01-0.08 mmol Ni) and iso-propanol (solvent, 5 mL) were loaded into the reactor. The reactor was sealed and purged with purified hydrogen and then pressurized to 4.0 MPa (99.999% purity) at room temperature. The reaction was conducted with stirring (250 rpm) at 60-120 $^{\circ}\text{C}$.

The reusability tests using phytocat-0.1 and phytocat-2.5 were performed to illustrate their stability and performance for at least four cycles. The catalyst was recovered, washed with isopropanol three times and dried overnight. The catalyst was then weighed and transferred in a stainless steel multipoint (6 \times 10 mL pots) reactor (manufactured at chemistry workshops, University of York). Following the same procedures, the reaction was carried out at 120 $^{\circ}\text{C}$ and pressurized to 40 bar H_2 . The sampling was done after 24 h of reaction, and the catalyst was recycled four times.

$$\text{CAL conversion (\%)} = \frac{\text{moles of CAL before reaction} - \text{moles of CAL after reaction}}{\text{moles of CAL before reaction}} \times 100\% \quad (1)$$

$$\text{Product selectivity (\%)} = \frac{\text{moles of product}}{\text{moles of CAL consumed}} \times 100\% \quad (2)$$

2.2.2. Gas chromatography coupled with mass spectrometry (GC–MS)

Gas chromatography coupled with mass spectrometry, GC–MS (JEOL AccuTOF-GCx plus, Agilent 7890B GC) was used for analysis of liquid products. The column used was Phenomenex ZB-5MSplus (30m x 0.25 mm id x 0.25um film thickness) with film composition of 5% Phenyl-Arylene, 95% Dimethylpolysiloxane.

The column oven was initially held at 45 °C for 1 min followed by a ramp at the rate of 5 °C min⁻¹ to 300 °C, and finally held at this temperature for 10 min to allow elution of all the compounds. Mr. Karl Heaton (Department of Chemistry, University of York) conducted the analysis. The constituents of samples were identified by comparing the mass spectra with national institute of standards and technology (NIST) research library. The response factor of each component was calculated using standard samples and was used to calculate the conversion and selectivity.

2.2.3. GC equipped with a flame ionization detector (GC-FID)

The reaction was stopped after a proper time (1-24h) and the products were analyzed using a GC (GC-2014, Shimadzu) equipped with a flame ionization detector (FID) and a capillary column (DM-WAX, 30 m × 0.32 mm × 0.25 μm).

2.2.4. Nuclear magnetic resonance spectroscopy (¹H-NMR and ¹³C-NMR)

After completion of the reaction, the solvent was removed under reduced pressure at 45 °C. The products were analyzed by ¹H-NMR and ¹³C-NMR spectroscopy in CDCl₃ solvent.

2.2.5. Fourier transform infrared spectroscopy (FTIR)

The products of the reaction were further characterized using FTIR (Perkin Elmer). Background scan was conducted before each sample is scanned. Samples were put on ATR crystal and scanned in the wavelength range of 600–4000 cm⁻¹.

2.3 Application of the phytocat for de-polymerization of plastics

2.3.1. Microwave assisted pyrolysis at varying ratios of phytocat and plastics

The phytocat produced using microwave pyrolysis was then mixed with plastics (PS, LDPE and PureFlexTM) respectively to produce mixtures (1:1, 1:2, 1:5, 1:10 and 1:20) by weight. Microwave pyrolysis of these mixtures (1g each) was performed on CEM Discover, equipped with 35 mL quartz vial at 250 °C and 200 W. The mass yields of biochar and pyrolysis oil produced were measured after every microwave run (up to 3 consecutive microwave runs) and the gas yield calculated as the mass balance of the original sample. The total conversion was evaluated based on the sum total of liquid and gas yields. Further, the de-polymerization efficiency of the phytocat materials was calculated based on the percentage conversion of polyethylene into de-polymerized products. The evolved gas was trapped using syringes (1 mL volume, Series A-2 pressure-lok precision analytical gas syringe) for qualitative analysis. The control experiments were carried out using willow bio-char without Ni (termed as control phytocat) and activated carbon. All the experiments were performed in triplicates.

2.3.2. Simultaneous thermal analyzer with gas chromatography equipped with mass spectrometry (TG-GC-MS)

The conventional study to monitor de-polymerization of LDPE was done using the simultaneous thermal analyzer with gas chromatography equipped with mass spectrometry (TG-GC-MS, Netzsch STA 449) profiles in the temperature range of 30 °C to 650 °C at a heating rate of 10 °C min⁻¹ under He. The analysis was performed using the phytocat materials or activated carbon and polyethylene mixtures (1:10 by weight).

2.3.3. Qualitative analysis of de-polymerization products

The qualitative analysis of gas was performed using an Agilent Technologies 7820A gas chromatograph, with a flame ionization detector (GC-FID), fitted with a Carboxen 1010 PLOT 30m x 0.53mm capillary column. Argon was used as the carrier gas at a flow rate of 2 mL/min with a split ratio of 10:1 and a 1mL injection. The initial oven temperature was 100°C (held for 2 minutes) and was increased at a rate of 25°C/min to 250°C and held at this temperature for 20 minutes, with a total run time of 28 minutes. Injection temperature was 200°C and the detector temperature was 250°C.

Product yields are expressed as per cent by weight of dry feed. The liquid and solid fractions were measured by weighing. Gas fraction mass was estimated by the difference between initial sample mass and sum of solid residue and liquid product mass.

$$\text{Conversion (\%)} = \frac{W_i - W_r}{W_i} \times 100 \dots\dots\dots(1)$$

$$\text{Yield of oil (\%)} = \frac{W_o}{W_i} \times 100 \dots\dots\dots(2)$$

$$\text{Yield of residue (\%)} = \frac{W_r}{W_i} \times 100 \dots\dots\dots(3)$$

$$\text{Yield of gas (\%)} = 100 - (\text{yield of oil} + \text{yield of residue}) \dots\dots\dots(4)$$

Here, W_i , W_o and W_r are defined as initial weight of plastic, weight of oil produced by microwave assisted pyrolysis of plastic and weight of solid residue after reaction, respectively.

The energy consumption analysis of microwave-assisted de-polymerization process was done in terms of energy consumption to pyrolyze unit g of feed to reach the set-point of $T = 250^\circ\text{C}$ at fixed MW power of 200 W, using the following equation

$$\text{Energy consumption (KJ/g)} = \frac{P (W) \times t (s)}{\text{Amount of feed-stock (g)}} \dots\dots\dots(5)$$

Chapter 3: The development of phytocat- structural and molecular insights

Parts of the work reported in this chapter (mainly **section 3.2**) have been published in:

- a) **Johar P**, Rylott EL, McElroy CR, Matharu AS, Clark JH. Phytocat—a bio-derived Ni catalyst for rapid de-polymerization of polystyrene using a synergistic approach. *Green Chemistry*. 2021;23(2):808-14.
- b) **Johar P**, McElroy CR, Rylott EL, Matharu AS, Clark JH. Biologically Bound Nickel as a Sustainable Catalyst for the Selective Hydrogenation of Cinnamaldehyde. *Applied Catalysis B: Environmental*. 2022; 121105.

The purpose of this Chapter is to investigate Aim 1 as described previously within **section 1.2.1**. Particularly, it deals with gaining the structural and molecular insights of the originally developed phytocat materials. The Chapter is divided into two main sections, primarily focusing on the results and discussion:

- (i) **Section 3.1**: The effect of phyto-accumulated nickel on de-polymerization of lignocellulose based on the unique interactions of the biologically bound Ni and the microwaves. This mainly involves the study of pyrolysis (section 3.1.1) and hydrolysis (section 3.1.2) protocols for the conversion of lignocellulose into value-added chemicals and materials.
- (ii) **Section 3.2**: Advanced material characterization of the developed phytocat materials to understand the unique interfaces of the biologically bound Ni in the plant matrix.

3.1. Effect of phyto-accumulated nickel on de-polymerization of lignocellulose

The process of the development of phytocat was initiated by dosing *Salix viminalis* (willow) with 100 mg kg^{-1} Ni for three weeks (as discussed previously in **Chapter 2; Figure 3.1**). Notably, the plants exhibited mild toxicity symptoms post dosing, notably the yellowing of younger leaves, which is known as chlorosis (see **Figure 3.1d**).¹⁷¹ *Salix viminalis* (willow) and the Ni hyper-accumulating plants (*Alyssum murale* and *Stackhousia tryonni* (collected from field on nickel-rich soils)) were used in this study. The *Salix* species contain a genetically diverse range of phenotypes, include broad variation in the ability to withstand Ni tolerance, and rate of Ni uptake.⁴⁵ The amount of Ni present within the biomass of each plant is determined by the biology of that species (including the gene-encoded metal transporters and associated detoxification enzymes).⁴³⁻⁴⁵ The biologically bound Ni catalysts (phytocat) were prepared using the ground plant materials in one- step, low temperature, microwave-assisted pyrolysis (MAP; 200W, 250 °C) to produce *S. viminalis* bio-char (0.1 wt% Ni, termed phytocat-0.1), *S. tryonni* bio-char (1.5 wt.% Ni, termed as phytocat-1.5), *A. murale* bio-char (2.5 wt% Ni, termed phytocat-2.5).¹⁷⁰ The control catalyst was prepared using *S. viminalis* bio-char that had not been dosed with Ni (<0.01 wt% Ni, termed as control phytocat). Metal accumulation was determined in leaves and stems using an inductively coupled plasma optical emission spectrometer (ICP-OES, Agilent 700 series) (see **Appendix Table A1**).

Phytocat as a good microwave absorber, aids in transferring the microwave energy leading to the *in-situ* synthesis of catalytically active Ni^0 from phyto-accumulated Ni^{2+} , which will be discussed in detail in **section 3.2**.³⁹

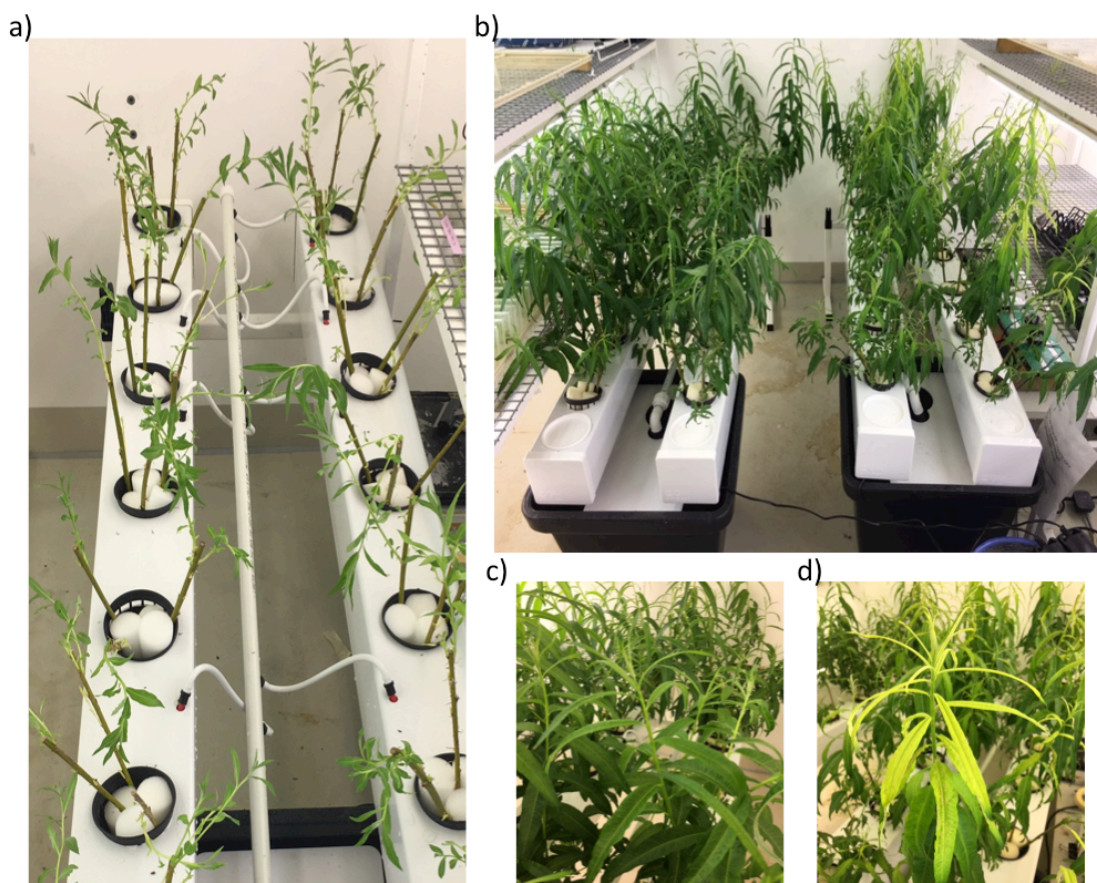


Figure 3.1: Aeroflo system (General Hydroponics) used to grow willow rods (*Salix viminalis*) a) Pre-dosing, b) Post-dosing (3 weeks duration) c) Undosed willow for preparation of control phytocatalyst and d) Dosed willow for preparation of phytocatalyst-0.1

In this work, the following observations were noted: first, the presence of biologically bound Ni brought about a higher heating rate (**Figure 3.2**), compared with the control experiments (using control phytocatalyst). Consequently, this increased the degree of pyrolysis, enhanced the secondary reactions of bio-oil and prevented the cracked products from reconstituting to form coke. Secondly, the interaction of microwaves and the biologically bound Ni enabled the early formation of bio-char, imposing the catalytic effect on the conversion of bio-oil into bio-gas *via* cracking or reforming, which will be discussed in detail in this chapter.

As summarized in **Figure 3.2**, during pyrolysis, as time progresses, the presence of biologically bound Ni (phytocat-2.5, phytocat-1.5 and phytocat-0.1) brought about the higher heating rate ($357\text{ }^{\circ}\text{C min}^{-1}$, $277\text{ }^{\circ}\text{C min}^{-1}$ and $238\text{ }^{\circ}\text{C min}^{-1}$ respectively) as compared to the control phytocat ($119\text{ }^{\circ}\text{C min}^{-1}$). For all the phytocat materials, the highest value of heating rates were observed to reach the set-point temperature of $250\text{ }^{\circ}\text{C}$, thereby leading to relatively less energy consumption alongside enhancing the rate of pyrolysis. Therefore, the optimum set-point temperature of $250\text{ }^{\circ}\text{C}$ was used for all the MAP experiments.

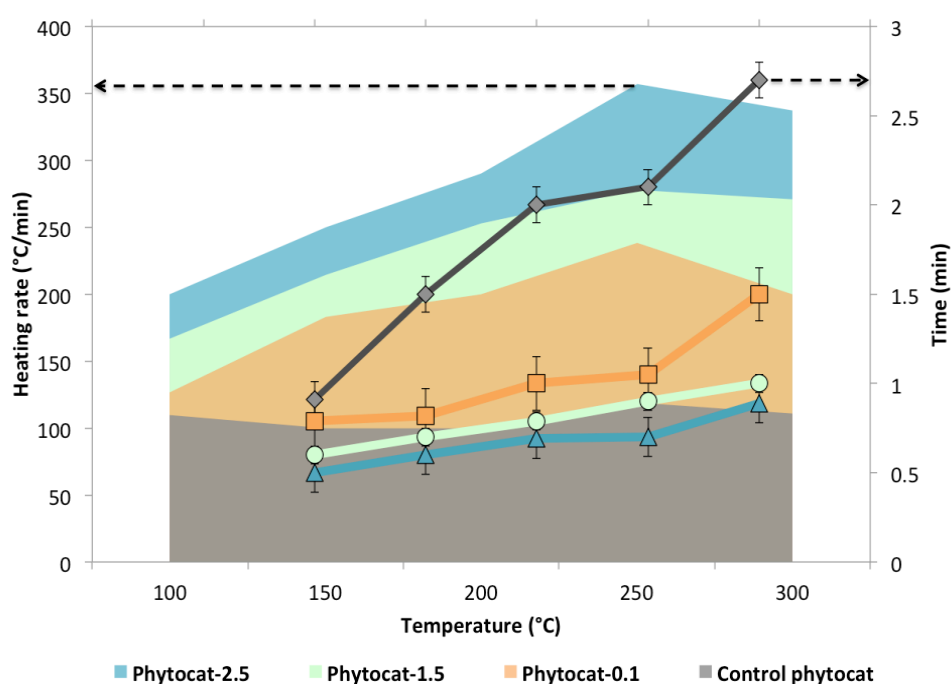


Figure 3.2: Heating rate profiles of phytocat materials at various time intervals to reach the set-point temperature in the microwave reactor

3.1.1. Microwave-assisted pyrolysis

When targeting chemicals from biomass, a key objective is to maximize the product selectivity to favor the subsequent separation.¹¹⁹ This can be achieved through the design of catalysts and optimization of catalytic systems. For production of chemicals, attention should be paid to the establishment of an energy-efficient process for high-value chemicals. This can be realized through the development of multifunctional

catalysts to minimize the reaction steps from lignocellulose to chemicals. In addition, the complete utilization of lignocellulose into biomaterials and chemicals in a single process is desirable, which is the focus of this study.

A review of the literature shows that artificial biomass doping is the most widely used approach to study and understand the effects of metal ions on biomass pyrolysis (catalytic activities and effects on the products distribution).^{64,65,172} This approach is based on the preparation of samples starting from a raw or a demineralized biomass purposely doped with increasing concentrations of a metal salt.^{64,65,172} Dry mixing, wet impregnation, and cation exchange are the most common doping methods.¹⁷² The first method consists of the physical mixing of the selected metal salt and the dry biomass.¹⁷³ The wet impregnation method is the most common and consists of obtaining the doped biomass sample by water evaporation after soaking it in a salt solution at a defined concentration.^{65,172} The ion exchange method uses the presence of exchangeable metal ions in biomass to replace with other metallic species. All these methods incorporate metal ions or salts in the biomass artificially.^{174,175}

Many authors have also showed the catalytic effect of the essential inorganic elements in promoting decomposition of lignocellulose.^{89,176,177} Among these inorganic elements, alkali and alkaline earth metals (AAEMs) were the most studied given their abundance in the plant biomass.^{89,176,177} However, the presence of other inorganic elements, which may also play an important role in decomposition pathways are seldom investigated. For example, agricultural residues such as rice husks rich in Si or hyperaccumulator plants grown on contaminated soils enriched with heavy metals.¹⁷⁸

As discussed in **Chapter 1 (section 1.1.3)**, the phyto-extracted Ni present within the biomass of each species is determined by the inherent biology of that species (including the gene-encoded metal transporters and associated detoxification enzymes).⁴⁵ In this section, the role of phyto-accumulated Ni to direct the distribution of pyrolysis products is discussed further. **Figure 3.3** represents the evolution of the pyrolysis products as a function of variation in the concentration of biologically bound Ni in the plant matrix. As the concentration of biologically bound Ni increases, the char yield decreases in favor of the production of gas and the condensable fraction. Under these conditions (set-point temperature of 250°C), de-

volatilization is promoted at the expense of char forming reactions. At such high heating rates, achieved using microwaves, the activities of the secondary reactions are enhanced, thus promoting gas production. From pyrolysis yields of individual feedstocks, it can be inferred that gas yield increased with increase in the Ni content in plant biomass, reaching its maximum value for phytocat-2.5 (36 wt.% of biomass (dry basis)) as compared to the control phytocat (20 wt.% of biomass (dry basis)). Taking into account the variations in the estimated Ni content within the plant biomass, the overall isolated oil yield was calculated to be between 40-45 wt.% of biomass (dry basis) which is nearly comparable for all the samples. Conclusively, the presence of biologically bound Ni did not affect bio-oil production, but its presence had implications on the composition of the extracted biooil fractions.

Conversely, the high temperature (500°C) conventional pyrolysis (CP) enhanced the production of char (up to 43 wt.%) at the expense of biogas and biooil. However, the gas yields were slightly higher during the production of phytocat-2.5 (up to 22 wt.%) as compared to the control phytocat (up to 15 wt.%). It should be noted that the yields of biooil fraction were found to be comparable to the biooil yields obtained from MAP.

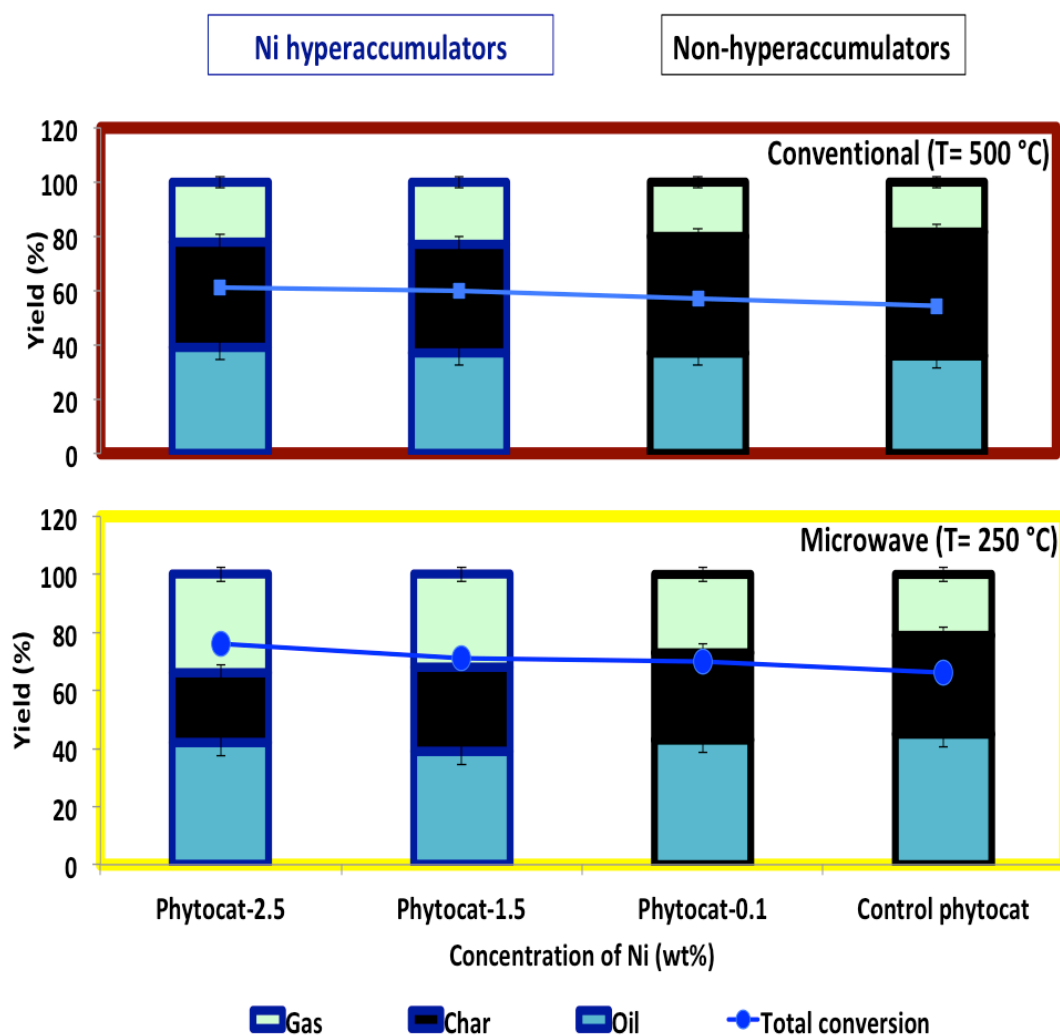


Figure 3.3: Comparison of the microwave assisted pyrolysis and conventional thermal pyrolysis: Evolution of the pyrolysis products as the function of variation in the concentration of biologically bound of Ni in the plant matrix

Fundamentally, lignocellulose is first separated to cellulose, hemicellulose, and lignin through pretreatment and then catalytically upgraded to value-added chemicals and fuels.^{56,57,179,180} However, this process is associated with several disadvantages, including complex separation, loss of biomass functionality, and high energy consumption.^{56,57,179,180} Therefore, the total or direct transformation of lignocellulose biomass into valuable chemicals and materials in a single process should be given more attention.⁵⁹

The chemistry of the condensable oil fraction is very complex, and it is the result of the composite nature of the biomass and the severity (time–temperature relationship) of the thermal treatment to which the biomass is exposed. As represented in **Figure 3.4a**, in the optimal conditions (250°C) for its yield maximization, the condensable fraction is mainly made up of furans, phenols, acids, alcohols, ketones, esters, sugars and some *N*-containing heterocyclic compounds. Over the years, the selective production of platform chemicals such as hydrocarbons, phenols, anhydrosugars, other oxygenates, and recently, nitrogen-containing compounds utilizing lignocellulose has been extensively studied. High costs and technical problems related to catalysts make the chemical routes less feasible and affordable.¹⁸¹

According to GC–MS analysis, phenolic hydrocarbons and derivatives are one of the major compounds in bio-oils under the optimized conditions, as summarized in **Figure 3.4b**. Evidently, the biologically bound Ni accelerates the degradation of lignin, leading to its conversion to phenolics and catechols (up to 24 % selectivity). The study by Zhu and co-authors also suggested that the presence of Pb^{2+} preferentially promoted the depolymerization of lignin based macromolecular compounds.¹⁸² Lignin is a non-fossil resource of distinct functionalized phenolic units, as described previously in **Chapter 1 (section 1.1.4, Figure 1.2)**. One of the most important lignin-derived monomers is 4-alkylphenol, which is among the major products in the extracted oil fraction during the production of phytocat-2.5 (**Figure 3.4c**). It was also stated that the use of Fe–Ni/HZSM-5 in the MAP of cellulose led to a promising selectivity towards phenols (20.86%) in the bio-oil.¹⁸³

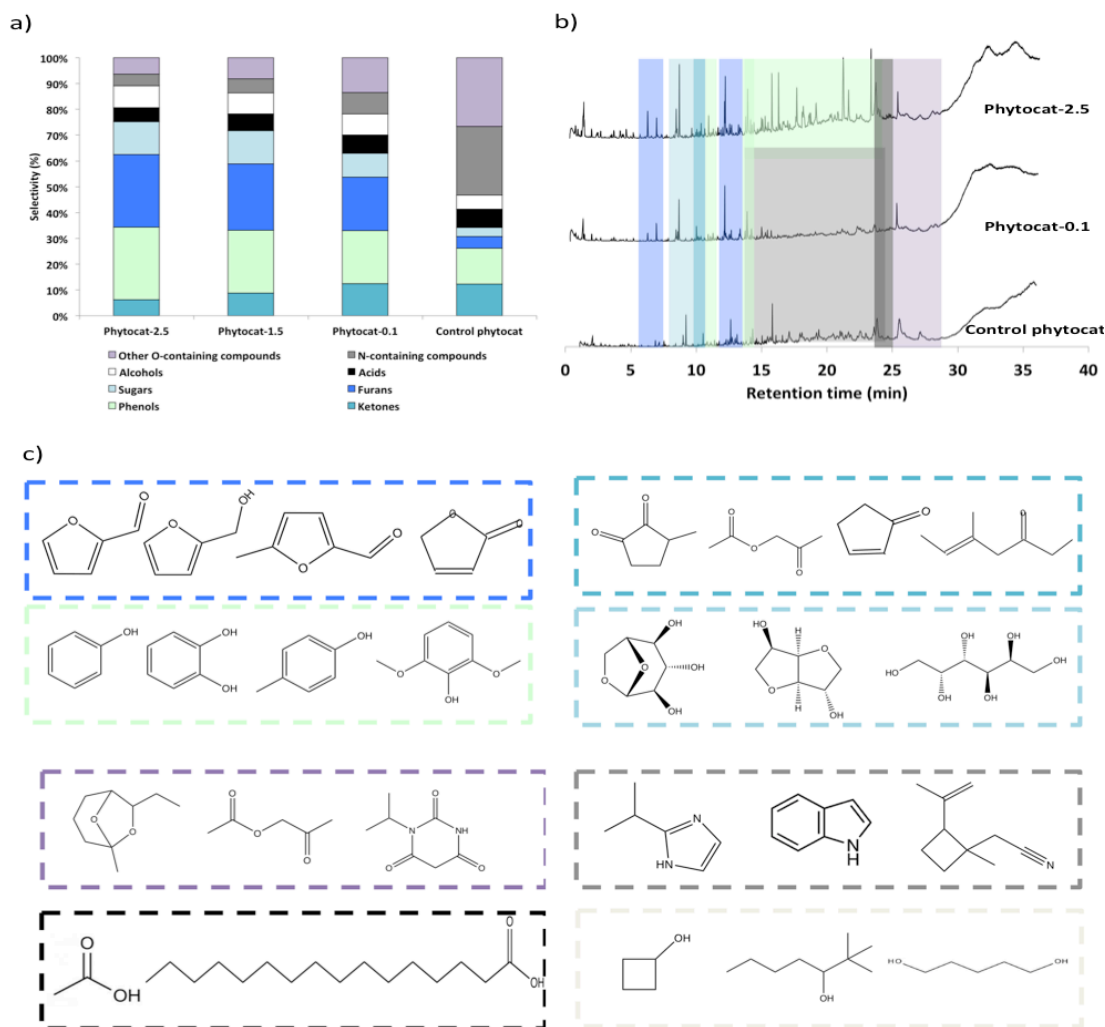


Figure 3.4: a) Role of the biologically bound Ni to direct the microwave-assisted pyrolysis products distribution; b) Total ion chromatograms obtained by GC-MS analysis of the extracted bio-oils and c) Major platform molecules formed during the microwave-assisted pyrolysis to generate phytocat materials.

Other than phenolics, furans become the major product in the extracted oil fractions. Notably, furfural (dehydrated product of C-5 sugar i.e. xylose, typically found in hemicellulose) is the major product among furans, reaching its highest selectivity for phytocat-2.5 (11%) as compared to the control phytocat (1.2%). As established previously by other authors, the presence of $ZnCl_2$ promoted the formation of furfural and inhibited the formation of sugars such as levoglucosan.⁹³ It was also suggested that AAEM can promote the cleavage of pyranose rings to form light oxygenates and

permanent gases *via* dehydration, enol-keto tautomerization, and retro-aldol mechanism, while reducing the formation of levoglucosan.¹⁷⁹ The enhancement in furfural formation could be related to the enhanced secondary cracking of dehydrated sugars.⁵² The same observations were noted with the phytocat-2.5, -1.5 and -0.1, which shows that the presence of biologically bound Ni accelerates the catalytic cracking of dehydrated sugars formed during the pyrolysis (see **Appendix Table A2**). Among the dehydrated sugars, isosorbide (C₆ sugar-based diol) was found to be the major product for phytocat-2.5 exclusively. The established literature reports suggest that isosorbide (1,4:3,6-dianhydro-d-glucitol/-sorbitol) is formed from sorbitol (a six carbon polyalcohol or sugar alcohol obtained by hydrogenation of carbonyl groups of corresponding aldoses or ketoses) *via* its conversion from sorbitan.^{184,118} Commercially, isosorbide can be used as a polymer precursor or to produce dimethyl isosorbide by esterification, an industrial solvent.¹⁸⁴ Remarkably, during the production of control phytocat, there was an enhancement in the formation of *N*-containing heterocyclic compounds, particularly, Indole. The formation of indole takes place *via* Millard and Amadori reactions, by combining carbonyl groups of sugars and the *N*-containing monomers.⁹³ Contrastingly, this observation was not noted during the production of Ni-phytocats. Overall, the presence of biologically bound Ni enhanced the relative amounts of deoxygenated aromatic compounds in the bio-oil (**Figure 3.5**).

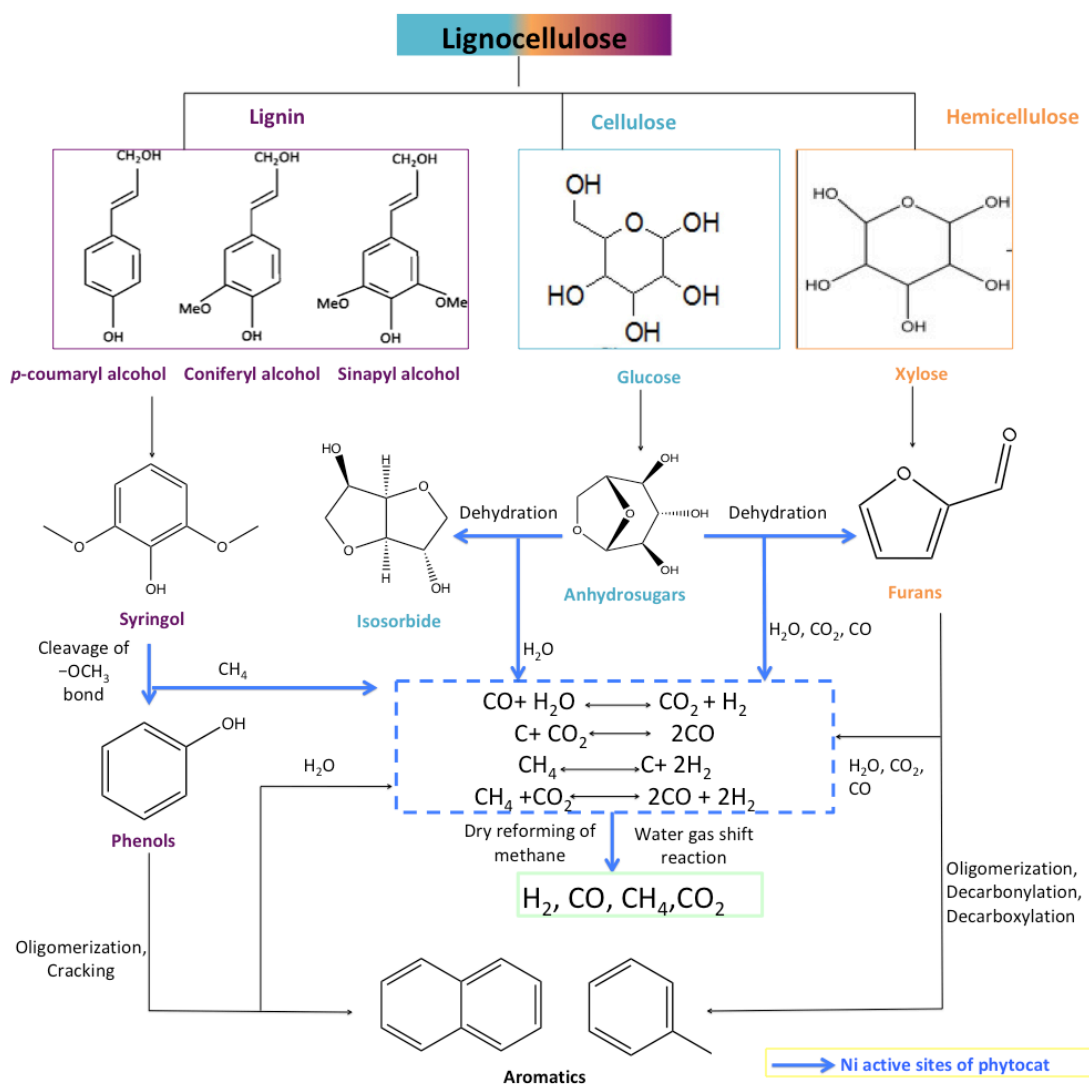


Figure 3.5: Mechanistic pathway of degradation of lignocellulose utilizing the synergistic interactions between microwaves and the biologically bound Ni

In order to clearly demonstrate the compound distribution of the bio-oil, ^1H NMR was also used for the analysis of the bio-oil (see **Appendix A, Figure A.1-A.7**). Proton assignment were made as follows: phenols (4-7 ppm); (hetero-)aromatics (8.5-6.0 ppm); carbohydrates, $-\text{OH}$ exchanging groups (6.0-4.3 ppm); alcohols, ethers (0.5-5ppm). The aromatics mainly included phenols and other hetero-aromatic compounds containing oxygen and nitrogen (5.5–9.5 ppm). The dominant presence of phenols and derivatives (4-7 ppm) was observed in the biooil extracted during the phytocat-2.5 decomposition process. While the oil extracted during the decomposition

of control phytocat showed the dominant presence of hetero-aromatic compounds containing oxygen and nitrogen, which was in agreement with the results obtained by GC–MS. Remarkably, the content of mono-cyclic aromatic compounds increased with the increasing concentration of the biologically bound Ni, while poly-aromatics were the major constituents in the oil extracted during the production of control phytocat. Among these poly-aromatics, naphthalene and indole formed the major fraction of the extracted oil, which is again in agreement with the results obtained by GC–MS. This observation can be explained by the Diels-Alder reaction mechanism that the elevated Ni content was likely to have promoted the occurrence of dehydrogenation, and also the H₂ production.^{56,185} At a higher Ni concentration, aromatic compounds were degraded into ring-opening compounds such as ketones and carboxylic acids that were finally degraded into CO₂, H₂, CH₄ and CO.^{52,56} The results obtained by ¹H NMR were in good accordance with that of GC–MS.

Considering all of the aforementioned observations, the Ni based phytocats could in principle be used to develop a route for production of fine chemicals from pyrolysis oil (e.g. phenols and furans) instead of fuels, increasing the economic value of the products and using less energy (**Figure 3.6**).

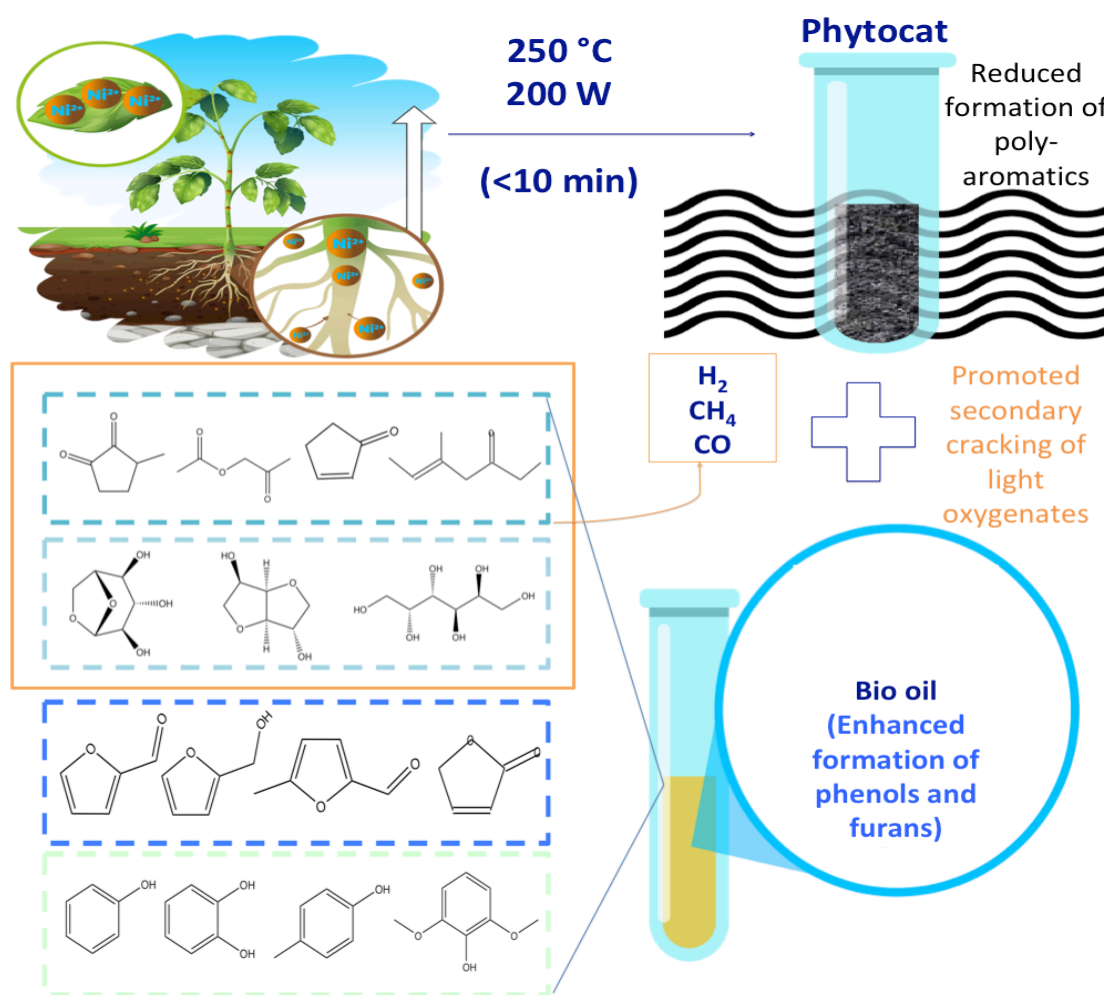


Figure 3.6: Primary perspective towards the development of phytocat

In addition to bio-oil, syngas is also a valuable product of pyrolysis. In this work, a series of experiments was conducted at $250\text{ }^{\circ}\text{C}$ to produce various phytocats, and the production of syngas was particularly investigated. The concentration of combustible gases (H_2 , CO and CH_4) accounted for 61vol.% in the biogas generated without the presence of the biologically bound Ni (control phytocat). The concentration of combustible gases produced with the presence of Ni increased to 74vol%, especially with an increase of syngas (i.e., H_2+CO) concentration by 9%. Compared with the biogas produced during the production of control phytocat, the ratio of H_2 to CO in the biogas under microwave-Ni interaction was slightly enhanced from 0.4 to 1.25. The reasons of the elevated H_2 concentration could be justified as follows: firstly, the

presence of biologically bound Ni raised the heating rate (as discussed previously in **section 3.1**), thereby promoting the cracking of methoxy groups and heterocyclic compounds; secondly, the interaction of microwaves and the biologically bound Ni facilitated methane cracking reaction (**Equation 3.1**), methane dry reforming reaction (**Equation 3.2**), and the reforming reaction of volatile matters (**Equation 3.3**), due to its synergistic effects.^{52,186} It could be deduced that H₂ production relied more on the tar reforming and the higher heating rates promoted this process. It should be noted that the Ni based phytocats produced more H₂ than control phytocat since Ni-based catalysts could strongly facilitate the cracking of C-H bonds, which was in good agreement with these results.¹⁸⁷ Considering **Figure 3.3** and **Figure 3.7**, it was inferred both the yield and the quality of biogas were remarkably improved under microwave-biologically bound Ni interaction, highlighting their potential synergy, especially for producing syngas with a desirable H₂/CO value at about 1.



Notably, it could be found the yields of CO and CO₂ were much more than other gases during the decomposition of control phytocat. Releasing of CO₂ was mainly caused by cracking of carbonyl (C=O) and COOH,¹⁸⁸ and was especially prominent in the decomposition products from the control phytocat. With regards to CO, it could be produced by the cracking of ether linkage (C-O-C) and carbonyl (C=O),¹¹⁹ and control phytocat showed its slight enhancement than Ni-phytocats. Additionally, the increase in Ni content in the phytocats contributed to a higher CH₄ output (from 1.1 to 3.6 vol.%), which was possibly due to the de-methylation of methoxyl groups of lignin enhanced by the higher concentrations of biologically bound Ni (phytocat-2.5).

To further elucidate the release of volatiles, the real time thermogravimetric analysis equipped with simultaneous fourier transform infrared spectroscopy (TGA-FTIR) was conducted. The TGA-FTIR spectra of the biomass pre-pyrolysis, later used to develop phytocat-2.5 and control phytocat is shown in **Figure 3.7b and c** respectively. As observed previously, CO₂ was the major gaseous product of pyrolysis during the production of control phytocat and is primarily generated *via* the

decarboxylation reaction and the release of carboxyl groups.¹⁸⁸ CO is attributed to the decomposition of ether and carbonyl groups *via* decarbonylation reactions, and CH₄ results from the cleavage of -OCH₃- bonds.¹⁸⁹ These results support the observations made during microwave-assisted pyrolysis, suggesting the presence of biologically bound Ni enhances the formation of CH₄, leading to elevated content of phenols in the oil fraction (as shown previously in **Figure 3.5**). The C-C/C-O group can be ascribed to the anhydrosugars (such as levoglucosan) and furans, which are preferentially formed during the decomposition of Phytocat-2.5. Importantly, the absorbance intensity of C=O was very high, which indicates that a large amount of ring-opening reactions occurred during the pyrolysis. During CP, it is evident that the H₂O, CO₂, and C=O groups began to form at low temperatures (T<300°C), while the CH₄, CO, and C-C/C-O groups formed within a narrow range of high temperatures (T>300°C). Contrary to CP, the production of H₂, CO, short chain aliphatics (C₂₋₄) and CH₄ was enhanced due to synergistic interactions of the biologically bound Ni and microwaves at relatively lower temperatures (T=250°C).

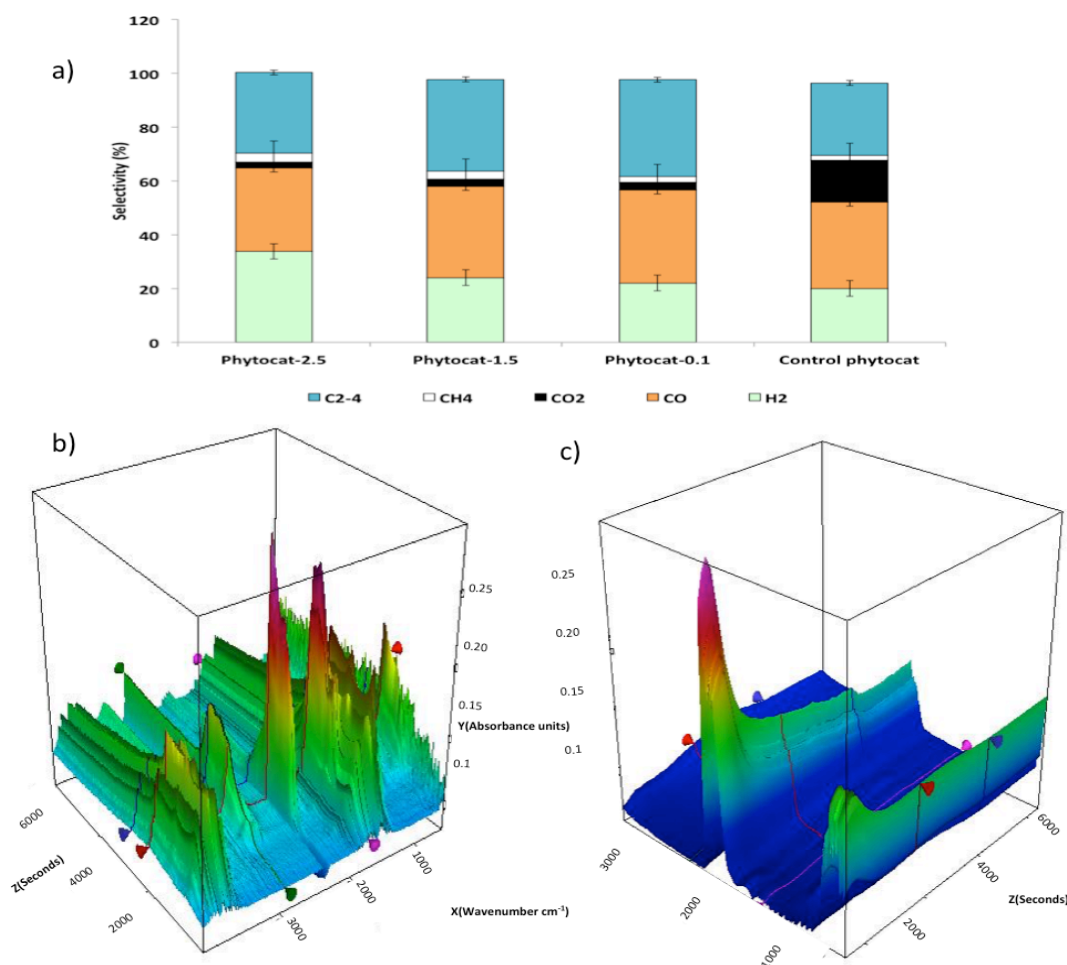


Figure 3.7: a) Composition of the gas released during microwave assisted pyrolysis for the development of various phytocat materials; Real time thermo-gravimetric analysis of the gas produced during conventional pyrolysis: b) Phytocat-2.5 and c) control phytocat

In the meantime, the biochars, whose structure and chemistry have been greatly altered by microwaves, evolves toward a carbonaceous structure with a reduced oxygen content (phytocats). These biochars can be studied as a multiphase system composed of a carbon network and a metallic phase. The C and O contents of the biomass pre-pyrolysis ranged between 50 and 40wt.% on a dry ash free basis, whereas the H content varies between 5 and 7wt.%. The most significant changes during production of Phytocat-2.5, where C and O contents reached around 77wt.% and 24wt. %, respectively. Data collected in this work show an unclear correlation between the presence of biologically bound Ni and the N content of the char. Based

on the elemental analysis results (**Figure 3.8**), it was seen that there was a dramatic reduction of H/C and O/C ratios in the developed phytocat materials. This could be related to the loss of H and O elements with the decomposition of hydroxyl, carboxyl, carbonyl and other functional groups. The presence of the biologically bound Ni had a noteworthy impact on the O/C ratio in phytocat, causing a decrease from 0.6 to 0.3. Instead, the H/C ratio in phytocat was just slightly affected by the presence of Ni. These observations were consistent with the finding that there is an intense release of volatile matters under the synergistic interaction of microwave and biologically bound Ni, thus raising the aromatic carbon content in phytocat.

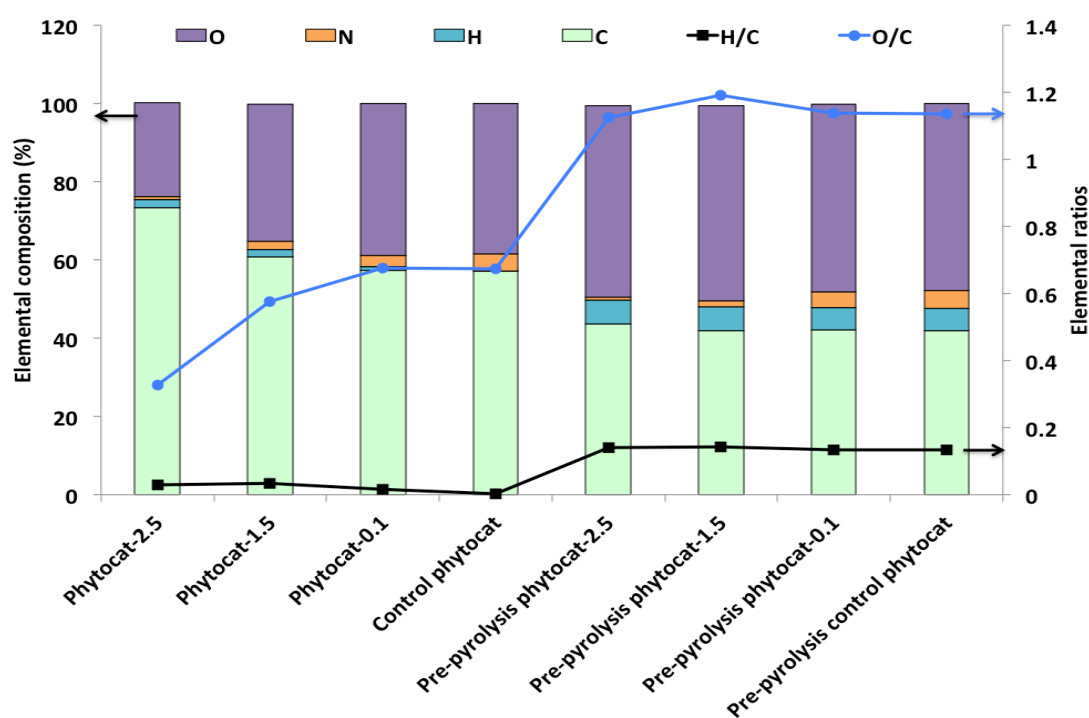


Figure 3.8: Elemental composition of the biomass pre-pyrolysis and the phytocat materials developed using microwave assisted pyrolysis

To elucidate the mechanism, detailed structural changes during MAP for the production of phytocat materials were studied thoroughly by FT-IR, XPS, XRD, CPMAS ^{13}C NMR and advanced electron microscopy techniques (HAADF-STEM,

HR-TEM, FE-SEM-EDS), which will be discussed in details in the next section (**Section 3.2**).

In order to gain further insights into the degradation mechanism of lignocellulose due to the presence of biologically bound Ni, microwave assisted hydrolysis was conducted and the results are discussed in greater details in the next sub-section (**Section 3.1.2**).

3.1.2 Microwave-assisted hydrolysis

With the aim to understand the mechanism of de-polymerization of lignocellulose biomass due to the synergistic interactions of microwaves and the biologically bound Ni, the scope of this study was expanded to examine microwave-assisted hydrolysis process. Importantly, combining the de-polymerization mechanism utilizing the MAP (as described in detail in the previous **section 3.1.1**) and microwave-assisted hydrolysis could help to provide for a more complete understanding of this synergy. A complex lignocellulose biomass comprises simplest carbohydrates (~75%), which naturally occur in the forms of monosaccharides such as glucose, xylose and fructose.¹⁹⁰

Over the years, hydrolysis and hydrogenolysis have been combined in one-pot using both acid functionality to transform cellulose and hemicelluloses into the respective monomers, as well as metal sites to convert the monomers into polyols.^{56,191} Enzymes and mineral acids have been widely used for the conversion of lignocellulosic biomass and its components but have serious drawbacks involving low activity, difficult separation of products and catalysts, waste and corrosion hazards, and harsh conditions.^{90,191–193} Carbon materials, such as AC and carbon nanotubes (CNTs), are known as heat- and water-tolerant supports, with high resistance to acid and base attack and excellent stability; for this reason, carbon-supported metal catalysts have been extensively studied.^{79,118,193,194} Carbon-based materials have excellent stability in the aqueous phase and are usually employed as water-tolerant supports.¹⁹⁵

Importantly, efforts toward green reaction medium without base or acid should be the major focus, and the use of water is the most desirable.

However, the studies must not only focus on the support material and its modification to enhance the hydrolysis but also on the metal sites because they are fundamental for directing the conversion pathway.

In this study, the role of biologically bound Ni to direct the microwave assisted hydrolysis of lignocellulose was examined under mild conditions (120°C, 100W, 10 min; detailed mention in **Chapter 2**). It should be noted that the raw biomass (i.e. pre-hydrolysis phytocat materials) were used for this study, are named accordingly based on the concentration of biologically bound Ni respectively for the ease of correlation. This section focuses on the characterization of the liquid fraction (hydrolysates) and the solid residue (hydrochar) just to gain further insights into mechanism and support the findings reported in the previous section (**section 3.1.1**). Therefore, the extracted products of hydrolysis were only meant for primary characterization followed by critical analysis and were not utilized further unlike pyrolysis char (used as catalyst, see **Chapter 4** and **Chapter 5**).

Initial characterization of the hydrolysates using HPLC showed that the depolymerization of lignocellulose produced monosacharides (mainly xylose and glucose), dehydration products (HMF, levoglucosan and furfural), rehydration products (levulinic acid and formic acid) and other acids (acetic acid and lactic acid) as the major products (**Figure 3.9**). Interestingly, the presence of biologically bound Ni facilitated the production of xylose and the rehydration products thereof. The maximum yields were obtained for xylose (13.1wt.%), acetic acid (12.4wt.%), levulinic acid (5.4wt.%), lactic acid (6.4wt.%) and formic acid (6.7wt.%), particularly using pre-hydrolysis phytocat-2.5 (**Figure 3.9 a, b**).

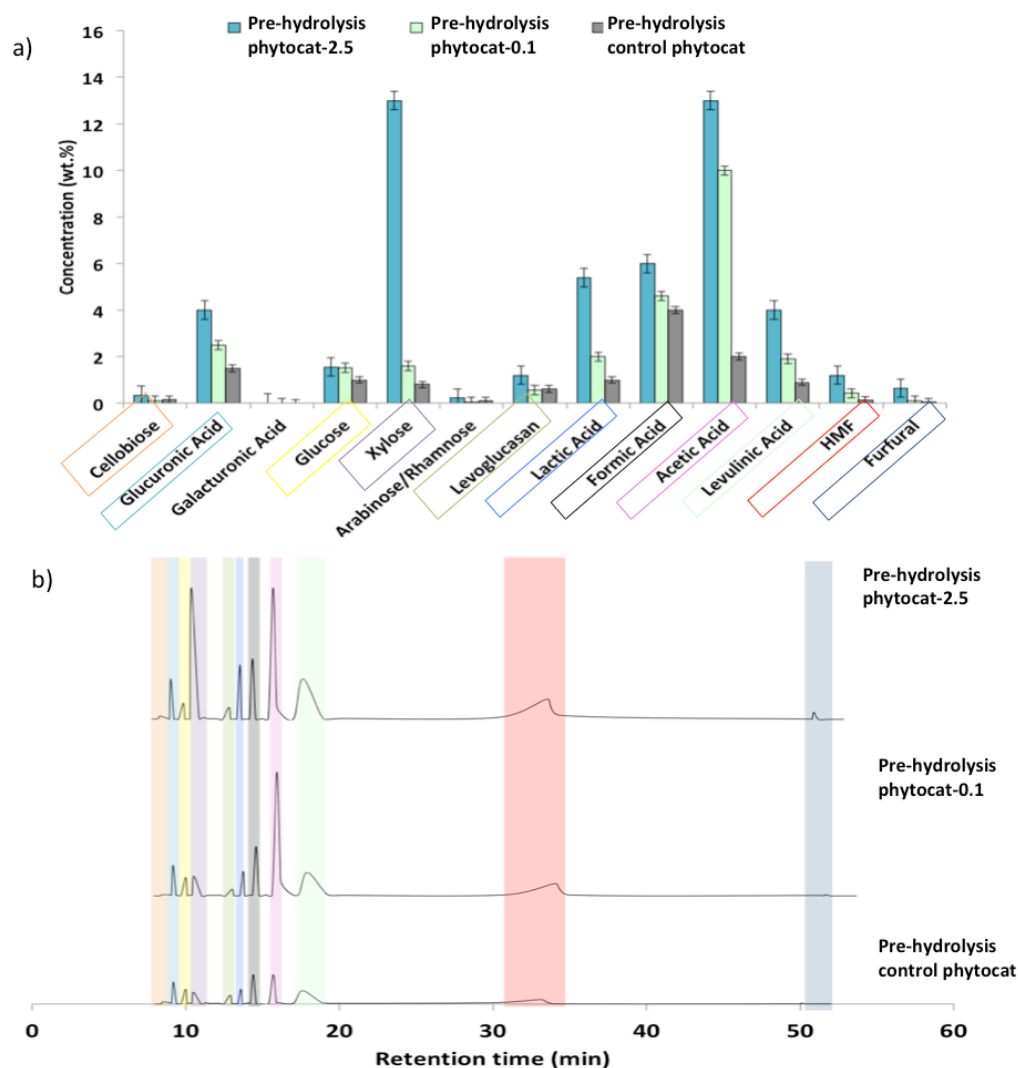


Figure 3.9: a) Composition of the products formed by microwave-assisted hydrolysis, b) HPLC chromatographs of the extracted hydrolysates

The xyloses connected by β -1-4-glycosidic linkages (C1–O1–C4) are generated from the glycosidic bond cleavage and serves as an intermediate for the formation of a range of intermediates and major products.¹⁸⁰ Another pathway involves decarboxylation and demethylation of the 4-*O*-methyl glucuronic acid groups, followed by ring-opening to form xylose and subsequent dehydration to form furfural (**Figure 3.10**).¹⁹⁵ This study shows that the major carboxylic acids resulting from hemicellulose decomposition were acetic acid and formic acid. The prevalent

mechanism of the formation of acetic acid is involved with the cleavage of *O*-acetyl groups, whereas the chemical pathway for formic acid production is attributed to the elimination of carboxyls in the uronic acid groups.^{52,196}

For the production of Levulinic acid (LNA) from lignocellulose, the first step involves the hydrolysis of cellulose and hemicellulose into monosaccharides, such as glucose and xylose, and the second step involves isomerization and dehydration of monosaccharides into HMF and furfural.^{189,195,197} Subsequently, HMF is converted into LNA and formic acid (as a co-product) by rehydration in the aqueous phase.¹⁹⁶ As a promising platform molecule, LNA is a starting material of various industrial applications, such as fine organic synthesis, animal feed and food as well as polymer materials, plasticizers, extenders for fuels, herbicides, solvents and coatings.^{189,192,198} One of the earliest works on LNA production is from Thomas and Schuette, who used HCl as the acid catalyst with sucrose, dextrose, levulose and starch in 1931.¹⁹⁷ Usually, to form LNA from sugars, higher acid strengths and longer residence times are required than to form HMF.¹⁹⁹ Pileidis and Titirici gathered the reported yield of LNA from previous studies, 81 % being the highest when fructose is used as a feedstock and 3.6–7.2 % when HCl is employed as a catalyst.¹⁹⁹ Wang *et al.* studied the hydrolysis of cellulose to levulinic acid in the presence of sulfated TiO₂ as a solid acid catalyst.¹⁹⁸ A maximum yield of levulinic acid (27.2%) was obtained at 240 °C in 15 min reaction time using 0.7 g of sulfated TiO₂ catalyst. Asghari and Yoshida reported the kinetics of fructose dehydration to 5-HMF and the rehydration of 5-HMF to form levulinic acid and formic acids using HCl catalyst at relatively high temperatures (up to 270 °C).¹⁹⁶ The main drawback of using mineral acids is the separation phase from the reaction medium. Its separation negatively affects downstream processes (such as GVL production).¹⁹⁹

However, this study reports the transformation of lignocellulose into platform chemicals such as levulinic acid, formic acid and lactic acid under mild conditions, as these conversions can be achieved without consumption of hydrogen or harsh conditions (higher temperatures, use of corrosive acids or longer reaction times) and thus are more economical than the hydrogenolysis or acid catalyzed hydrolysis. Notably, the presence of biologically bound Ni was found to promote the rehydration, retro-aldol and demethylation reactions to selectively produce LNA, lactic acid and

formic acid as the major fraction of the hydrolysates at the mild conditions used in this study.

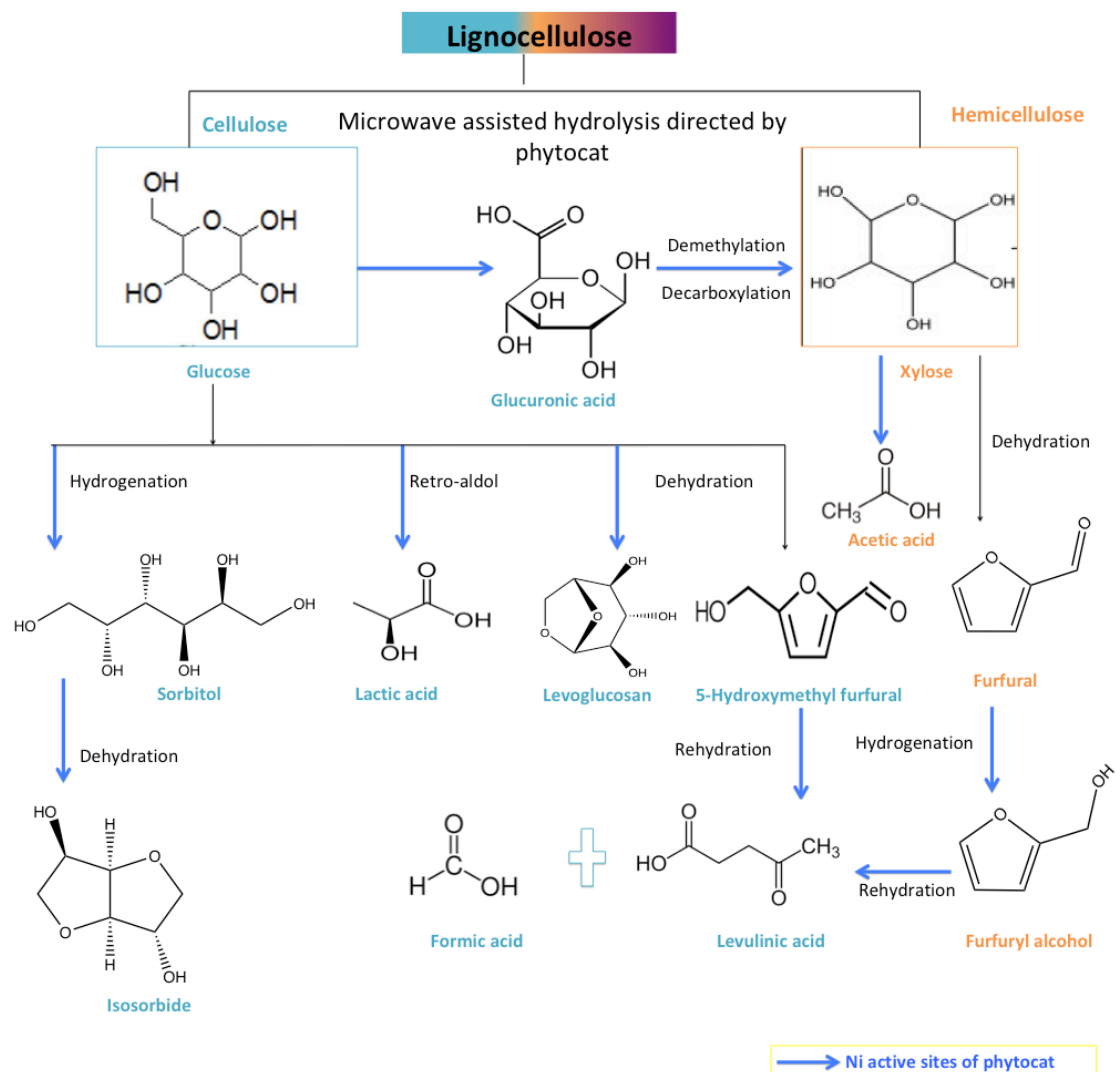


Figure 3.10: Proposed mechanistic pathway of microwave assisted hydrolysis directed by phytocatalysis

Intrigued by these findings, the isolated hydrochar was characterized using CPMAS ^{13}C NMR spectroscopy to get further insight into the modified molecular structure of the biomass post-hydrolysis (**Figure 3.11**). As shown in **Figure 3.11 a, c and e**, the raw biomass (pre-hydrolysis phytocat materials) show the resonances of *O*-alkyl C ($\delta = 70\text{-}90$ ppm), carboxyl C ($\delta = 165\text{-}190$ ppm), alkyl C ($\delta = 0\text{-}45$ ppm) and aryl C ($\delta = 100\text{-}150$ ppm), which are typically assigned to cellulose, hemicellulose, and lignin compositions, respectively.^{200,201} Post-hydrolysis (**Figure 3.11 b, d and f**), as the content of biologically bound Ni is increased from ~ 0 to 2.5wt.%, the alkyl C and carboxyl C structures disappear, while the *O*-aryl C signal becomes stronger, resulting in more aromatic C structures ($\delta = 130$ ppm). It should be noted that the peaks appearing around 20-25 ppm (which corresponds to the hemicellulose fragment of lignocellulose) disappeared completely, particularly for phytocat-2.5. This suggests the near complete hydrolysis of hemicellulose fragment into xylose and subsequent formation of furfural, thereby leading to an enhanced production of the rehydrated products (LNA and formic acid). These findings strongly correlated with the results obtained from HPLC analysis, as discussed in the previous section.

The typical spectra of the cellulose fragment had broad resonances that extend over chemical shift ranges attributed to C_1 ($\delta=102\text{-}108$ ppm), C_4 ($\delta=80\text{-}92$ ppm) and C_6 ($\delta=57\text{-}67$ ppm) of cellulose, respectively.¹⁸⁹ It should be noted that these resonances showed the major shift and broadening for the post-hydrolysis phytocat-2.5, which further reveals the transformations in the molecular structure and alterations in the cellulose fragments. Evidently, this transformation supports the results obtained from HPLC analysis, which suggested the enhanced formation of the lactic acid, LNA and formic acid *via* retro aldol reaction and rehydration reaction of glucose respectively.

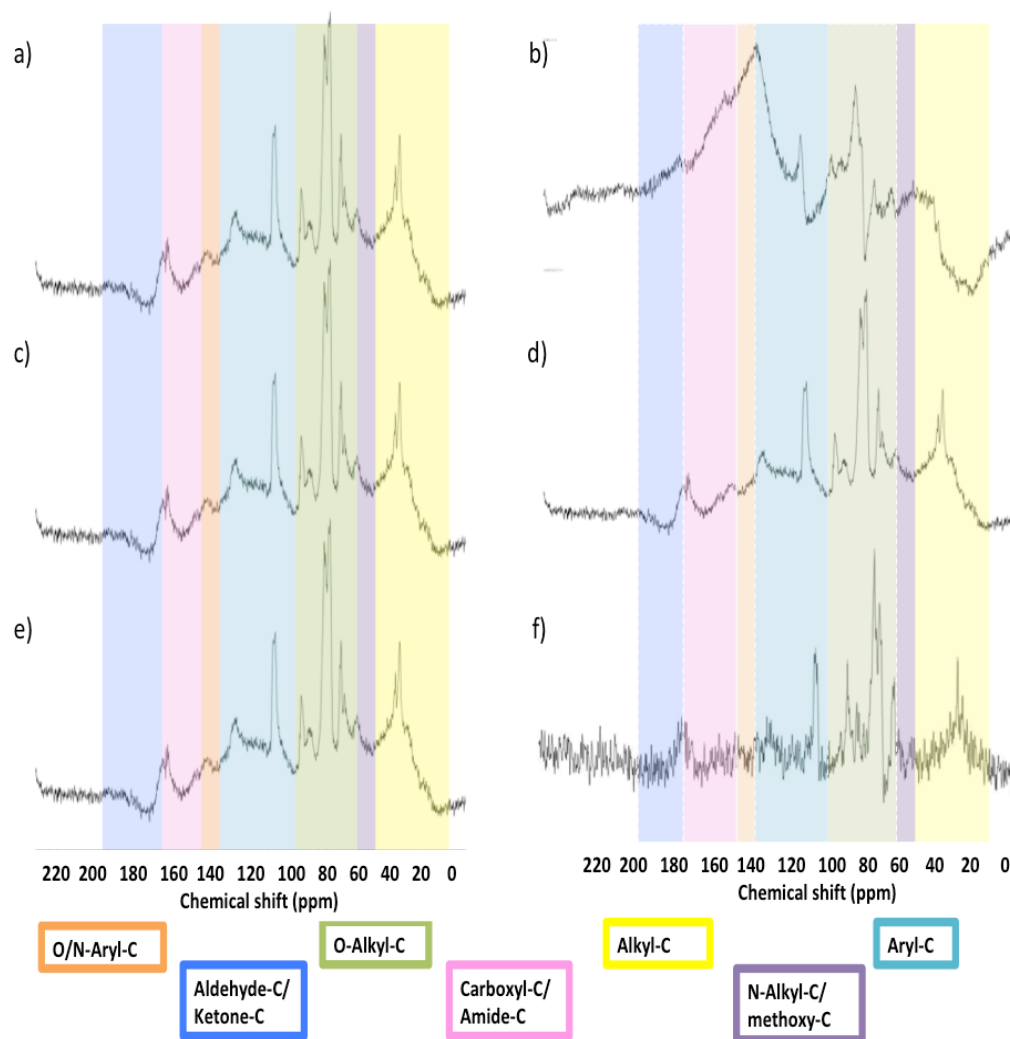


Figure 3.11: Cross-polarization magic angle spinning (CPMAS) ^{13}C NMR spectra of a) Pre-hydrolysis phytocat-2.5, b) post-hydrolysis phytocat-2.5, c) Pre-hydrolysis phytocat-0.1, d) post-hydrolysis phytocat-0.1, e) Pre-hydrolysis control phytocat and f) post-hydrolysis control phytocat

3.2 Advanced material characterization of phytocat

Initial characterization of the developed phytocat materials involved various surface characterization techniques to understand its surface functionality and morphology.

The changes in the chemical structure of various phytocat materials were analyzed by the CPMAS ^{13}C NMR spectra (**Figure 3.12**). As shown in **Figure 3.12 a, c and e**, the raw biomass (phytocat materials pre-pyrolysis) show the resonances of *O*-alkyl C ($\delta = 70\text{--}90$ ppm), carboxyl C ($\delta = 165\text{--}190$ ppm), alkyl C ($\delta = 0\text{--}45$ ppm) and aryl C ($\delta = 100\text{--}150$ ppm), which are typically assigned to cellulose, hemicellulose, and lignin compositions, respectively.^{200,201} Post-pyrolysis (**Figure 3.12 b, d and f**), as the content of biologically bound Ni is increased from ~ 0 to 2.5wt.%, the *O*-alkyl C and carboxyl C structures disappear, while the aryl C signal becomes stronger, resulting in more aromatic C structures ($\delta = 130$ ppm).

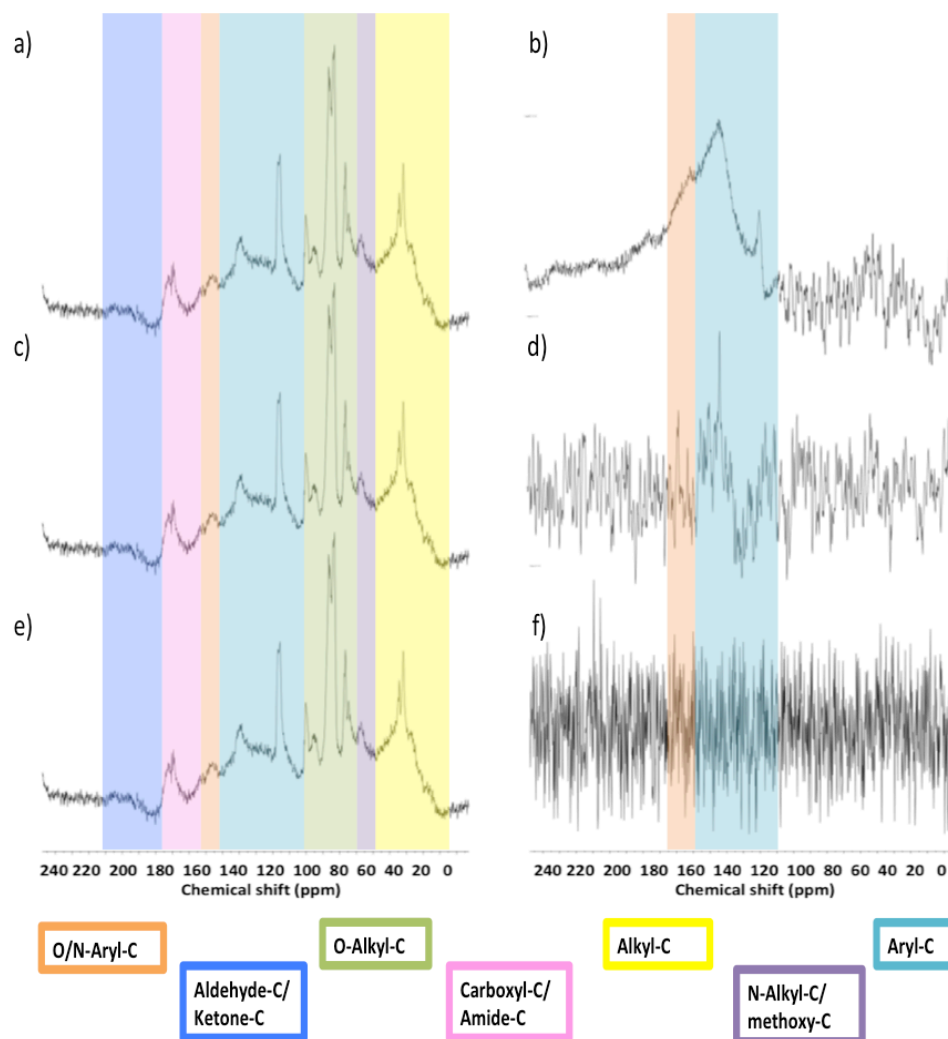


Figure 3.12: Cross-polarization magic angle spinning (CPMAS) ^{13}C NMR spectra of a) Pre-pyrolysis phytocat-2.5, b) Phytocat-2.5, c) Pre-pyrolysis phytocat-0.1, d) Phytocat-0.1, e) Pre-pyrolysis control phytocat and f) Control phytocat

The elemental composition and chemical states of biologically bound nickel in the bio-carbon matrix were analyzed by X-ray photoelectron spectroscopy (XPS) analysis.

Various plant based ligands like histidine, nicotianamine and various organic acids form complexes with Ni^{2+} ions, enabling its uptake by plants.³⁹ Our one-step, low temperature microwave assisted pyrolysis approach leads to *in-situ* formation of Ni^0 . This chemical valence state of the biologically bound Ni was determined using the

corresponding binding energies (eV) of Ni 2p_{3/2} peaks, as shown in **Figure 3.13a**. Generally, catalysts with low nickel metallic loadings are dominated by Ni²⁺ along with some sequestered Ni⁰ sites.⁸⁶ The differences in metallic nickel lead to changes in the surface chemistry and consequently the catalytic activity. However, an oxide layer formed around supported Ni particles can suppress coke formation while preserving high catalytic activity.⁸⁶ The peak around 852 eV is assigned to Ni⁰ and peaks between 855 and 861 eV are assigned to Ni²⁺ in the form of Ni(OH)₂ and NiO.² The surface of the phytocat consisted of both Ni⁰ and Ni²⁺. However, with increasing nickel content, there is an increase in intensity of Ni⁰ peak with a simultaneous decrease in intensity of Ni²⁺ peak.

Deconvoluted high-resolution N 1s XPS spectra of phytocat display peaks located at 399.1, 399.7, 400.7, and 402.3 eV (**Figure 3.13b**) attributed to pyridinic N, pyrrolic N, graphitic N, and oxidized N, respectively.²⁰² The shift in the position of the pyrrolic N peak to a higher value for the higher Ni loadings, could be due to charge transfer between Ni and pyrrolic N species.²⁰²

Deconvoluted high-resolution C 1s XPS spectra of phytocat show characteristics peaks for C–C (284.6 eV), C–N (285.4 eV), C–O (286.3 eV), C=O (287.2 eV), and O–C=O (288.9 eV) bonds.²⁰² The prominent peaks at 284.3–284.5 eV reveal that most carbons in the phytocat are aromatic. The presence of these functional groups on the surface of phytocat facilitates its binding with nickel nano-particles (**Figure 3.13c**). It should be noted that the peaks corresponding to π – π^* transition (290.4 eV) were found to intensify for phytocat-2.5, which again provides evidence for the enhanced aromatic nature due to the presence of biologically bound Ni.

In order to understand the crystal structure and phase purity of the phytocat materials, X-ray diffraction (XRD) was used. Initial x-ray powder diffraction (XRD) analysis revealed metallic nickel particles along with a carbon rich phase. As shown in **Figure 3.13d**, the diffraction peaks at 44.6°, 52.2°, and 77.3° belong to metallic Ni ([111], [200] and [220] diffraction peaks of Ni⁰).²⁰³ Both the phytocat materials exhibits a broad graphitic (002) peak at about 25°, which belongs to the hexagonal conjugated carbon structure. This confirms that the structure of the phytocat is relatively stable

and the majority of entrapped NiO is reduced to Ni metal by the surrounding bio-carbon matrix during the microwave-assisted pyrolysis.

It was noticed that the peak (002) of phytocat-2.5 achieved with the interaction of microwave and biologically bound Ni moved the peak (26.5°) of graphite, also pointing to an enhancement of graphite degree. Further, the graphite peak of phytocat-2.5 was featured by the narrower deformation, compared to the phytocat-0.1. This signified the decrease of amorphous carbon and increase of aromatic carbon in the phytocat produced under the synergistic interactions of microwave and biologically bound Ni, thus improving the crystalline structure of phytocat.

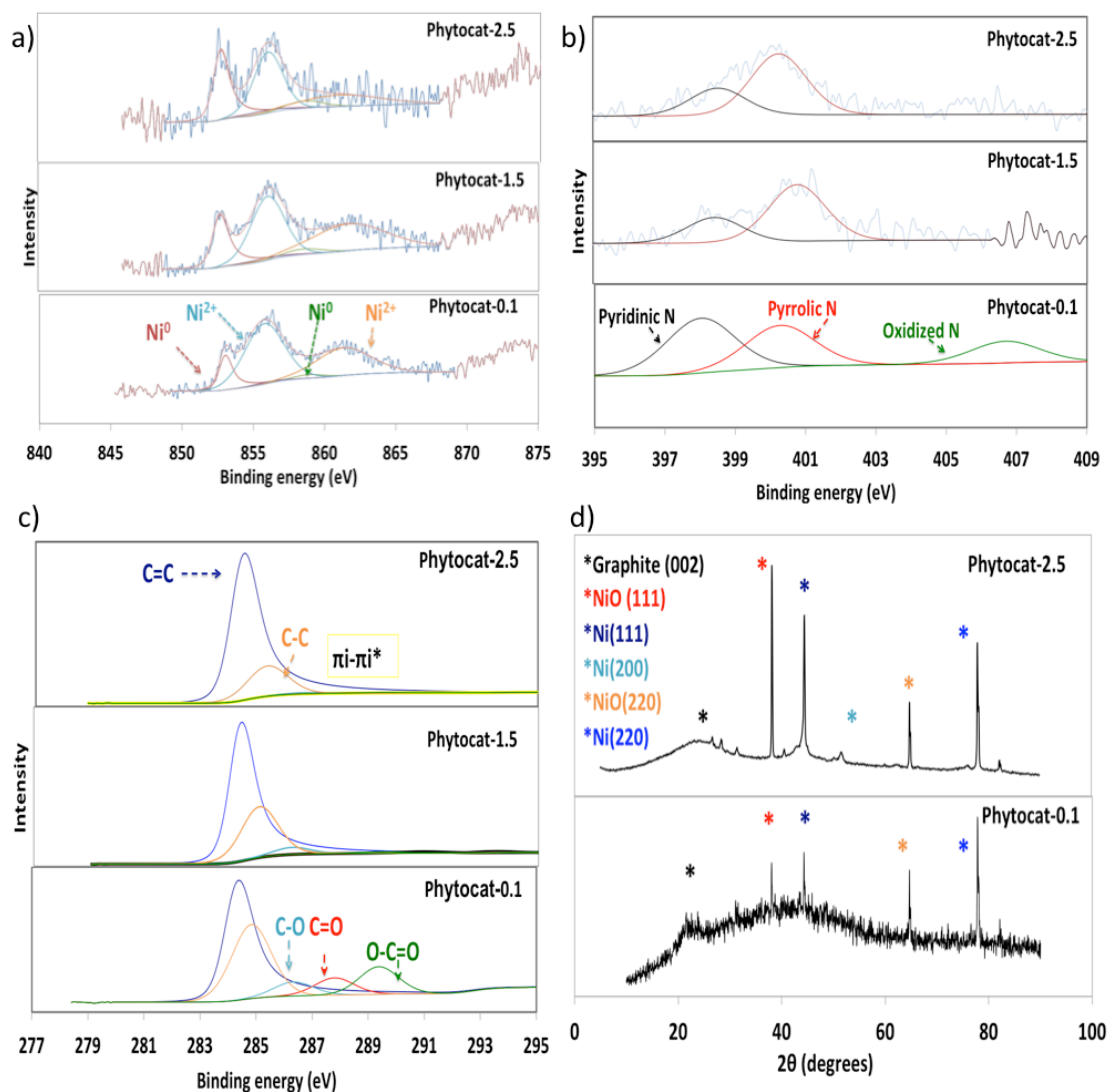


Figure 3.13: X-ray photoelectron spectroscopy (XPS) analysis of phytocat materials a) deconvoluted high-resolution Ni 2p_{3/2} spectra, b) deconvoluted high-resolution N 1s XPS spectra, c) deconvoluted high-resolution C 1s spectra, d) X-ray diffraction (XRD) pattern of Ni-phytocat-2.5 and -0.1

Besides surface functional group analysis, the morphologies and lattice structures of the phytocat materials were also analyzed by comparison.

Interestingly, energy-dispersive x-ray (EDX) spectroscopy analysis of the Ni phytocat revealed the presence of small amounts of oxygen, which is evident of nickel oxide formation on the particle surface due to storage in air. As can be seen from **Figure 3.14a**, Ni nanoparticles embedded in the bio-carbon matrix of phytocat showed the traces of calcium, silicon and oxygen. Notably, the traces of these elements were also found to be present in the control phytocat (see **Appendix Figure A.8**).

Field emission scanning electron microscopy (FESEM) images of phytocat materials were observed to understand their structural design. They exhibited irregular spherical morphologies and high dispersion of Ni species on the surface of phytocat-2.5 (**Figure 3.14b**) and relatively moderate dispersion on the surface of phytocat-0.1 (**Figure 3.14c**). On the contrary, the presence of Ni was not detected on the surface of irregular clusters of control phytocat (**Figure 3.14d**). It should be noted that numerous carbon nanostructures (outgrowths) were formed on the surface of phytocat-2.5, which encapsulated Ni nanoparticles within their irregular matrix, while no formation of such carbon nanostructures were observed on the surface of control phytocat. The thermal stability of these carbon nanostructures encapsulated Ni nanoparticles was investigated and discussed in detail later in this chapter.

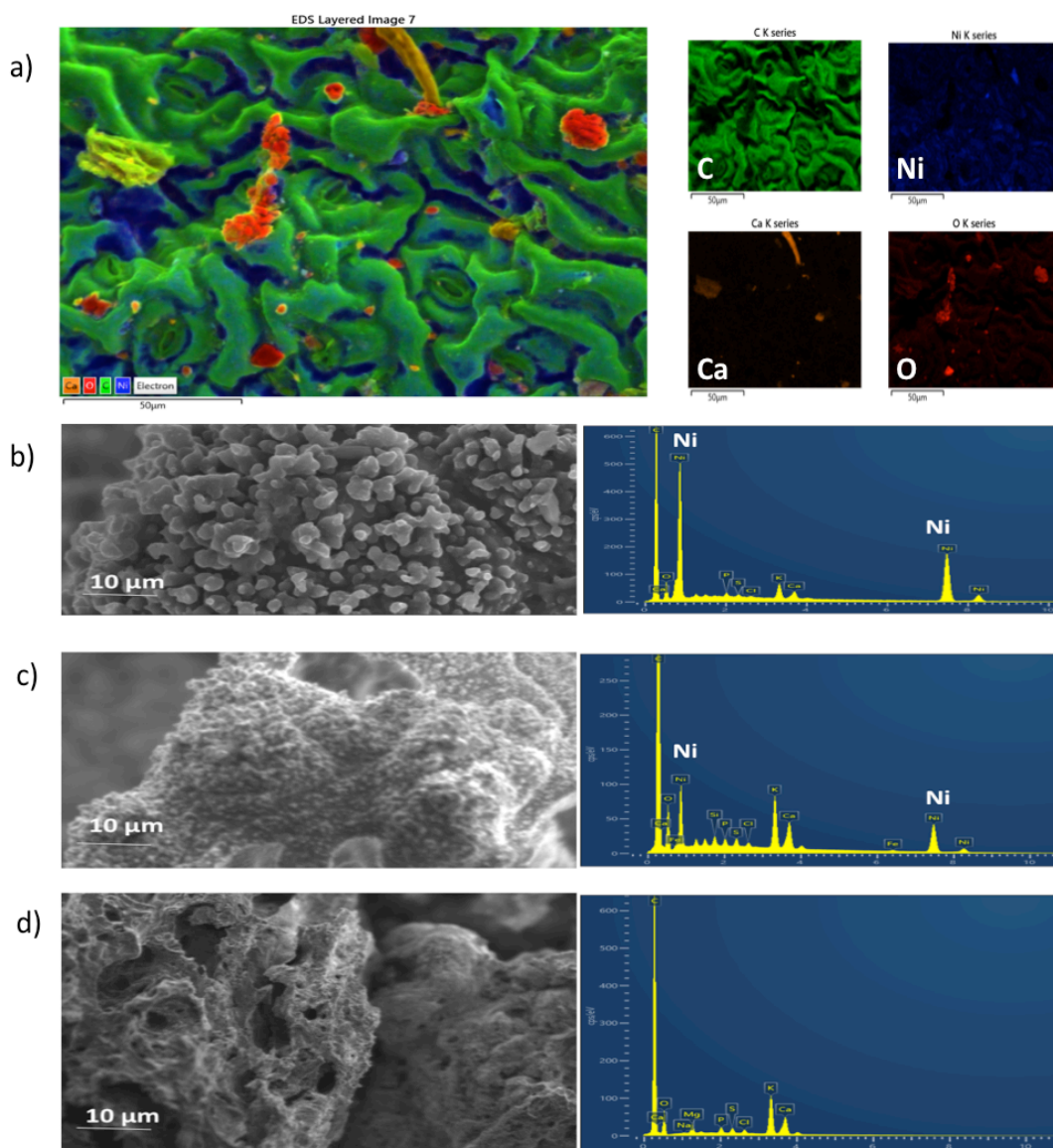


Figure 3.14: a) Energy-dispersive x-ray (EDX) spectroscopy analysis of Ni-phytoCAT-2.5 highlighting carbon (green), nickel (blue), oxygen (red) and calcium (orange), Scanning electron microscopy (SEM) images equipped with energy-dispersive X-ray spectroscopy (EDX): b) phytoCAT-2.5, c) phytoCAT-0.1 and d) control phytoCAT

Intrigued by these features, high-resolution transmission electron microscopy (HR-TEM) measurement was then employed to observe the lattice fringes corresponding to the biologically bound nickel in the phytoCAT materials. It should be noted that the HR-TEM image (see **Appendix Figure A.9**) reveals irregular fringes, mainly with a planar spacing of 0.242 nm and 0.216 nm point to (111) and (200) crystal planes,

respectively, which corresponds to the cubic phase of Ni (see **Appendix Figure A.10**). Further information regarding the graphitization process can be gained by TEM. According to TEM data, control phytocat is mostly made of amorphous carbon while phytocat-2.5 and phytocat-0.1 show the combination of amorphous as well as graphitic carbon. In phytocat-2.5, the graphitic biocarbon matrix contains nanoscale particles, which are Ni⁰ according to selected area electron diffraction pattern (see **Appendix Figure A.11**). Notably, Ni particles were encapsulated in a graphitic layer with a thickness of about 1-3 nm (see **Appendix Figure A.12**). This was due to the enhancement of the degree of pyrolysis in accordance with the relatively higher heating rate using phytocat-2.5, leading to the de-polymerization of cross-linking bonds of lignocellulose and the formation of the ordered aromatic structure. As a result, the micro-crystalline structure of phytocat-2.5 tended to be regular and the graphitic degree enhanced with the synergistic interactions of microwave and the biologically bound Ni.

Following the microstructural features, high-angle annular dark-field scanning transmission electron microscopy (HAADF-STEM) images were used to gain further structural insight. In the field of view of HAADF-STEM images, intensity is relative to the square of atomic number of the element.²⁰⁴ Therefore, the atomically dispersed Ni particles can be clearly distinguished as the brighter spots on bio-carbon matrix. As shown in **Figure 3.15b**, the formed Ni nanoparticles were uniformly distributed and exhibited an average particle size of 5.2 ± 1.1 nanometers. Most of the observed nano-particles were within a range of 4.5 to 7.3 nm; however, a few particles up to 11 nm were observed.

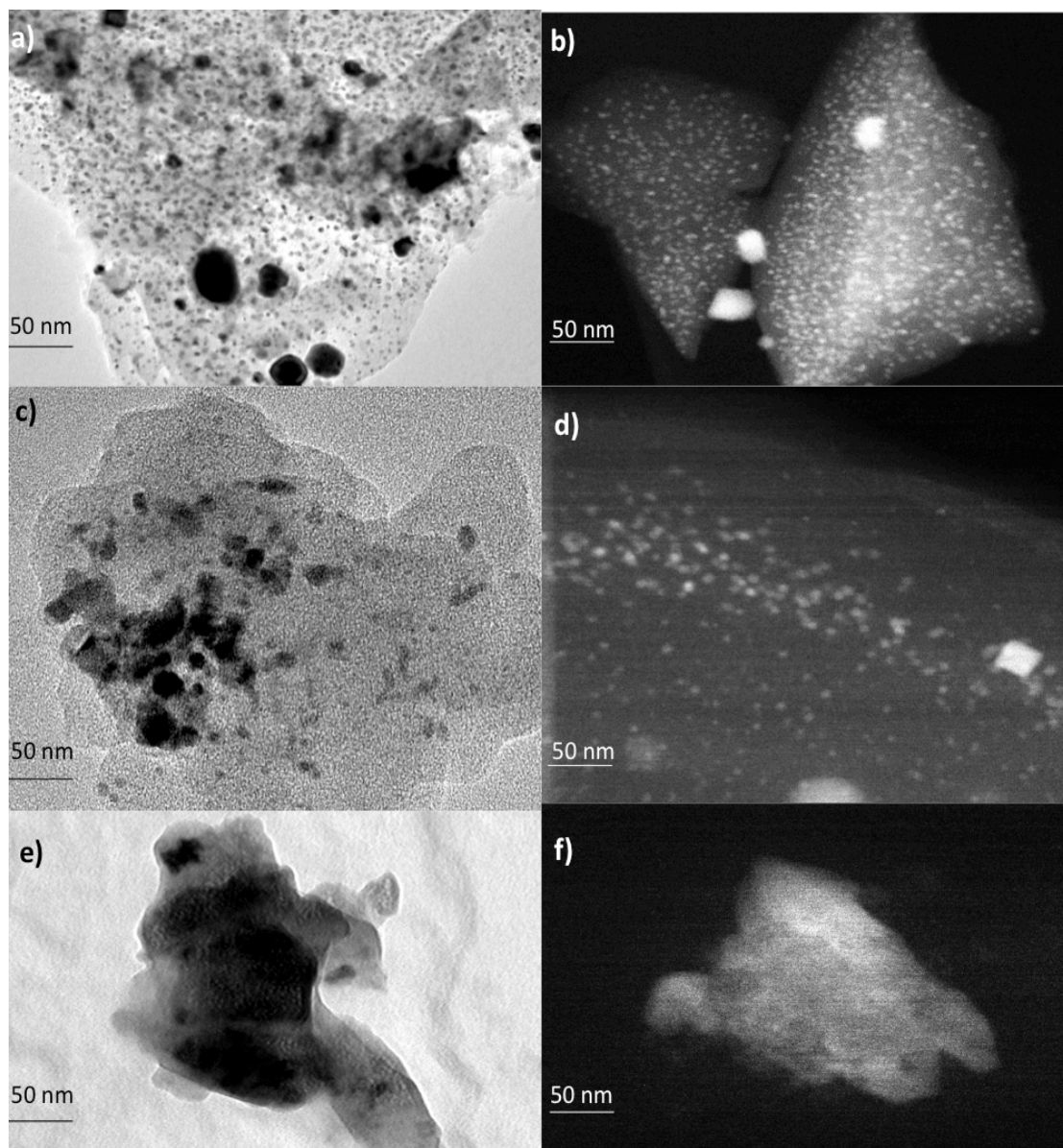


Figure 3.15: High-resolution transmission electron microscopy (HRTEM) image of a) Phytocat-2.5, c) Phytocat-0.1, e) control phytocat; High-angle annular dark-field scanning transmission electron microscopy (HAADF-STEM) image of b) Phytocat-2.5 d) Phytocat-0.1, f) control phytocat

The real time thermogravimetric analysis equipped with simultaneous fourier transform infrared spectroscopy (TGA-FTIR) experiments were conducted to understand the thermal stability of the pre-pyrolysis phytocat-2.5, phytocat-0.1 and control phytocat as well as the phytocat materials therefrom (**Figure 3.16**).

The pre-pyrolysis phytocat materials had a sharp mass loss in the temperature range of 150–400 °C (**Figure 3.16 a, d, g**). Two obvious peaks were found in the DTG curve. The first shoulder peak centered at 240 °C is related to the cleavage of side chains, such as residual acetyl and 4-O-methylglucuronic acid groups.⁵⁰ Remarkably, its peak intensity was increased by the presence of biologically bound Ni, particularly for pre-pyrolysis phytocat-2.5. The results suggested that the presence of biologically bound Ni achieved the cleavage of side chains at a relatively high rate.

The second peak depicts an initial weight loss around 370 °C, which was relatively similar for all the pre-pyrolysis phytocat materials. As shown in **figure 3.16 c, f, i**, the TGA plots of phytocat-2.5, phytocat-0.1 and control phytocat respectively, indicated a slight weight loss of about 6.1%, 7.2% and 7.5% at low temperature ($T \leq 150$ °C), which may be assigned to the removal of the adsorbed water or residual solvents from the surface. This reveals the remarkable thermal stability of phytocat even at high temperatures ($T \leq 700$ °C). Therefore, it was ascertained that there are numerous advantages of using microwave-heating, which promotes high dispersion of Ni species, easy reduction of surface Ni species, and formation of uniformly nano-sized Ni particles with good thermal stability.²⁰⁵

In order to further investigate the role of biologically bound Ni on the release of volatiles during the pyrolysis process, real time and simultaneous TGA-FTIR was used (**Figure 3.16 b, e and h**). It should be noted that the presence of biologically bound Ni accelerated the ring breaking and cracking reactions of lignocellulose to form light oxygenates and permanent gases. The effect of Ni on the evolution profiles of CO₂, CO, CH₄, H₂, C₂₋₄, and H₂O from pyrolysis was investigated. CO₂ was mainly generated from the decomposition of side chains and its derived pyrolysis intermediates, mostly acetyl groups and carboxylic groups.¹⁸⁹ CO was primarily produced through the cleavage of carbonyl ending groups left from the dehydration reactions.¹¹⁹

The results revealed that the presence of Ni relatively lowered the required initial temperature ($T < 300\text{ }^{\circ}\text{C}$) for the release of CO/CO_2 and improved the yield of CO/CO_2 , suggesting enhancement of the degree and rate of pyrolysis, particularly for phytocat-2.5. CH_4 was predominantly produced from the de-methylation *via* primary and secondary reactions, as discussed previously **in section 3.1.1**. It should be noted that the presence of Ni again facilitated the evolution of CH_4 at relatively lower temperature for phytocat-2.5 ($T < 300\text{ }^{\circ}\text{C}$) as compared to phytocat-0.1 and control phytocat ($T > 300\text{ }^{\circ}\text{C}$).

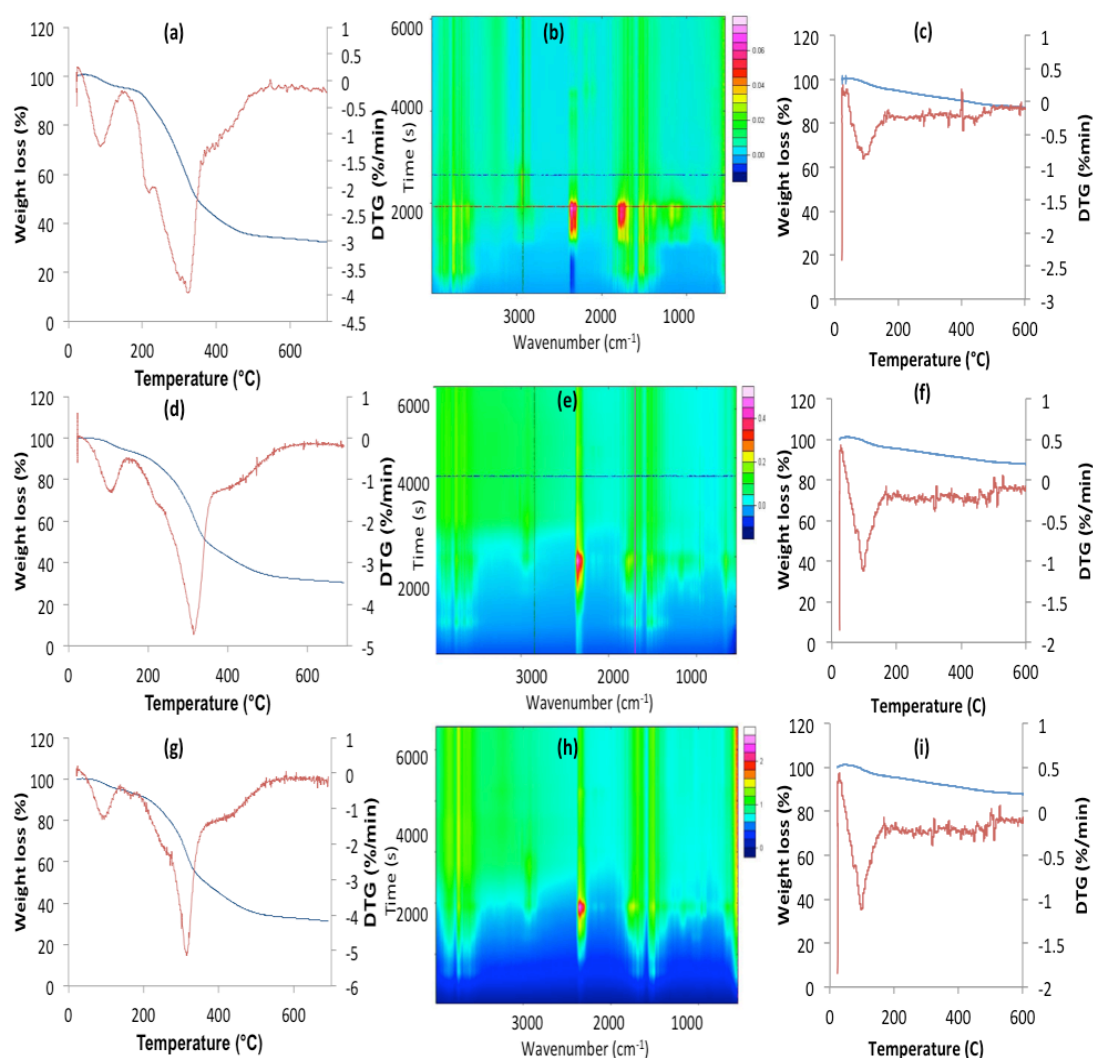


Figure 3.16: Real time thermogravimetric analysis coupled with fourier transform infrared spectroscopy (TGA-FTIR) for functional groups analysis of evolved gases in real-time for (a-b) Pre-pyrolysis phytocat-2.5, (c) phytocat-2.5, (d-e) pre-pyrolysis

phytocat-0.1, (f) Ni-phytocat-0.1, (g-h) pre-pyrolysis control phytocat (i) control phytocat .

3.3. Summary

Phytocat materials are envisioned as an air-stable and inexpensive, biologically bound Ni catalysts prepared from Ni-rich plant biomass. These Ni-based biocatalysts represent a hybrid platform consisting of naturally occurring, inorganic components with lignocellulose providing an exciting opportunity to advance green chemistry applications. The study focuses on developing biocatalysts from plants that have taken up nickel through natural, biological processes. This process allows both the recapturing of a limited, natural resource, remediation of land, and once the catalyst is used-up, the metal can be reused, presenting a sustainable circularity. The single step, low- temperature, microwave-assisted biosynthesis of catalytically active Ni makes it cost-effective alternative to conventional catalysts, which are typically fabricated using precious metals, involving multi-step, energy intensive synthesis.

The presence of biologically-bound Ni brought about the higher heating rate compared with the control experiments (using control phytocat). Consequently, this improved the pyrolysis degree, enhanced the secondary reactions of bio-oil and prevented the cracked products from reconstituting as coke. Secondly, the synergistic interaction of microwaves and the biologically bound Ni enabled the early formation of bio-char in advance, imposing a catalytic effect on the conversion of bio-oil into bio-gas *via* cracking or reforming reactions. These synergistic interactions enhanced the relative amounts of deoxygenated aromatic compounds in the bio-oil.

The dominant presence of phenols and derivatives was observed in the biooil extracted during the production phytocat-2.5. While the oil extracted during the production of control phytocat showed the dominant presence of hetero-aromatic compounds containing oxygen and nitrogen. Remarkably, the content of mono-cyclic aromatic compounds increased with the increasing concentration of the biologically

bound Ni, while poly-aromatics were the major constituents in the oil extracted during the production of control phytocat. Among these poly-aromatics, naphthalene and indole formed the major fraction of the extracted oil. At higher Ni concentrations, aromatic compounds were degraded into ring-opened compounds such as ketones and carboxylic acids that were finally degraded into CO₂, H₂, CH₄ and CO. It was inferred both the yield (up to 74vol%) and the quality of biogas were remarkably improved under microwave-biologically bound Ni interaction, highlighting their potential synergy, especially for producing syngas with a desirable H₂/CO value at about 1. Considering all of the aforementioned observations, the Ni based phytocats could in principle be used to develop a route for production of fine chemicals from pyrolysis oil (e.g. phenols and furans) instead of fuels, increasing the economic value of the products and using less energy

Moreover, the transformation of lignocellulose into platform chemicals such as levulinic acid, formic acid and lactic acid under mild conditions was reported. Importantly, these conversions can be operated without consumption of hydrogen or harsh conditions (higher temperatures, use of corrosive acids or longer reaction times) and thus, are more economical than hydrogenolysis or acid catalyzed hydrolysis.

Conclusively, the enhancement of the degree of pyrolysis (in accordance with the relatively higher heating rate) using phytocat-2.5, leads to the de-polymerization of cross-linking bonds of lignocellulose and the formation of an ordered aromatic structure. As a result, the microcrystalline structure of phytocat-2.5 tended to be regular and the graphitic degree enhanced with the synergistic interactions of microwave and the biologically bound Ni.

Chapter 4: Phytocat as a sustainable catalyst for the selective hydrogenation of platform molecules

Parts of the work reported in this chapter (mainly **section 4.1**) have been published in:

- c) **Johar P**, McElroy CR, Rylott EL, Matharu AS, Clark JH. Biologically Bound Nickel as a Sustainable Catalyst for the Selective Hydrogenation of Cinnamaldehyde. *Applied Catalysis B: Environmental*. 2022; 121105.

The purpose of this Chapter is to investigate Aim 2 as described previously within **section 1.2.2**. Particularly, this chapter explores the potential of the developed phytocat for hydrogenation of the model renewable platform molecules. The Chapter is divided into three main sections, primarily focusing on the results and discussion:

- (i) **Section 4.1**: Application of phytocat for the selective hydrogenation of cinnamaldehyde
- (ii) **Section 4.2**: Application of phytocat for the selective hydrogenation of furfural
- (iii) **Section 4.3**: Application of phytocat for the selective hydrogenation of levoglucosenone

4.1. Hydrogenation of cinnamaldehyde

The catalytic performance of the developed phytocat materials was evaluated following the insights of their structural characterization (as discussed previously in **Chapter 3, section 3.2**). Cinnamaldehyde (CAL) represents a typical model compound of the coniferyl aldehydes derived from lignin.¹⁰⁸ It can be produced by electron abstraction of the phenoxy radicals followed by disruption of the $C\alpha$ - $C\beta$ bond through retro-aldol cleavage of lignin.¹⁰⁸ Lignin-derived chemicals can serve as platform molecules for the production of a wide range of value-added chemicals, with implementation motivating the transformation towards a sustainable chemical industry. Chemoselective hydrogenation of $C=C$ and, or $C=O$ in α,β -unsaturated aldehydes is an imperative approach in fine chemical manufacturing. Cinnamaldehyde is an industrially important molecule, because its partial hydrogenation products, i.e. cinnamyl alcohol (COL) and hydrocinnamaldehyde (HCAL) are key intermediates for the synthesis of high-value products, including perfumes, flavorings.^{106,112,206,207} The production of saturated aldehydes from unsaturated ones also industrial and biological applications. For example, hydrocinnamaldehyde derived from cinnamaldehyde hydrogenation can be used in the synthesis of an intermediate reagent of anti-viral pharmaceuticals, particularly HIV protease inhibitors.²⁰⁸ At present, the major pathway of HCAL synthesis is the toluene chlorination-hydrolysis method.¹⁰⁶ Another method for the synthesis of HCAL and its derivatives (11–67% yield) is through a five-step process from the Knoevenagel condensation of aldehydes with Meldrum's acid.²⁰⁹ Moreover, Frost *et al.* reported the hydrosilylation of Meldrum's acid by a multi-step process, using palladium or molybdenum catalysts.^{210,211} Instead of these complex multi-step processes, selective hydrogenation of CAL to a HCAL reaction does not produce any corrosive byproduct or toxic waste.^{65,66,106,206} Most of the accomplished work on the partial reduction of CAL reported either poor selectivity (<13%) or poor conversion (<63%).^{212–214} Moreover, there remain challenges associated with the overall sustainability of the transformation i.e. relatively high cost or complex synthetic protocol for catalyst preparation or high reaction temperatures ($T > 150$ °C).^{212–214} In this study, an air-

stable, inexpensive and highly selective, biologically bound Ni catalyst (phytoCAT) was developed (as described in **Chapter 3**) and utilized for hydrogenation transformations.

Selective hydrogenation of a CAL entails reduction of different functional groups, that is, a carbonyl group (C=O) or a carbon–carbon double bond (C=C) to give the corresponding products cinnamyl alcohol (COL) or hydrocinnamaldehyde (HCAL) (**Figure 4.1**).

Based on thermodynamic and kinetic theory, hydrogenation of the C=C bond is more favorable due to lower bond energy of the C=C group (615 kJ/mol).^{112,215} It is vital to improve the selectivity to a certain group (C=O or C=C bond) and to avoid the hydrogenation of another one. Selectivity can be correlated with a metal d-bandwidth, and a smaller radial expansion of the d orbitals, leading to higher selectivity to HCAL.²¹⁴ Thus, some metals with a relatively large d-bandwidth (i.e. Ru, Ir and Pt) can be used as catalysts to synthesize COL, while the ones with small d-bandwidth (like Ni) favored HCAL.²¹⁴ The nature of adsorption and desorption of reactants (CAL) is governed by the changes in catalyst compositions, electronic structure, chemical state, and morphology of metal and supports, thereby determining the selectivity and yield of different products i.e. COL, HCAL or hydrocinnamyl alcohol (HCOL).^{68,216} One of the main approaches to catalyst design to enhance catalytic performance is to tune the metal–metal oxide interactions in the catalyst, which could lead to charge transfer between the metal and support.^{68,216}

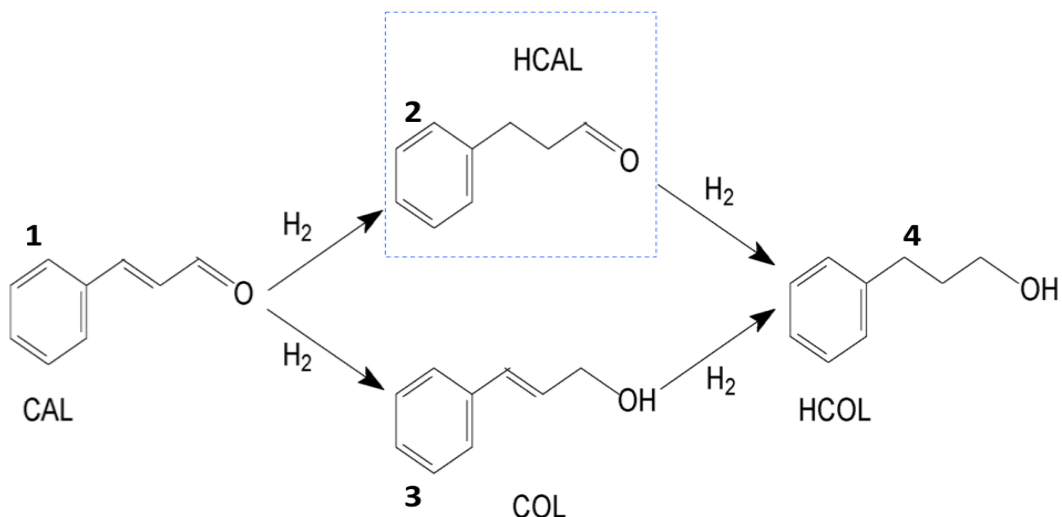


Figure 4.1: Mechanistic pathway for the hydrogenation of cinnamaldehyde

Although it has been reported that Ni favors the production of HCAL owing to its narrow d-bandwidth, this does not ascertain that all Ni-based catalysts show high C=C hydrogenation selectivity.¹⁰⁶ For instance, Ceatra *et al.* prepared carbon supported nickel catalyst using synthetic impregnation method (as discussed earlier in **section 1.2**), which displayed high catalytic activity (97% conversion of CAL), but low selectivity of C=C hydrogenation (21%).⁶⁵ In an attempt to improve the selectivity towards HCAL, some strategies such as introduction of another metallic constituent or doping heteroatoms in the support have been proposed.^{104,107,114,213} For instance, Yadav *et al.* demonstrated that HCAL selectivity of 100% alongside CAL conversion of 82% could be achieved over bimetallic Ni-Cu/RGO catalyst at 150 °C under 2 MPa, which was much better than the monometallic Ni-RGO catalyst (52% conversion, 28% HCAL selectivity).²¹³ Although nickel-based catalysts displayed high hydrogenation activity, the metallic nickel is unstable in air and prone to be oxidized.²¹⁷ Several reports have showcased pretreatment of Ni-based catalysts under H₂ before use to improve their catalytic performances.^{65,107,113} Furthermore, it has been reported that encapsulating the metal nanoparticles by a layer of inert materials (such as carbon and SiO₂) is an effective approach to prevent the oxidation and agglomeration.^{65,206} For instance, Li *et al.* coated a layer of SiO₂ shell on the surfaces of nickel silicate hollow spheres, which was reduced at 650 °C in H₂ to form a core-shell catalyst (*m*SiO₂@Ni/SiO₂@*m*SiO₂), showing 100% selectivity to HCAL.²¹⁶

However, the recyclability of the catalyst needs to be improved and the preparation procedure is very complex. Therefore, developing effective Ni-based catalyst using a simple approach is still under continuous exploration.

To showcase the activity and selectivity of Ni-based phytocat, its performance was compared with the commercial Raney Ni catalyst. Notably, the hydrogenation of CAL afforded HCAL from C=C hydrogenation and HCOL from complete hydrogenation (C=C and C=O reduction) using Ni-based phytocat materials and Raney Ni respectively. The control phytocat (pristine bio-carbon, <0.01 wt% Ni) was also tested. Remarkably, phytocat-2.5 exhibited relatively high activity (up to 97% CAL conversion and 96% HCAL selectivity) as compared with phytocat-0.1 (up to 89% CAL conversion and 87% HCAL selectivity). In comparison to phytocat-2.5 and 0.1, negligible conversion of CAL to products was observed using the control phytocat. Contrastingly, Raney Ni exhibited excellent activity (up to 99.9% CAL conversion) but lower selectivity towards HCAL (up to 82%). Although Raney Ni is non-selective towards the desired product, it works well under mild reaction conditions (40 bar H₂, 60 °C) as compared to the Ni-based phytocat. In order to optimize the conversion of CAL and the selectivity to HCAL, some factors influencing the reaction such as reaction temperature, reaction time and concentration of catalysts were explored.

The influence of reaction temperature on the hydrogenation of CAL to HCAL was investigated in the range of 60–120 °C (**Figure 4.2**). Increasing the hydrogenation temperature favored the conversion of CAL at different rates for various catalysts (**Figure 4.2a**). Notably, there was an enhancement of CAL conversion from 22% (60 °C) to 89% (120 °C), 43% (60 °C) to 97% (120 °C) and 94% (60 °C) to 99.9% (120 °C) for phytocat-0.1, phytocat-2.5 and Raney Ni respectively. For comparison, products obtained after hydrogenation reactions at various temperatures were analyzed using FTIR (**Figure 4.2b-c**) and NMR analysis (see **Appendix B**). Notably, as the temperature rises from 60 °C to 120 °C, the disappearance of the CO stretching peak of the cinnamaldehyde (1667 cm⁻¹) and the appearance of the CO stretching of hydrocinnamaldehyde (1720 cm⁻¹) was observed. Furthermore, the conversion after

24 h at 120°C was observed as intensity of the aldehyde peaks corresponding to cinnamaldehyde, which appeared at 9.71 ppm as a doublet decreases while intensity of peaks corresponding to hydrocinnamaldehyde, which appeared at 9.83 ppm as a triplet increases (see ^1H NMR spectra in **Appendix B**).

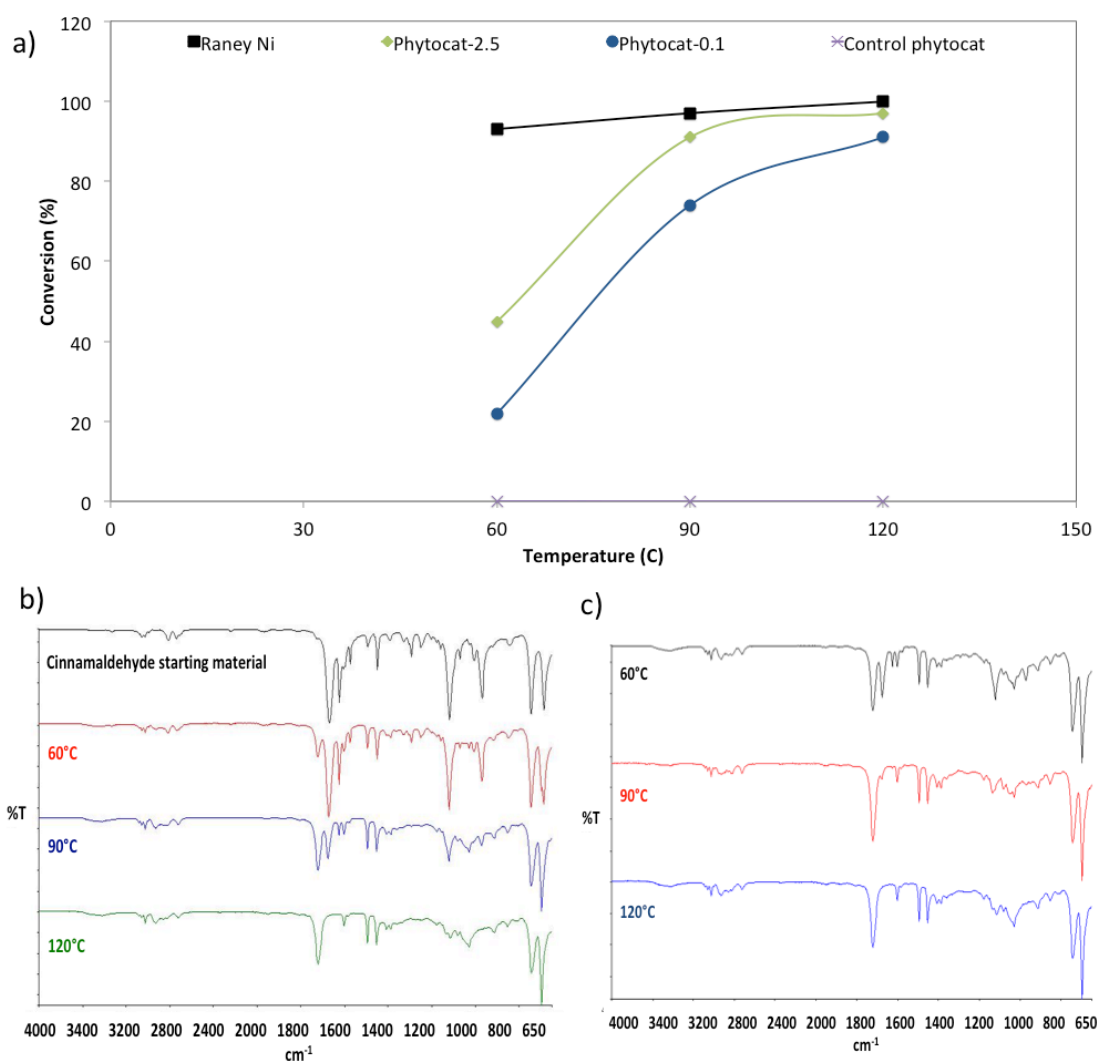


Figure 4.2: (a) Influence of reaction temperature on the catalytic conversion of cinnamaldehyde using various catalysts; FTIR spectrum of the products formed by hydrogenation of cinnamaldehyde at various temperatures using (b) phytocat-0.1 and (c) phytocat-2.5

As the temperature continued to increase, the selectivity towards HCAL increased from 79 to 84% (phytocat-0.1) and 92 to 97% (phytocat-2.5), while decreased from 96% to 9% using Raney Ni at 120 °C (**Figure 4.3a-c**). Therefore, the optimum temperature for conducting the hydrogenation reaction using phytocat was chosen to be 120°C. As listed in **Appendix B Table B1**, when Ni-based catalysts were applied, a higher reaction temperature and H₂ pressure were required, as compared to that when noble metal catalysts were used. This shift from mild reaction conditions could be due to the relatively low activity of Ni as compared to other precious noble metal catalysts.^{66,213} Therefore, it is essential that the performance of Ni-based catalysts is further improved through novel structure design. Many researchers have demonstrated the use of synthetic catalysts such as Ni supported on reduced graphene oxide (RGO) or Ni supported on activated carbon for conducting hydrogenation at high temperatures (T>150 °C) and achieved up to 91% CAL conversion with upto 82% HCAL.^{213,114} In this study, the maximum conversion of CAL (up to 97%) and highest selectivity towards HCAL (up to 97%) could be achieved at 120 °C using phytocat-2.5.

Furthermore, the products were characterized using gas chromatography equipped with mass spectrometer and flame ionization detector using anisole as internal standard (**Figure 4.3d** and **Appendix B Figure B1**). As observed in **Figure 4.3d**, the maximum CAL conversion was achieved using Raney Ni (99.9%), followed in decreasing order by phytocat-2.5 (97%) and phytocat-0.1 (89%), whereas no conversion was observed using control phytocat. Remarkably, the maximum selectivity towards HCAL was achieved using phytocat-2.5 (97%), followed in decreasing order by phytocat-0.1 (84%) and Raney Ni (9%). It should be noted that with the simultaneous decrease in the selectivity towards HCAL using Raney Ni, there was an immediate increment of HCOL production (91% selectivity), which is the final product of the hydrogenation reaction.

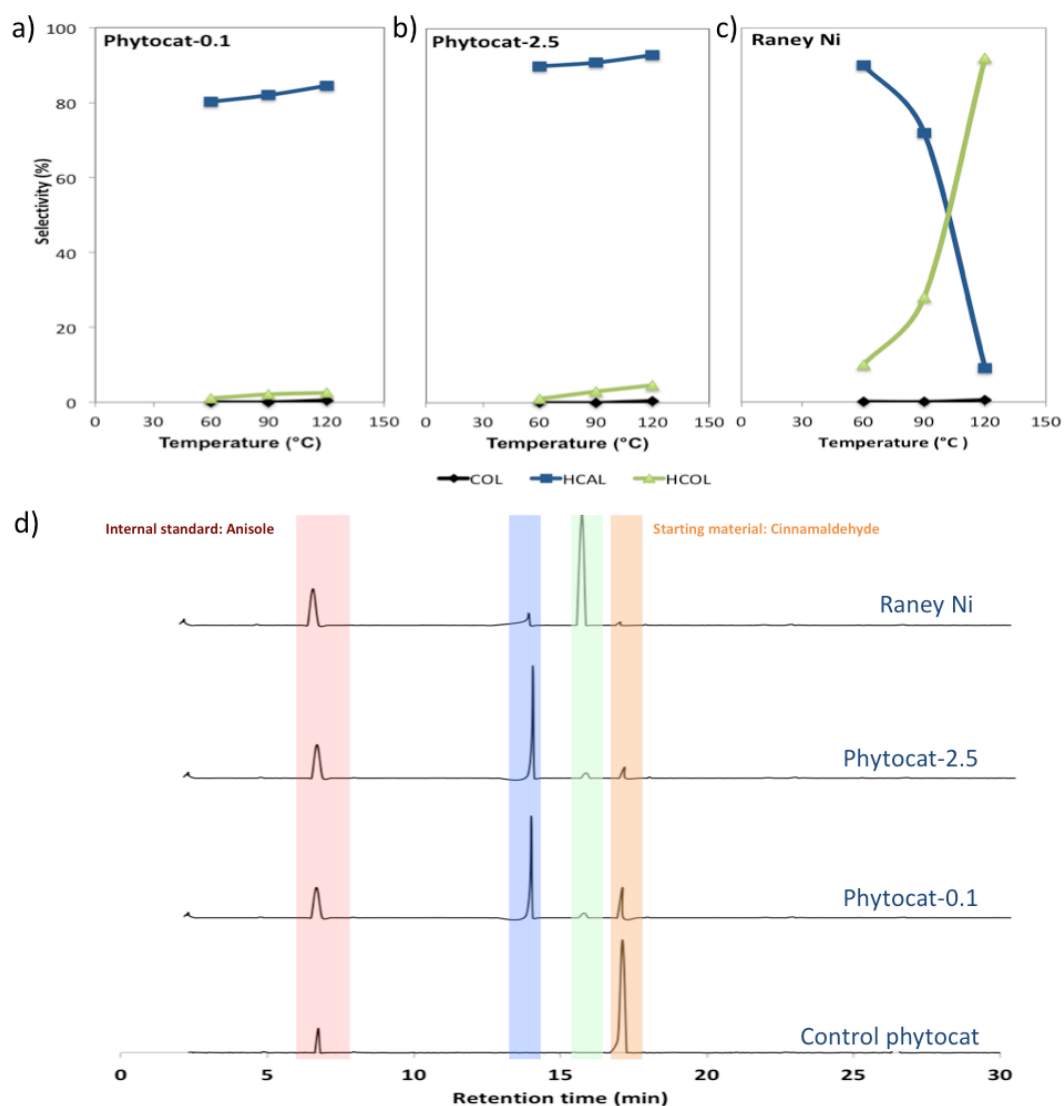


Figure 4.3: Influence of reaction temperature on the products selectivity using (a) phytocat-0.1, (b) phytocat-2.5, (c) Raney Ni; (d) GC-MS spectra of the products formed after hydrogenation of cinnamaldehyde at 120°C using different catalysts

Influence of concentration of catalysts on the selective hydrogenation of cinnamaldehyde: Several reports revealed that preparation methods affected the Ni crystal size and the nature of metal–support interactions and, thereby, influenced the activity of the catalysts.^{216,204,86} After studying the structural characteristics of the phytocat materials, it is clear that the phytocat-2.5 has highly dispersed catalytically active Ni⁰ sites. Due to the presence of highly dispersed and uniformly nano-sized Ni

particles, phytocat-2.5 showed superior catalytic performance. With increasing catalyst concentration, there was an increase in CAL conversion, leading to creation of the target product (97% and 89% HCAL) using phytocat-2.5 and 0.1 respectively (**Figure 4.4a**). Although Raney Ni was found to be non-selective towards HCAL, it worked efficiently even at lower concentrations (0.01 mmol) and showed a stable reaction profile throughout (**Figure 4.4b**).

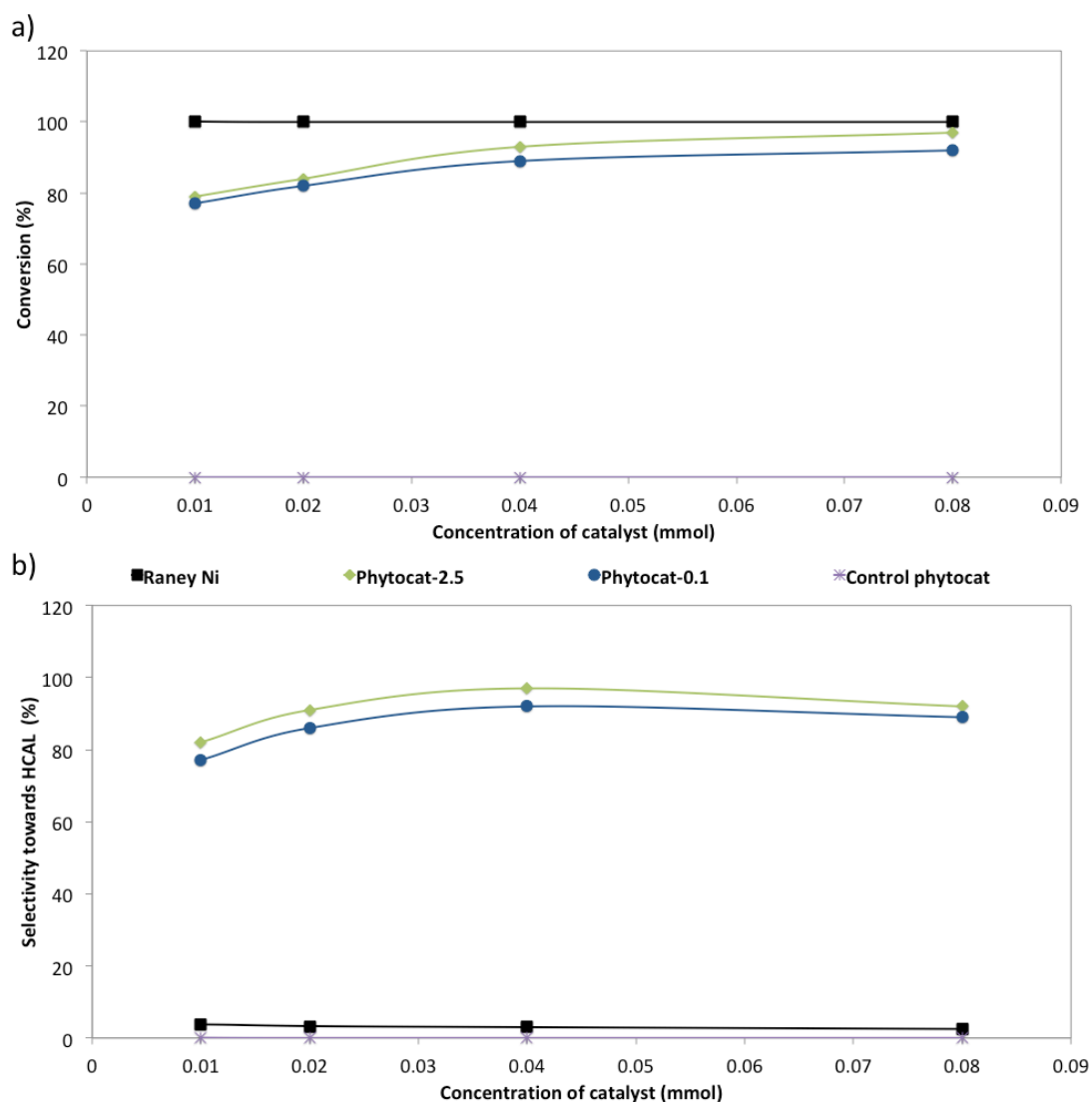


Figure 4.4: Influence of concentration of catalysts on the (a) conversion of cinnamaldehyde, (b) selectivity towards HCAL (Reaction conditions: 1 mmol substrate, 0.01-0.08 mmol Ni, 24 h, 40 bar H₂, 120 °C)

Influence of reaction time on the selective hydrogenation of cinnamaldehyde:

The variations in the CAL conversion and selectivity towards HCAL with varying reaction time (1-24h) at constant reaction temperature of 120 °C was monitored (**Figure 4.5**). As time progresses, the conversion of CAL increases from 45% to 84%, 77% to 97% and 94% to 99.9% using phytocat-0.1, phytocat-2.5 and Raney Ni respectively (**Figure 4.5a**). Although the selectivity remained stable after 2h at about 90% as the reaction proceeded and reached the maximum of 97% at 6 h (**Figure 4.5b**). This further indicated the difficulty of C=O bond reduction as compared to the C=C bond reduction.²¹⁸ As the reaction time is prolonged to above 6 h, the selectivity towards HCAL remains unaltered. As shown in **Appendix B Table B1**, the NiAl-LDH/G (Ni–Al layered double hydroxide/graphene) and Ni-Cu@RGO (RGO: reduced graphene oxide) catalysts showed high activity and high selectivity towards HCAL as well.^{213,219} Despite the high activity of Ni-Cu@RGO, its fabrication was done using a synthetic route and the catalytic performance was tested at high temperature ($T > 150$ °C).²¹³

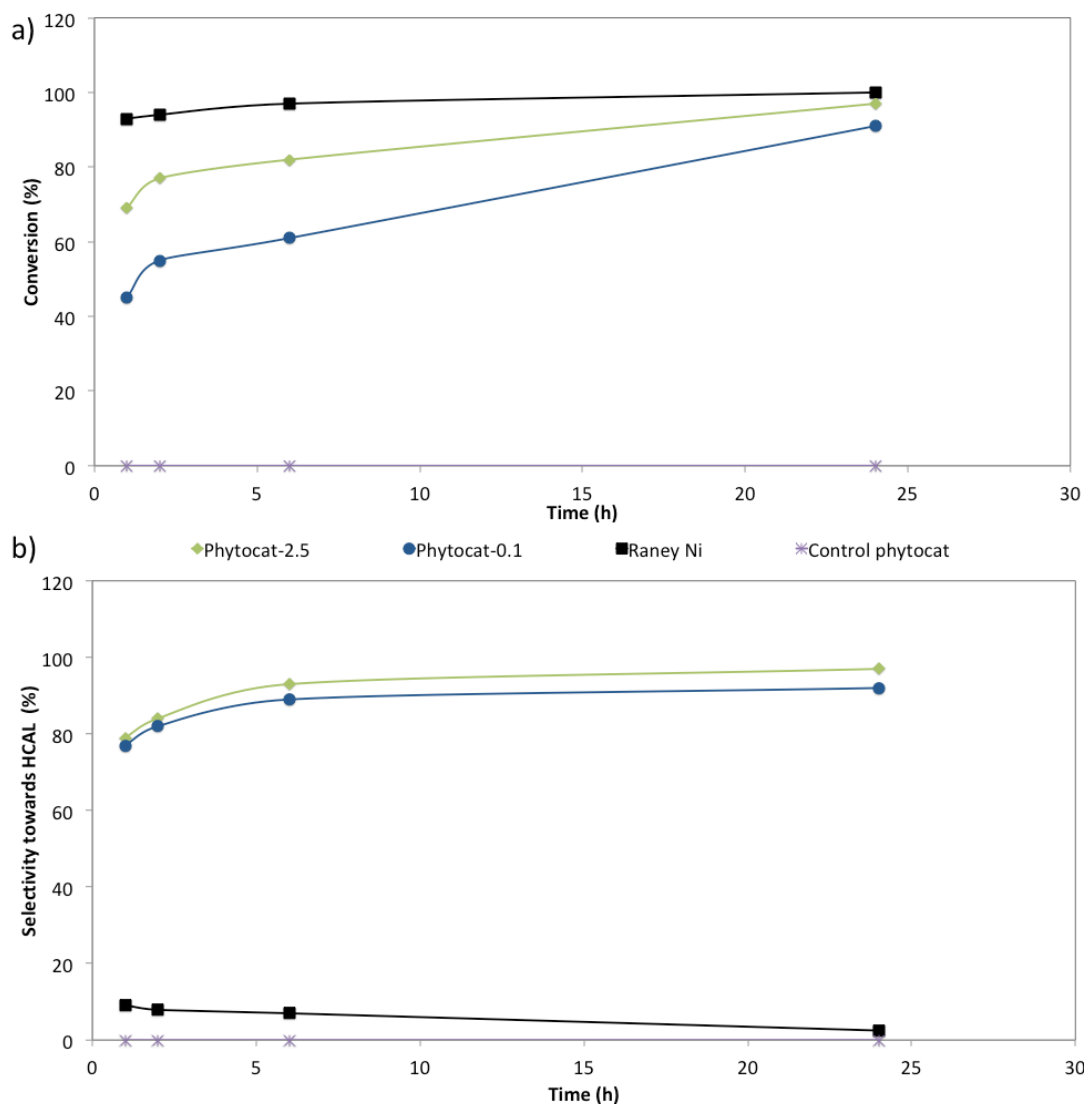


Figure 4.5: Influence of reaction time on (a) the catalytic conversion of cinnamaldehyde, (b) selectivity towards HCAL (Reaction conditions: 1 mmol substrate, 1-24 h, 40 bar H₂, 120 °C)

Stability of the catalysts: Reusability is an important catalyst performance indicator and was therefore investigated here (**Figure 4.6**). The reusability tests were performed using recovered phytocat-0.1 and phytocat-2.5 to illustrate their stability and performance for four consecutive cycles. The catalyst was recovered, washed with isopropanol three times and dried overnight. The catalyst was then weighed and transferred in a stainless steel multipoint (6 × 10 mL pots) reactor (manufactured at chemistry workshops, University of York). Following the same procedures, the

reaction was carried out at 120 °C and pressurized to 40 bar H₂. The sampling was done after 24 h of reaction, and the catalyst was recycled four times. Notably, after the third cycle, the conversion of CAL remained at 96% with 94% selectivity towards HCAL (**Figure 4.6a-c**), as demonstrated by Fourier transform infrared spectroscopy (FT-IR) analysis of the products formed after catalytic hydrogenation of cinnamaldehyde using pristine and recycled phytocat-0.1 and phytocat-2.5 (**Figure 4.6d-e**). For the first to the third catalytic cycles the conversions of >94% were achieved; a decrease in conversion was observed in the fourth catalytic run due to the mass lost during recycling and possibly due to deactivation of the catalyst.

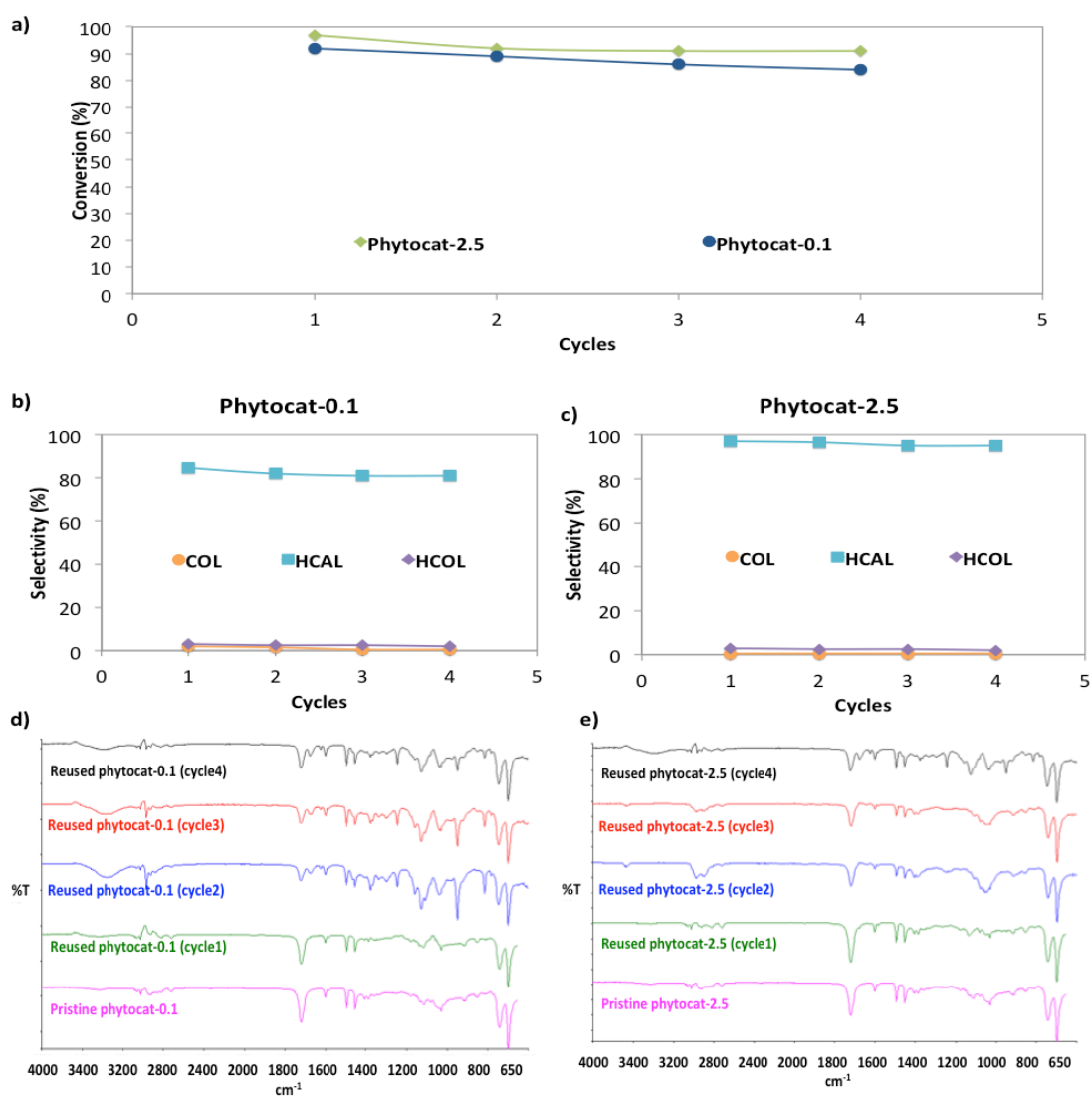


Figure 4.6: Reusability of the phytocat for (a) catalytic conversion of cinnamaldehyde, (b) Reusability of phytocat-0.1 for selectivity towards HCAL, (c) Reusability of phytocat-2.5 for selectivity towards HCAL, FTIR spectra of the products formed after the catalytic hydrogenation of cinnamaldehyde using recycled catalysts (d) phytocat-0.1 and (e) phytocat-2.5 (Reaction conditions: 1 mmol substrate, 24 h, 40 bar H₂, 120 °C)

The structural integrity of the catalyst remained intact after as many as four catalytic cycles. The high-angle annular dark-field scanning transmission electron microscopy (HAADF-STEM) image of the recycled catalyst shows structural features that are the same as the pristine catalyst (**Figure 4.7**). The shape and the sizes of the NPs are comparable to the pristine catalysts (6.1 ± 1.1 nm). After reuse, the catalyst was recovered and analysed, and the average particle size was found to be 7.2 ± 1.9 nm. These Ni NPs contained within the bio-carbon matrix of phytocat possess good thermal stability because of the constraints of the carbon support, which limit its aggregation and leads to excellent catalytic activity.

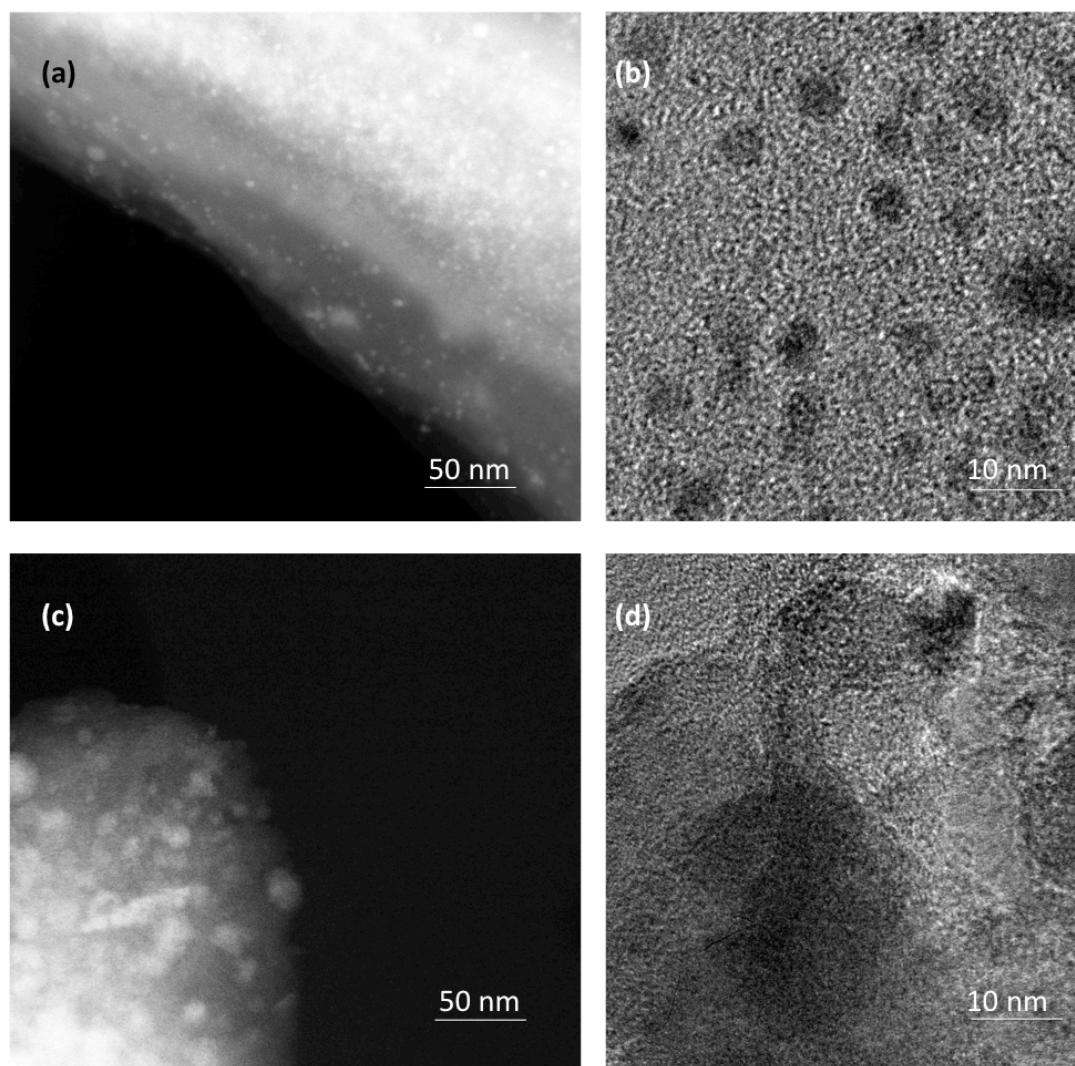


Figure 4.7: (a, c) High-angle annular dark-field scanning transmission electron microscopy (HAADF-STEM) image of recycled Ni-phytocat-2.5 and Ni-phytocat-0.1 respectively, (b, d) high-resolution TEM (HRTEM) image of recycled Ni-phytocat-2.5 and Ni-phytocat-0.1 respectively.

The elemental composition and chemical states of naturally bound nickel in the bio-carbon matrix were analyzed by X-ray photoelectron spectroscopy (XPS) analysis (**Figure 4.8a**). Generally, catalysts with low nickel metallic loadings are dominated by Ni^{2+} along with some sequestered Ni^0 sites.⁸⁶ The differences in metallic nickel leads to changes in the surface chemistry and consequently the catalytic activity. [40] The peak around 852 eV is assigned to Ni^0 and peaks between 855 and 861 eV are

assigned to Ni^{+2} in the form of $\text{Ni}(\text{OH})_2$ and NiO .² The surface of the phytocat consisted of both Ni^0 and Ni^{2+} . However, with increasing nickel content, there is an increase in intensity of Ni^0 peak with a simultaneous decrease in intensity of Ni^{+2} peak. After use, the recycled catalyst was analyzed and found to have a slight decrease in the intensity of the Ni^0 peak. Taking into consideration that these valence states only belong to the outer layers of the phytocat, these results suggest the formation of a unique structure where a pure nickel core is surrounded by a shell of NiO and $\text{Ni}(\text{OH})_2$.

To understand the crystal structure and phase purity of the phytocat material, X-ray diffraction (XRD) was used. Initial x-ray powder diffraction (XRD) analysis revealed metallic nickel particles along with a carbon rich phase. As shown in Figure 3e, the diffraction peaks at 44.6° , 52.2° , and 77.3° belong to metallic Ni ([111], [200] and [220] diffraction peaks of Ni^0).²⁰³ Both the phytocat materials exhibits a broad graphitic (002) peak at about 25° , which belongs to the hexagonal conjugated carbon structure. This confirms that the structure of the phytocat is relatively stable compared to Raney Ni and the majority of entrapped NiO is reduced to Ni metal by the surrounding bio-carbon matrix during the microwave-assisted pyrolysis. Similarly, after use, the characteristic peaks of bio-carbon ($2\theta = 24.5^\circ$) and Ni metal ($2\theta = 44.5^\circ$, 51.9° and 76.9°) are observed for all the phytocat materials, in which the intensity of [111], [200] and [220] diffraction peaks due to Ni^0 is gradually increased with increasing Ni content (**Figure 4.8b**).²²⁰

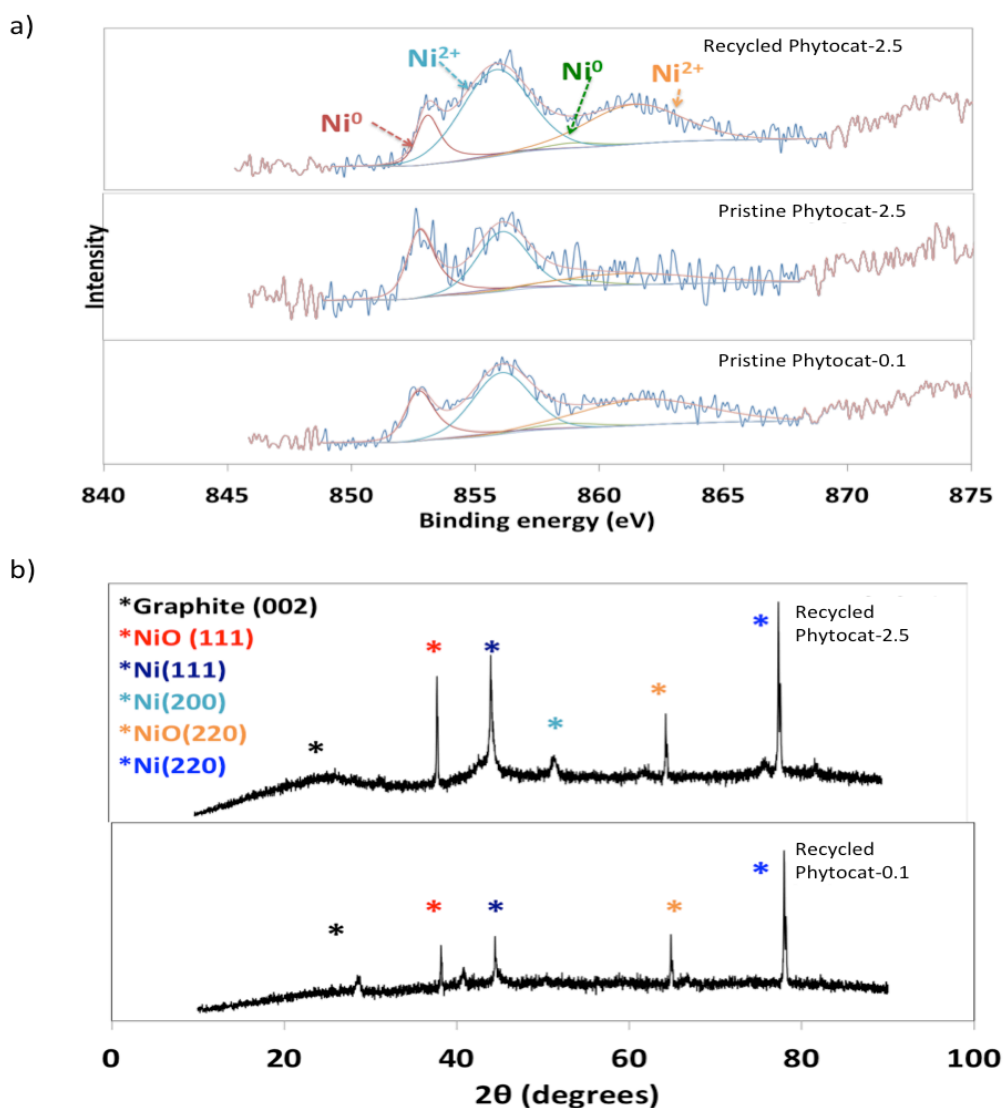


Figure 4.8: X-ray photoelectron spectroscopy (XPS) analysis of the pristine and recovered phytocat-2.5 and phytocat-0.1 (a) de-convoluted high-resolution Ni $2p_{3/2}$ spectra (b) X-ray diffraction (XRD) pattern of the recovered phytocat-2.5 and phytocat-0.1.

The well-maintained catalytic performance for four-consecutive runs demonstrates a high stability and reusability of Ni-phytocat. This can be attributed to the superior structural stability of Ni-phytocat as evidenced by the almost unchanged structure, morphology, and crystal phase and chemical forms of the reused Ni-phytocat.

To further illustrate the role of the bio-carbon matrix around the phyto-extracted Ni, which enables an efficient suppression of the over-hydrogenation reaction pathway and prevented further dissociation of adsorbed hydrocinnamaldehyde molecules, the catalytic hydrogenation tests were performed on furfural and levoglucosenone (LGO) (as discussed later in **section 4.2** and **4.3**).

4.2. Hydrogenation of furfural

Furfural (FF) is also a typical α , β -unsaturated aldehyde bearing C=C and C=O groups and one of the important intermediates derived from the dehydration of a hemicellulose-derived pentose.¹⁰² It is one of the main components in the bio-oil (as discussed previously in **Chapter 3**), serving as a major platform molecule in biomass conversion. Due to the presence of dual functionalities, the products of its hydrogenation are complex in nature and therefore, will be investigated further in this section. Currently, one of the most relevant use of FF as a chemical feedstock is in the production of furfuryl alcohol (FA). FF hydrogenation can also lead to the formation of other chemicals besides FA (**Figure 4.9**), such as 2-methylfuran (2-MF, by hydrogenolysis of the C–OH bond), tetrahydrofurfuryl alcohol (THFA, by hydrogenation of the furan ring of FOL), and 2-methyl tetrahydrofuran (2-MTHF, from the hydrogenation of MF).^{102,118}

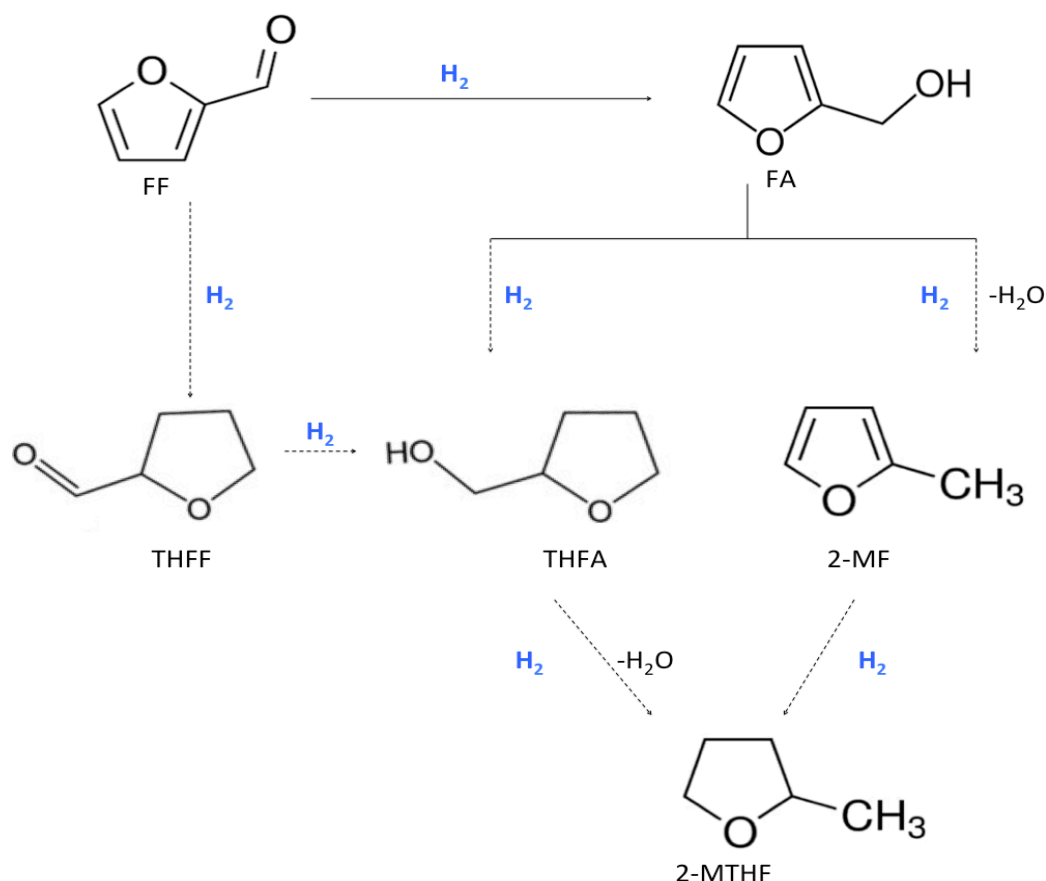


Figure 4.9: Mechanistic pathway for the hydrogenation of furfural¹⁰²

Primarily, the influence of various phytocat materials at various temperatures was investigated for the hydrogenation of FF. At temperature below 120°C, almost negligible conversion took place (<3%), whereas, a slight improvement was observed at 120°C (5.6% conversion) using phytocat-2.5 (**Figure 4.10a**). In contrast, the control phytocat (pristine bio-carbon matrix) was found to be ineffective in all the hydrogenation tests even after long reaction times (24h) and high temperature (120°C). As can be seen in **Figure 4.10b**, both the Ni based phytocat materials were found to be non selective towards FA (with selectivity <10%). This further demonstrated the difficulty of C=O bond reduction as compared to the C=C bond reduction, as observed previously during hydrogenation of CAL (**section 4.1**).

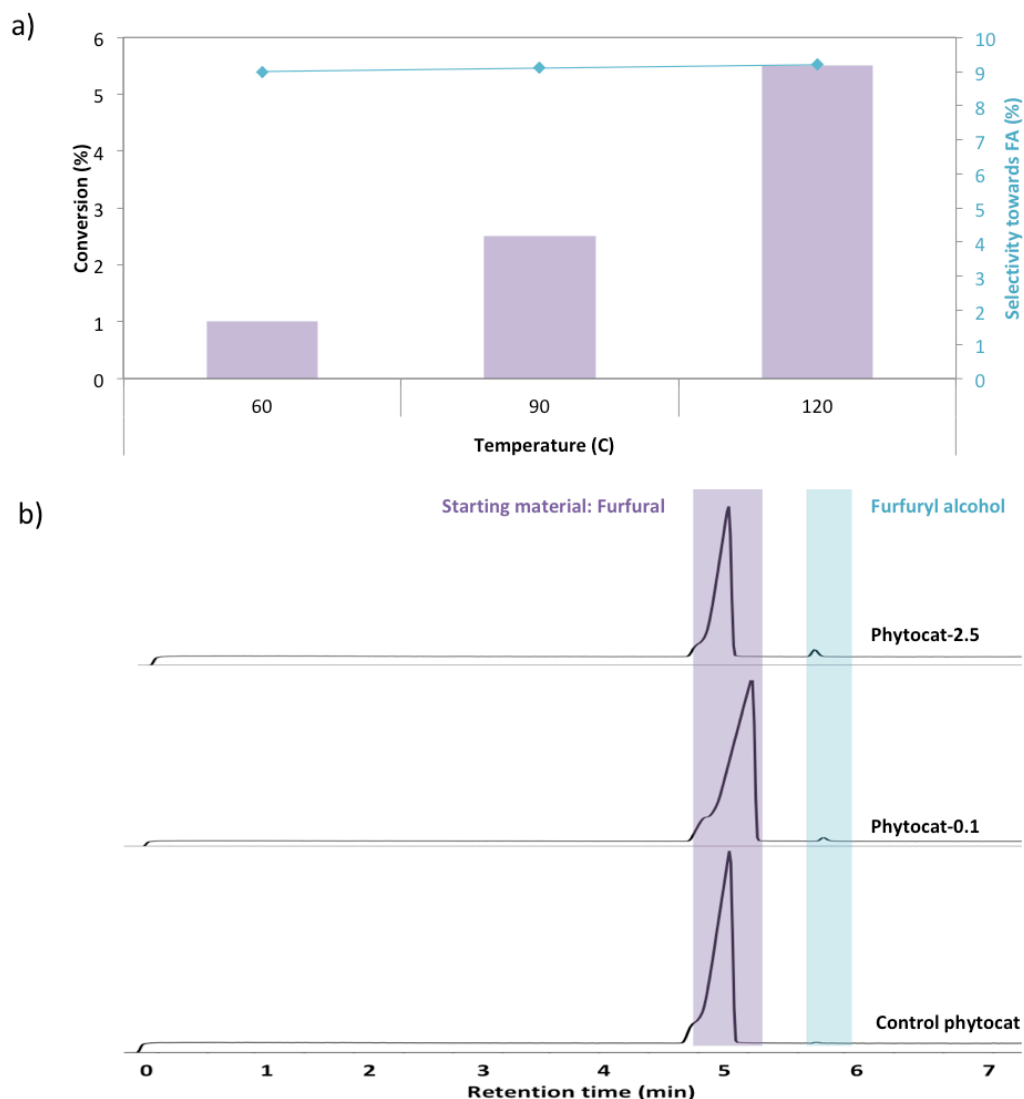


Figure 4.10: (a) Conversion of furfural using phytocat-2.5 at various temperatures and its selectivity towards furfuryl alcohol, (b) GC-MS chromatograms of the products formed (Reaction conditions: 1 mmol substrate, 24 h, 40 bar H_2 , 60-120 °C)

Therefore, these findings clearly demonstrate that the biologically bound Ni enables an efficient suppression of the over-hydrogenation reaction pathway, making it non-selective towards the formation of alcohols while preferring the formation of saturated aldehyde (as observed previously in **Section 4.1**). In order to validate these findings, the hydrogenation tests were performed on levoglucosenone (**section 4.3**).

4.3. Hydrogenation of levoglucosenone

Levoglucosenone (LGO) is another promising renewable platform molecule usually produced from pyrolysis of cellulose-containing raw materials.^{103,120} LGO presents dual functionalities susceptible to hydrogenation, the C=O group at position C-2 and the C=C at position C-3 (**Figure 4.11**).^{103,109,120} On the one hand, selective C=C hydrogenation leads to dihydrolevoglucosenone (Cyrene™), a saturated compound, which preserves the C=O group at C-2.^{103,120} Generally, this ketone is difficult to obtain without simultaneous partial hydrogenation of C=O to C–OH, thus generating the saturated alcohol or levoglucosanol (Lgol), having two stereoisomers (exo-Lgol and endo-Lgol).¹²⁰ Cyrene (CY) has been used as a nontoxic renewable dipolar aprotic solvent and has been reported as a very promising substitute for dipolar aprotic solvents, such as *N*-methyl pyrrolidone.¹²¹ Based on the previous research results using commercial Pd, Pt and Ru supported on carbon catalysts, the study and application of the supported Pd and Pt metals showed selectivity towards one specific hydrogenated product.^{103,109} The Pd/C catalyst was reported to give higher yield of CY compared to Ru/C and Raney Ni catalysts, which mostly resulted in low CY yield (4.9–8.4%).¹⁰⁹

However, the distribution of products obtained in each case differs according to the type of metal used. Therefore, using 5 wt% Pd/C catalyst showed a high selectivity (up to 82%) towards the hydrogenation of the C=C group, with CY being the major product. While, 5 wt% Pt/C succeeded in hydrogenating both the C=C and the C=O of LGO, thus producing the saturated alcohol, Lgol with a selectivity of around 50%.¹⁰³

In this section, the role of phytocat will be investigated for the selective hydrogenation of LGO in order to gain further insights into the preference of phytocat to selectively hydrogenate C=C or C=O bond of such α , β -unsaturated carbonyl compounds.

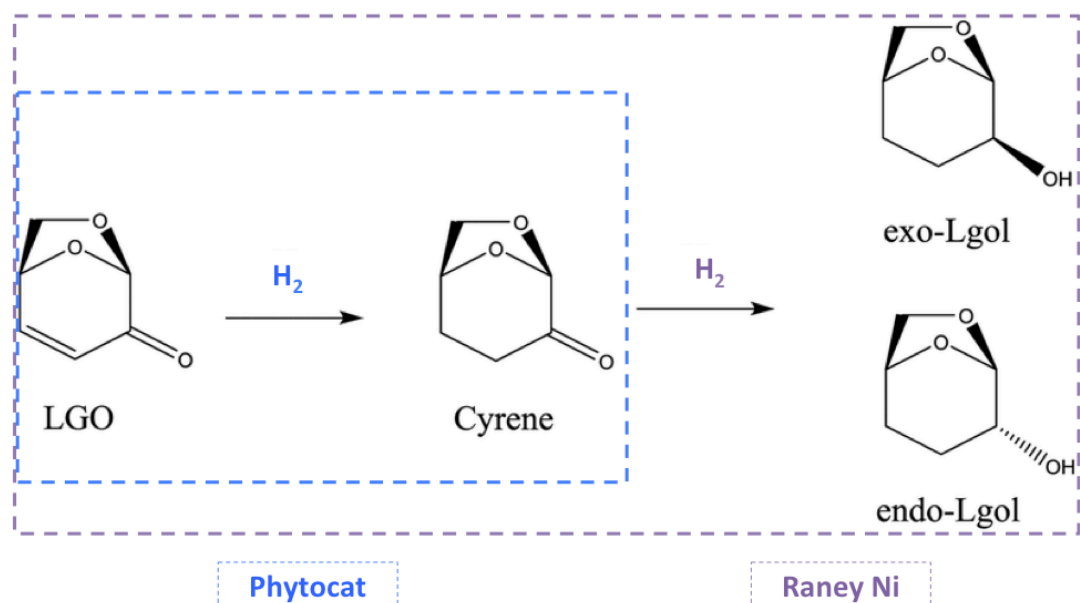


Figure 4.11: Mechanistic pathway for the hydrogenation of Levoglucosenone

The influence of reaction temperature on the hydrogenation of LGO was investigated in the range of 60–120 °C (**Figure 4.12**). Overall, increasing the hydrogenation temperature favored the conversion of LGO (**Figure 4.12a**). Notably, there was an enhancement of LGO conversion from 15.5% (60 °C) to 69% (120 °C) using phytocat-2.5. It should be noted that the major product of the reaction was CY with the selectivity up to 99%. However, the selectivity towards CY remained unaffected by the variation in temperature, which shows that phytocat-2.5 was highly selective towards the hydrogenation of C=C bond of LGO rather than C=O, which leads to subsequent production of CY rather than Lgol. For comparison, products obtained after hydrogenation reactions at various temperatures were analyzed using FTIR (**Figure 4.12b**) and NMR analysis (see **Appendix B**). Notably, as the temperature rises from 60 °C to 120 °C, the disappearance of the CO stretching peak of the LGO (1665 cm^{-1}) and the appearance of the CO stretching of CY (1710 cm^{-1}) was observed. Furthermore, the reaction products at 90°C were found to contain characteristic peaks corresponding to LGO (1665 cm^{-1}) as well as CY (1710 cm^{-1}), which demonstrated relatively lower conversion at temperature below 120°C. The FTIR, ^1H NMR and ^{13}C NMR analysis together with the GC-MS spectrum proved that CY was, in fact, the

major product of this reaction (see **Figure 4.12b, 4.13** and **Figure B6-9 in Appendix B**). In general, the parameter of enthalpy is more important than the parameter of entropy to produce CY, during the pathway of further hydrogenation of CY to Lgol, based on the literature studies.¹²⁰ Due to this, as temperature rises, the thermodynamics of the system prevents complete hydrogenation, leading to CY as the major product of this reaction.

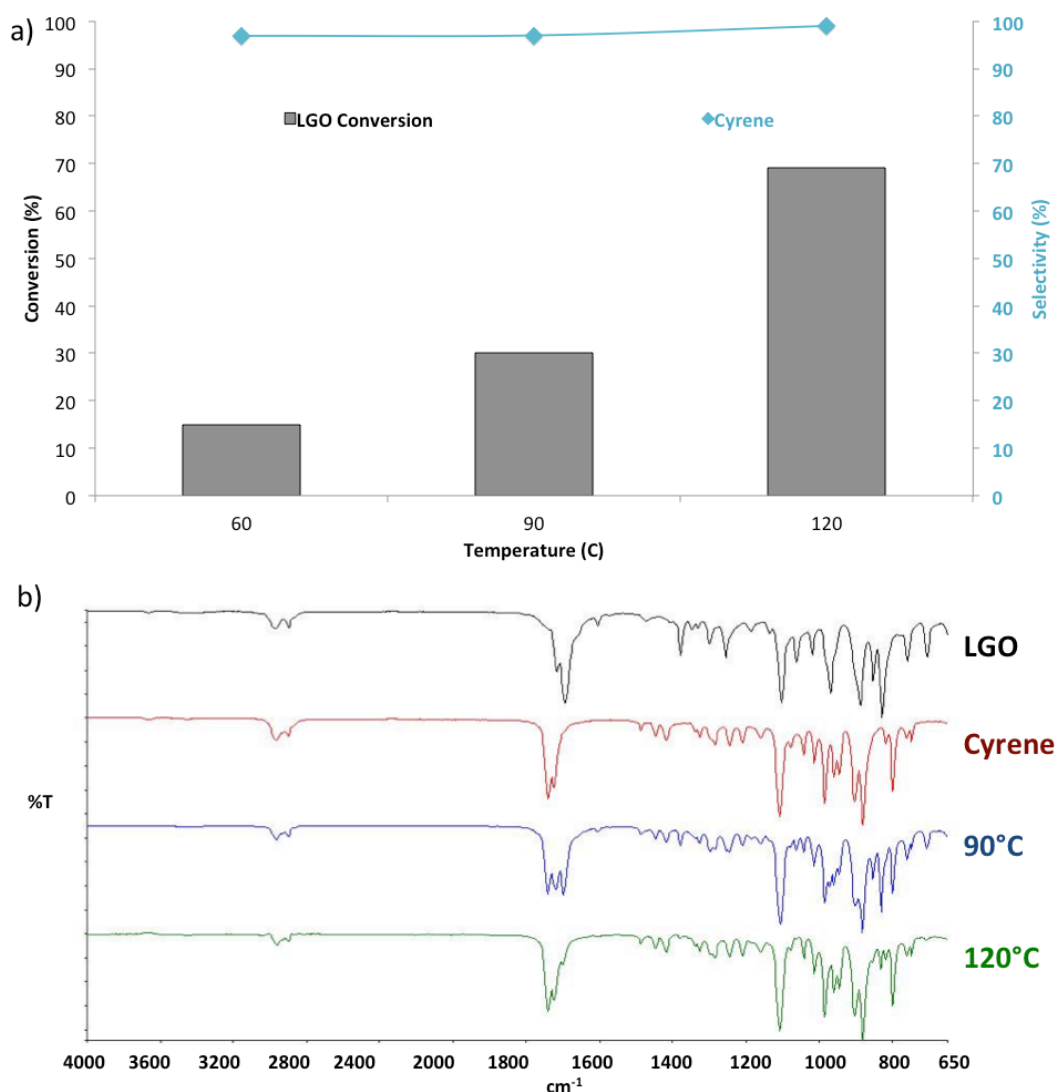


Figure 4.12: (a) Conversion of LGO using phytocat-2.5 at various temperatures and its selectivity towards Cyrene, (b) FTIR spectra of the products formed by hydrogenation of LGO using phytocat-2.5 (Reaction conditions: 1 mmol substrate,

24 h, 40 bar H₂, 60-120 °C)

In order to ascertain and compare the role of various catalysts, the hydrogenation tests were performed at 120°C using phytocat-2.5, phytocat-0.1, control phytocat and the commercial Raney Ni catalyst. Notably, the hydrogenation of LGO afforded CY from C=C hydrogenation and Lgol from complete hydrogenation (C=C and C=O reduction) using Ni-based phytocat materials and Raney Ni respectively (**Figure 4.13a**). The control phytocat (pristine bio-carbon, <0.01 wt% Ni) was also tested and found to be ineffective in all the hydrogenation tests even after long reaction times (24h) and high temperature (120°C). Remarkably, phytocat-2.5 exhibited relatively high activity (up to 69% LGO conversion and 99% CY selectivity) as compared to phytocat-0.1 (up to 60% LGO conversion and 97% CY selectivity). In contrast, Raney Ni exhibited excellent activity (up to 99.9% LGO conversion) but lowest selectivity towards CY (<0.1%). Although Raney Ni was found to be non-selective towards the desired product, it worked well to convert LGO into Lgol (up to 99% selectivity) as compared with the Ni-based phytocat. As shown in **Figure 4.13b**, LGO can be selectively hydrogenated to two stereoisomers of Lgol (exo-Lgol and endo-Lgol) using Raney Ni. Therefore, the Ni-based phytocat materials were found to be highly selective towards CY, whereas Raney Ni led to complete hydrogenation to produce Lgol as the major product of the reaction.

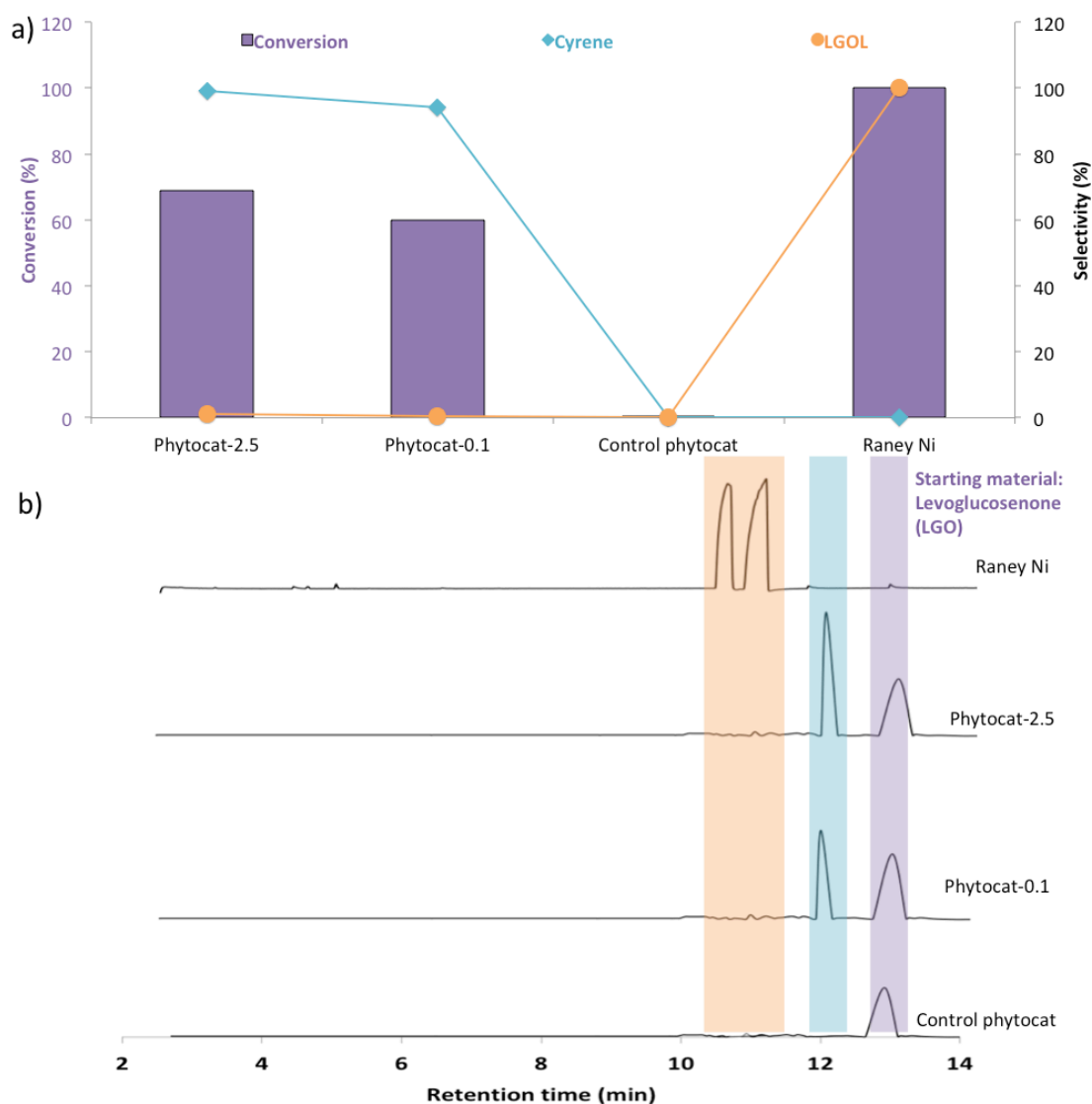
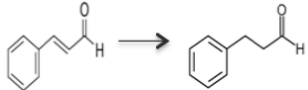






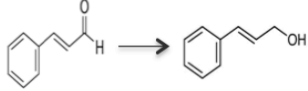






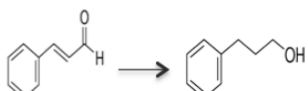






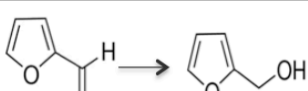















Figure 4.13: (a) Conversion of LGO using various catalysts, (b) GC-MS analysis of the products formed by hydrogenation of LGO at 120 °C using various catalysts.

4.4 Summary

Utilizing non-noble and inexpensive materials to achieve the same or better level of functionality has become crucial to ensure overall sustainability of the chemical transformation. With this thought, a biologically bound non-noble metal catalyst (low metallic loadings: 0.1-2.5 wt.% Ni) was prepared using a simple, one-step, energy efficient, low temperature MAP (as described previously in **Chapter 3**). The Ni-based phytocat materials represent a hybrid platform consisting of naturally occurring, inorganic components with lignocellulose providing an exciting opportunity to

advance green chemistry applications. Interestingly, the biologically bound Ni in the plant matrix directs the selective hydrogenation of cinnamaldehyde (up to 97% conversion at $T \leq 120$ °C), thereby removing the need for traditionally mined metal. Most of the reported work on the partial reduction of cinnamaldehyde (CAL) shows either poor selectivity (<13%) or poor conversion (<63%).^{107,114} Moreover, there remain challenges associated with the overall sustainability of the transformation i.e. relatively high cost or complex synthetic protocol for fabrication of catalyst or high reaction temperatures ($T > 150$ °C).^{213,114} HCAL and its derivatives have established themselves as industrially and biologically valuable in the synthesis of natural products, anti-viral pharmaceuticals, fragrances and chemosensors.^{208,207,221,222} The findings of this study indicates that the presence of bio-carbon matrix around the naturally entrapped Ni enables an efficient suppression of the over-hydrogenation reaction pathway and carbonaceous accumulation on the surface. That is, the natural encapsulation of nickel on bio-carbon not only inhibits the unselective hydrogenation pathway but also regulates the electronic structure of Ni. Therefore, it suppresses the further dissociation of adsorbed HCAL molecules, leading to its high selectivity (up to 96%) at low temperatures ($T \leq 120$ °C). Based on the results, the control phytocat (pristine bio-carbon matrix) was found to be ineffective in all the hydrogenation tests even after long reaction times (24 h) and high temperature (120 °C). Furthermore, the Ni-based phytocat materials were successful in converting LGO into dihydrolevoglucosenone (CyreneTM, up to 69% conversion and 99% selectivity), while it was unable to convert furfural into furfuryl alcohol. However, using Raney Ni, the formation of levoglucosan (Lgol) was observed instead of CyreneTM. These findings clearly demonstrate that the presence of the bio-carbon matrix around the biologically bound Ni enables an efficient suppression of the over-hydrogenation reaction pathway, making it highly selective towards the formation of saturated aldehydes over alcohols (**Figure 4.14**).

Reaction*	P-2.5-60	P-2.5-90	P-2.5-120	P-0.1-60	P-0.1-90	P-0.1-120
						
						
						
						
						





Selectivity (%):  >80%  40-80%  <40%  no reaction
--

Figure 4.14: Comprehensive outlook of the selective hydrogenation using phytocat at various temperatures

(*Reaction conditions: 1 mmol substrate, 0.01-0.08 mmol Ni, 24 h, 40 bar H₂, 60-120 °C; P-2.5 denotes phytocat-2.5 and P-0.1 denotes phytocat-0.1 at the particular temperature)

Interestingly, Ni-phytocat was found to be selective towards the hydrogenation of C=C bonds over C=O bonds, resulting in the formation of the corresponding saturated aldehyde rather than the unsaturated alcohol. Conclusively, the overall sustainability and stability of Ni-phytocat is considerably higher in comparison with the traditional synthetic catalysts.

Chapter 5: Phytocat accelerated de-polymerization of plastics

Parts of the work reported in this chapter (mainly **section 5.1**) have been published in:

Johar P, Rylott EL, McElroy CR, Matharu AS, Clark JH. Phytocat—a bio-derived Ni catalyst for rapid de-polymerization of polystyrene using a synergistic approach. *Green Chemistry*. 2021;23(2):808-14.

The purpose of this Chapter is to investigate Aim 3 as described previously within **section 1.2.3**. Particularly, it deals with gaining mechanistic insights for the accelerated de-polymerization of plastics using the developed phytocat materials. The Chapter is divided into three main sections, primarily focusing on the results and discussion:

- (i) **Section 5.1**: The role of phytocat in accelerating microwave-assisted de-polymerization of polystyrene (PS).
- (ii) **Section 5.2**: The role of phytocat in accelerating microwave-assisted de-polymerization of polyethylene (PE).
- (iii) **Section 5.3**: The role of phytocat in accelerating microwave-assisted de-polymerization of PureFlex™ Film (PF).

5.1. De-polymerization of polystyrene

Both the biologically bound Ni (phytocat-1.5) and hydroponically-infused Ni (phytocat-0.1) play a significant role in the microwave assisted de-polymerization of PS. Remarkably, the energy consumption was relatively less (18 kJ/g and 24 kJ/g of microwave energy was consumed to reach the set-point of 250 °C in less than 2 min) using phytocat-1.5 and phytocat-0.1 respectively, as compared to the control phytocat (42 kJ/g of microwave energy consumed) and activated carbon (36 kJ/g of microwave energy consumed) (**Appendix C Figure C1**). This could be due to the synergistic interactions of biologically bound Ni and microwaves to accelerate the de-polymerization process. Notably, the synergistic interactions of metal and microwaves could be related to the similar study by Larry *et al.*, where copper wire was used as antenna for producing low temperature plasma during MAP of bituminous coal.²²³

Remarkably, phytocat-1.5 offered advantages in enabling rapid de-polymerization of PS (up to 91% conversion efficiency) as compared to Ni-phytocat-0.1 (up to 84%), control phytocat (up to 81%) and activated carbon (up to 79%) within 5 min under microwave irradiation (**Figure 5.1a**). This further demonstrates the highly energy efficient route to PS de-polymerization under microwave irradiation to produce mono-aromatics (particularly styrene monomer) in high yields (**Figure 5.1b**), which will be discussed further in detail.

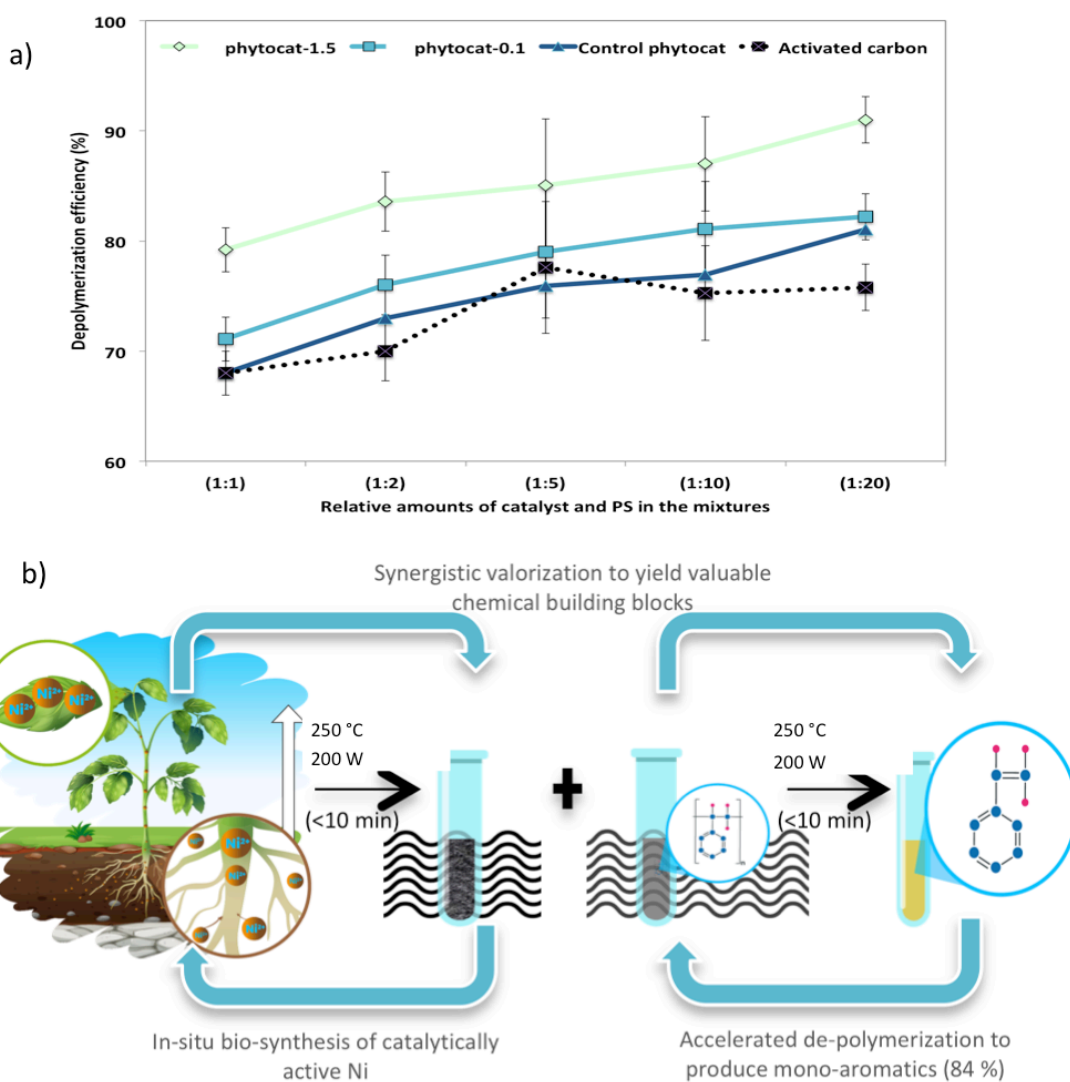


Figure 5.1: (a) Comparison of efficiency of various catalysts for rapid de-polymerization of PS, (b) graphical illustration of the accelerated de-polymerization process of PS to produce monomer units.

In general, phytocat, and activated carbon aid in transferring microwave energy as heat energy to PS, achieving high heating rates ($150\text{-}200^{\circ}\text{Cmin}^{-1}$). Furthermore, the addition of phytocat and activated carbon to PS affected the product yield and composition (**Figure 5.2 and 5.3**). The maximum oil (72.5%) and gas (21.4%) yields were relatively higher using phytocat-1.5 as compared to phytocat-0.1 (67% oil and 16.7% gas), the control phytocat (64.5% oil and 15.9% gas) and activated carbon (61.0% oil and 14.4% gas), thereby showing the influence of Ni in promoting side

cracking reactions. The relative increase in gas yield using phytocat-1.5 and phytocat-0.1 could be attributed to the greater extent of cracking of hydrocarbons in the presence of biologically bound Ni. This observation was well supported in a previous literature report, which showed that the addition of NiO to the cracking catalysts tended to increase gas yield.¹⁸⁵

The pyrolysis oils produced post microwave irradiation of PS were rich in aromatic hydrocarbons (evidently, styrene, α -methyl styrene, toluene and ethyl benzene were the major compounds) and consistent with the literature (**Figure 5.2a-c** and **Appendix C Table C1-2**). Notably, phytocat-1.5 leads to the production of relatively higher contents of monocyclic aromatics (up to 84.7% selectivity) as compared to phytocat-0.1 (79.2%), control phytocat (66.5%) and activated carbon (65.1%). The highest selectivity towards styrene was observed using phytocat-1.5 (up to 72.1%) as compared with phytocat-0.1 (up to 65.4%), control phytocat (up to 56.1%) and activated carbon (up to 59.1%). The enhanced yield of mono-aromatics originating from the primary radicals of PS showed that more chain scissions occur, which usually requires a higher decomposition temperature. However, using phytocat, it was possible to achieve the primary radicals chain scission under much milder conditions (250 °C, <10 min) than normal (>400 °C, >10 min).

During the de-polymerization process, primary and secondary benzyl radicals were formed.^{150,224} The product distribution showed a relatively higher generation of styrene within the liquid product while using phytocat-1.5 and phytocat-0.1, indicating the elevated formation of secondary benzyl radicals. The formation of styrene and α -methyl styrene depends on the β -scission (which usually has low activation energy) of secondary benzyl radicals.¹⁵⁰ In contrast, the formation of dimers is usually associated with the competing pathways for the conversion of secondary benzyl radicals.¹⁵⁰ It should be noted that no formation of dimers was observed using the conditions applied in this study. The relative abundance of styrene in the product indicates that there is considerable secondary benzyl radical formation, and β -scission dominates. During catalytic cracking, the styrene dimers are usually converted to toluene, ethyl benzene, styrene, and alpha-methyl styrene, which

explains the elevated formation of these monocyclic aromatics using phytocat-1.5 and phytocat-0.1.^{150,225}

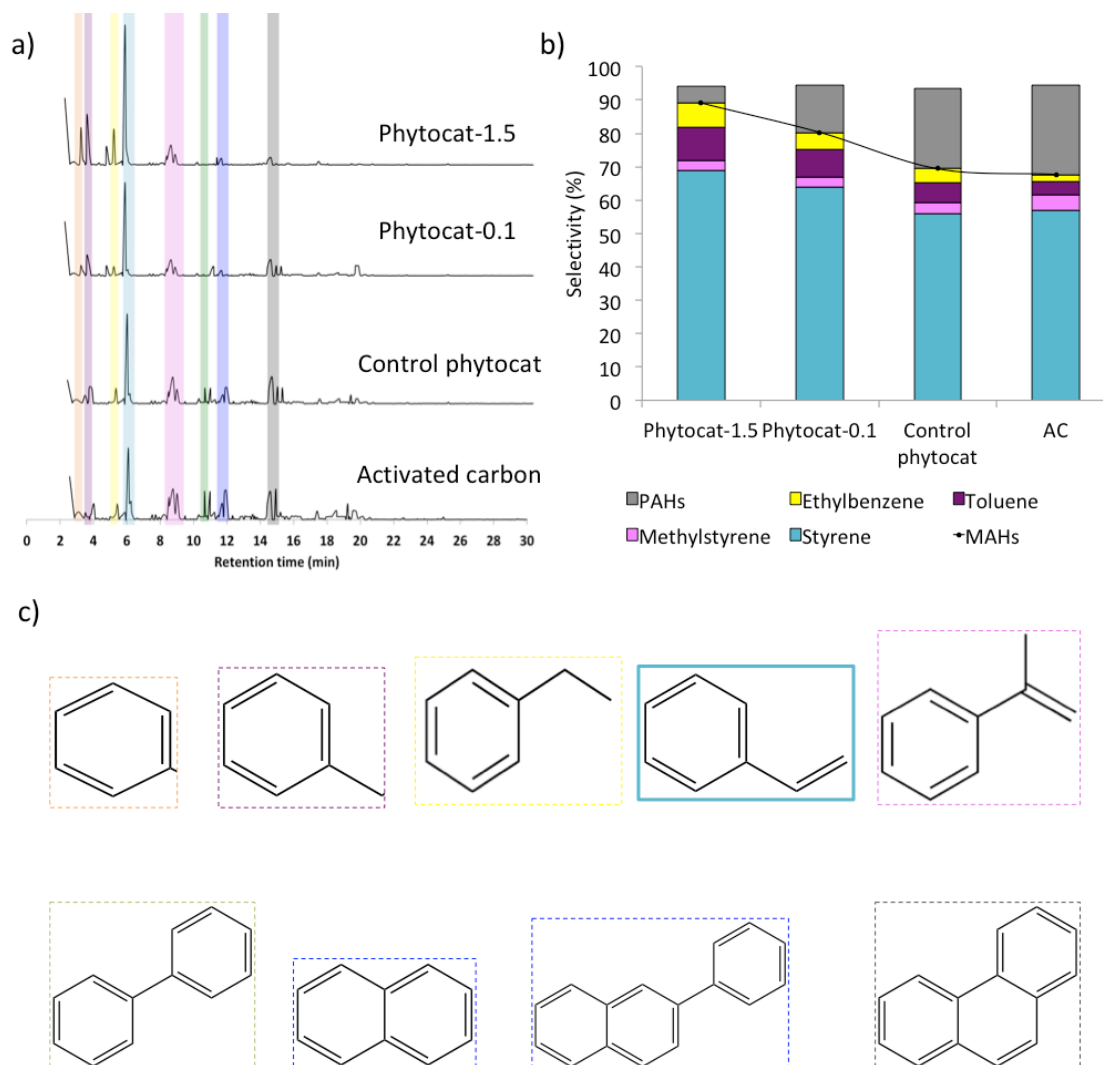


Figure 5.2: (a) Gas chromatography-mass spectrometry (GC-MS) characterization of oils formed by MAP of PS using various catalysts (1:10 catalyst to polymer ratio, by weight); (b) Product selectivity and (c) chemical structures of the major compounds formed during the de-polymerization process

The relative amounts of PS and catalyst significantly affected the de-polymerization efficiency and hence, the composition of products formed. It should be noted that using phytocat materials, de-polymerization efficiency improved on increasing PS

content up to 1: 20 ratio of catalyst to polymer by dry weight (83-92% conversion efficiency). In contrast, using activated carbon, the maximum conversion efficiency was achieved at 1:5 ratio (76%) with a gradual decrease on increasing PS content to 1:20 ratio (as described previously in **Figure 5.1a**). Overall, the peak reduction in time and energy consumption using microwave irradiation (to reach the set-point of 250 °C) was observed with a catalyst to PS ratio of 1:5 by weight, followed in order by 1:10, 1:1, 1:2 and 1:20 by weight (as described previously, see **Appendix C Figure C1**).

Notably, the volume of pyrolysis gas produced was found to reduce with increasing PS content. This is possibly due to an increased production of aromatic compounds with better thermal stability, leading to lower thermal cracking and thus lower gas yields (**Figure 5.3 a, c, e and g**).^{137,170,226,227} The literature suggest that short residence time also favours the suppression of cracking reactions.^{137,226,228,229} The char yield is reduced with increasing PS content up to 1:10 ratio, although slightly increasing at 1:20 ratio. The peak reduction was observed using a 1:10 ratio using phytocat-1.5 (11.2%), followed by phytocat-0.1 (14.1%), control phytocat (21.4%) and activated carbon (22.2%). The maximum total conversion (oil + gas yields) was achieved at 1:10 ratio using phytocat-1.5 (93.9%), followed in order by phytocat-0.1 (84%) and control phytocat (76%). However, it should be noted that the 1:5 ratio worked best while using activated carbon to achieve the maximum total conversion (77.5%). Either side of this window, the conversion efficiency of activated carbon showed a declining trend.

As time progresses, there is a relative reduction in production of styrene monomer which could be due to its subsequent hydrogenation and secondary condensation reactions.^{150,225} Similar observations were noted for the pyrolysis oil obtained using a 1:20 ratio, whereas the styrene production was reduced to around 47% (phytocat-1.5), 46.1% (phytocat-0.1), 45.4% (control phytocat) and 45.6% (activated carbon) respectively. In contrast, the formation of toluene and ethyl benzene increased to around 11% (phytocat-1.5), 7.2% (phytocat-0.1), 6.3% (control phytocat), 7.3% (activated carbon) and 10% (Ni-phytocat-1.5), 4.3% (phytocat 0.1), 2.5% (control phytocat), 4.8% (activated carbon) respectively. Generally, longer residence time and

a higher concentration of various pyrolysis products in the reaction medium give rise to the generation of PAHs from oligomers, thereby decreasing styrene selectivity.²²⁵ Correspondingly, a similar observation was noted while using the catalyst to PS ratios of 1:1 and 1:20, which lead to the enhanced formation of PAHs (**Figure 5.3 b, d, f and h**). Therefore, the relative amounts of catalyst and PS dictate both efficiency and selectivity of the de-polymerization reaction.

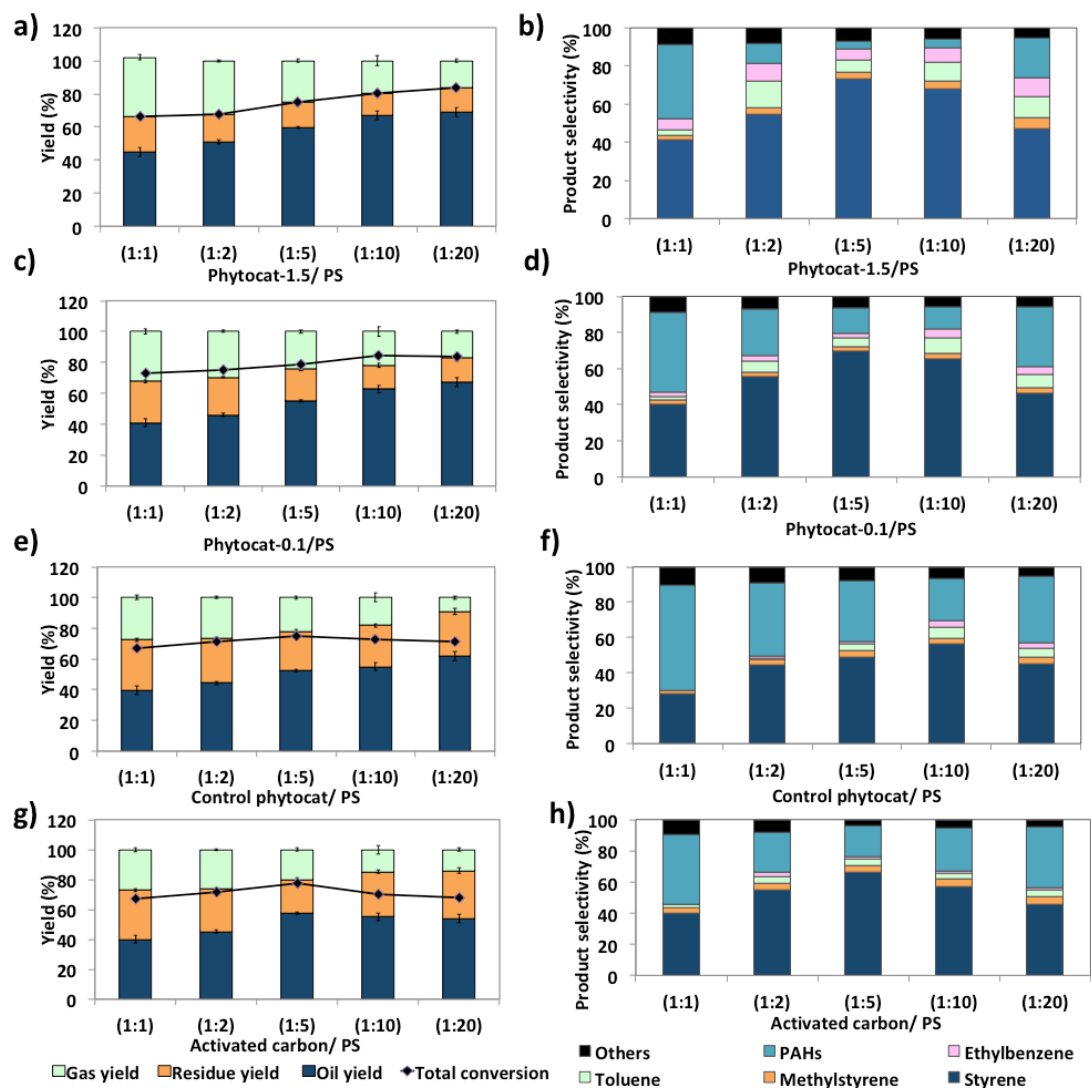


Figure 5.3: Product distribution and composition on de-polymerization of PS using microwaves (200 W and 250°C) (a, b) phytocat-1.5; (c, d) phytocat-0.1; (e, f) control phytocat and (g, h) activated carbon using various mixing ratios with polystyrene.

Overall, this process yielded a higher liquid content (>70%) at low temperatures (250 °C) compared to other thermal pyrolysis processes (400-900 °C) available in the literature.^{150,227,229} Interestingly, use of phytocat leads to higher styrene monomer selectivity (up to 74%) as compared to the other catalytic pyrolysis systems studied in the literature (390 °C, Nb₂O₅ catalyst, up to 40% styrene) and the bentonite catalyst, which yielded only 32% of styrene monomer at 400 °C.^{150,230}

The functional groups of evolved gases were determined using simultaneous TGA/FT-IR analysis in real-time (**Figure 5.4a-c**). Under a conventional set-up, de-polymerization of PS initiated once the temperature had reached approximately 425 °C. (**Appendix Figure C5**). However, under MAP, the de-polymerization temperature in the presence of phytocat significantly decreased to 250 °C, which lead to 90% conversion of PS to monomers within 5 minutes. It should be noted that no such effect was observed in the absence of phytocat, even after 30 minutes under microwave irradiation at 200 W and 250 °C.

During pyrolysis, short chain radicals are produced from C-C bond cleavage and reaction with PS.^{60,61} De-polymerization of PS leads to the predominant production of styrene monomers, as observed from the changes in the Fourier-transform infrared (FTIR) fingerprint region occurring (1000 and 700 cm⁻¹). The interactions of formed radicals, which lead to the evolution of volatiles during catalytic pyrolysis using phytocat could be observed in the 3-D spectra obtained by TG-FTIR analysis of phytocat and PS mixtures (**Figure 5.4b-c**). There is an observed increase in production of short chain hydrocarbons C₂-C₄ (3100 – 2800 cm⁻¹) and aromatics (1650-2000 cm⁻¹ and 700-1000 cm⁻¹) due to interaction of phytocat and PS, particularly using phytocat-1.5.

The gaseous fraction produced during de-polymerization of PS using microwave irradiation was analyzed separately using GC-TCD for qualitative analysis (**Figure 5.4d**). The evolved gas mainly consisted of H₂, CH₄, and C₂-C₄, which suggests that the main reaction leading to the formation of volatiles is de-hydrogenation, de-alkylation of the styrene formed and de-alkylation of methyl-substituted bi- and tricyclic aromatic hydrocarbons.^{150,228,231} Both Ni based phytocat materials showed maximum selectivity towards H₂ gas and relatively higher selectivity towards short

chain hydrocarbons (C₂-C₆), while slightly lower towards CH₄ gas as compared to activated carbon. The increase in the H₂ selectivity could be attributed to the dehydrogenation of the light hydrocarbons formed over the biologically bound Ni due to synergistic interactions of phytocat and microwaves.²³²

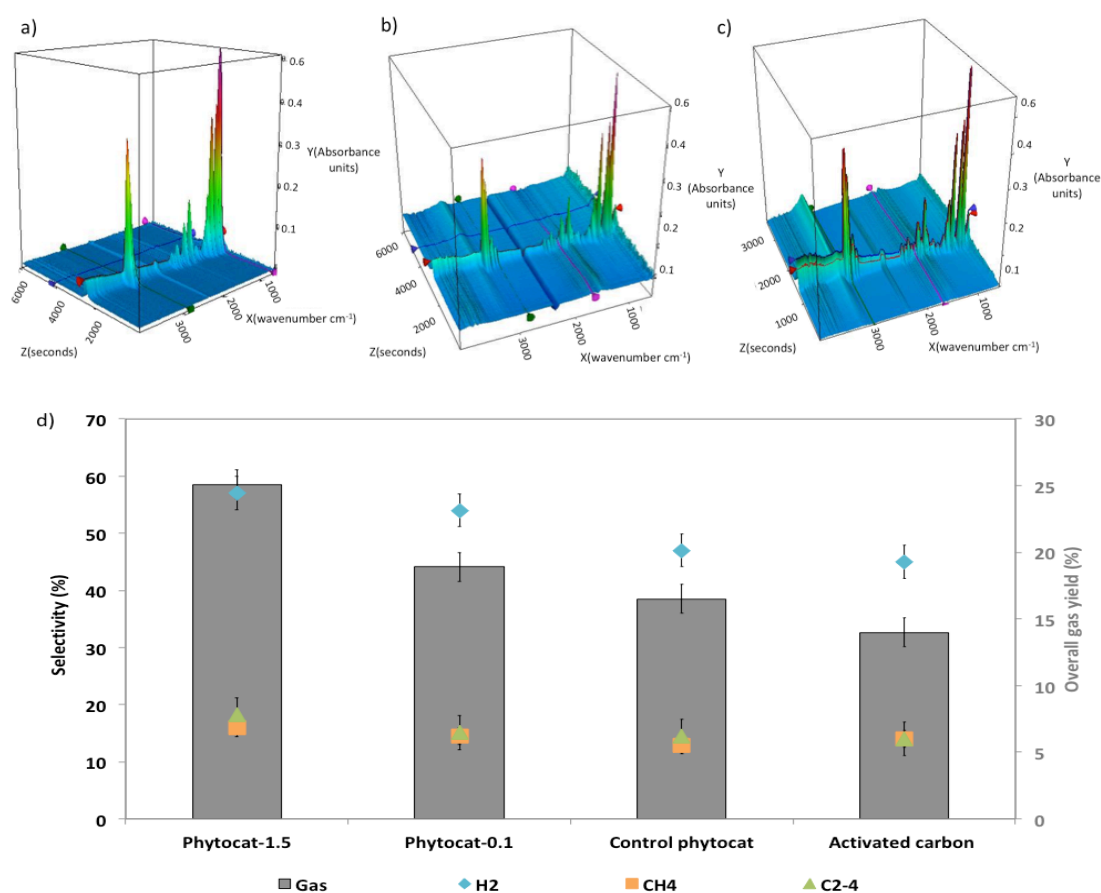


Figure 5.4: Conventional pyrolysis (400-900 °C, TG-FTIR analysis) (a) PS, (b) control phytocat and polystyrene mixture (1:10 by weight) (c) phytocat-1.5 and polystyrene mixture (1:10 by weight); (d) Characterization of the gas evolved during MAP (250 °C) of PS using GC-TCD analysis

The results from published studies on the pyrolysis ($T < 700$ °C) of plastics were compared with this study (see **Appendix C, Table C9**). In this study, a significant reduction in reaction time ($t < 5$ min) and temperature (250 °C) meant less energy consumption to valorize the plastic waste as compared with other studies. This is an

important improvement if we are to develop industrial plastic waste based chemical production processes.

The possible mechanistic pathway for de-polymerization of PS using phytocat is illustrated in **Figure 5.5**. It is well known that the double bond located on the aliphatic chain is far more easily attacked as compared to the double bond in the aromatic ring.⁸⁷ This is because the aliphatic double bond is less stable and sterically less hindered, requiring lower dissociation energy than the aromatic double bond.⁸⁷ During MAP of PS using lower content of catalyst (particularly 1:10 catalyst to PS ratio), the aliphatic chain in styrene dimers being attacked by phytocat/ activated carbon, leads to subsequent formation of styrene monomers. In this study, no formation of styrene dimers was observed, whereas styrene monomers were the major product of the reaction.

While using a higher content of catalyst (particularly 1:2 catalyst to PS ratio), aromatic double bonds in styrene dimers could be attacked by the surface active sites of phytocat/ activated carbon to produce benzene and alkenyl aromatic cation due to the better contact with the catalyst. These alkenyl aromatic cations could further react to generate naphthalene and derivatives (as observed with activated carbon/control phytocat) by internal cyclization, or benzene, toluene and ethyl benzene by side chain cleavage facilitated by biologically bound Ni (phytocat-1.5 and phytocat-0.1).

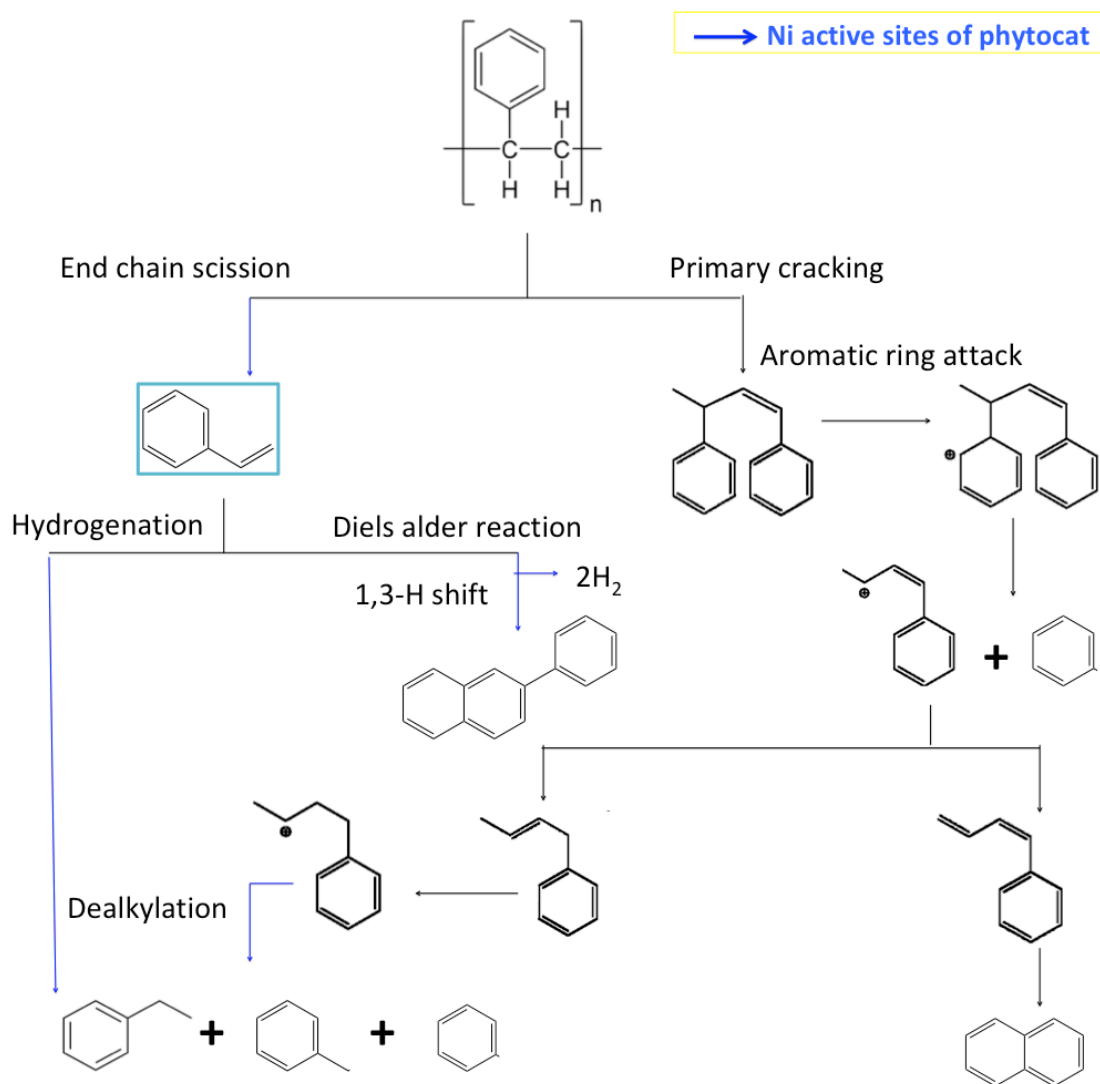


Figure 5.5: Possible reaction mechanism of de-polymerization of PS using phytocat

In order to gain further insights into the structural features and surface chemistry of the phytocat post de-polymerization of PS, various material characterization techniques were used. Field emission scanning electron microscopy (FESEM) image of phytocat post MW assisted de-polymerization of PS was observed. As shown in the FESEM image (**Figure 5.6a**), carbon deposits on the recovered catalyst showed the formation of carbon filaments on the surface of phytocat-1.5. Notably, the presence of a dense, entangled growth of small filamentous carbons covering the surface of Ni-phytocat was observed.

Intrigued by these features, the HR-TEM image (**Figure 5.6b**) of the recovered catalyst post de-polymerization of PS was also observed. These images confirmed that the solid carbon deposition on the surface of the recovered catalyst contained filamentous carbon, and that the black nanoparticles encapsulated within the filamentous carbons were related to Ni⁰. In addition, as shown in **Figure 5.6b**, there were multiple Ni particles in the middle or top of the carbon filaments, indicating that the tip growth mode dominates the formation of filamentous carbon for plastic waste.²³³ It should be noted that both filamentous and amorphous carbon was present on the surface of phytocat-1.5 post-reaction. The amorphous carbon might originate from the oligomerisation reaction of lower molecular weight polycyclic aromatic compounds.¹⁷² The morphology of the graphitic structures is the consequence of the movement of the Ni nanoparticles throughout the amorphous bio-carbon matrix, leaving behind a trail of graphitic carbon.²³⁴

Furthermore, to understand the crystal structure and phase purity of the recovered phytocat material, X-ray diffraction (XRD) was used. Post de-polymerization of PS, the recovered phytocat showed the characteristic peaks of bio-carbon ($2\theta = 24.5^\circ$ - 26.5°) and Ni⁰ ($2\theta = 44.5^\circ$, 51.9° and 76.9°) (**Figure 5.6c**).²²⁰ Notably, the XRD pattern and the HR-TEM image of the recovered phytocat revealed the presence of both amorphous and graphitic carbon. The HR-TEM image showed that graphitic carbon is detected around the Ni nanoparticles or in their vicinity whereas the carbon distant from the Ni nanoparticles remains amorphous. This is consistent with a suspension of amorphous carbon in the metallic nanoparticles and its precipitation as graphitic carbon, which then remains in the vicinity of the catalyst nanoparticles.²³⁴

To obtain insight into the surface chemistry of the recovered phytocat, the elemental composition and chemical states were analyzed using spectroscopy XPS analysis (**Figure 5.6d**). Notably, the prominent peaks at 284.3–284.5 eV revealed that the majority of carbons in the phytocat were aromatic. Interestingly, the peaks corresponding to $\pi-\pi^*$ transition (290.4 eV) were found to intensify for the recovered phytocat, which again suggests an increase in filamentous carbon growth on the surface of phytocat.

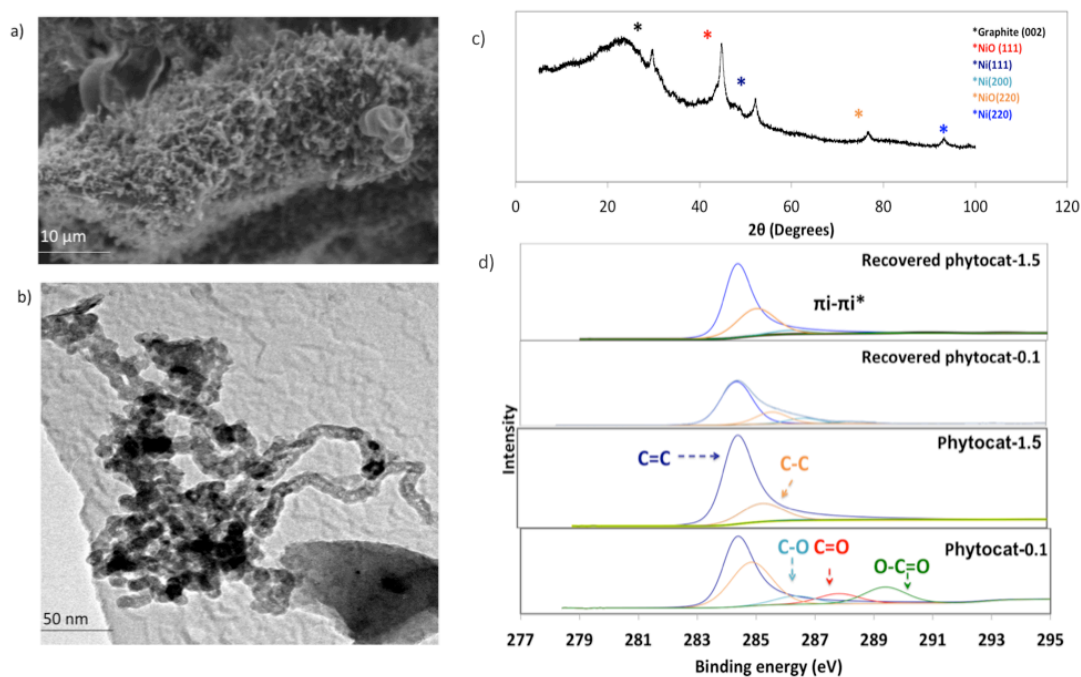


Figure 5.6: Characterization of phytocat post MW assisted de-polymerization of PS
a) Field emission scanning electron microscopy (FESEM) image, b) High resolution transmission electron microscopy (HR-TEM) image, c) X-ray diffraction and d) X-ray photoelectron spectroscopy (XPS) analysis (C 1s XPS spectra)

Conclusively, this study demonstrated the use of biologically bound Ni in phytocat for the synergistic valorization of PS to produce predominantly monocyclic aromatics (up to 84 %). Remarkably, the presence of biologically bound Ni was shown to accelerate de-polymerization of PS (up to 74 % styrene selectivity in an oil yield up to 72%; 18 kJ/g microwave energy consumed) using microwaves under much milder conditions (200 W, 250 °C, <10 min) than at which de-polymerization is normally conducted (>400 °C, >10 min).^{225,227,229} The Ni based phytocat offered significant advantage in enabling rapid de-polymerization of PS with up to 91% conversion efficiency as compared to control phytocat (up to 82%) and activated carbon (up to 79%) within 5 min. Using the phytocat materials, the de-polymerization efficiency improved on increasing PS content up to a 1: 20 ratio while the activated carbon was

most effective up to a 1: 5 ratio, with a gradual decrease in efficiency with increasing PS content. These observations elucidate the highly energy efficient mechanism of Ni-phytoact to de-polymerize PS, even at low metal concentrations.

5.2. De-polymerization of polyethylene

Experiments using catalyst blends of varying composition of Ni were studied to understand the synergy between the Ni active sites and bio-carbon matrix for de-polymerization of LDPE (**Figure 5.7**). Notably, the presence of bio-carbon matrix lead to the formation of $C_{>17}$ compounds as well as C_{13-16} and C_{8-12} molecules with slight deep cracking to C_{5-7} and C_{1-4} gases but was found to be incapable of complete conversion of the plastic at mild conditions and short reaction times. The bio-carbon or activated carbon was likely responsible for the initiation steps in the de-polymerization by converting large paraffins to large olefins.

It should be noted that with an increase in catalyst loading, there was an improvement in gas yields. This increase in gaseous fraction could be explained by the fact that the larger amount of catalyst surface sites could increase secondary cracking, thereby enhancing the diffusion of low molecular weight hydrocarbon molecules formed. Subsequently, an increase in residence time also favored the cracking reactions, which eventually lead to the formation of light gas molecules.^{147,185}

Overall, the yield of oil decreased with an increase in catalyst loading due to excessive cracking, which lead to the formation of gas molecules. Notably, the selectivity to aromatic hydrocarbons in the oil fraction increased and that of long chain aliphatic decreased with an increase in catalyst loading. However, the Ni-based phytocat materials were found to be effective even at low catalytic loadings in the mixture, which shows their relatively higher efficiency in de-polymerization of LDPE. Furthermore, the presence of Ni-based phytocat materials also induced the enhancement of oil and gas yields with simultaneous reduction in char formation.

In order to obtain a detailed understanding of the de-polymerization process, composition of oil fraction was analyzed by grouping the major compounds according to their carbon number (**Figures 5.7b, d, f, h**). Largely, C_6-C_{20} hydrocarbons were the main constituents in pyrolysis oils. It should be noted that almost negligible $C_{n>23}$ hydrocarbons were present in the oil fraction. Furthermore, the lack of heavier

products could indicate that polymer cracking proceeds with one chain adsorbed and reacting until being completely consumed without releasing medium-sized products.¹⁵¹ The optimized reaction condition was found to be 10% of catalyst loading at 250 °C. Under this condition, the oil was primarily composed of monocyclic aromatics and short chain aliphatic hydrocarbons (**Figure 5.7b**). While utilizing Ni-phytocat proved to be effective even at low catalytic loadings, with decreasing content of activated carbon, the selectivity towards mono-aromatics and short chain aliphatics declined sharply (**Figure 5.7h**).

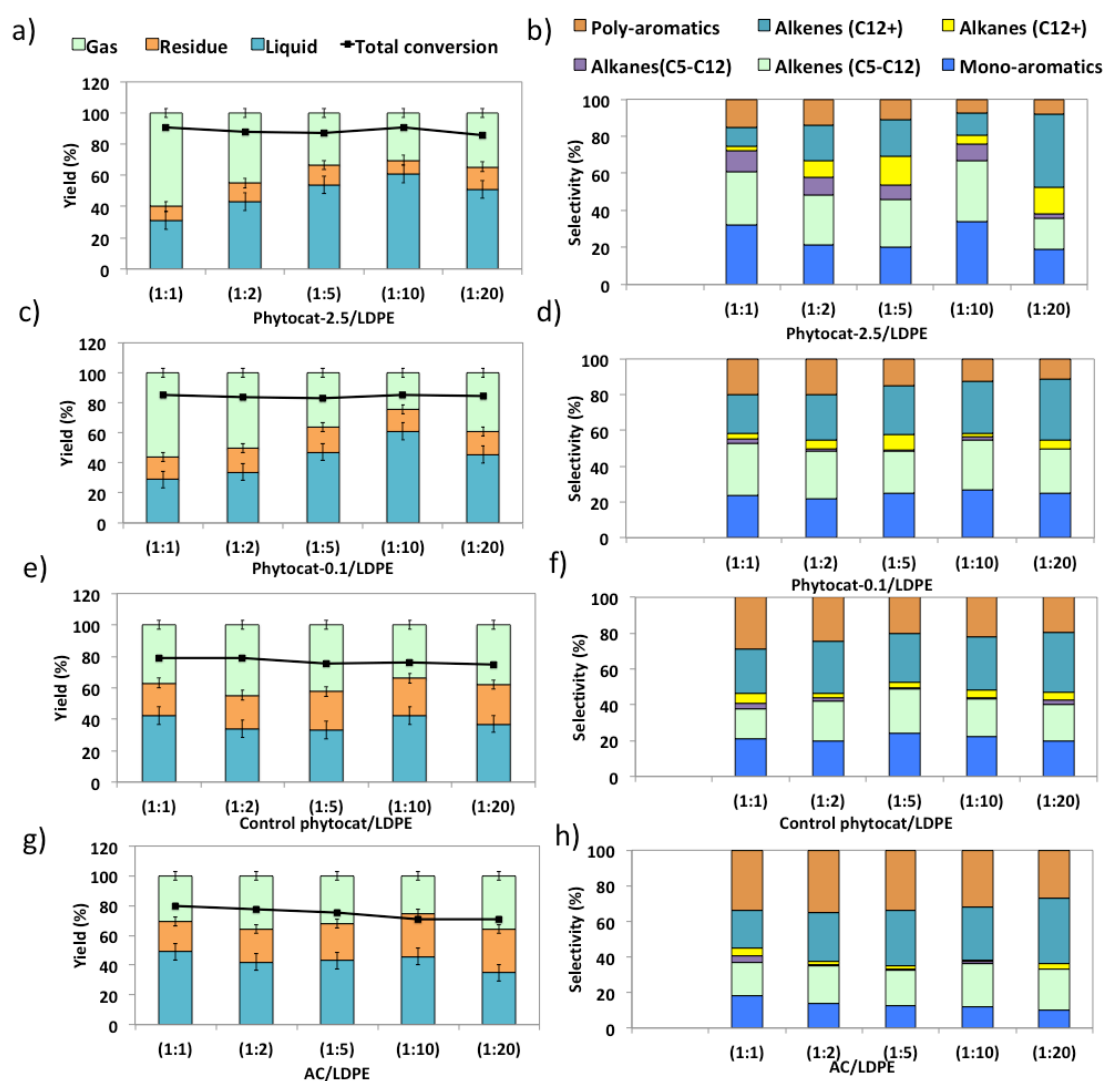


Figure 5.7: Comparison of experimental results of microwave-assisted depolymerization of LDPE using varying catalyst to polymer ratio: (a-b) phytocat-2.5, (c-d) phytocat-0.1, (e-f) control phytocat and (g-h) activated carbon

Notably, the bio-carbon matrix (control phytocat) alone showed relatively lower activity for LDPE conversion at 250°C, leading to predominant formation of long chain aliphatic and poly-aromatics (an average of 39 and 29%, respectively) (**Figure 5.8**) with a broad carbon number distribution centered at C₁₀. Activated carbon, under the same reaction conditions, showed little LDPE conversion with extensive coking, leading to 36% solid residue (**Figure 5.8a, e**). Using Ni-based phytocat materials, the product distribution becomes narrower and shifted to short-chain aliphatics and mono-aromatic hydrocarbons (**Figure 5.8c-d**). These observations further elucidate a strong synergy between Ni⁰/Ni²⁺ and bio-carbon matrix to effectively depolymerize plastics. It could be deduced that in the initial phase the polymer undergoes random scission over bio-carbon into relatively large olefins (C₁₂₊) or alkanes. Later, these intermediates diffuse into Ni active sites, where they crack relatively quickly into smaller C_{<12} alkenes and alkanes.¹⁸⁵

Particularly, with reduction of Ni content in the phytocat, there was an observed decline in the short-chain aliphatic (C₅₋₁₂) fraction from 47 to 29% and an enhancement of the long chain aliphatic (C₁₂₊) fraction from 16 to 31%. At the same time, the yield of solid residue was found to increase using phytocat-0.1, which has comparatively lower dispersion of Ni, leading to relatively lower surface active sites. Thus, the presence of Ni active sites can significantly affect the consumption of C_{>12} intermediates produced by bio-carbon matrix (**Figure 5.8f**). Good dispersion of Ni active sites is essential for tuning product distribution from heavier fractions to low-molecular weight alkanes and alkenes, depending upon varying fractions of catalyst and polymer blends, as discussed in the previous section.¹⁸⁵

The de-polymerization experiments over these catalysts with varying metallic dispersion indicated that the LDPE conversion to liquid and gaseous products follows the order, phytocat-2.5 > phytocat-0.1 > activated carbon > control phytocat (**Figure 5.8e**). Moreover, the product distribution reflects catalytic ability during cracking; phytocat-2.5 favors short-chain aliphatic and monocyclic aromatics and Ni-phytocat-0.1 favors C₁₋₄ gas products. Although phytocat-2.5 produced relatively large quantities of gaseous fraction compared to phytocat-0.1, the former favors hydrogen production as opposed to C₁₋₄ gas products. This selectivity could arise primarily from slower diffusion of reaction intermediates over phytocat with narrower pores

due to presence of Ni, which could block the surface pores, thereby leading to their secondary cracking to smaller products.¹⁸⁵ Additionally, the presence of relatively well-dispersed Ni active sites found over the surface of phytocat-2.5 could favor further aromatization of these alkanes and alkenes formed during de-polymerization, thereby increasing proportions of monocyclic aromatics. As observed in **figure 5.8f**, a small proportion of alkenes ($C_{>12}$) were produced, providing sufficient reactants for both alkylation reaction of aromatics and the de-hydrocyclization process. When the oil obtained using activated carbon was analyzed, higher yields of polycyclic aromatics (particularly naphthalene (~20%) and pyrene (~15%)) were obtained.

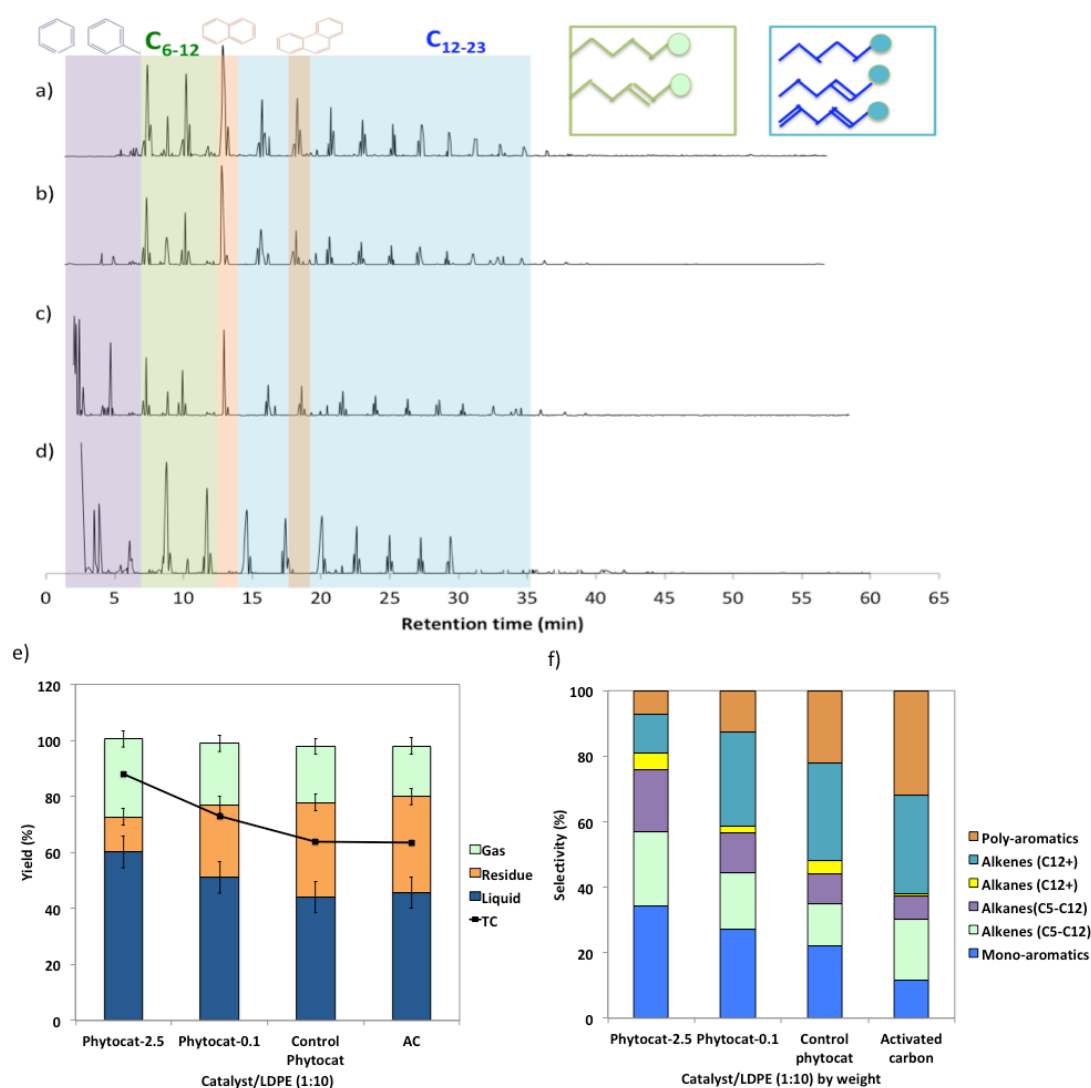


Figure 5.8: Gas chromatography-mass spectrometry (GC-MS) characterization of oils formed on microwave-assisted pyrolysis of LDPE using (a) activated carbon, (b)

control phytocat, (c) phytocat-0.1 and (d) phytocat-2.5; Product yields (e) and selectivity (f) using various catalysts (1:10 catalyst to polymer ratio, by weight)

Random scission of the polymer chains dominated the de-polymerization of LDPE, leading to the formation of several small molecule hydrocarbon species, such as alkenes and alkanes, alongside monocyclic aromatics.²³⁵ This study indicates that two active sites with different functions take part in the de-hydro-cyclization step involved in the degradation reaction. One was bio-carbon or activated carbon surface sites, on which the abstraction of hydrogen atoms occurred predominantly; the other was Ni active sites which catalyzed desorption of the hydrogen atoms. Desorption was a slow step of the de-hydro-cyclization on the bio-carbon or activated carbon, but was enhanced by the presence of biologically bound Ni, resulting in an increase in the yield of aromatics.

Remarkably, phytocat-2.5 resulted in maximum conversion of LDPE into high value chemicals (short-chain aliphatic and monocyclic aromatics; up to 89%) at low temperature (250°C), which is essential for practical implementation of a catalytic technology. The phytocat preferentially cracked the $C_{>12}$ compounds formed over the biologically bound Ni active sites at first to C_{8-12} , then to smaller C_{5-7} hydrocarbons, eventually producing monocyclic aromatics as its fraction in the mixture increases. The bio-carbon matrix (control phytocat) alone showed lower activity for LDPE conversion (up to 71%), which is comparable to commercially used activated carbon (up to 70%). Surprisingly, the best phytocat (phytocat-2.5) maintains its activity even at quite low loadings (5% catalyst) (**Figure 5.9a**).

As shown in **Figure 5.9b**, the relative volume fractions of the gaseous components produced by catalytic de-polymerization of LDPE using different catalysts were compared. The gaseous products were mainly H_2 and CH_4 . Simultaneously, some C_2 + hydrocarbons were also detected. Notably, there was a significant reduction in selectivity towards ethylene production using Ni-phytocat-2.5 as compared to the other catalysts. This could be due to the strong interaction of ethylene molecules with the surface of Ni-phytocat, which leads to subsequent bond breaking and enhances

carbon deposition (as shown later in **Figure 5.12**).²³⁶ Furthermore, this could be attributed to the increasing formation of aromatics at the expense of olefins. The aromatization enhanced by Ni-phytocat also gives rise to hydrogen generation, resulting in a significant increase in hydrogen volume yield (70%), as compared to activated carbon and control phytocat (<50%). These observations highlight the excellent dehydrogenation ability of NiO present on the surface of Ni-phytocat. For this reason, Ni-based catalysts have been extensively used in industry to generate both H₂ and CNTs (carbon nanotubes) from catalytic reforming of plastics.^{167,233} The decrease in hydrogen content using control phytocat and activated carbon could be due to the breakage of C-C bonds, which results in a significant increase of hydrocarbon compounds in the gaseous product. As the reaction progresses, more microwave energy input is provided, leading to an increase in C-C and C-H bond breaking and increased hydrocarbon yields. In contrast, the yield of liquids shows the opposite trend. The additional energy input also promotes aromatization reactions, forming polycyclic aromatic hydrocarbons and increasing coking. In addition, the concentration of biologically bound Ni also affected the performance of the catalyst. With increasing Ni content, more catalytic sites were formed on the bio-carbon surface, making the process more favorable for the upgrading of liquid products rather than the loss of liquid product quality (conversion to coke). Interestingly, Ni active sites in phytocat promote the occurrence of hydrogen transfer reactions and catalyze the aromatization of long-chain olefins and alkanes.

Importantly, the active Ni sites could also facilitate the occurrence of hydrogen transfer reactions, where alkane cyclization produces cycloalkanes as hydrogen donors and olefins as hydrogen donors reacting to produce alkanes and aromatics. The end result of the catalytic reaction is the catalytic conversion of long-chain hydrocarbons to short- chain aliphatic and aromatics (**Figure 5.9c-d**).

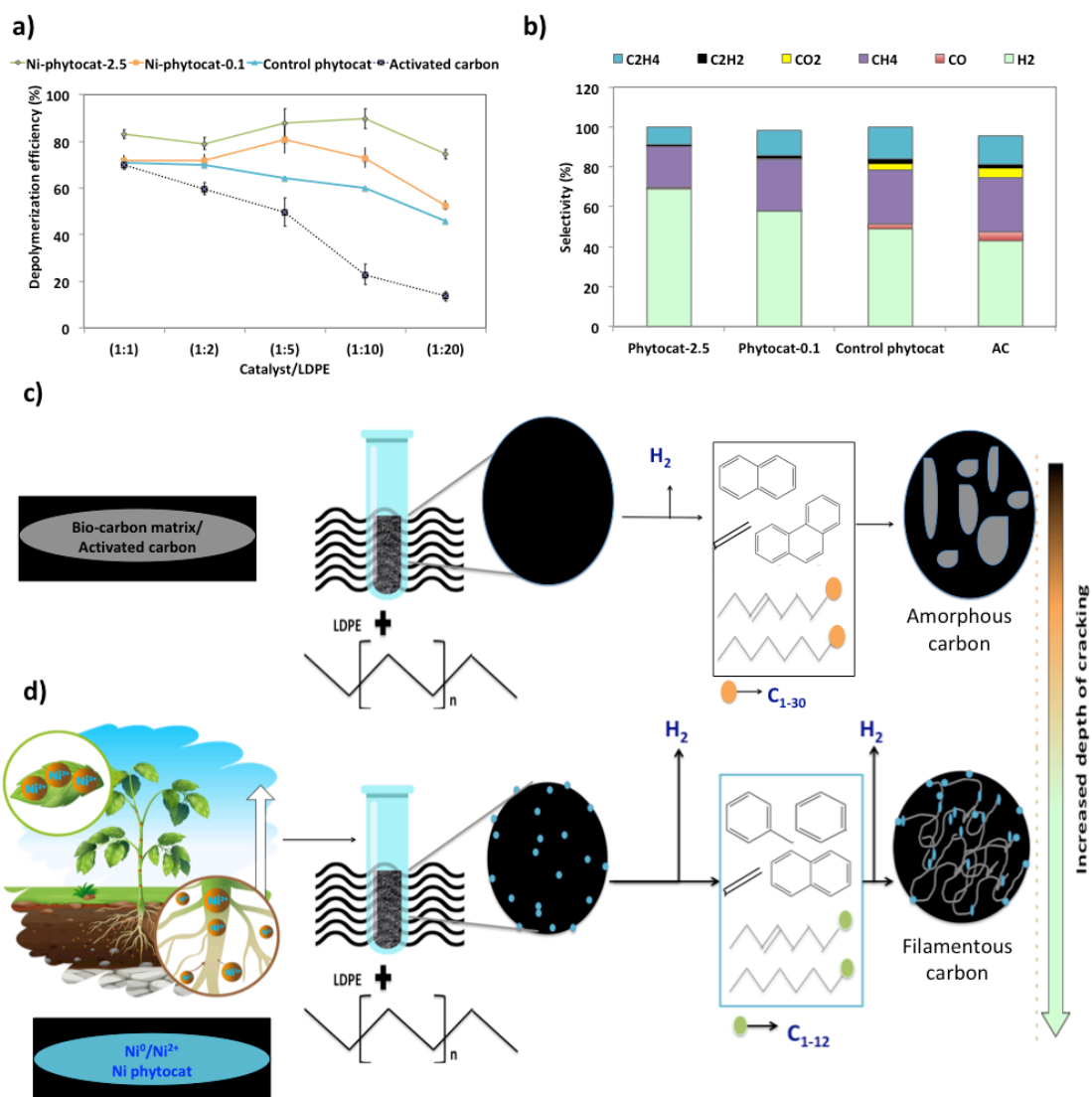


Figure 5.9: (a) Comparison of efficiency of various catalysts for accelerated depolymerization of LDPE, (b) Relative amounts of the gaseous molecules formed during microwave-assisted accelerated de-polymerization of LDPE using various catalysts, Depth of cracking of various hydrocarbons formed during microwave-assisted accelerated de-polymerization of LDPE on the surface of (c) control phytocat or activated carbon and (d) Ni-phytocatalyst

Compared with catalytic thermal pyrolysis, catalytic microwave pyrolysis led to an increased gas yields and a reduction in oil yields (**Figure 5.10**). Furthermore, MAP of LDPE resulted in a narrower carbon atoms number distribution, producing mainly monocyclic aromatics and short chain aliphatic. During conventional pyrolysis, polycyclic aromatics were the main constituents of the aromatic fraction (see

Appendix C, Figure C6). These polycyclic aromatics were mostly derived from the secondary reactions (e.g., alkylation, transalkylation, dehydrogenation, and condensation) of monocyclic aromatics, which were promoted due to high temperatures under CP ($T > 500^{\circ}\text{C}$).^{130,151}

The synergistic influence of microwaves and the presence of Ni in the phytocat increased the gas yield from 20wt.% to 27wt.%. Besides, the addition of Ni-based phytocat materials also decreased the carbon residue yield to 14.5 wt.%, as compared to 33-34.5wt.% for activated carbon or control phytocat. This decline in the residue yields could be due to promotion of the primary degradation of larger fragments into smaller fragments, which reduced the possibility of coke deposition caused by larger molecules.¹⁷² Notably, with the successive microwave cycles, the oil yields increased (from 43-45% without Ni to 61% with the phytocat-2.5), while gas and coke yields decreased simultaneously (**Figure 5.10a**). This observation is well supported by the fact that an increase in residence time favors the cracking reactions, which eventually lead to short chain hydrocarbons alongside monocyclic aromatics, the detailed mechanism of which is discussed later.¹⁶⁴

In comparison to MAP, two major technical challenges hinder the scale-up of CP technology for use in de-polymerization of plastics. The first one is the production of high molecular weight, waxy hydrocarbons and high temperature ($T > 700^{\circ}\text{C}$) operation for de-polymerization into lighter compounds.^{229,237} Secondly, the conventional high temperature catalytic cracking leads to the deactivation by coking and poisoning of the catalyst.²³⁷ Therefore, active sites available to the reactant molecules affect the product selectivity in a conventional process. Catalyst coking also reduces the useful lifetime of the catalyst and increases the overall operational cost.²³⁷

Taking into consideration the release of volatile after each successive MW cycle, it was noted that olefins from pyrolysis were largely converted to aromatics through dehydrogenation; consequently, the hydrogen proportion in the gas products using Ni-based phytocat materials were higher than that from the control phytocat or activated carbon (**Figure 5.10b, d, f, h**). On the contrary, a much lower selectivity towards ethylene was observed, specifically using phytocat-2.5. This decline in ethylene

selectivity could be ascribed to the Diels-Alder reactions promoted by Ni active sites, which resulted in the consumption of ethylene (as discussed later in **Figure 5.11**).¹⁵¹ Increasing hydrogen yields are important as we move towards a Hydrogen Economy – the conversion of plastic waste to hydrogen in a process that does not consume virgin metals and is energy efficient, is very attractive.

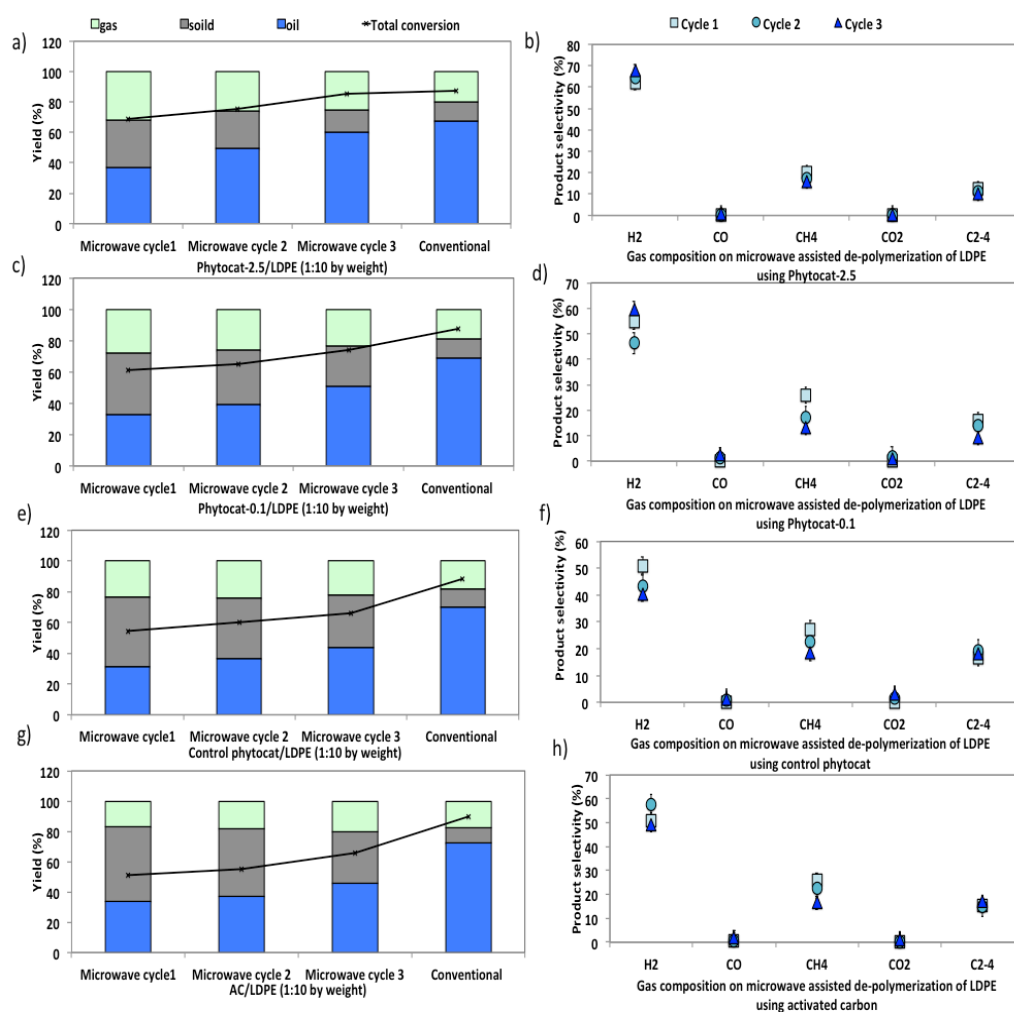


Figure 5.10: Comparison of experimental results of the microwave-assisted (for 3 successive cycles to reach the set-point of 250°C) and conventional thermal (500°C) de-polymerization of polyethylene (Low density polyethylene, LDPE) using (a-b) Ni-Phytocat-2.5, (c-d) Ni-Phytocat-0.1, (e-f) Control phytocat and (g-h) activated carbon (1:10, catalyst: LDPE by weight)

Based on the yield distribution, and chemical compositions of the products, possible reaction pathways for the de-polymerization of LDPE using phytocat are proposed in **Figure 5.11**. Broadly, numerous LDPE-derived large molecular weight hydrocarbons from individual catalytic microwave pyrolysis were transformed into light hydrocarbons, which formed hydrocarbon pools on the surface of phytocat or activated carbon and were subsequently converted into aromatic hydrocarbons through oligomerization and aromatization over the active sites.

Hydrogen transfer reaction from hydrogen-rich materials (polyolefin chains) to hydrogen-deficient materials (phytocat) occurred during polyethylene and phytocat's interaction. The dehydrogenation process was enhanced by the abstraction of hydrogen from hydrogen-enriched hydrocarbons like alkanes onto the carbon surface, and thus, the production of alkenes increased substantially.¹⁸⁵

It has been reported that a pure carbon support is also effective in promoting the hydrogen transfer reaction and cyclization of a straight-chain intermediate.¹⁴⁷ In this study, the dehydrogenation step in hydrogen transfer could be enhanced by the surface functional groups on the carbon surface such as carbonyl groups. However, the step of hydrogen release was relatively limited due to the lack of metal sites in control phytocat, leaving more hydrogen atoms on the carbon surface available for the hydrogenation of hydrogen acceptors such as alkenes. The slight decrease in aromatic content was probably caused by the restrained hydrogen transfer reaction due to the lack of Ni active sites.^{66,185}

During the initiation stage, the main chain scission (generally random scission) is activated by the energy input of microwave, producing unstable long-chain hydrocarbon radicals. The addition of Ni phytocat tends to increase the heating rate at maximum degree, which aids in effective heat transfer, lowers the degradation energy of C–C bond, thereby enhancing the chain scission reactions. Moreover, the required energy for cracking C–H bond is also reduced by NiO, which may enhance formation of carbenium ions.¹⁸⁵ Similar to Diels-Alder reactions, cyclization and aromatization reactions could also contribute to the production of aromatics.¹⁸⁵ In this regard, cyclization between the unsaturated chain ends and the chain ends with a radical tend to produce cyclohexane products.¹⁵¹ Further dehydrogenation of these products over

phytocat results in the generation of aromatics. Besides, a chain-end radical could also terminate by recombining with another chain-end radical and thus produce a saturated and enlarged chain.¹⁸⁵

Furthermore, addition of Ni-based phytocat materials tends to abstract hydrogen from the hydrocarbon fragments and enhance the production of alkenes and H₂ with a slight reduction in the yield of alkanes. Among the alkenes, the increase in diene compounds could be advantageous to the production of aromatics through Diels-Alder reactions promoted by phytocat or activated carbon.¹⁸⁵ These reactions could possibly explain the enhanced aromatic content while using Ni-based phytocat materials as compared to the control phytocat or activated carbon alone. Moreover, Ni active sites could further form short chain olefins by promoting β -scission reactions, and olefins aromatize on active sites to form aromatic hydrocarbons.^{237,238} In addition, Ni active sites can adsorb carbonaceous intermediates and activate C-H bonds and catalyze hydrogen transfer reactions between cycloalkanes and olefins, upgrading them to alkanes and aromatics.^{172,233} Additionally, the formed dienes can be oligomerized with alkenes to form cycloalkenes, and then dehydrogenate to form aromatics or reaction with butadiene and dehydrogenate to naphthalene (as observed with control phytocat and activated carbon).¹⁸⁵

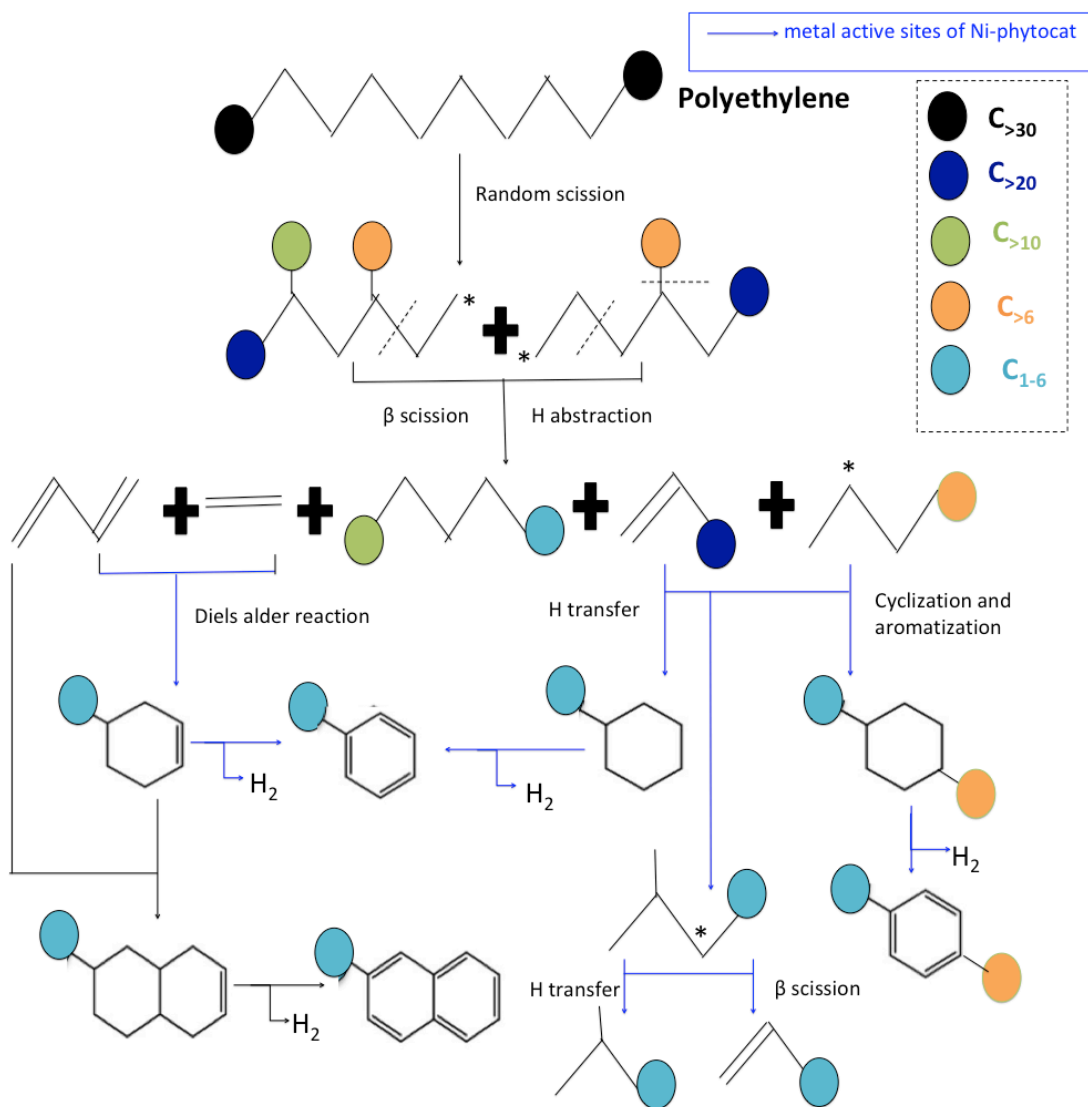


Figure 5.11: Mechanistic pathway for accelerated de-polymerization of low-density polyethylene utilizing synergistic interactions of microwave and Ni-phytocat.

In the TEM images of the used catalysts (**Figure 5.12a-c**), filamentous carbon generation was observed on the metal particles, which confirmed that the metal sites can adsorb carbonaceous intermediates and catalyze C-H breakage. Moreover, carbon deposited on the metal particles and further growth was found to be similar to the process of carbon nanotube growth on the metal sites at high temperatures in other studies.^{167,172} In addition, as shown in **Figure 5.12a-b**, there were many metal particles in the middle or top of the carbon filaments, indicating that the tip growth mode dominates the formation of filamentous carbon for plastic waste. Furthermore,

as shown in **Figure 5.12b-c**, both filamentous and amorphous carbon was observed on phytocat-0.1 post-reaction, whereas only amorphous carbon was detected on the surface of control phytocat. The amorphous carbon might originate from the oligomerisation reaction of lower molecular weight polycyclic aromatic compounds.

To understand the crystal structure and phase purity of the recovered phytocat materials, X-ray diffraction (XRD) was used. As shown in **figure 5.12d**, the diffraction peaks at 44.6° , 52.2° , and 77.3° belong to metallic Ni ([111], [200] and [220] diffraction peaks of Ni^0).²⁰³ Both Ni-phytocat materials exhibits a broad graphitic (002) peak at about 25° , which belongs to the hexagonal conjugated carbon structure. This result confirms that the structure of the Ni-phytocat is relatively stable and the majority of entrapped NiO is reduced to Ni metal by the surrounding bio-carbon matrix during the MAP. Moreover, the presence of unreacted polyethylene residue was observed over the recovered phytocat-0.1, as characterized by the peak at about 22° , whereas no such peak was observed over recovered phytocat-2.5.

Temperature programmed oxidation (TPO) was used to characterize the carbon deposits as the oxidation temperature is influenced by the nature of carbon. **Figure 5.12e** describes the TPO profiles and the association between the measured carbon content and the oxidation peak temperatures. Oxidation at temperatures exceeding 500°C could be assigned to graphitic coke, while oxidation at lower temperatures was attributable to amorphous or encapsulating carbon species.^{172,233} The high temperatures for coke combustion indicate that the formation of graphitic coke was more favored than that of amorphous coke from LDPE pyrolysis volatiles. Two stages of carbon oxidation were identified: i) amorphous carbons ($\sim 550^\circ\text{C}$) and ii) filamentous carbons ($\sim 660^\circ\text{C}$). The TPO results indicate that the carbon formed over control phytocat consists of amorphous type carbons that oxidize at lower temperature compared to filamentous carbon (phytocat-2.5 and phytocat-0.1) that oxidizes at higher temperature. The carbon with a high degree of graphitization would have a high thermal stability and would decompose at higher temperatures compared with the less graphitized/amorphous carbon.²³⁹

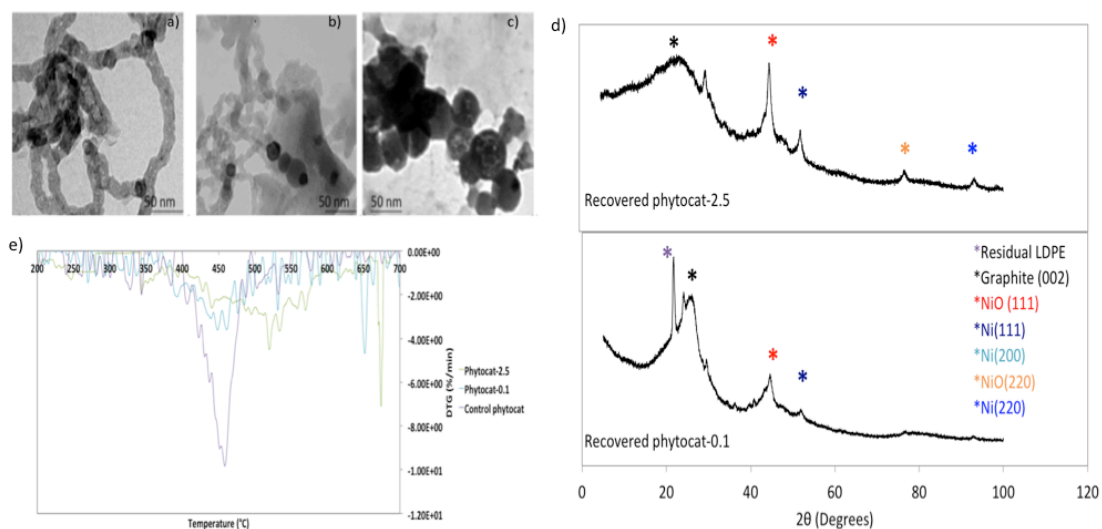


Figure 5.12: Characterization of phytocat post MW assisted de-polymerization of LDPE: HR-TEM images of a) phytocat-1.5, b) phytocat-0.1, c) control phytocat; d) XRD analysis; e) TPO profiles

The literature studies reported by various authors about the quantitative distribution of products obtained from pyrolysis of LDPE using other catalysts were reviewed for comparative analysis (see **Appendix C, Table C9**). Past studies have reported predominantly zeolite catalysts, which have high activity and stability but conversely are relatively costly, easy to coke, and easily deactivated. The liquid yield of products from catalytic pyrolysis of LDPE with these zeolite catalysts is relatively low, typically 30%.^{151,185,187} Compared with zeolite catalyst, activated carbon is cheaper, both acidity and porosity can be simply adjusted by changing activation conditions, so that the distribution of products can be tuned. The liquid yield obtained by pyrolysis of LDPE using activated carbon can reach 75.3% at most, which is much higher than that from using a zeolite catalyst.^{240–242} Therefore, it is more advantageous to use activated carbon support to convert plastic into high value chemicals. The presence of phytocat was conducive to altering product distribution and enhancing production of aromatic hydrocarbons, together with dehydrogenation of intermediate hydrocarbons (C_nH_m) to generate H_2 and other valuable products especially at the low catalytic temperature (250 °C) as compared to conventional technique ($T > 500^\circ C$).¹⁶⁷

Polyethylene is almost entirely transparent to incident microwaves, and thus the resulting temperature rise is very small, yielding in a relatively large temperature difference with the catalyst.¹⁸⁵ As a result, a heat flow from the catalyst surface to the PE is generated. At the optimum temperature of 250°C, PE reacts on the surface of the catalyst for dehydrogenation. This localized heating effect reduces energy loss, increases product selectivity, and reduces side reactions. The de-polymerization products composition can be adjusted by changing the reaction time, temperature, and concentration of the catalyst. Microwave-assisted catalysis can speed up the reaction from a few hours to a few minutes, or even a few seconds; the short reaction time inhibits many side reactions, allowing for products to be obtained with high purity and yield. Microwave heating relies on electricity to produce microwaves, but the overall process overall has a high energy utilization efficiency.^{96,205}

Oils obtained from microwave pyrolysis are different from those from conventional pyrolysis. Particularly, the synergistic use of microwaves and Ni-phytocat establishes a balance between cracking and cyclization to improve selectivity towards aromatics. The microwaves along with phytocat were able to produce the liquid compounds with narrow distribution of carbon numbers compared to the conventional thermal pyrolysis, which resulted in the broader range (predominantly poly-aromatics and aliphatics C_{>12}). Furthermore, the lower operating temperature of MAP is also advantageous.

Using microwave irradiation, phytocat-2.5 increased the heating rate up to 190-200 °C min⁻¹, depending on the amount of catalyst added to de-polymerize LDPE at fixed power of 200 W. Therefore, phytocat favors selective reaction pathways by minimizing the overall energy requirement of decomposition (**Figure 5.13**). Hence, the energy requirement can also be reduced apart from the production of value-added chemicals. Remarkably, the energy consumption was less (14.5 kJ/g and 22.4 kJ/g of microwave energy was consumed to reach the set-point of 250 °C in less than 2 min) using phytocat-2.5 and phytocat-0.1 respectively, as compared to the control phytocat (30 kJ/g of microwave energy consumed) and activated carbon (36 kJ/g of microwave energy consumed).

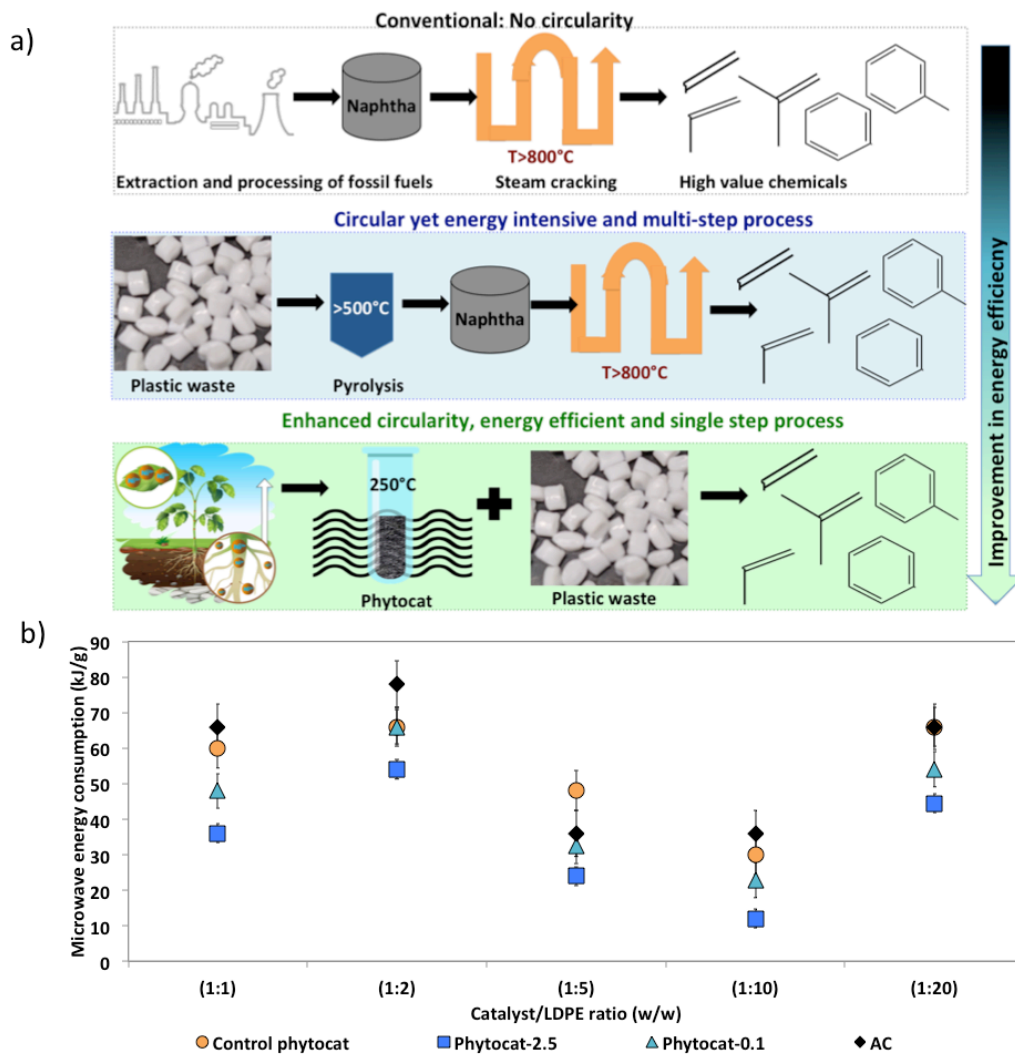


Figure 5.13: (a) Schematic illustration of the processes to generate high value chemicals, (b) Microwave energy consumption for accelerated de-polymerization of PE (to reach the set point of 250°C) using varying catalyst to polymer ratio.

To conclude, the catalytic effect of Ni- based phyto-cat materials were mainly characterized by promoting the hydrogen transfer process, which increased the yield of short chain aliphatic and monocyclic aromatics at the expense of high molecular weight aliphatic and poly-aromatics.

The novelty of this work is that the biologically bound Ni directs sustainable de-polymerization process, allows for product-tunable decomposition of PE for rapid (at least 40 times faster than the corresponding high temperature thermally driven reaction) production of high value low molecular weight hydrocarbons, with no added H₂ or artificially fabricated catalyst. Indeed hydrogen becomes a major product in these reactions.

5.3. De-polymerization of PureFlex™ Film

PureFlex™ film (PF) is a high-purity, monolayer, coextruded film used in the construction of the single-use process containers employed throughout the biopharmaceutical production process.²⁴³ As shown in **Figure 5.14a**, the fluid contact material is made of ultra low-density polyethylene (ULDPE), the gas barrier is made of polyethylene vinyl alcohol copolymers (EVOH) and the outer layers are made of ethylene vinyl acetate (EVA) and ULDPE.

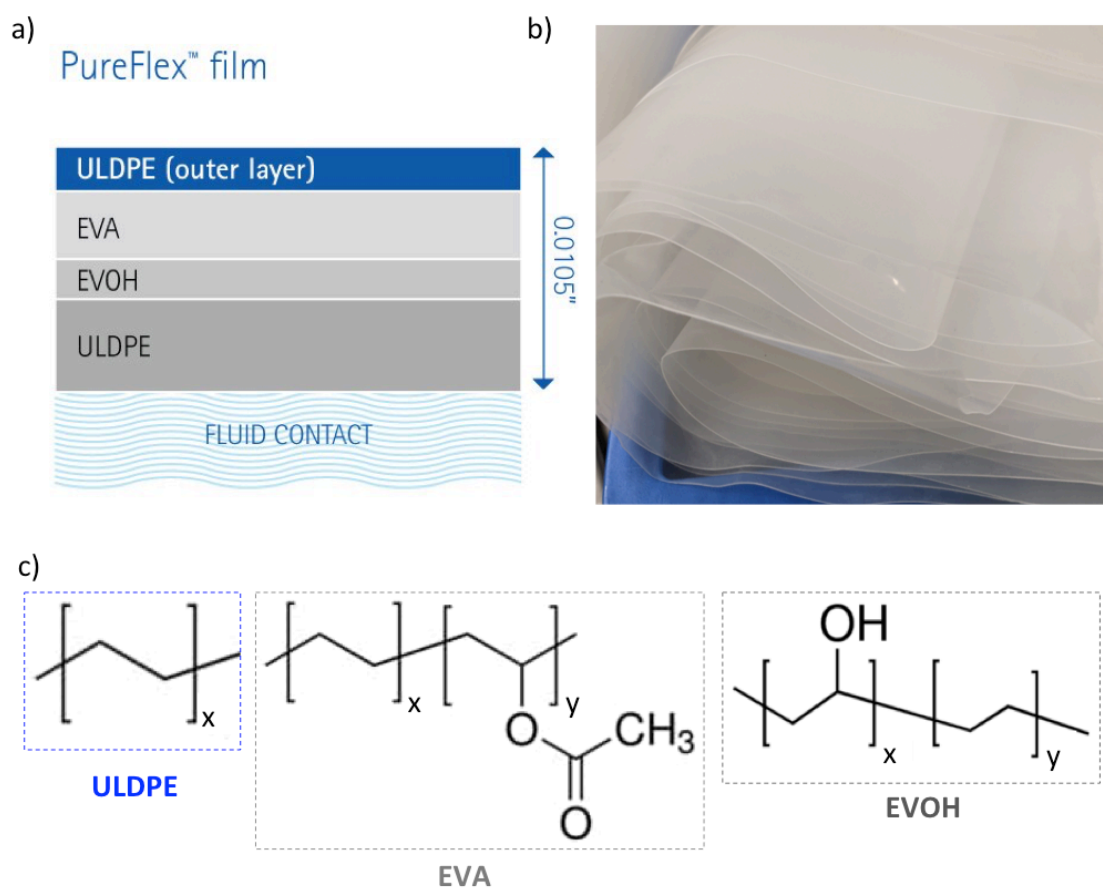


Figure 5.14: a) Layers of PureFlex™ film²⁴³; b) visual appearance of PureFlex™ film (As provided by Merck KGaA) and c) structural formulae of the polymeric units of PureFlex™ film

Utilizing the same methodology as used for the de-polymerization of PS and PE (described previously in **section 5.1 and 5.2**), MAP of these films was conducted to further evaluate the de-polymerization efficiency of phytocat. As shown in **figure 5.15**, after processing the PF sample without the aid of phytocat or activated carbon (MW cycle 1: 200W, 250 °C), there were no observed changes in the visual appearance of PF (**Figure 5.15 a, e**). It should be noted that de-polymerization of PF was not initiated without the addition of catalyst. This could be due to the microwave transparency of PF. Notably, under the synergistic effect of MW irradiation and on addition of phytocat or activated carbon; the de-polymerization was initiated at different rates, as observed in **Figure 5.15b-h**.

The synergistic interaction of biologically bound Ni and microwaves accelerated the de-polymerization process (as discussed previously in **section 5.1 and 5.2**). These synergistic interactions of metal and microwaves could be related to the similar study by Larry *et al.*, where copper wire was used as antenna for producing low temperature plasma during MAP of bituminous coal.²²³ Basically, metal immobilised on activated carbon supports aids in heat transfer, thereby accelerating the degradation of MW transparent plastic materials. The rate of heat transfer during MAP directs the de-polymerization efficiency of these catalysts. As can be seen from **Figure 5.15i** and **Appendix Figure C14**, the maximum heating rates under MW irradiation (leading to relatively lower energy consumption) as well as the maximum de-polymerization efficiency (up to 59%) were both observed using phytocat-2.5, followed in decreasing order by phytocat-0.1 (up to 51%), activated carbon (up to 39%) and control phytocat (up to 37%). It should be noted that the degree of de-polymerization increases with consecutive microwave cycles; leading to its maximum conversion after the third cycle under the condition used in this study (200W, 250 °C). This observation verifies highly effective heat transfer using the synergistic interactions of biologically bound Ni and the microwaves, thereby leading to maximum degree of de-polymerization of PF using phytocat-2.5.

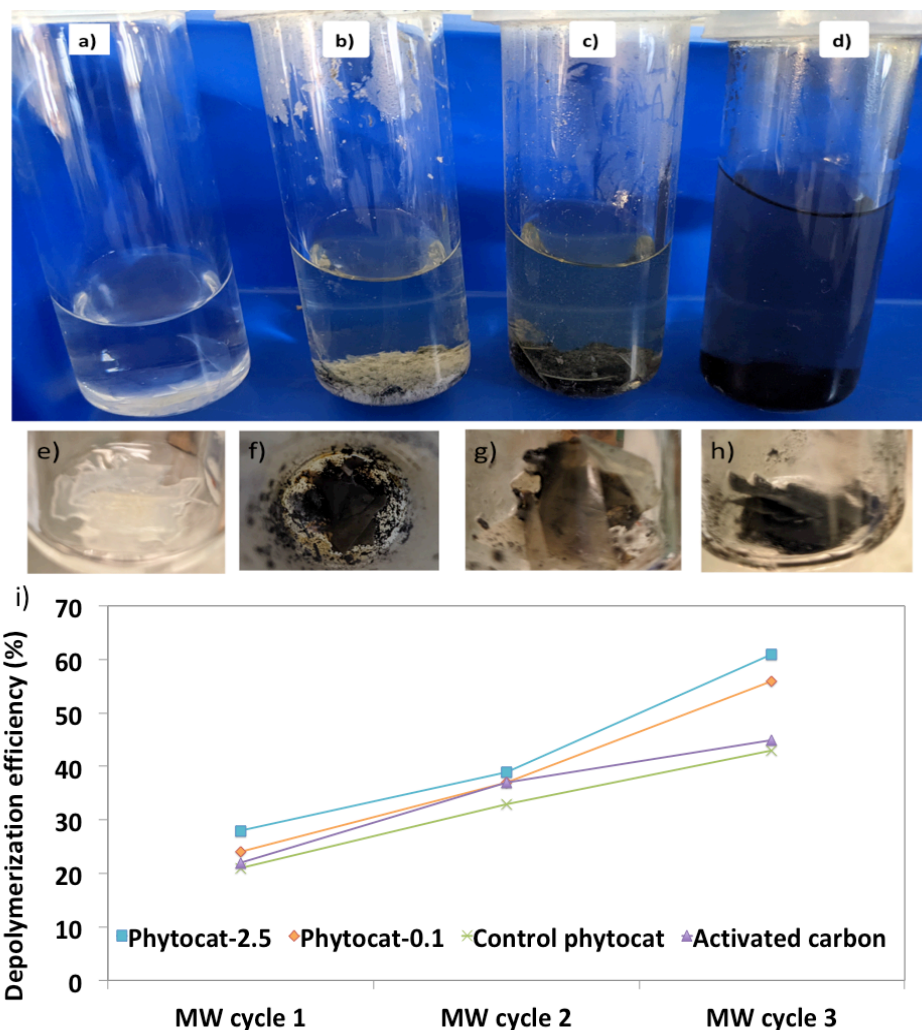


Figure 5.15: Visual appearance of the samples post MW irradiation (cycle 1): (a, e) PF, mixtures of (b, f) Phytocat-2.5 and PF (1:10 by weight), (c, g) control phytocat and PF (1:10 by weight) and (d, h) activated carbon and PF (1:10 by weight); (i) Comparison of efficiency of various catalysts for rapid de-polymerization of PF

These synergistic interactions of the biologically bound Ni and microwaves also have an effect on the product distribution post de-polymerization of PF (**Figure 5.16**). As noted previously, the degree of de-polymerization increases with the consecutive microwave cycles; leading to its maximum conversion after the third cycle under the condition used in this study (200W, 250°C) for all the catalysts. Overall, with successive MW cycles, the residue yields decreases with a simultaneous increase in the oil yields alongside slight variation in the gas yields, depending on the type of catalyst used. Remarkably, the maximum gas yield was obtained using phytocat-2.5

(up to 24wt.%), followed in decreasing order by phytocat-0.1 (18wt.%), control phytocat (16.5wt.%) and activated carbon (12wt.%). Contrarily, the residue yields followed an opposite trend leading to the maximum residue from using control phytocat (up 61wt.%), followed in decreasing order by activated carbon (up to 59wt.%), phytocat-0.1 (55wt.%) and phytocat-2.5 (51wt.%). Furthermore, the oil yields were found to vary at different ranges for various catalysts as follows: phytocat-2.5 (25- 55wt.%), activated carbon (19-45wt.%), phytocat-0.1 (19.5-43wt.%), and control phytocat (18.5-39.5wt.%). These observations were found to be in accordance with the previous observations, stating the maximum degree of de-polymerization of PF using phytocat-2.5.

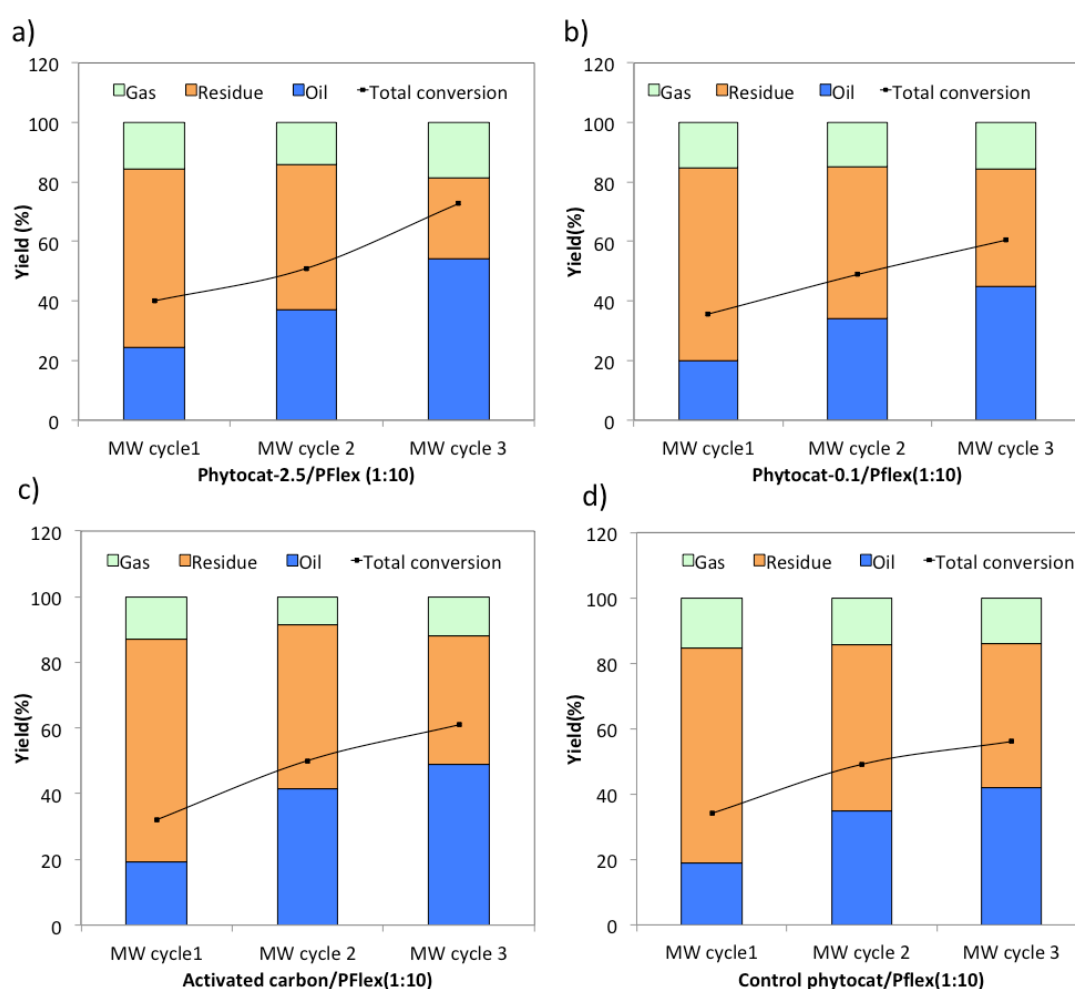


Figure 5.16: Product distribution post microwave-assisted de-polymerization of PF (for 3 successive cycles at 200W to reach the set point of 250°C) using (a) phytocat-

2.5, (b) phytocat-0.1, (c) activated carbon and (d) control phytocat (1:10, catalyst: PF by weight)

To obtain a molecular perspective of the chemical variations undergone by the PF during the MAP using phytocat-2.5, the various products formed during the reaction were characterized. The initial characterization was performed on the residues obtained post-MAP of PF with phytocat-2.5 using FTIR spectroscopy (**Figure 5.17**). The highlighted FTIR spectra depict the changes observed post-MAP (**Figure 5.17d**). Notably, FTIR analysis of the residue post-MAP (cycle 3) shows a peak at 1739 cm^{-1} (resulting from C=O group) corresponding to the ester group degradation of EVA with increasing MW-irradiation, which was absent in the PF pre-MAP and post-MAP (cycle 1). Peaks at 1739 , 1237 and 1015 cm^{-1} characterize the vinyl acetate moiety. This clearly shows that during the first cycle of MAP, the phytocat-2.5 was able to effectively de-polymerize the primary layer of PF, which comprises ULDPE (as shown previously in **Figure 5.14a**). After the successive MAP (cycle 3), the degradation of the secondary and tertiary layers of PF, which comprises EVA and EVOH was initiated.

Notably, the presence of a weak signal around 3600 cm^{-1} and 1600 cm^{-1} suggests the release of water from vinyl alcohol units and formation of volatiles containing C=C bonds from ethylene units.²⁴⁴ Moreover, the spectra obtained in the presence of the phytocat-2.5 (post MAP cycle 3) show the following characteristics in comparison with the post-MAP (cycle 1): (i) a slight increase of the band at 1379 cm^{-1} , related to the symmetrical bending of $-\text{CH}_3$ groups, (ii) a slight decrease of the bands at 1640 cm^{-1} (C=C stretching) and at 966 and 911 cm^{-1} (olefinic out-of-plane C-H bending), which indicates a slight decrease in the yield of alkenes and (iii) differences in the $910\text{--}670\text{ cm}^{-1}$, which can be related to differences in the composition of aromatic compounds evolved. This behavior reveals that during MAP using phytocat-2.5, the yield of alkenes decreases and that the formation of shorter and/or more branched saturated hydrocarbons is favored.

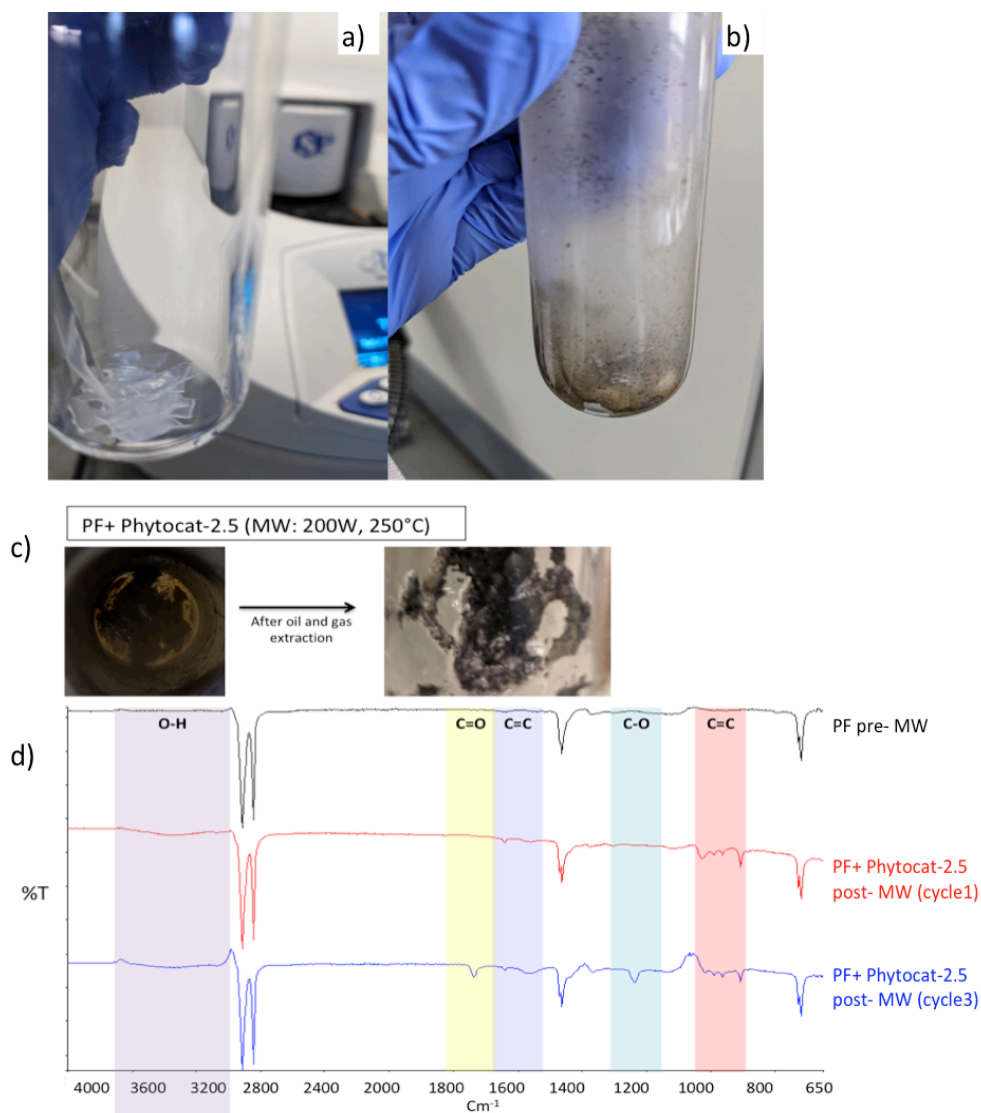


Figure 5.17: Visual appearance of PF in the microwave reactor (a) pre-pyrolysis, (b) post-pyrolysis using phytocat-2.5, (c) post MW cycle 3 (before and after the extraction of oil and gas); (d) FTIR spectra of PF pre-pyrolysis, mixtures of PF and phytocat-2.5 (1:10, by weight) post MW cycle 1 and 3 respectively.

To further gain insights into the degradation behavior of PF using various catalysts, a qualitative analysis of the liquid and gaseous fractions produced was performed using gas chromatography equipped with mass spectrometer and thermal conductivity detector respectively (**Figure 5.18**). Based on the composition of liquid fraction, the monocyclic aromatics formed the major fraction of oils produced using phytocat-2.5 (up to 24% selectivity), while the selectivity towards monocyclic aromatics was found

to decrease for phytocat-0.1 (up to 20.7% selectivity), control phytocat (up to 11% selectivity) and activated carbon (up to 7.9% selectivity). Contrastingly, the polycyclic aromatics and O-containing compounds were found to be the major fractions of the oil produced using control phytocat (up to 74% selectivity) and activated carbon (up to 81% selectivity). Notably, the aliphatic hydrocarbons (including short chain alkanes and alkenes (C_{6-12}) and long chain alkanes and alkenes ($C_{>12}$) with selectivity up to 21% and up to 34% respectively) were the major fractions of the oil produced using phytocat-2.5 (**Figure 5.18a**).

Taking into consideration the composition of gas fractions, it should be noted that the yields and selectivity towards H_2 increases predominantly using phytocat-2.5 (up to 57% selectivity towards H_2 in 20 wt.% of gaseous fraction). In contrast, a declining trend was observed while using control phytocat (up to 42% selectivity towards H_2 in 14 wt.% of gaseous fraction) and activated carbon (up to 41% selectivity towards H_2 in 12 wt.% of gaseous fraction). Other than H_2 , hydrocarbons (mainly CH_4 and C_2H_4) together with some gaseous products i.e. CO , CO_2 , were formed in a similar way as observed with the PE derived gas products (as discussed previously in **section 5.2**). The only difference is the slight increase in the CO and CO_2 fractions, which could be explained due to the degradation and EVOH and EVA during MAP of PF (**Figure 5.18b**). The degradation of EVOH is characterized by the primary release of volatiles deriving from ethylene units and vinyl alcohol units, with numerous other chain scissions, whereas the secondary degradation step is correlated to further release of species containing aliphatic C-H groups from ethylene units.²⁴⁴ The presence of both signals around 3600 cm^{-1} and 1600 cm^{-1} suggested the water release from vinyl alcohol units and formation of volatiles containing C=C bonds from ethylene units (as described previously in **Figure 5.17d**).²⁴⁴ This further elucidates the observation that carbon structure (residue formed as a result of MAP of PF using phytocat-2.5 with the elimination of hetero-atomic compounds) was further improved by the occurrence of aromatization, cyclization, and condensation processes, which were primarily related to dehydrogenation and de-alkylation, in polymeric chains.

It is likely that the main source of CO_2 and CO is the degradation of ester groups, an increased concentration of which was demonstrated during MAP of PF.²⁴⁵ However,

it must be noted that there is a sharp and parallel increase in CO and H₂ concentrations, in contrast to the slight CO₂ decrease using phytocat-2.5. It could be assumed that fragment of acetic acid formed during degradation of EVA decomposes to carbon monoxide and hydrogen.^{246–248}

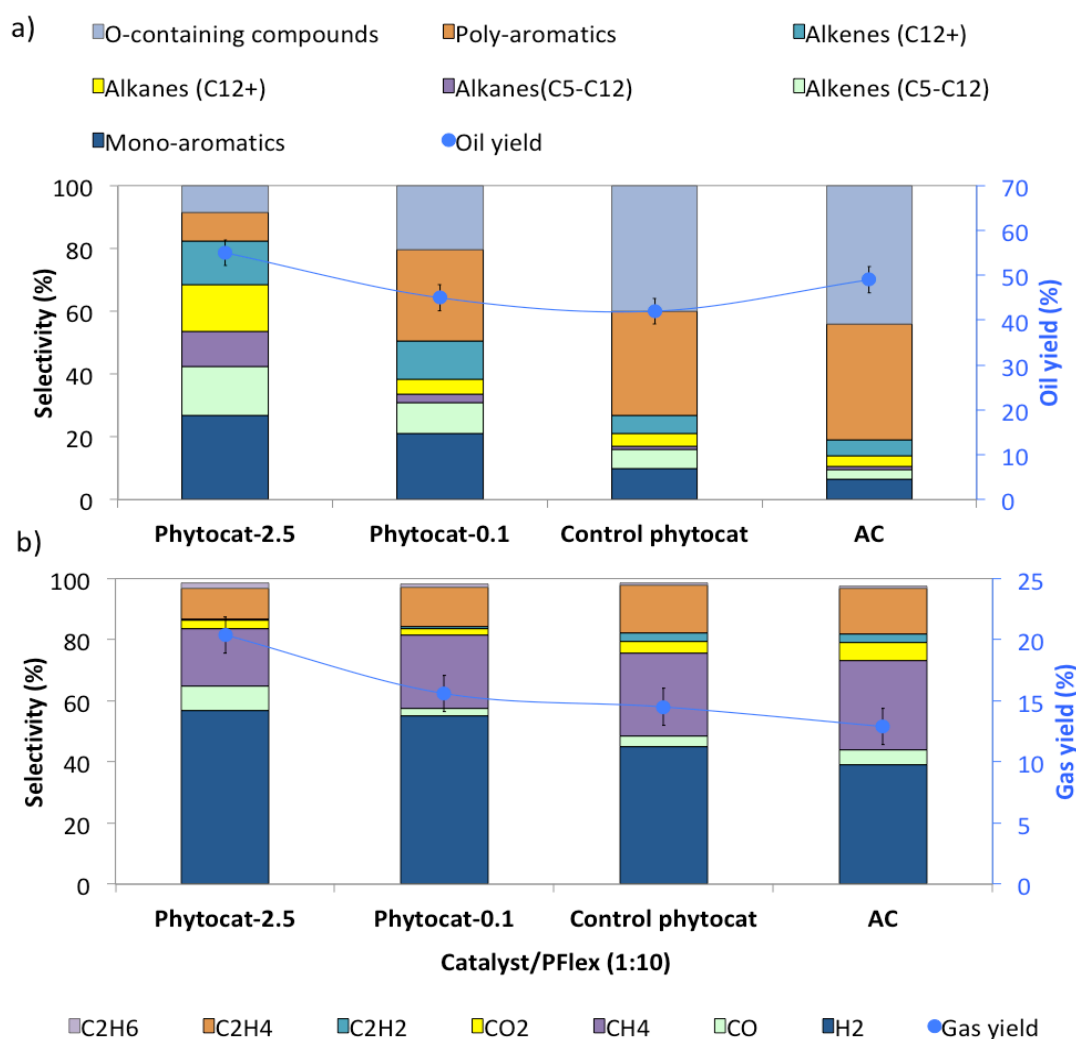


Figure 5.18: Product yields and selectivity using various catalysts (1:10 catalyst to polymer ratio, by weight) of (a) liquid fraction and (b) gaseous fraction formed on MAP of PF

Taking a closer look into the distribution of products formed during the depolymerization of PF, the gas chromatograms of the oils produced were characterized in detail (**Figure 5.19**). Notably, the peaks corresponding to the various compounds

formed otherwise were absent in the spectrum obtained post de-polymerization of PF without catalysts, which suggests that no reaction took place without the addition of catalyst. Furthermore, on addition of activated carbon, polycyclic aromatics (particularly naphthalene, biphenyl and derivatives) and oxygenated compounds (particularly esters and alcohols) were formed as the major fraction of the oil. Similar observation was noted with the use of control phytocat, alongside slight increase in the formation of mono-aromatics and aliphatic hydrocarbons. Contrastingly, there was a remarkable increase in the production of monocyclic aromatics (predominantly benzene and toluene) and the aliphatic hydrocarbons (including short chain alkanes and alkenes (C_{6-12}) and long chain alkanes and alkenes ($C_{>12}$) while using phytocat-2.5. This observation further elucidates that MAP of PF using phytocat-2.5 proceeds with the elimination of hetero-atomic compounds, which was further improved by the occurrence of cyclization, which was primarily related to dehydrogenation and de-alkylation, in polymeric chains. Therefore, the synergistic interactions of microwaves and the biologically bound Ni play a remarkable role in de-polymerization of microwave transparent polymers.

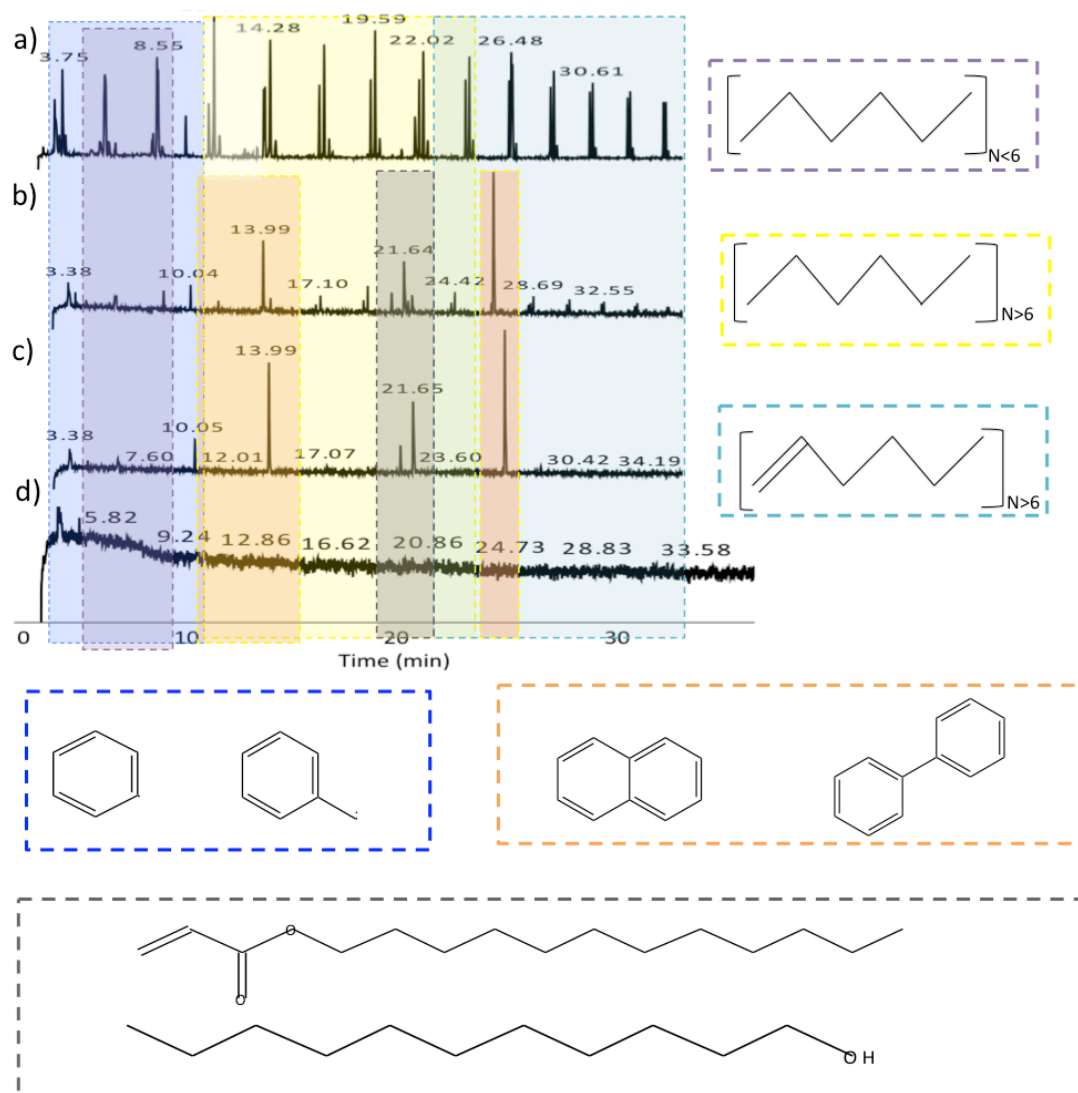


Figure 5.19: Gas chromatography-mass spectrometry (GC-MS) characterization of oils produced by MAP of PF (1:10 catalyst to polymer ratio, by weight) using (a) phytocat-2.5, (b) control phytocat, (c) activated carbon and (d) without catalyst; alongside structural formulae of the major compounds formed (highlighted in various colors).

Summary

The successful demonstration of the accelerated de-polymerization process based on a combination of waste-sourced Ni-phytocat and microwaves is extremely promising for recovering H_2 as well as valuable hydrocarbons and filamentous carbon from plastic waste.

The MAP of plastics under mild reaction conditions (250 °C, 200W, up to 5 min) is a promising energy-saving approach toward plastic waste-to-chemicals as compared to high temperature and long duration CP. Remarkably, under microwave irradiation, the heat transfer was faster during de-polymerization of PE as compared to PS and PF, thereby leading to relatively less energy consumption during the process. However, the total conversion to the monomers was found to be higher for PS, followed in decreasing order by PE and PF. The synergy of the Ni-phytoact and microwave driven process allows the fine-tuning of activity and selectivity to highly desirable monocyclic aromatics and low molecular weight hydrocarbon products, and H₂. Because the proposed catalyst is active in rapidly de-polymerizing of different types of plastics, including the least recycled polystyrene and low density polyethylene, pre-separation of waste feed-stocks may sometimes not be required.¹⁷⁰

Chapter 6 Concluding remarks and future work

6.1 Summary of key results

This research envisioned the development of phytocat material, which is an air-stable and inexpensive, biologically bound Ni catalyst prepared from Ni-rich plant biomass. The single step, low-temperature, microwave-assisted biosynthesis of catalytically active Ni makes it cost-effective alternative to conventional catalysts, which are typically fabricated using precious metals, involving multi-step synthesis. To date, several synthetic procedures have been reported for fabricating bio-catalysts including wet impregnation, ion-exchange, co-precipitation, reduction, high-temperature pyrolysis, atomic layer deposition and so on. However, these protocols focus on artificial incorporation of noble and non-noble metallic species onto bio-derived carbon materials. The interest of this study is in developing biocatalysts from plants that have taken up nickel through natural, biological processes. This process allows both the recapturing of a limited, natural resource, remediation of land, and once the catalyst is used-up, the metal can be reused, presenting a sustainable circularity.

This study proposes a new approach towards microwave-driven de-polymerization of plastics as well as hydrogenation of renewable platform molecules, enabled by sustainable Ni⁰/Ni²⁺/bio-carbon synergistic effects of phytocat. This study demonstrated the successful use of nickel captured by plants from contaminated soils as a catalyst for industrially important hydrogenation processes. Thus, toxic soils can be remediated, and at the same time, the need for the wasteful and energy-demanding mining of virgin metal could be reduced. Furthermore, it was found that the natural encapsulation of Ni on bio-carbon not only inhibits the unselective hydrogenation pathway but also regulates the electronic structure of Ni.²⁴⁹ As an added bonus in the use of the phytocat in the hydrogenation of α,β -unsaturated carbonyl compounds, the natural encapsulation of nickel inhibits the undesired reduction of the carbonyl group.

The phytocat's functionality and the spatial dispersion of nickel on it play a significant role in plastic de-polymerization. Remarkably, the de-polymerization was achieved at moderate temperatures (250 °C) in very short periods of time (<5 min), and can be tuned to maximize the production of hydrogen and/or smaller, fuel-suitable hydrocarbons. This product flexibility could be very important given the shifting, and politically dependent balance in energy requirements and the emergence of the hydrogen economy.

To summarize, this work emphasizes the importance of the following UN sustainable development goals:

- Affordable and clean energy (SDG 7),
- Industry, innovation, and infrastructure (SDG 9)
- Climate action (SDG 13)

6.2 Recommendations for future work

The particular area of research investigated in this study has the potential to be expanded further. Therefore, various recommendations for future work have been specified below.

Development of more “phytocats” involving different metals, especially where they can be used instead of scarce, difficult to refine and increasingly expensive noble metals.

Further investigation of the plastics pyrolysis process with continuous feeding mode. This preliminary study has paved the way for advancing the experimental end-of-life plastics pyrolysis. According to conventional chemical engineering principles, scaling up of the continuous processing capacity is considered best practice.^{149,237} Therefore, a further investigation on plastics pyrolysis with continuous feeding is suggested as it offers the flexibility of operating at different temperatures and pressure levels, with an additional advantage of processing mixed plastic waste.

Use of plastic pyrolysis oils as a carbon source to be metabolized by *Galdieria* (red microalga) to understand the composition of the high value products obtained from it. This idea is aligned with the realization of the goal of a carbon-neutral society for which closing of carbon and hydrogen cycles in plastics would be extremely important. This would help to improve the prospects of chemical recycling of plastics and better understand this as a recycling model. Therefore, oils at kg scale would be needed for further downstream processing. So, future work should be conducted on the 20 kg per hour high temperature pyrolysis MW housed at the Biorenewables Development Centre (BDC, York, UK).

Appendix A

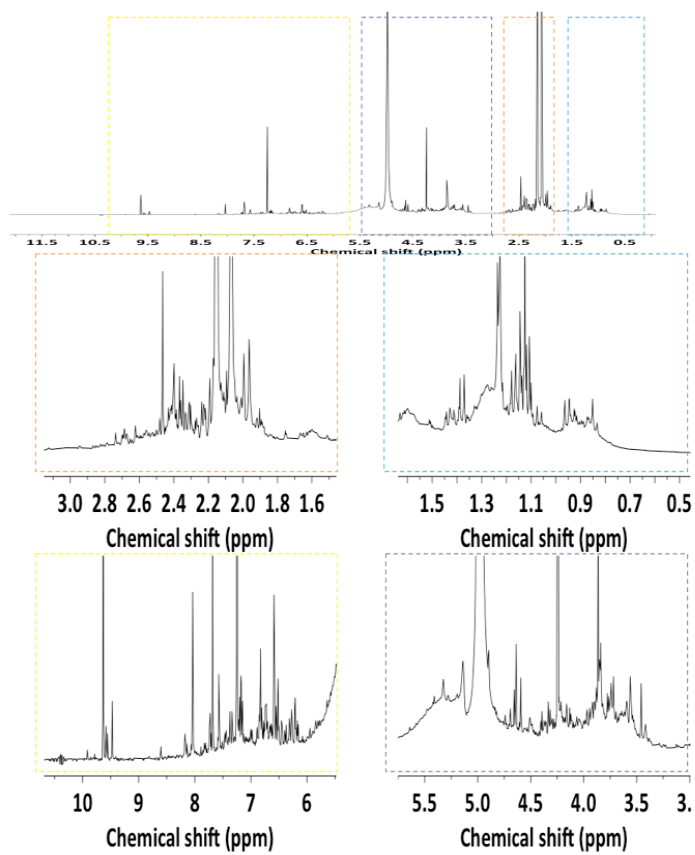


Figure A.1: ^1H NMR spectra of the MAP oil extracted during the formation of phytocatal-2.5

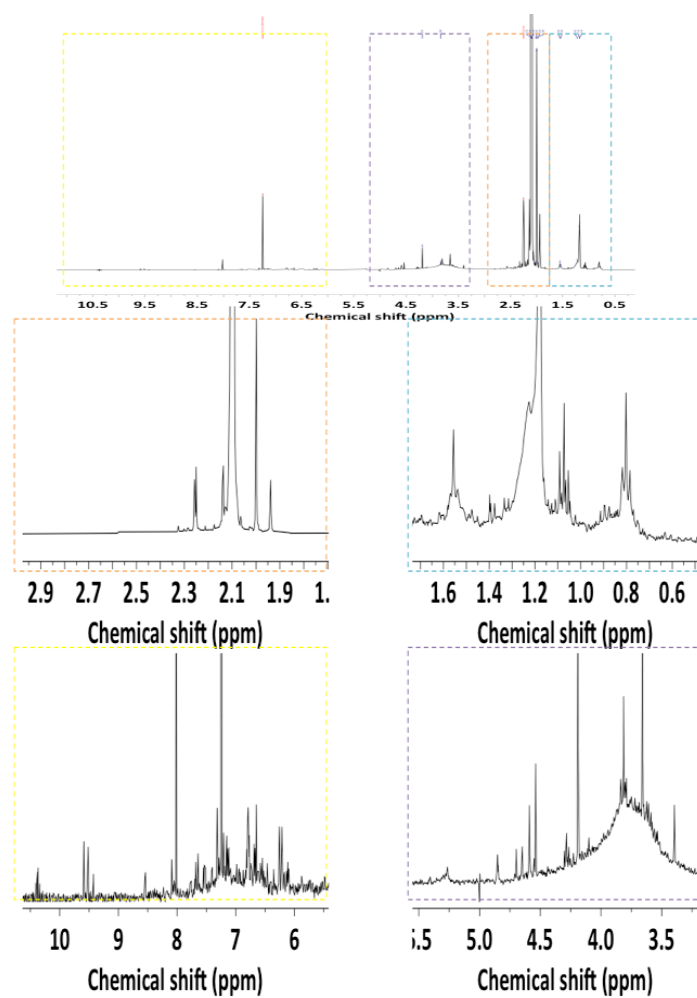


Figure A.2: ^1H NMR spectra of the MAP oil extracted during the formation of phytocat-1.5

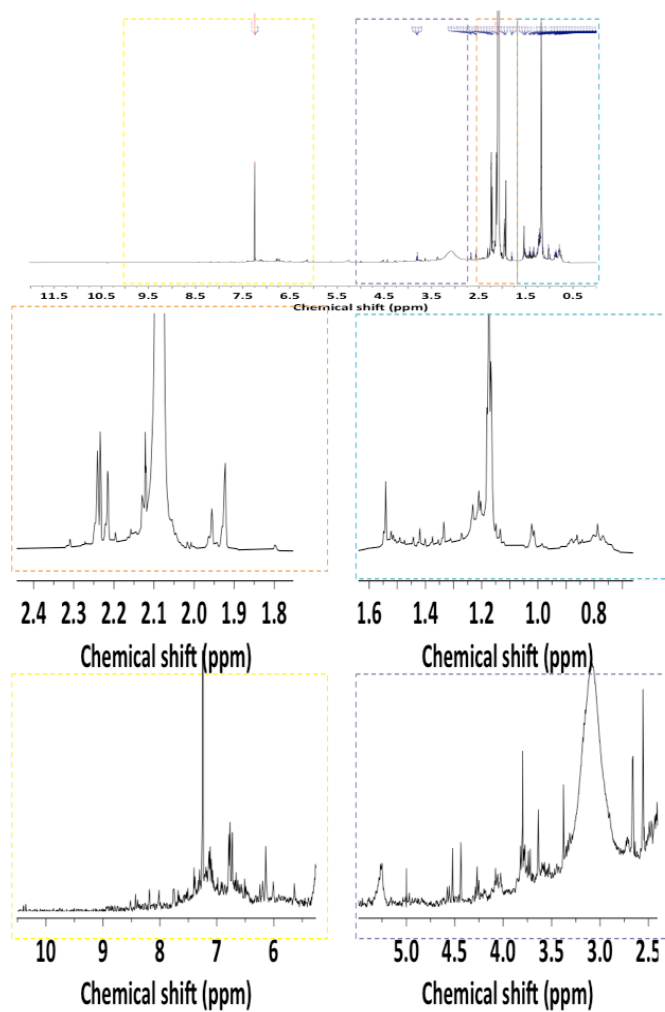


Figure A.3: ^1H NMR spectra of the MAP oil extracted during the formation of phytocat-0.1

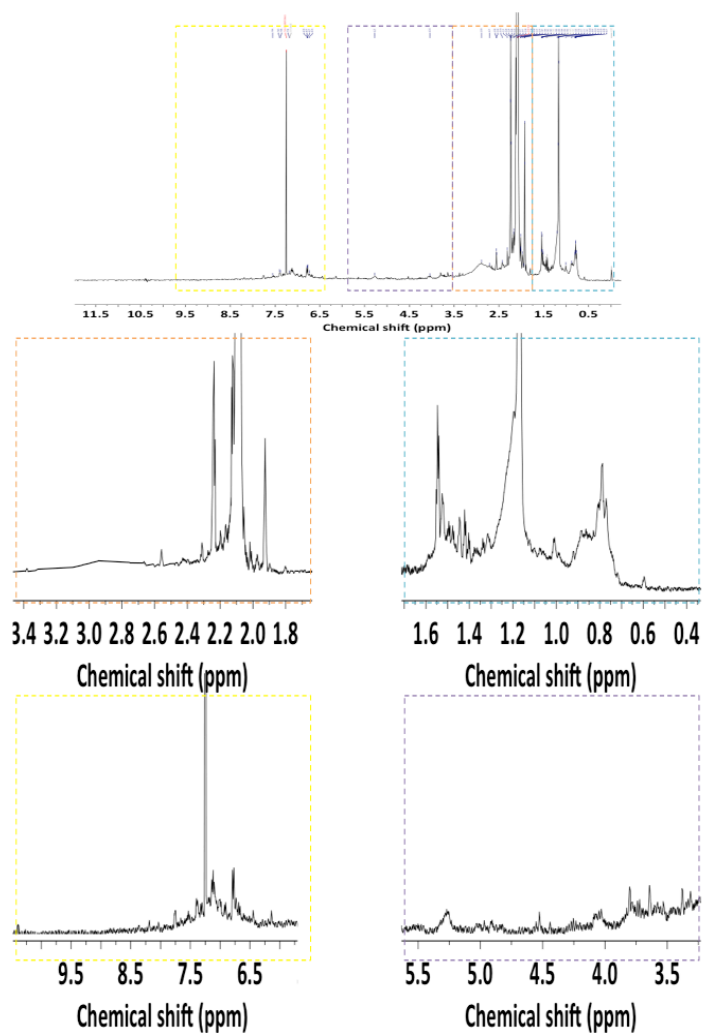


Figure A.4: ^1H NMR spectra of the MAP oil extracted during the formation of control phytocat

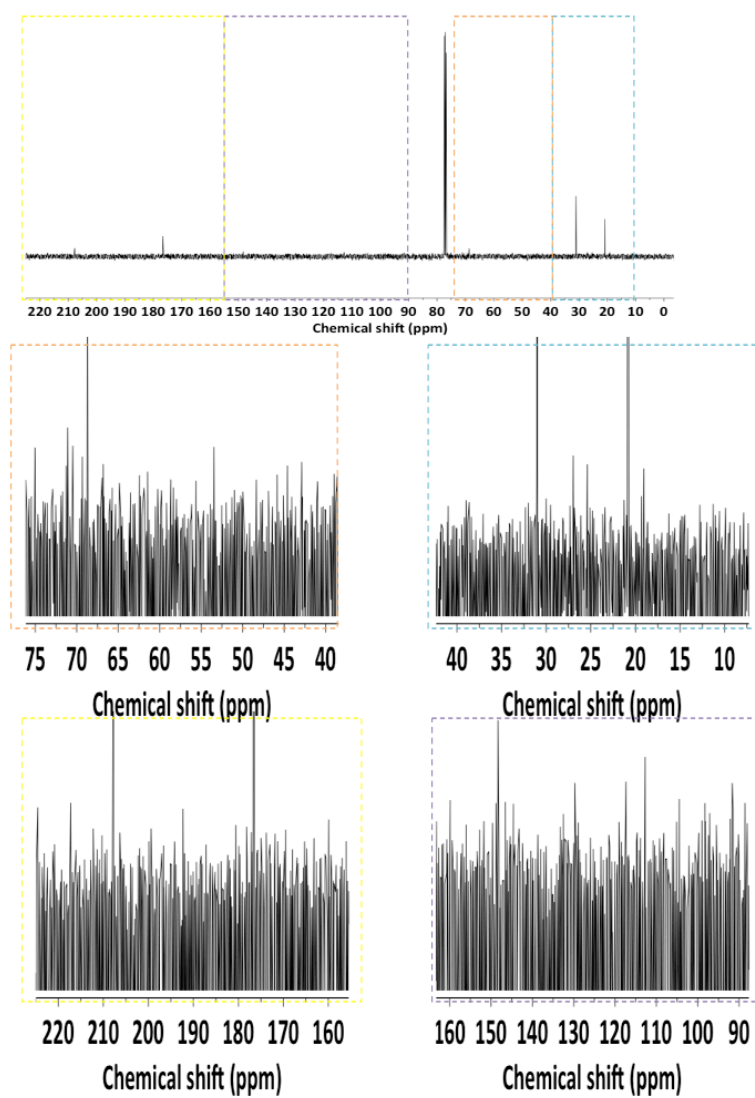


Figure A.5: ^{13}C NMR spectra of the MAP oil extracted during the formation of phytocat-2.5

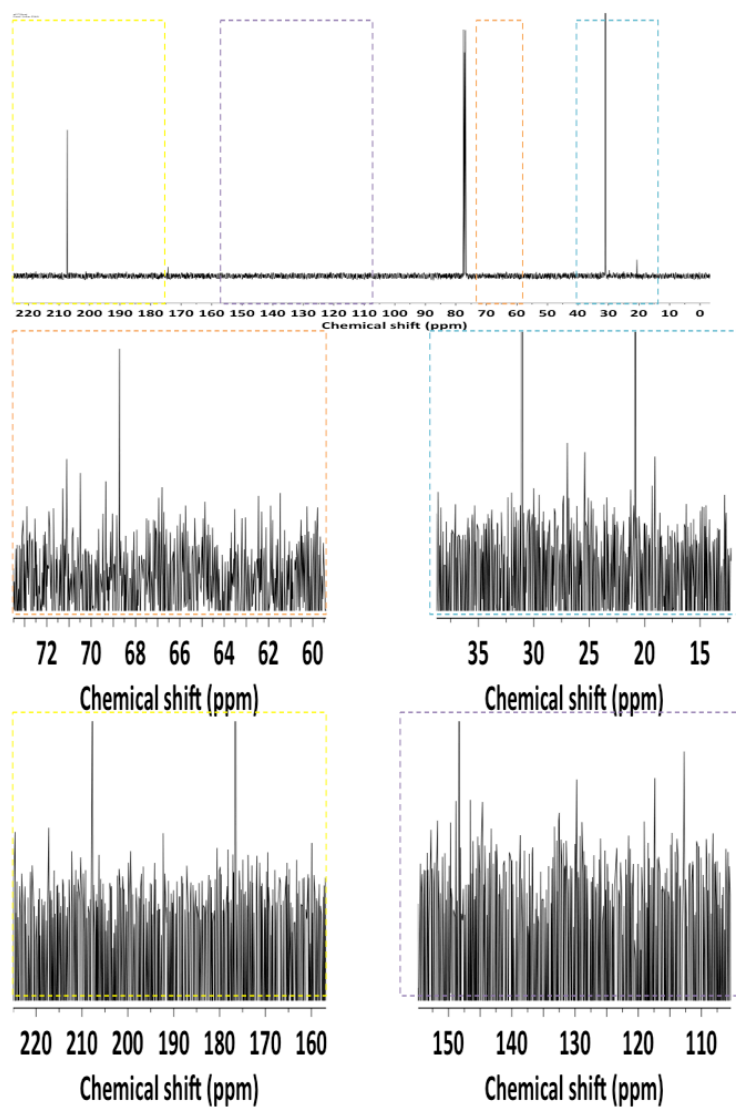


Figure A.6: ^{13}C NMR spectra of the MAP oil extracted during the formation of phytocat-1.5

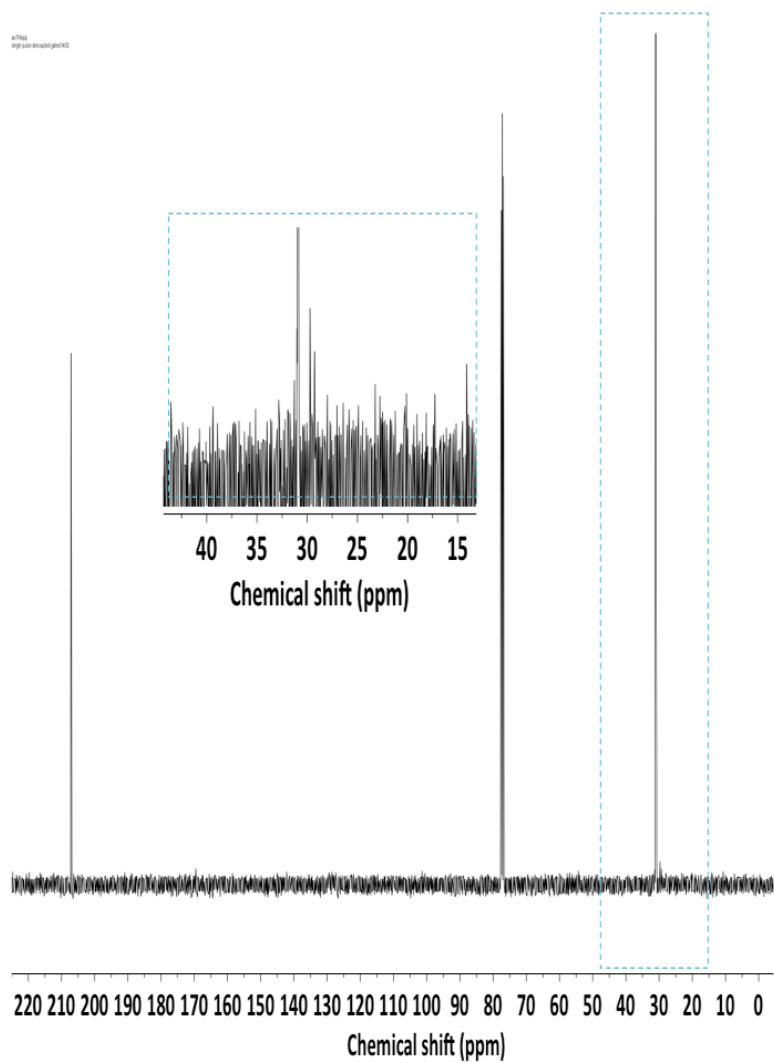


Figure A.7: ^{13}C NMR spectra of the MAP oil extracted during the formation of control phytocatal

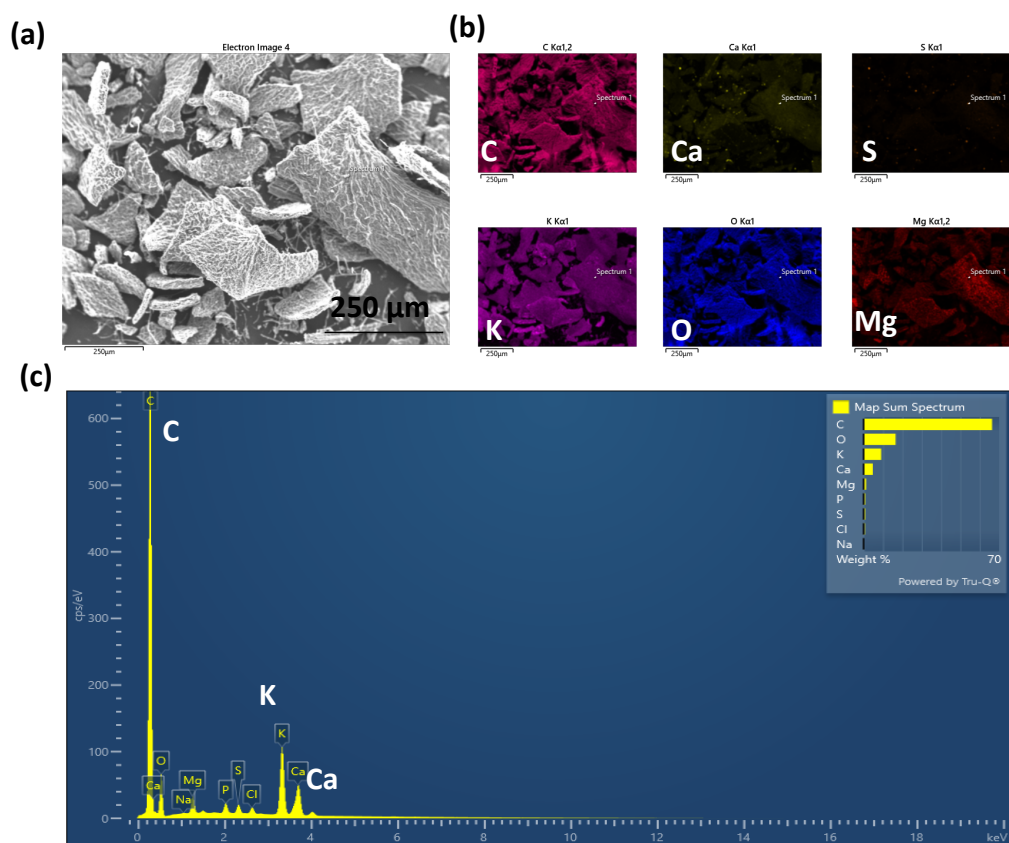


Figure A.8: (a) Scanning electron microscopy (SEM) images equipped with energy-dispersive X-ray spectroscopy (EDX) analysis of control phytocat, (b) Elemental mapping of control phytocat highlighting carbon, calcium, sulfur, potassium, oxygen and magnesium, (c) Energy-dispersive x-ray (EDX) spectroscopy analysis of control phytocat.

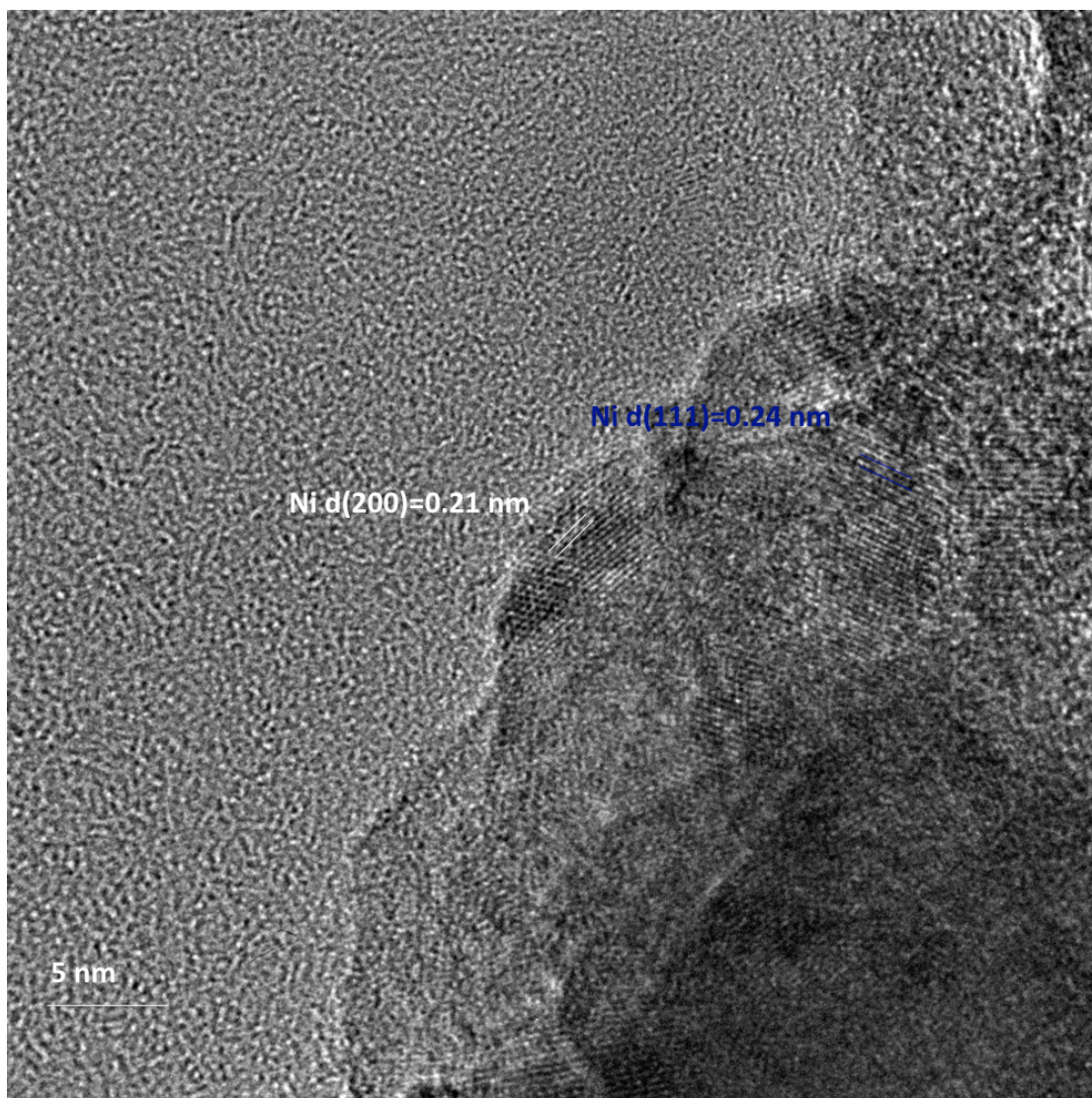


Figure A9: High-resolution TEM (HRTEM) image of Ni-phytocat-2.5 showing lattice fringes corresponding to (111) and (200) crystal planes, respectively, of cubic Ni phase.

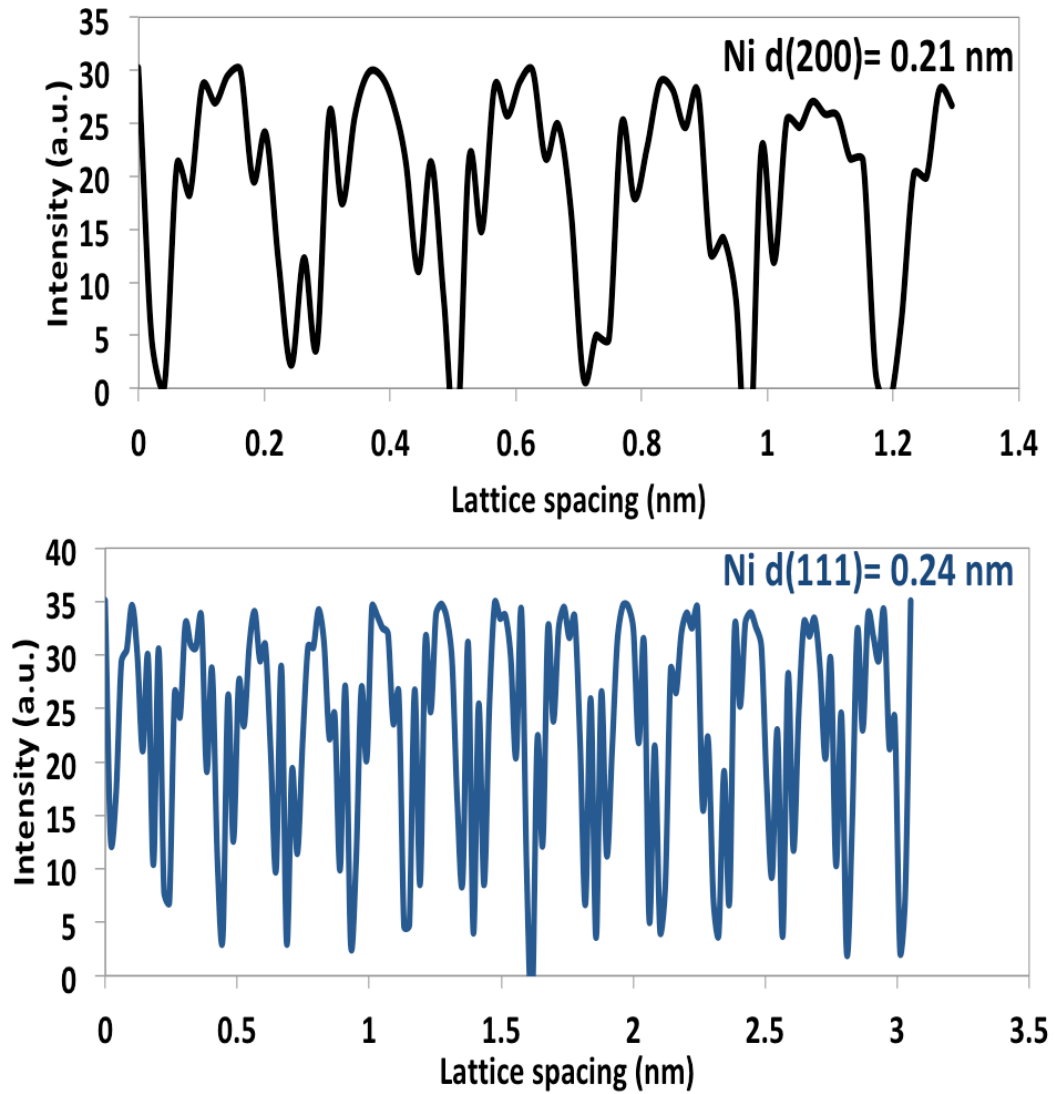


Figure A10: Plots of lattice spacing corresponding to the fast fourier transform (FFT) pattern of the high-resolution TEM (HRTEM) image of Ni-phyto-cat-2.5

Table A1: Detailed elemental distribution of phytocat precursors and phytocat using ICP-MS analysis

Sample Name	Sample type	Ni (mg kg ⁻¹)	Cu (mg kg ⁻¹)	Fe (mg kg ⁻¹)	Co (mg kg ⁻¹)	Pd (mg kg ⁻¹)
Pre-pyrolysis phytocat-2.5	Bio-mass	6691.7 ± 39	4.9 ± 2.1	1118.4 ± 22.4	25.1 ± 2.1	0.15 ± 0.1
Pre-pyrolysis phytocat-0.1	Bio-mass	84.7 ± 2.9	9.7 ± 1.4	1116.1 ± 21.1	16.1 ± 1.1	0.09 ± 0.01
Pre-pyrolysis control phytocat	Bio-mass	0.997 ± 0.5	8.9 ± 1.5	1119.2 ± 11.2	17.2 ± 1.4	0.09 ± 0.02
Phytocat-2.5	Bio-char	25377.9 ± 97	11.2 ± 2.6	1734.9 ± 12	25 ± 1.2	0.27 ± 0.16
Phytocat-0.1	Bio-char	199.45 ± 25	16.9 ± 4.5	1719.1 ± 14	16.5 ± 1.9	0.12 ± 0.1
Control phytocat	Bio-char	2.37 ± 1.5	15.6 ± 3.2	1782.4 ± 22	17.9 ± 1.3	0.11 ± 0.1

Table A2: List of major compounds identified in the MAP oils of phytocat-2.5 based on the GC-MS data

Compound	Peak area (%)	RT (min)
Propanoic acid, 2-oxo methyl ester	1.26	4.09
Furfural	12.82	5.11
2-pentanone, 4-hydroxy-4-methyl	0.66	5.34
2-furanmethanol	1.15	5.72
Butanoic acid, 3-hydroxy-3-methyl	0.52	5.91
2-propanone, 1-acetyloxy	1.36	6.15
Ethanone, 1,2-furanyl	3.40	7.33
2-cyclopenten-1-one, 2-hydroxy	1.03	7.74
2-furancarboxaldehyde, 5-methyl	2.48	8.97
Phenol	7.39	9.57
Oxazolidine, 2,2-diethyl-3-methyl	1.12	10.17
1,2-cyclopentanedione, 3-methyl	1.83	10.91
Cyclobutaneacetonitrile, 1-methyl 2(1 methyl ethenyl)	0.69	11.13
Phenol, 4-methyl	2.90	12.57
Cyclopent-2-ene-1-one, 2,3,4-trimethyl	1.71	12.87
Cyclobutanol	1.21	13.10
1H-1,2,4-triazole	0.79	15.08
Isopropyl barbituric acid	1.27	15.90
1,2-benzenediol	1.57	16.08
3-heptanol,2,2-dimethyl	1.04	16.67
Isosorbide	4.51	18.82
Phenol, 2,6-dimethoxy	1.27	20.39
6,8-Dioxabicyclo[3,2,1]octane, 7 ethyl -5-methyl	1.82	23.56
β -D-Glucopyranose, 1,6-anhydro	1.65	24.10
1,4-Anhydro-d-galactitol	0.72	28.55
n-Hexadecanoic acid	1.61	34.31

Appendix B

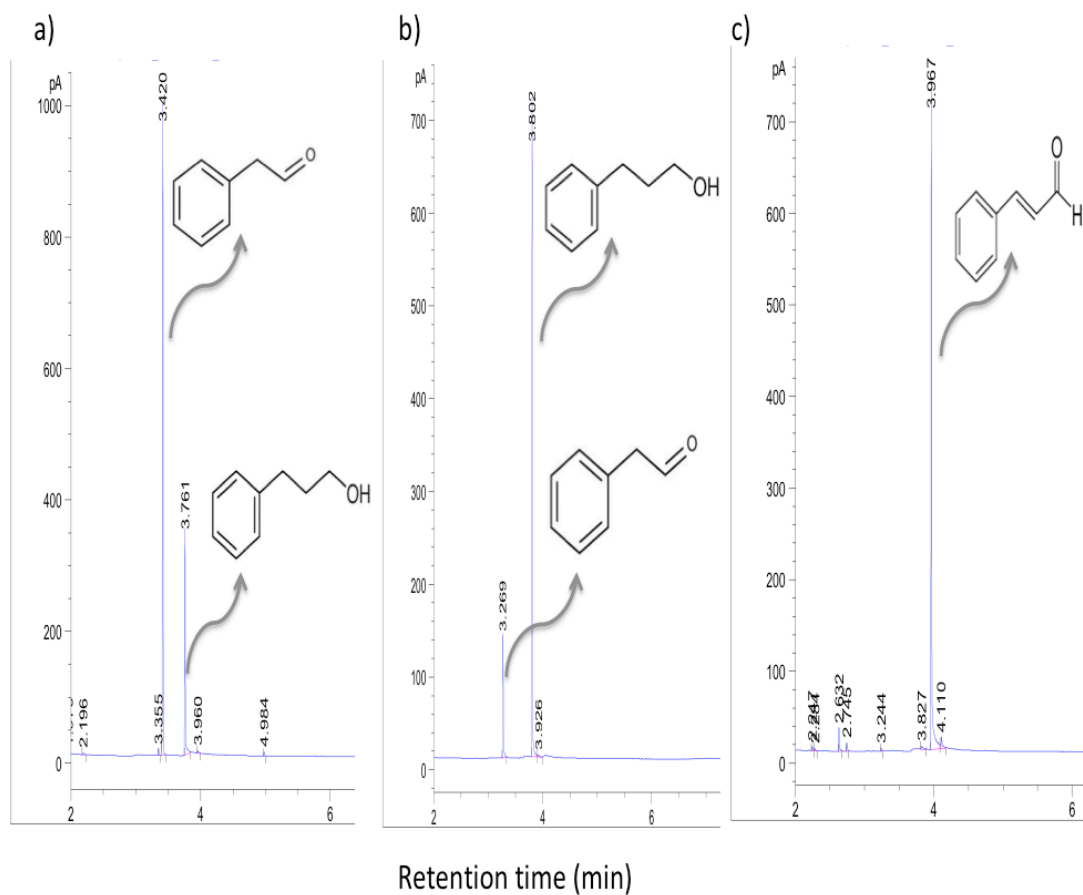


Figure B1: Gas-chromatography equipped with flame ionization detector (GC-FID) analysis of the products formed by hydrogenation of CAL using (a) phytocat-2.5, (b) Raney Ni and (c) control phytocat

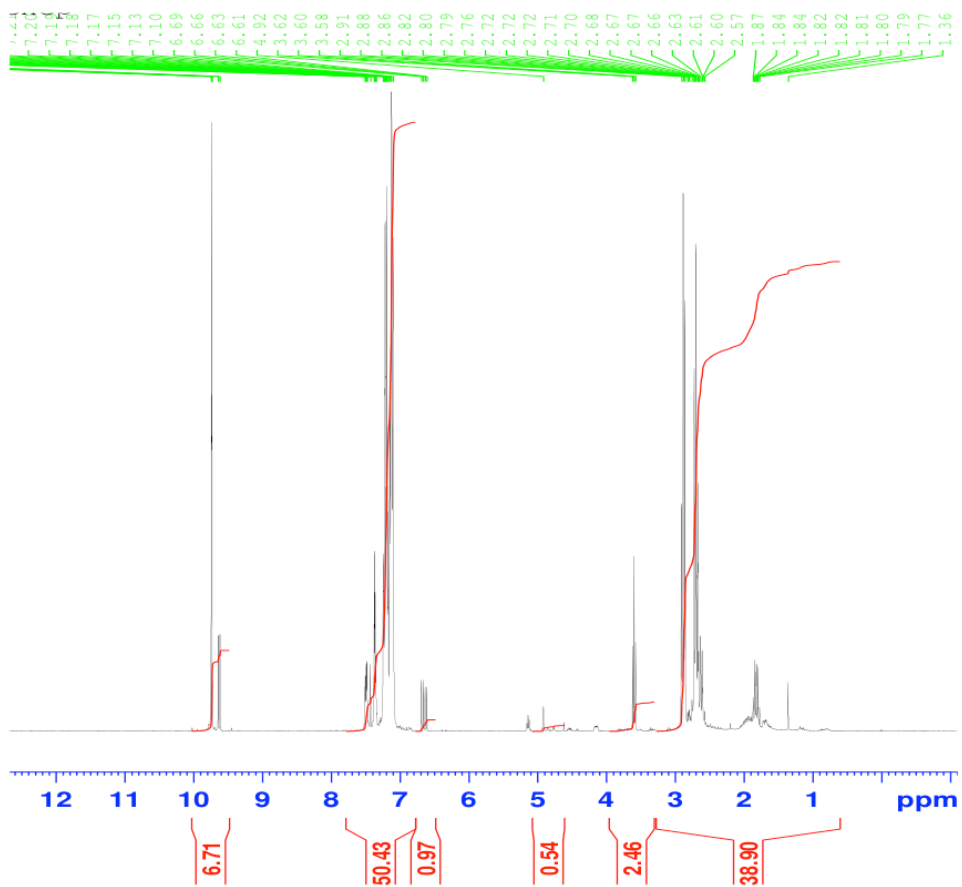


Figure B2: ^1H NMR analysis of the products formed after catalytic hydrogenation of cinnamaldehyde using phytocat-2.5 at 120 °C

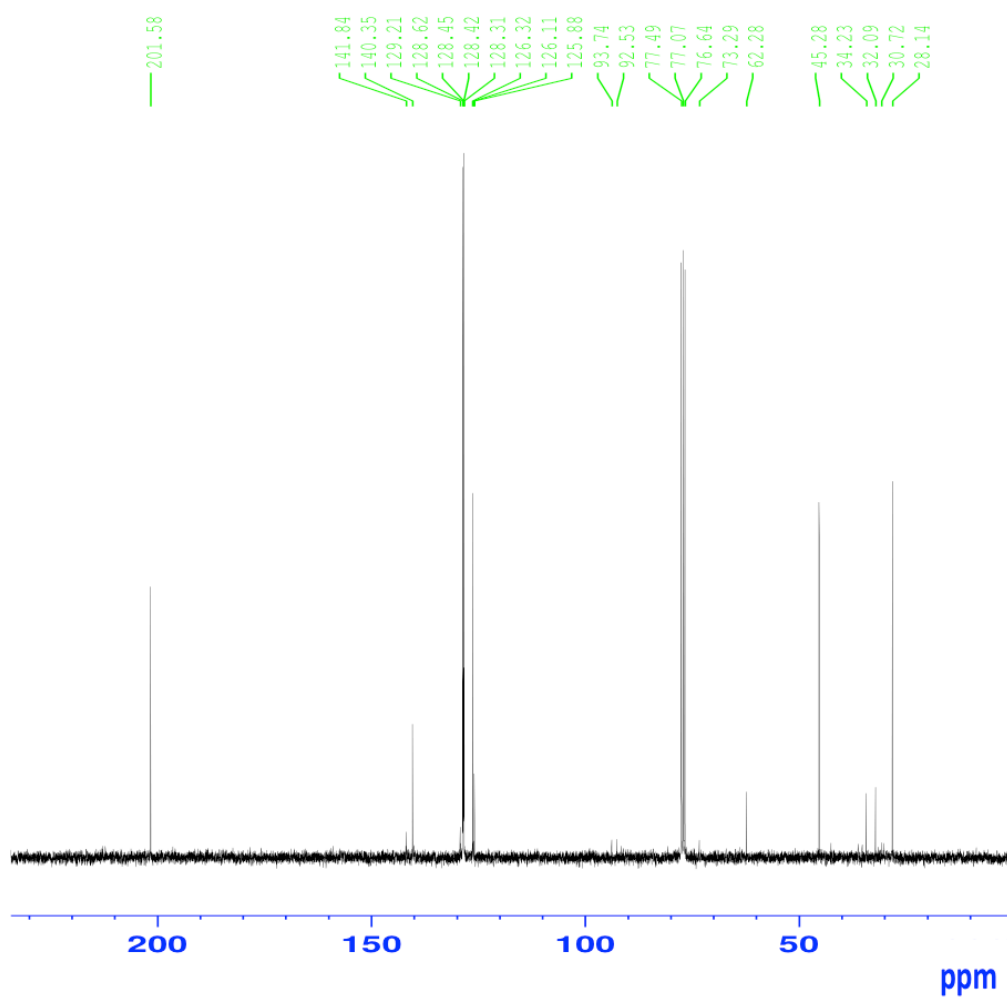


Figure B3: ^{13}C NMR analysis of the products formed after catalytic hydrogenation of cinnamaldehyde using phytocat-2.5 at 120 °C

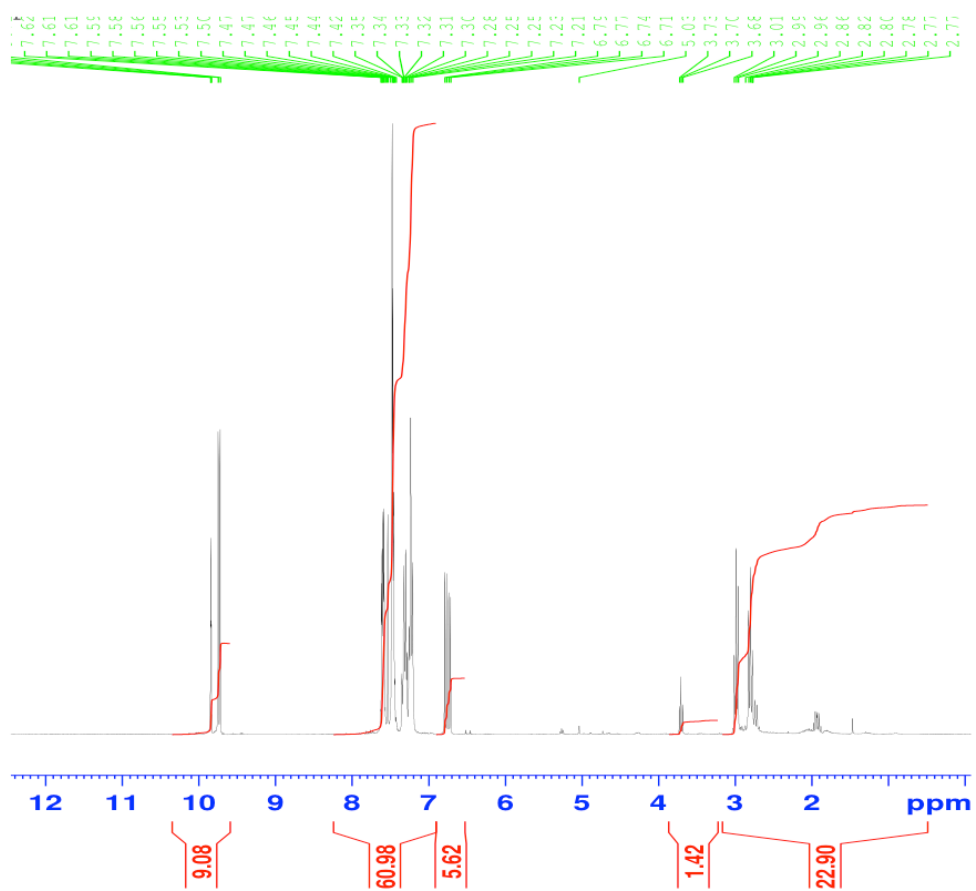


Figure B4: ^1H NMR analysis of the products formed after catalytic hydrogenation of cinnamaldehyde using phytocat-0.1 at 120 °C

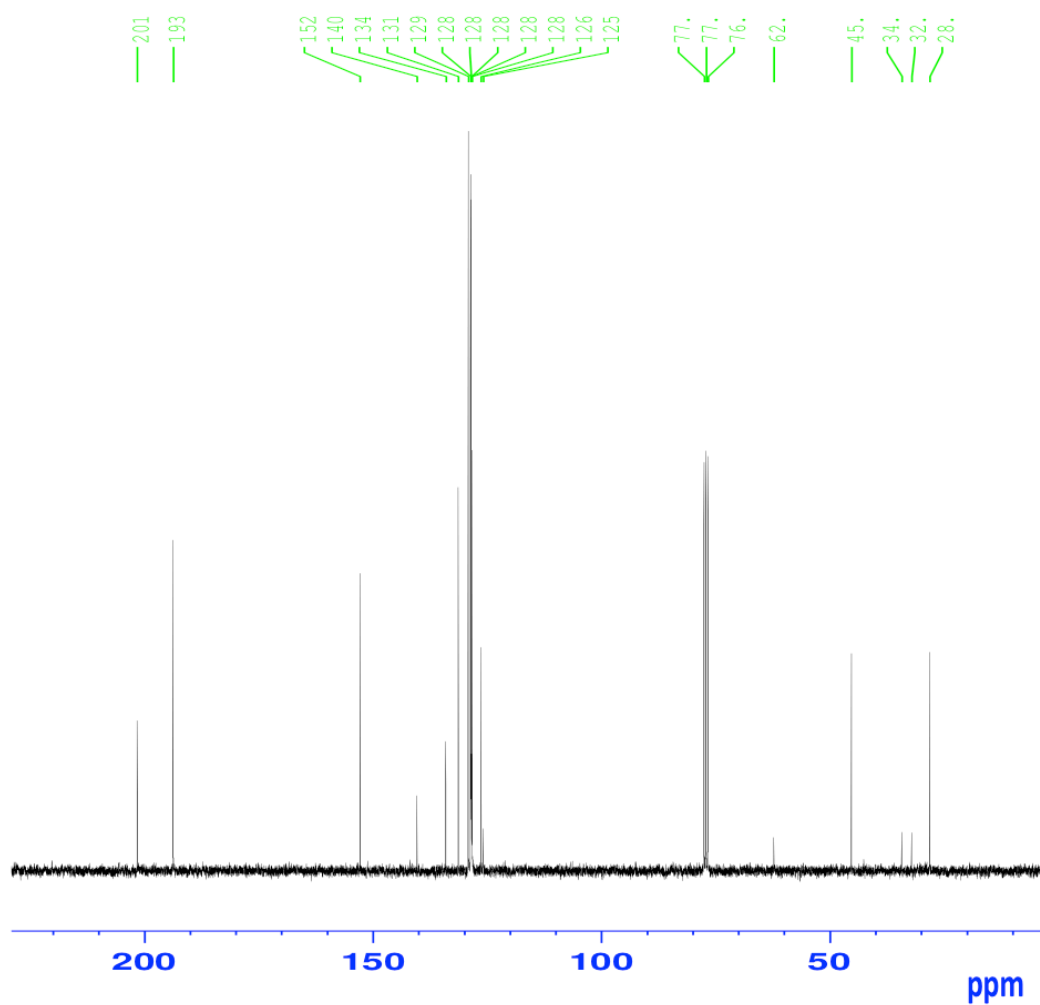


Figure B5: ^{13}C NMR analysis of the products formed after catalytic hydrogenation of cinnamaldehyde using phytocat-0.1 at 120 °C

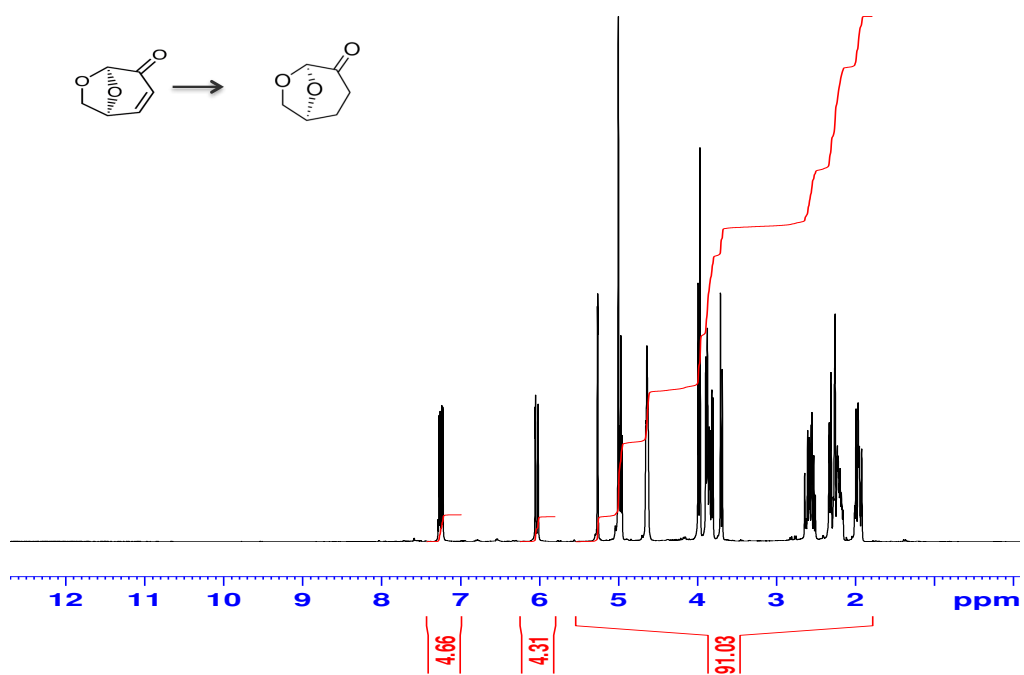


Figure B6: ¹H NMR analysis of the products formed after catalytic hydrogenation of levoglucosenone (LGO) using phytocat-2.5 at 120 °C

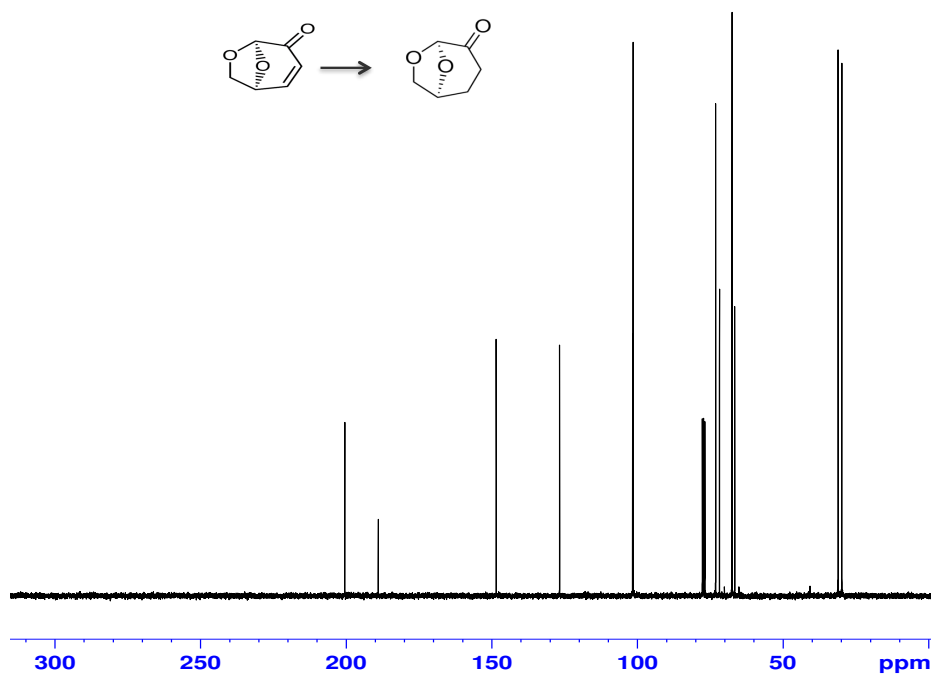


Figure B7: ¹³CNMR analysis of the products formed after catalytic hydrogenation of levoglucosenone (LGO) using phytocat-2.5 at 120 °C

Table B1: Comparison of this work with the literature reports on catalytic hydrogenation of cinnamaldehyde using Ni based catalysts

Catalysts	Time (h)	P_{H2} (bar)	T (°C)	Conversion (%)	HCAL Selectivity (%)	References
Phytocat-2.5	1 h	40	120	67.5	91.1	This work
	2 h	40	120	74	92	This work
	6 h	40	120	81.1	94.3	This work
	24 h	40	120	97	96	This work
	24 h	40	90	76	91	This work
	24 h	40	60	42	89.2	This work
Phytocat-0.1	1 h	40	120	41	81	This work
	2 h	40	120	47	82	This work
	6 h	40	120	59	84.5	This work
	24 h	40	120	89	87	This work
	24 h	40	90	73	82	This work
	24 h	40	60	22	79	This work
Raney Ni	1 h	40	120	97	34	This work
	2 h	40	120	97	27	This work
	6 h	40	120	97	11	This work
	24 h	40	120	99.9	9.1	This work
	24 h	40	90	99.9	72	This work
	24 h	40	60	99.9	91	This work

Catalysts	Time (h)	P_{H2} (bar)	T (°C)	Conversion (%)	H₂ Selectivity (%)	References
Ni/C	8 h	30	60	97	21.1	65
Ni-Cu@RGO	6 h	20	150	89	100	213
Ni/hCNF	1.5 h	30	160	91	82	66
Ni/TiO ₂ -HH	1 h	20	120	99	25.3	113
Ni-Co/AC	9.5 h	5	150	63.2	50.5	114
Ni-Cu/TiO ₂	1 h	20	80	76	13.9	107
Ni-Co/MWCNT	8 h	5	150	62.6	37.9	114
Ni-Ag/TiO ₂	1 h	20	80	76	12.7	107
NiAl-LDH/G	3 h	10	120	100	94.8	250
Ni-Au/TiO ₂	1 h	20	80	77	13.1	107
Ni/SiO ₂	1.4 h	20	110	99	12	251

Table B2: Comparison of turn over numbers (TON) for hydrogenation of cinnamaldehyde at various temperatures and concentration of catalysts

Catalyst	Temperature (°C)	Concentration (mmol)	Turn over number (TON)
Phytocat-2.5	60	0.01	21.0
		0.02	19.5
		0.04	11.5
	90	0.01	56.0
		0.02	34.5
		0.04	19.0
	120	0.01	67.0
		0.02	46.5
		0.04	24.5
Phytocat-0.1	60	0.01	4.3
		0.02	5.5
		0.04	7.2
	90	0.01	21.7
		0.02	29.5
		0.04	18.2
	120	0.01	59.0
		0.02	37.0
		0.04	22.3
Control phytocat	60	0.01	0
		0.02	0
		0.04	0
	90	0.01	0
		0.02	0
		0.04	0
	120	0.01	0
		0.02	0
		0.04	0
Raney Ni	60	0.01	99

90	0.01	100
120	0.01	100

Appendix C

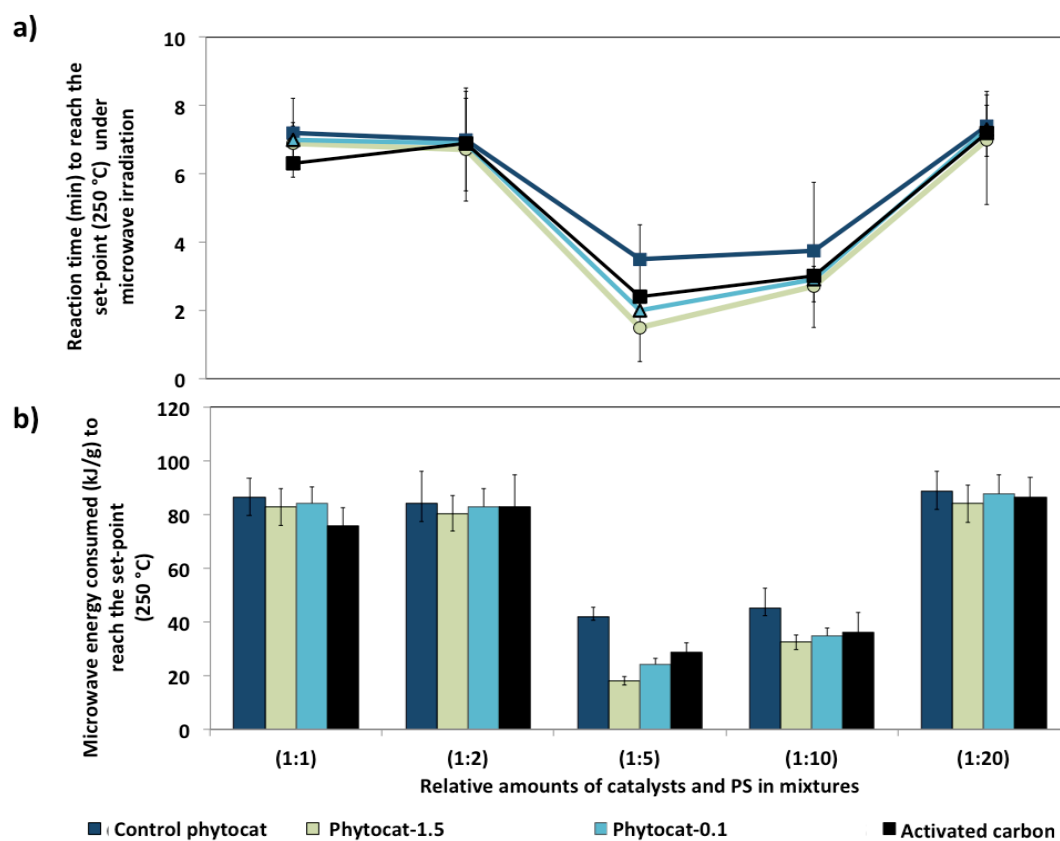


Figure C1: Time (a) and energy consumption (b) under microwave irradiation to reach the set point of 250 °C for de-polymerization of polystyrene using various mixing ratios with phytocat and activated carbon

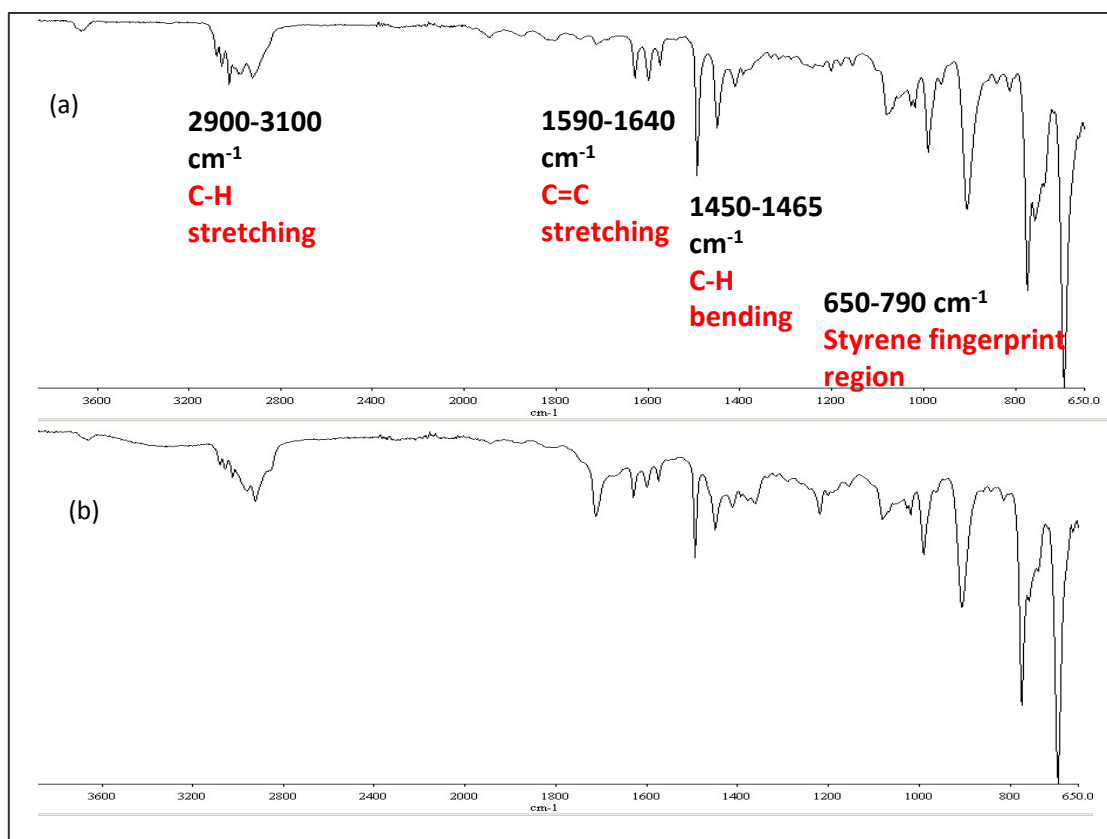


Figure C2: FTIR analysis of pyrolysis oil produced by microwave assisted de-polymerization of Polystyrene using (a) phytocat-0.1 and (b) control phytocat.

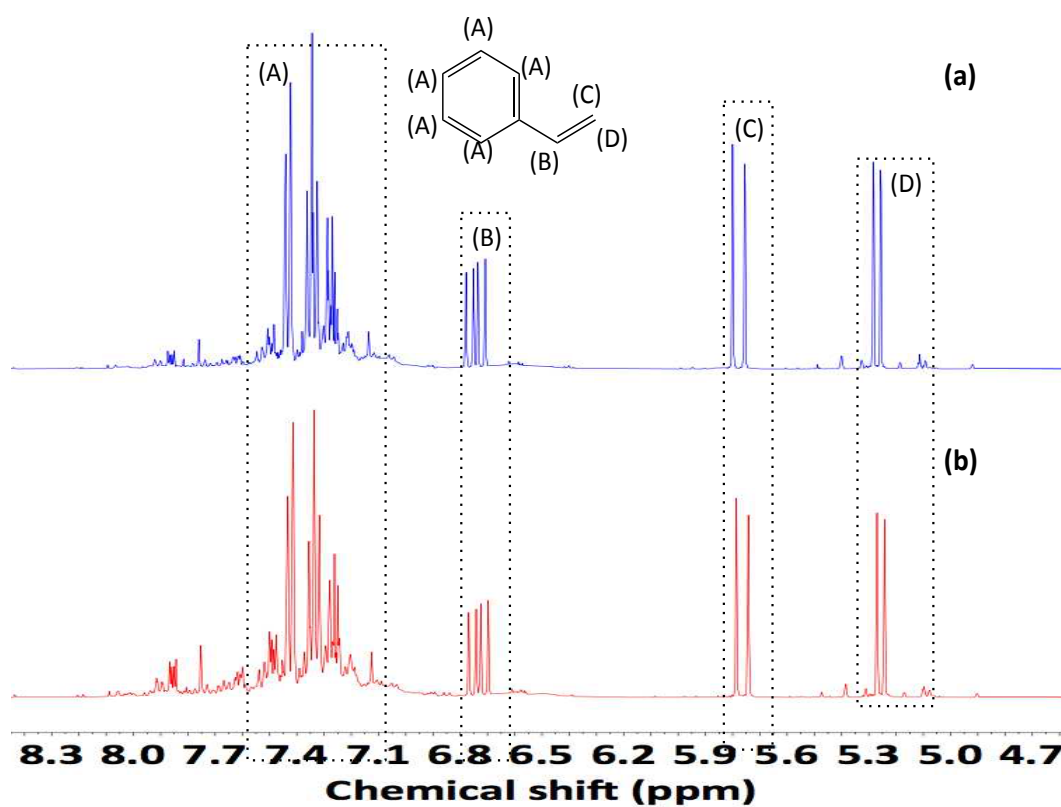


Figure C3: ^1H NMR spectrum of pyrolysis oil produced by microwave assisted de-polymerization of Polystyrene using (a) phytocat-0.1 and (b) control phytocat.

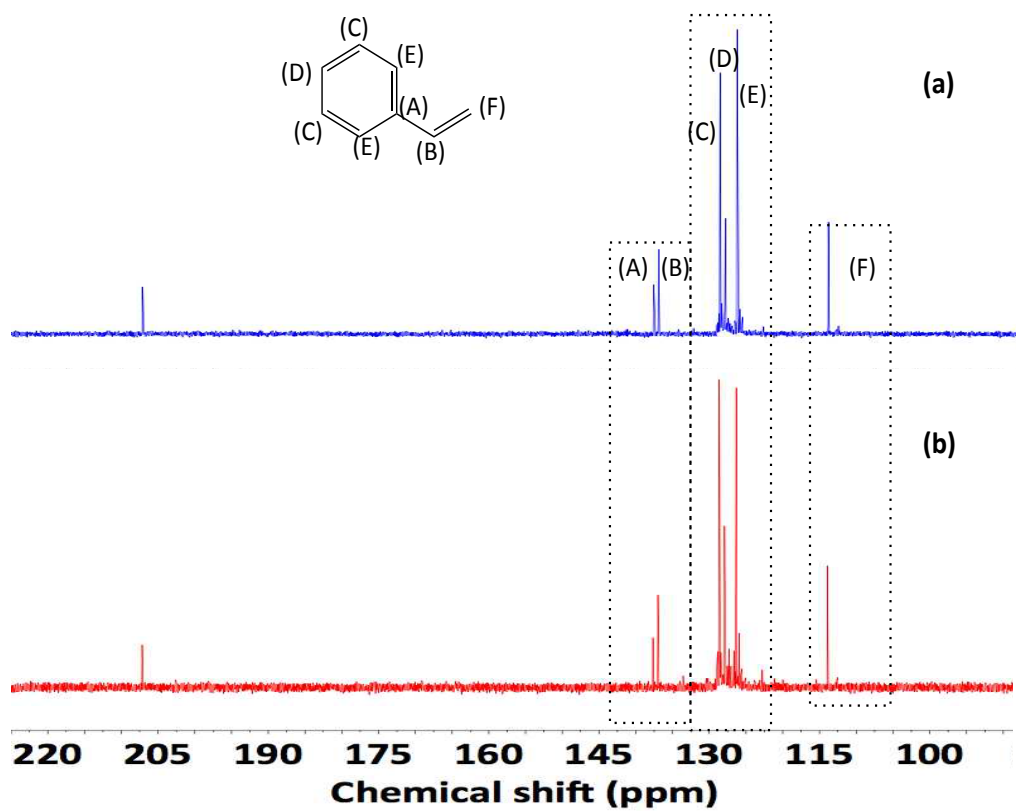


Figure C4: ^{13}C NMR spectrum of pyrolysis oil produced by microwave assisted de-polymerization of Polystyrene using (a) phytocat-0.1 and (b) control phytocat.

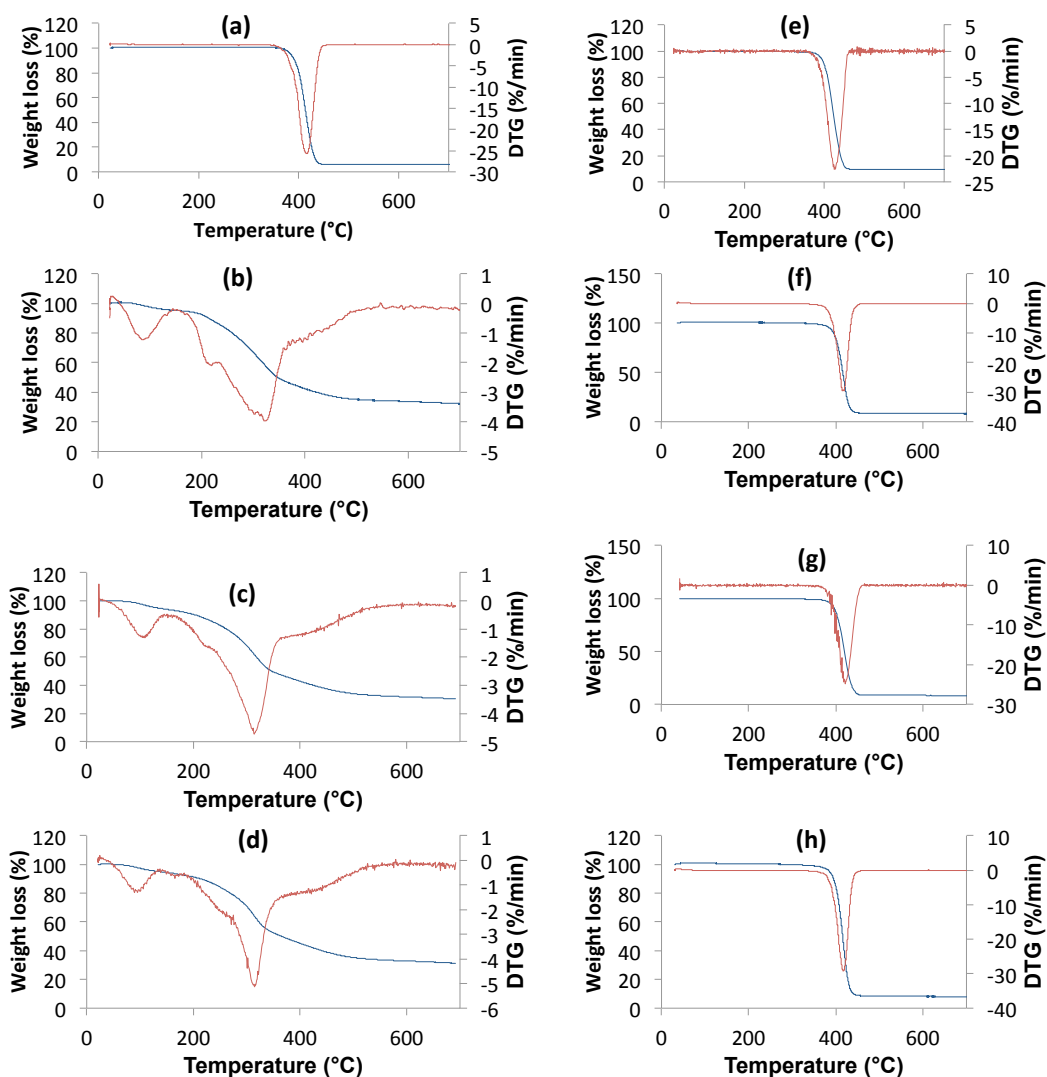


Figure C5: Conventional TGA profiles of (a) polystyrene (PS), (b) *S. tryonii* (pre-pyrolysis phytocat-1.5), (c) *S. viminalis* (pre-pyrolysis phytocat-0.1), (d) *S. viminalis* (<0.01 wt% Ni; pre-pyrolysis control phytocat), (e) activated carbon: PS (1:10), (f) phytocat-1.5: PS (1:10), (g) phytocat-01: PS (1:10) and (h) control phytocat: PS (1:10) with a heating rate of $10^{\circ}\text{C min}^{-1}$ under nitrogen atmosphere of 100 ml min^{-1} flow rate.

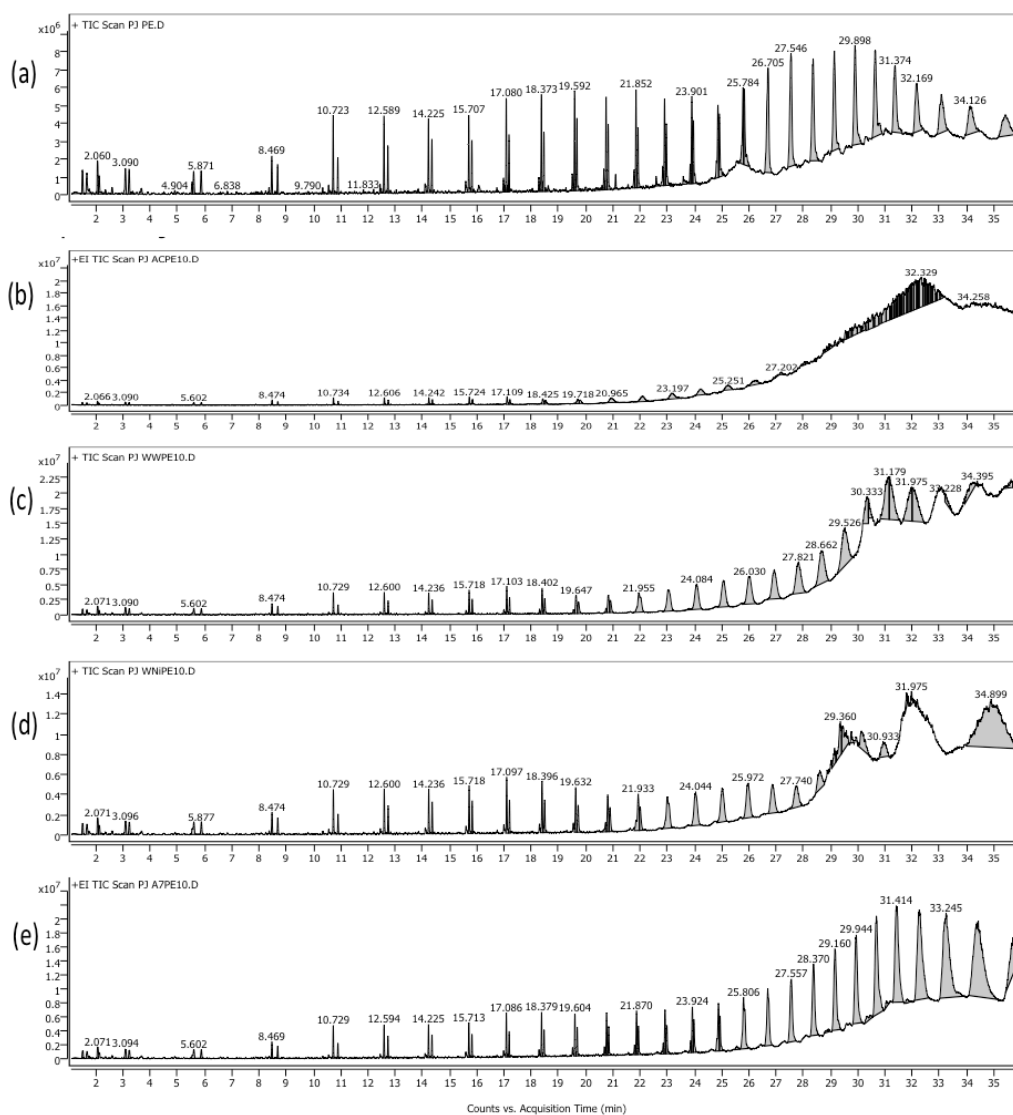


Figure C6: Gas chromatograms of the pyrolysis oils produced using conventional pyrolysis of (a) low density polyethylene (LDPE), (b) activated carbon: LDPE, (c) control phytocat: LDPE, (d) phytocat-0.1: LDPE and (e) phytocat-2.5: LDPE (1:10 by weight)

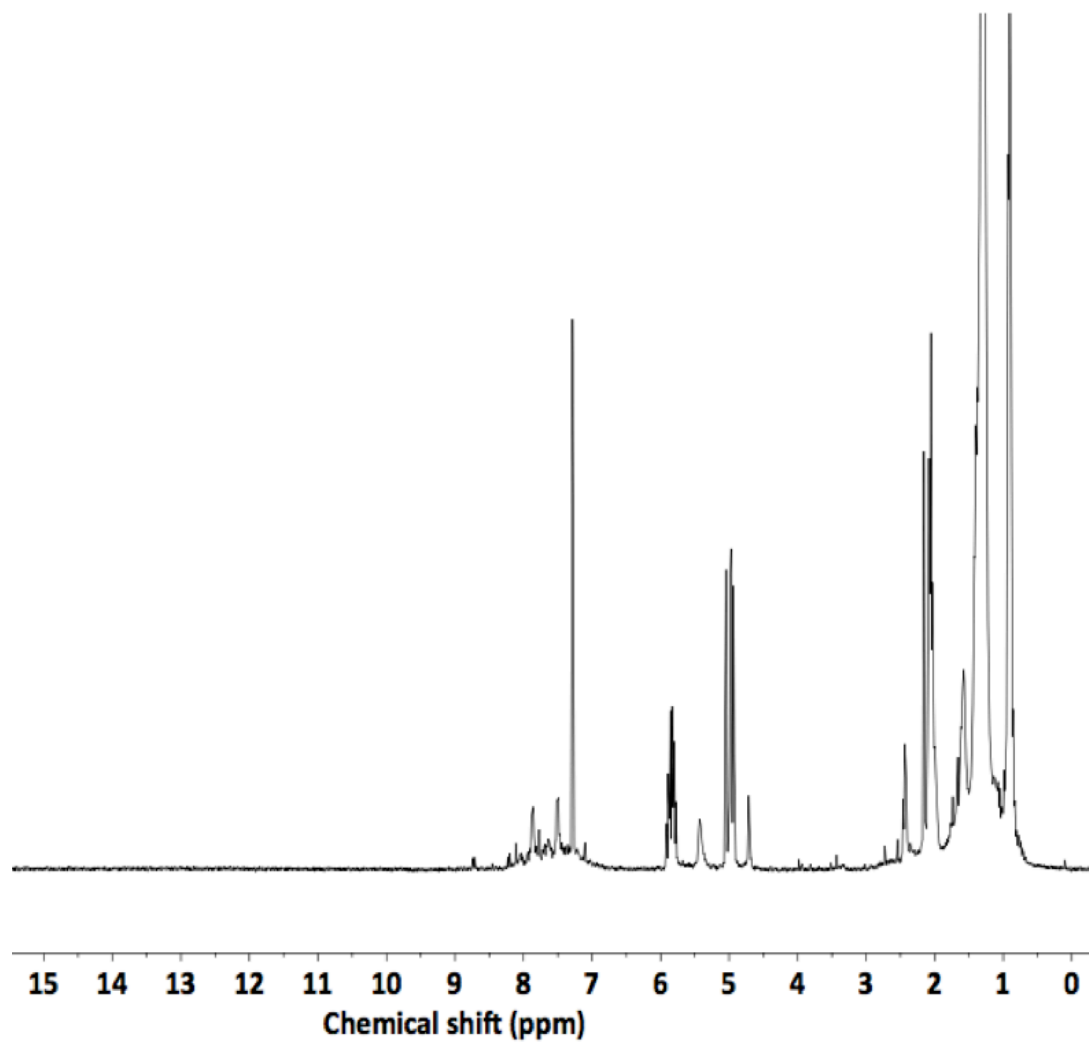


Figure C6: ^1H NMR analysis of the oil formed after microwave-assisted depolymerization of LDPE using phytocat-2.5

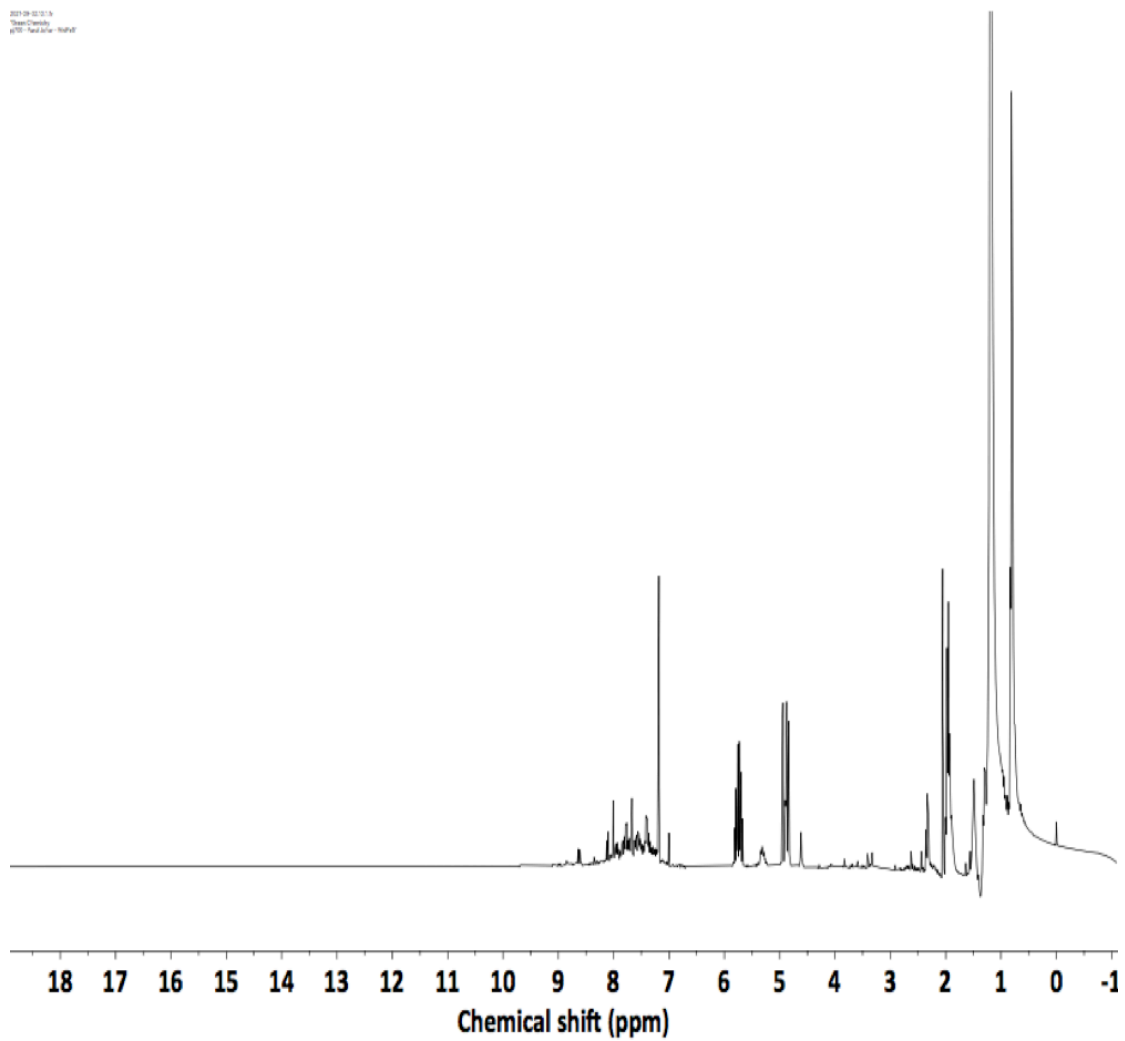


Figure C7: ^1H NMR analysis of the oil formed after microwave-assisted depolymerization of LDPE using phytocat-0.1

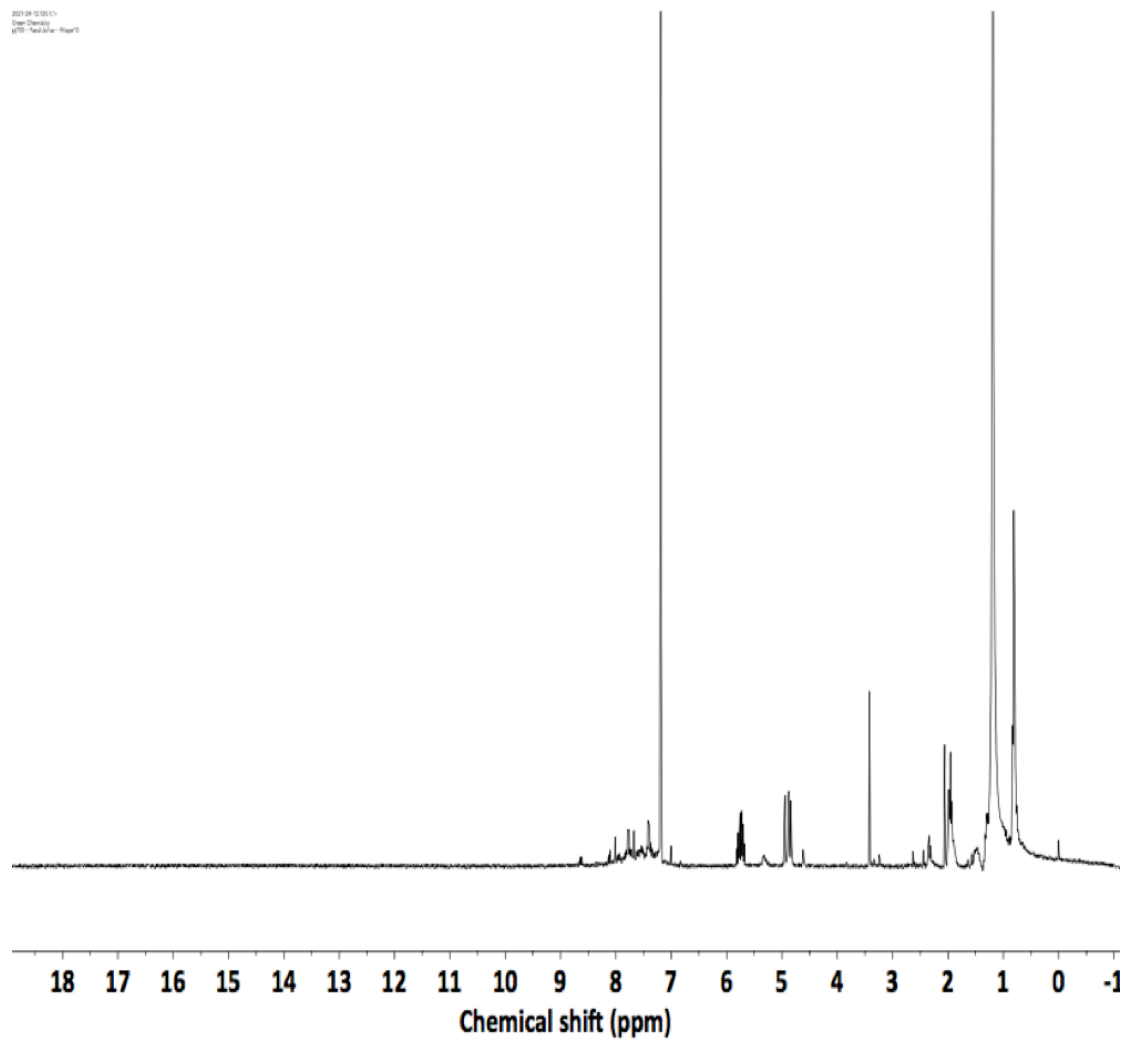


Figure C8: ^1H NMR analysis of the oil formed after microwave assisted depolymerization of LDPE using control phytocat

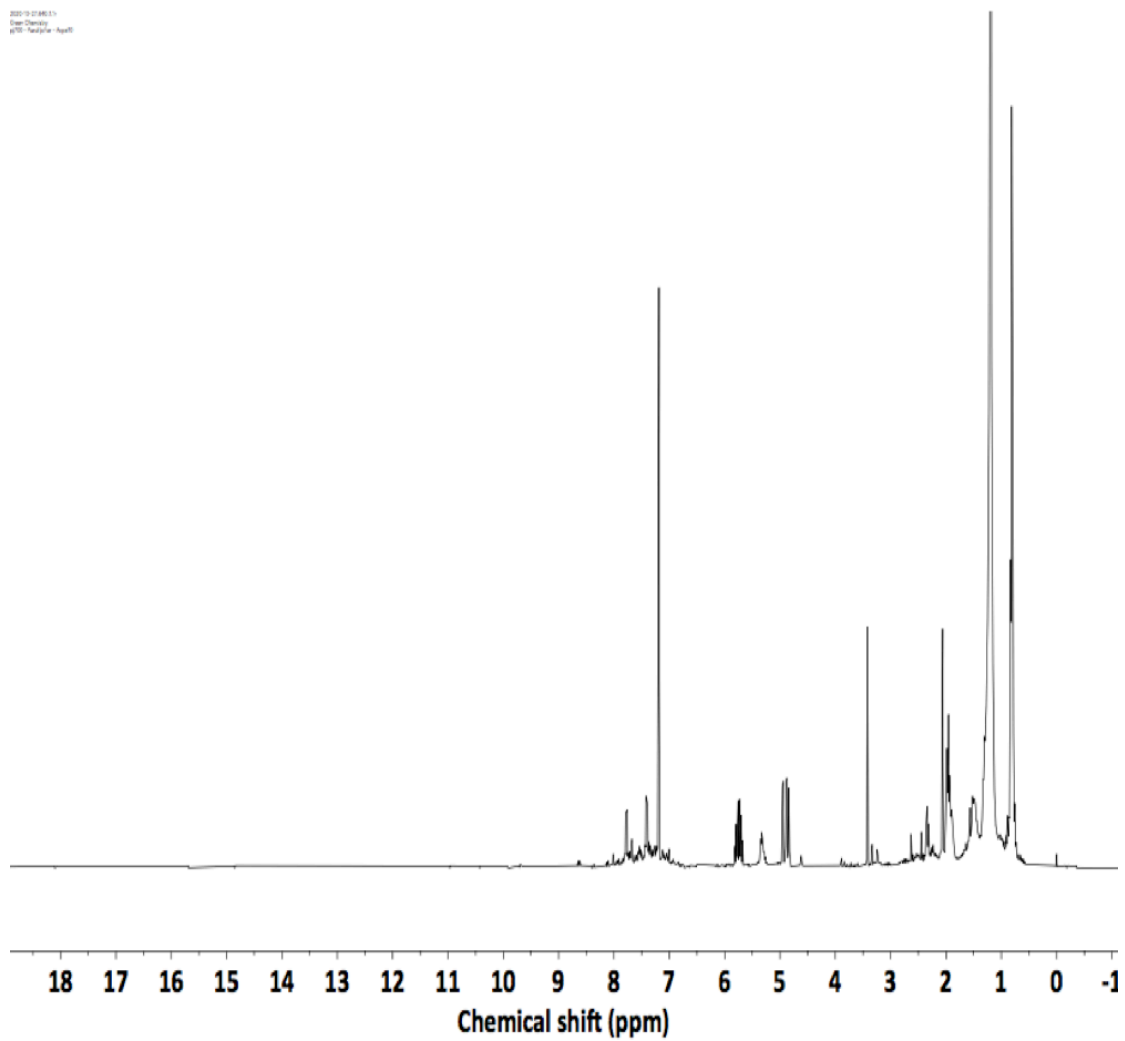


Figure C9: ¹H NMR analysis of the oil formed after microwave-assisted depolymerization of LDPE using activated carbon

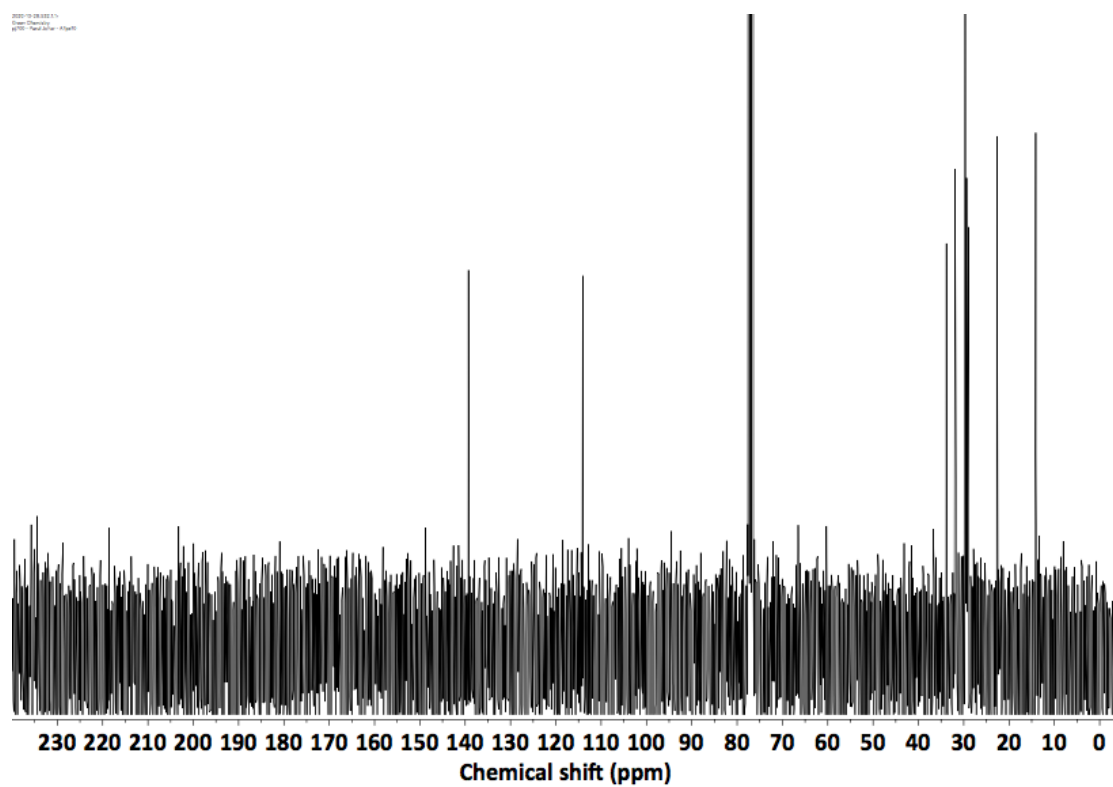


Figure C10: ^{13}C NMR spectrum of pyrolysis oil produced by microwave assisted de-polymerization of LDPE using phytocat-2.5

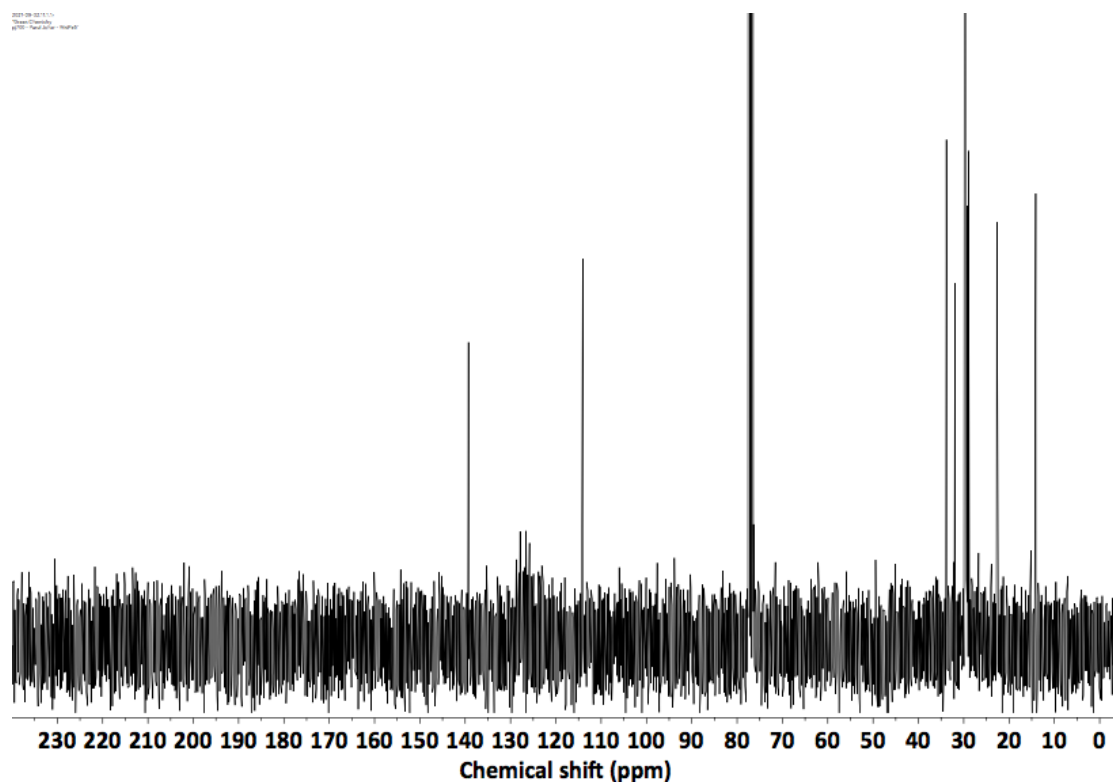


Figure C11: ^{13}C NMR spectrum of pyrolysis oil produced by microwave assisted de-polymerization of LDPE using phytocat-0.1

2025-10-27 16:11:13
Chem 7000001
2025-10-27 16:11:13

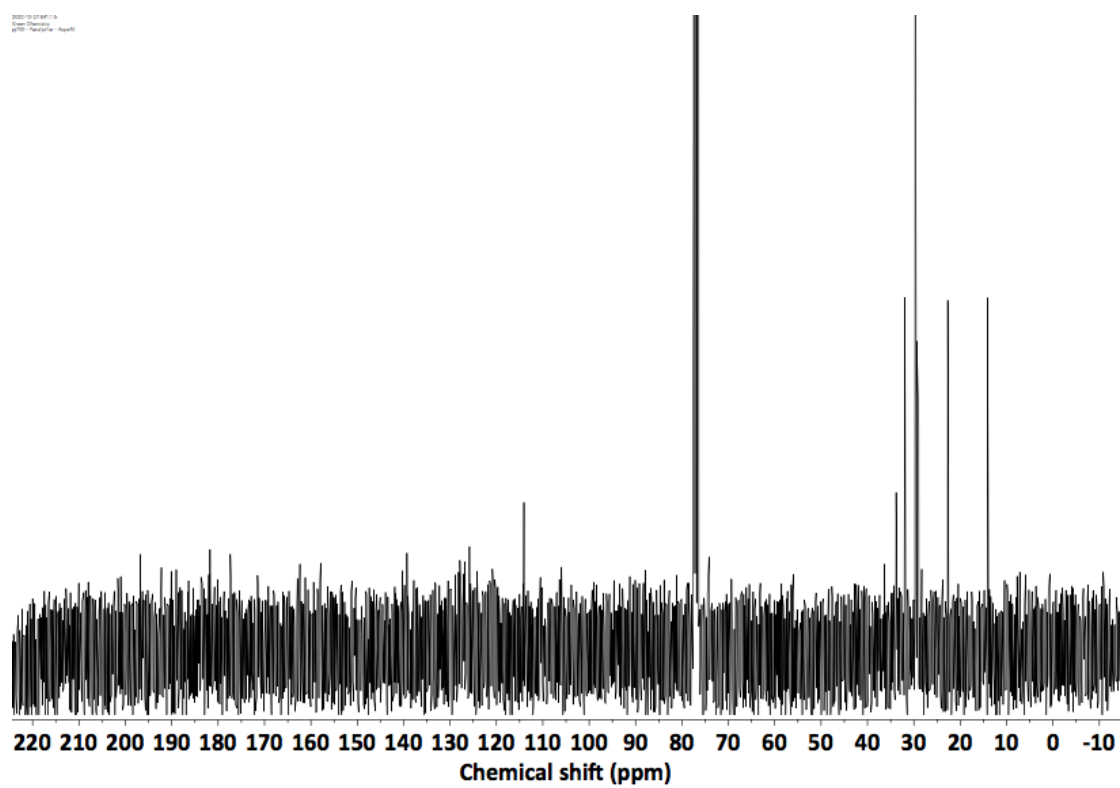


Figure C12: ¹³CNMR spectrum of pyrolysis oil produced by microwave assisted de-polymerization of LDPE using activated carbon

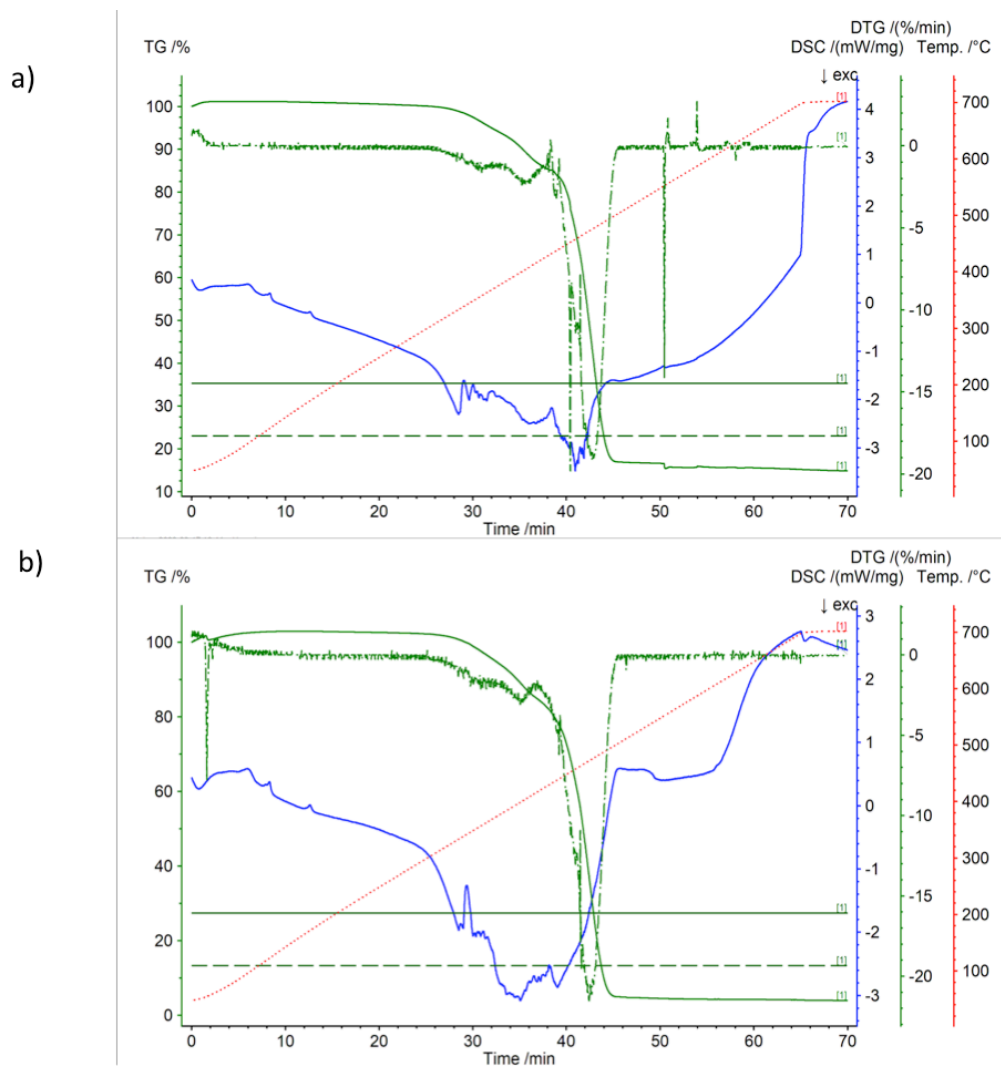


Figure C13: Conventional TGA profiles of PF (a) with phytocat-2.5 (1:10 by weight) and (b) without phytocat-2.5

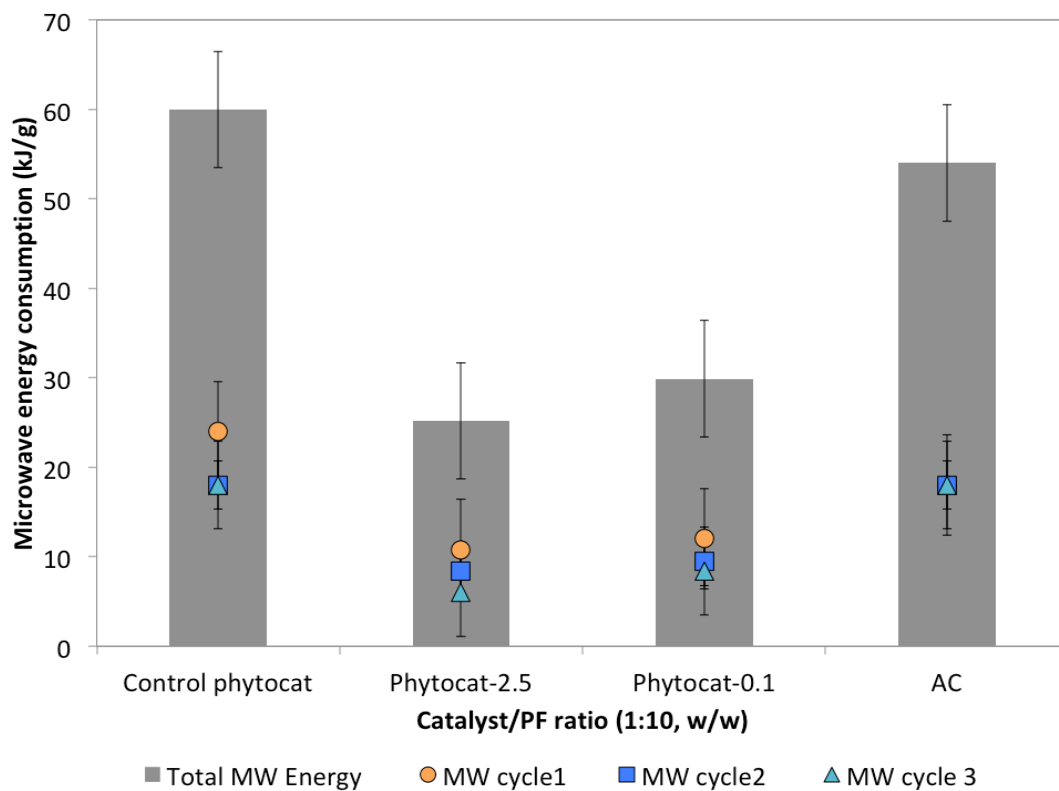


Figure C14: Microwave energy consumption for accelerated de-polymerization of PF (to reach the set point of 250°C) using various catalysts

Table C1: List of compounds identified using total ion chromatograms of pyrolysis oil of Phytocat-1.5/PS (1:10 by weight)

Compound	Peak area (%)	RT (min)
Toluene	7.66	2.94
Ethyl benzene	3.59	4.46
Phenylacetylene	1.41	4.79
Styrene	72.1	5.2
α -methyl styrene	3.95	7.33
Indene	1.35	9.00
Naphthalene	2.07	12.99
Biphenyl	1.06	18.28
Bibenzyl	0.35	21.76
Benzene 1,1'-(1,3-Propanediyl)bis-	0.86	24.84
Stilbene	1.42	26.14
Naphthalene 1,2,3,4-tetrahydro-2-phenyl	1.49	26.3
Anthracene	1.40	27.58
1-Phenylnaphthalene	0.76	29.16
2-Phenylnaphthalene	1.65	31.44
(2,3-Diphenylcyclopropyl)methyl phenyl sulfoxide, trans-	1.50	39.56

Table C2: List of compounds identified using total ion chromatograms of pyrolysis oil of control phytocat/PS (1:10 by weight)

Compound	Peak area (%)	RT (min)
Toluene	1.81	2.94
Ethylbenzene	0.76	4.46
Styrene	56.1	5.20
α -methyl styrene	3.39	7.33
Indene	5.76	9.01
Naphthalene	4.96	13.02
Biphenyl	3.36	18.30
Bibenzyl	1.68	21.76
Fluorene	2.69	23.23
Benzene, 1,1'-(1,3-propanediyl)-bis-	1.69	24.84
Stilbene	3.62	26.15
Naphthalene 1,2,3,4-tetrahydro-2-phenyl	3.19	26.31
Anthracene	5.41	27.61
1-Phenylnaphthalene	1.52	29.17
1H-Indene-1-phenyl	1.03	29.35
2-Phenylnaphthalene	3.57	31.46
(2,3-Diphenylcyclopropyl)methyl phenyl sulfoxide, trans-	3.89	39.56

Table C3: Experimental results of the microwave-assisted de-polymerization of polyethylene (Low density polyethylene, LDPE) using Phytocat-2.5 (varying catalyst: LDPE ratio by weight) at 250°C

	(1:1)	(1:2)	(1:5)	(1:10)	(1:20)
Oil yield (wt%)	31.0	43.0	54.0	60.7	54.9
Solid yield (wt%)	15.0	16.7	15.9	14.5	19.1
Gas yield (wt%)	54.0	40.3	30.1	24.8	19.5
Oil composition (% Selectivity)					
Mono-aromatics	31.9	21.2	20.1	34.2	19.2
Benzene	9.2	7.9	7.4	9.9	6.7
Toluene	15.1	9.5	9.2	16.7	7.9
Xylene	7.6	3.8	3.5	7.6	4.6
C₆-C₁₂ alkanes	11.1	9.2	7.9	9.1	2.5
Octane	2.4	1.5	0.9	2.7	0.5
1,2-dicyclopropyl ethane	1.9	1.2	0.5	1.5	0.1
Octyl-cyclopropane	1.9	1.2	0.5	0.6	0.1
Nonane	2.1	1.9	0.9	1.1	0.4
Decane	1.5	0.4	0.9	1.5	0.4
2,4-Dimethyldecane	0.9	0.2	0.5	0.4	0.5
Undecane	0.2	1.9	2.1	0.9	0.5
Dodecane	0.2	0.9	1.6	0.4	0.4
C₆-C₁₂ alkenes	29.0	27.4	25.6	32.7	16.7
Octene	7.4	6.5	4.9	9.2	3.3
Nonene	9.1	10.1	9.6	10.5	5.6
Decene	4.9	7.9	9.1	9.6	4.5
1-Tridecene	4.1	1.1	0.1	1.1	2.2

1,9-Decadiene	2.4	0.5	0.5	1.1	0.2
1,10-Undecadiene	0.2	0.5	0.1	0.5	0.2
1-Undecene	0.9	0.9	1.3	0.7	0.7
C_{>12} alkanes	2.5	9.2	15.4	4.9	14.4
Tridecane	1.5	2.1	4.5	2.4	3.7
Pentadecane	0.5	2.5	2.7	1.1	2.9
Hexadecane	0.5	4.6	8.2	1.4	7.8
C_{>12} alkenes	10.5	18.9	20.0	11.9	39.3
1,13-Tetradecadiene	5.9	6.5	6.5	4.5	2.9
1,12-Tridecadiene	1.5	2.5	5.5	2.0	6.5
1-Tridecene	1.5	3.1	2.5	1.1	5.5
Cetene	0.5	2.5	2.3	1.5	4.9
Octadecene	0.5	1.5	1.5	0.1	2.0
Eicosene	0.5	1.5	1.1	0.5	9.5
1,19-Eicosadiene	0.1	1.3	0.6	2.2	8.0
Poly-aromatics	15.0	14.1	11.0	7.2	7.9
Indene	2.5	2.4	2.5	1.5	2.0
Naphthalene	9.0	7.5	6.5	4.5	3.1
Phenanthrene	1.5	2.0	1.5	1.1	2.5
Pyrene	2.0	2.2	0.5	0.1	0.3
Microwave energy consumption (KJ/g)	36	54	24	12	44.4

Table C4: Experimental results of the microwave-assisted de-polymerization of polyethylene (Low density polyethylene, LDPE) using Phytocat-2.5 (1:10, catalyst: LDPE by weight) for 3 successive cycles (each cycle takes $t < 70$ s to reach the set-point of 250°C)

	Cycle 1	Cycle 2	Cycle 3
Oil yield (wt%)	37.0	49.6	60.7
Solid yield (wt%)	31.1	24.5	14.5
Gas yield (wt%)	31.9	25.9	24.8
Gas composition (% selectivity)			
H ₂	61.9	64.5	67.9
CH ₄	20.1	17.21	15.66
CO	0.37	0.48	0.64
CO ₂	0.14	0.14	0.32
C ₂₋₄	12.7	11.2	10.1
Total conversion (%)	68.9	75.5	85.5

Table C5: Comparison of experimental results of the microwave-assisted (250°C, up to 2 min) and conventional thermal (500°C, up to 2 h) de-polymerization of polyethylene (Low density polyethylene, LDPE) using Phytocat-2.5 (1:10, catalyst: LDPE by weight)

	Conventional	Microwave
Oil yield (wt%)	67.5	60.7
Solid yield (wt%)	12.7	14.5
Gas yield (wt%)	19.8	24.8
Oil composition (% selectivity)		
Mono-aromatics	6.5	34.2
C ₅ -C ₁₂ alkanes	2.1	9.1
C ₅ -C ₁₂ alkenes	39.3	32.7
C _{>12} alkanes	11.9	4.9
C _{>12} alkenes	8.1	11.9
Poly-aromatics	32.1	7.2
Total conversion (%)	87.3	85.5

Table C6: Experimental results of the microwave-assisted de-polymerization of low density polyethylene (LDPE) using phytocat-0.1 (1:10, catalyst: LDPE by weight) for 3 successive cycles (each cycle took $t < 70$ s to reach the set-point of 250°C)

	Cycle 1	Cycle 2	Cycle 3
Oil yield (wt%)	33.0	39.0	51.0
Solid yield (wt%)	39.0	34.9	25.9
Gas yield (wt%)	28.0	26.1	23.1
Gas composition (% selectivity)			
H ₂	55.0	46.4	59.7
CH ₄	26.0	17.21	13.3
CO	0.33	1.15	2.45
CO ₂	0.22	1.56	0.97
C ₂₋₄	15.9	14.1	9.2
Total conversion (%)	61.0	65.1	74.1

Table C7: Experimental results of the microwave-assisted de-polymerization of low density polyethylene (LDPE) using control phytocat (1:10, catalyst: LDPE by weight) for 3 successive cycles (each cycle took $t < 70$ s to reach the set-point of 250°C)

	Cycle 1	Cycle 2	Cycle 3
Oil yield (wt%)	31.0	36.5	43.9
Solid yield (wt%)	45.5	39.5	33.9
Gas yield (wt%)	23.5	24.0	22.2
Gas composition (% selectivity)			
H ₂	51.0	43.2	40.4
CH ₄	27.2	22.7	18.4
CO	0.26	0.84	1.37
CO ₂	0.20	1.68	3.1
C ₂₋₄	16.7	19.1	18.3
Total conversion (%)	54.5	60.5	66.1

Table C8: Experimental results of the microwave-assisted de-polymerization of low density polyethylene (LDPE) using activated carbon (1:10, catalyst: LDPE by weight) for 3 successive cycles (each cycle takes $t < 70$ s to reach the set-point of 250°C)

	Cycle 1	Cycle 2	Cycle 3
Oil yield (wt%)	34.0	37.0	45.5
Solid yield (wt%)	49.0	45.0	34.5
Gas yield (wt%)	17.0	18.0	20.0
Gas composition (% selectivity)			
H ₂	51.0	55.4	49.0
CH ₄	25.9	22.27	16.5
CO	0.61	0.46	1.9
CO ₂	0.26	0.14	0.91
C ₂₋₄	15.6	15.0	16.9
Total conversion (%)	51.0	55.0	65.5

Table C9: Comparison between literature reports on catalytic microwave assisted pyrolysis of plastics and this research

References	Raw material	Temperature (°C)	Catalyst to plastic ratio	Oil yield (wt.%)	Oil composition
This work	PS	250 °C	Phytocat: polymer (1:1, 1:2, 1:5, 1:10, 1:20)	47-72.5% (phytocat-1.5), 41-67 % (phytocat-0.1) 39.6-64.5% (control phytocat), 38.1-62% (activated carbon)	Up to 84% MAHs, up to 72% styrene using phytocat-1.5
This work	PE	250 °C	Phytocat: polymer (1:1, 1:2, 1:5, 1:10, 1:20)	31-61% (phytocat-2.5) 29-51% (phytocat-0.1) 33-42% (control phytocat) 34-49% (activated carbon)	Up to 97% C _{≤23} , Up to 47% aromatics (~39% MAHs), Up to 42% C _{<12} aliphatic (using phytocat-2.5)
This work	PF	250 °C	1:10	22-55% (phytocat-2.5) 18-45% (phytocat-0.1) 18-41% (control phytocat)	Up to 90% C _{≤23} , Up to 30% aromatics (~24% MAHs), Up to 30% C _{<12} aliphatic

References	Raw material	Temperature (°C)	Catalyst to plastic ratio	Oil yield (wt.%)	Oil composition
				18-43% (activated carbon)	(using phytocat-2.5)
152	PS	450-500 °C	Coconut sheath carbon 1:10	86.1%	Styrene (67%)
241	HDPE	400–600 °C	Activated carbon, ratio not given	27.3–54.9%	>90% for C ≤ 21, ~45–58% aliphatic; ~35–45% aromatics
157	HDPE	Not given	Tire/Carbon: plastic = ~1:3–2:1	43.9–83.9%	38.73–88.37% aliphatics; only 6.61–17.31% aromatics
252	LDPE	480 °C	ZSM-5: plastic = 1 :4.68–1:1.32	24.44–32.58 wt%	>94% aromatics; 74.73–88.49% C ₈ -C ₁₂ MAHs
253	LDPE	375 °C	ZSM-5: plastic = 1 :10	64.41 ± 5.20 wt %	97% C ₈ -C ₁₆ aromatics
235	LDPE	350–550 °C	MgO: plastic = 1	24.2–38.5 wt%	79.5–96.0% gasoline

References	Raw material	Temperature (°C)	Catalyst to plastic ratio	Oil yield (wt.%)	Oil composition
				:15–1:3	fraction; ~15–50% MAHs
185	LDPE	450–600 °C	NiO: HY: plastic = (1–5):15:150	48.08–51.23 wt%	>92% C ₅ -C ₁₂ gasoline fraction; 34.56–46.61% aromatics; 25.99–30.00% isomerized aliphatics

References

- 1 L. J. Sonter, M. C. Dade, J. E. M. Watson and R. K. Valenta, *Nat. Commun.*, 2020, **11**, 4174.
- 2 É. Lèbre, M. Stringer, K. Svobodova, J. R. Owen, D. Kemp, C. Côte, A. Arratia-Solar and R. K. Valenta, *Nat. Commun.*, 2020, **11**, 4823.
- 3 S. M. Jowitt, G. M. Mudd and J. F. H. Thompson, *Commun. Earth Environ.*, 2020, **1**, 13.
- 4 T. E. Graedel, E. M. Harper, N. T. Nassar, P. Nuss and B. K. Reck, *Proc. Natl. Acad. Sci.*, 2015, **112**, 4257–4262.
- 5 N. R. Council, *Natl. Acad. Sci. United States*.
- 6 C. W. Babbitt, S. Althaf, F. Cruz Rios, M. M. Bilec and T. E. Graedel, *One Earth*, 2021, **4**, 353–362.
- 7 T. E. Graedel, B. K. Reck and A. Miatto, *Nat. Commun.*, 2022, **13**, 150.
- 8 N. N. T., G. T. E. and H. E. M., *Sci. Adv.*, 2022, **1**, e1400180.
- 9 T. Watari, K. Nansai and K. Nakajima, *Resour. Conserv. Recycl.*, 2020, **155**, 104669.
- 10 A. J. Bebbington, D. H. Bebbington, L. A. Sauls, J. Rogan, S. Agrawal, C. Gamboa, A. Imhof, K. Johnson, H. Rosa and A. Royo, *Proc. Natl. Acad. Sci.*, 2018, **115**, 13164–13173.
- 11 S. Luckeneder, S. Giljum, A. Schaffartzik, V. Maus and M. Tost, *Glob. Environ. Chang.*, 2021, **69**, 102303.
- 12 P. N. Nkrumah, G. Echevarria, P. D. Erskine and A. van der Ent, *Sci. Total Environ.*, 2022, **827**, 154092.
- 13 K. Nakajima, K. Nansai, K. Matsubae, M. Tomita, W. Takayanagi and T. Nagasaka, *Sci. Total Environ.*, 2017, **586**, 730–737.
- 14 M. Azadi, S. A. Northey, S. H. Ali and M. Edraki, *Nat. Geosci.*, 2020, **13**, 100–104.
- 15 G. M. Mudd, *Ore Geol. Rev.*, 2010, **38**, 9–26.
- 16 M. Pascal, B. Deforges, H. Leguyader and D. Simberloff, *Conserv. Biol.*, 2008, **22**, 498–499.
- 17 T. Jaffré, J. Munzinger and P. P. Lowry, *Biodivers. Conserv.*, 2010, **19**, 1485–1502.

- 18 K. Nakajima, S. Noda, K. Nansai, K. Matsubae, W. Takayanagi and M. Tomita, *Environ. Sci. Technol.*, 2019, **53**, 1555–1563.
- 19 *Mineral commodity summaries 2020*, Reston, VA, 2020.
- 20 C. S. Simons, *Extr. Metall. Nickel Cobalt*, 1988, 91–134.
- 21 A. Elshkaki, B. K. Reck and T. E. Graedel, *Resour. Conserv. Recycl.*, 2017, **125**, 300–307.
- 22 G. Tóth, T. Hermann, M. R. Da Silva and L. Montanarella, *Environ. Int.*, 2016, **88**, 299–309.
- 23 M. G. Siebecker, R. L. Chaney and D. L. Sparks, *Geochem. Trans.*, 2018, **19**, 14.
- 24 S. B. K., A. S. H., B. Morgan, R. Ben, N. Benoit, O. Julia and M. Dustin, *Science (80-.)*, 2020, **367**, 30–33.
- 25 D. Hou, D. O’Connor, A. D. Igalavithana, D. S. Alessi, J. Luo, D. C. W. Tsang, D. L. Sparks, Y. Yamauchi, J. Rinklebe and Y. S. Ok, *Nat. Rev. Earth Environ.*, 2020, **1**, 366–381.
- 26 V. Maus, S. Giljum, J. Gutschlhofer, D. M. da Silva, M. Probst, S. L. B. Gass, S. Luckeneder, M. Lieber and I. McCallum, *Sci. Data*, 2020, **7**, 289.
- 27 A. M. Abioye and F. N. Ani, *Renew. Sustain. energy Rev.*, 2015, **52**, 1282–1293.
- 28 R. L. Chaney, A. J. M. Baker and J. L. Morel, in *Agromining: farming for metals*, Springer, 2021, pp. 1–22.
- 29 A. L. D. Paul, S. Isnard, F. Q. Brearley, G. Echevarria, A. J. M. Baker, P. D. Erskine and A. van der Ent, *For. Ecol. Manage.*, 2022, **509**, 120049.
- 30 A. van der Ent, A. J. M. Baker, R. D. Reeves, R. L. Chaney, C. W. N. Anderson, J. A. Meech, P. D. Erskine, M.-O. Simonnot, J. Vaughan and J. L. Morel, 2015.
- 31 P. Merrot, F. Juillot, L. Flipo, M. Tharaud, E. Viollier, V. Noël, P. Le Pape, J.-M. Fernandez, B. Moreton and G. Morin, *Chemosphere*, 2022, 134643.
- 32 L. Van der Pas and R. A. Ingle, *Plants*, 2019, **8**, 11.
- 33 R. D. REEVES, A. J. M. BAKER, A. BORHIDI and R. BERAZAÍN, *New Phytol.*, 1996, **133**, 217–224.
- 34 J. T., B. R. R., L. J. and R. R. D., *Science (80-.)*, 1976, **193**, 579–580.
- 35 A. van der Ent and D. Mulligan, *J. Chem. Ecol.*, 2015, **41**, 396–408.
- 36 C. Minguzzi and O. Vergnano, *Attidella Soc. Toscana di Sci. Nat. Ser. A*, 1948,

- 55, 1–28.
- 37 S. Clemens, M. G. Palmgren and U. Krämer, *Trends Plant Sci.*, 2002, **7**, 309–315.
- 38 T.-H.-B. Deng, A. van der Ent, Y.-T. Tang, T. Sterckeman, G. Echevarria, J.-L. Morel and R.-L. Qiu, *Plant Soil*, 2018, **423**, 1–11.
- 39 A. van der Ent, D. L. Callahan, B. N. Noller, J. Mesjasz-Przybylowicz, W. J. Przybylowicz, A. Barnabas and H. H. Harris, *Sci. Rep.*, 2017, **7**, 41861.
- 40 E. Montargès-Pelletier, V. Chardot, G. Echevarria, L. J. Michot, A. Bauer and J.-L. Morel, *Phytochemistry*, 2008, **69**, 1695–1709.
- 41 T. Centofanti, M. G. Siebecker, R. L. Chaney, A. P. Davis and D. L. Sparks, *Plant Soil*, 2012, **359**, 71–83.
- 42 T. Jaffré, Y. Pillon, S. Thomine and S. Merlot, *Front. Plant Sci.*, 2013, **4**, 279.
- 43 L. Wang, D. Hou, Z. Shen, J. Zhu, X. Jia, Y. S. Ok, F. M. G. Tack and J. Rinklebe, *Crit. Rev. Environ. Sci. Technol.*, 2020, **50**, 2724–2774.
- 44 J. Luo, S. Qi, X. W. S. Gu, J. Wang and X. Xie, *J. Clean. Prod.*, 2016, **119**, 25–31.
- 45 D. Tózsér, S. Harangi, E. Baranyai, G. Lakatos, Z. Fülöp, B. Tóthmérész and E. Simon, *Environ. Sci. Pollut. Res.*, 2018, **25**, 3275–3290.
- 46 B.-H. Cheng, B.-C. Huang, R. Zhang, Y.-L. Chen, S.-F. Jiang, Y. Lu, X.-S. Zhang, H. Jiang and H.-Q. Yu, *Sci. Adv.*, , DOI:10.1126/sciadv.aay0748.
- 47 R. A. J., W. C. K., D. B. H., B. George, C. John, E. C. A., F. W. J., H. J. P., L. D. J., L. C. L., M. J. R., M. Richard, T. Richard and T. Timothy, *Science (80-)*, 2006, **311**, 484–489.
- 48 C. J. M., C. A. M. and G. Ramon, *Science (80-)*, 2017, **355**, aag0804.
- 49 R. P. Lopes and D. Astruc, *Coord. Chem. Rev.*, 2021, **426**, 213585.
- 50 J. Grams, *J. Anal. Appl. Pyrolysis*, 2022, **161**, 105429.
- 51 M.-M. Titirici, M. Antonietti and N. Baccile, *Green Chem.*, 2008, **10**, 1204–1212.
- 52 F. Cheng, V. Dupont and M. V. Twigg, *Appl. Catal. B Environ.*, 2017, **200**, 121–132.
- 53 Z.-L. Yu, N. Yang, L.-C. Zhou, Z.-Y. Ma, Y.-B. Zhu, Y.-Y. Lu, B. Qin, W.-Y. Xing, T. Ma, S.-C. Li, H.-L. Gao, H.-A. Wu and S.-H. Yu, *Sci. Adv.*, 2018, **4**, eaat7223.
- 54 A. Kirui, W. Zhao, F. Deligey, H. Yang, X. Kang, F. Mentink-Vigier and T.

- Wang, *Nat. Commun.*, 2022, **13**, 538.
- 55 Y. Jing, Y. Guo, Q. Xia, X. Liu and Y. Wang, *Chem*, 2019, **5**, 2520–2546.
- 56 M. Talebi Amiri, G. R. Dick, Y. M. Questell-Santiago and J. S. Luterbacher, *Nat. Protoc.*, 2019, **14**, 921–954.
- 57 C. Chen, J. Song, S. Zhu, Y. Li, Y. Kuang, J. Wan, D. Kirsch, L. Xu, Y. Wang, T. Gao, Y. Wang, H. Huang, W. Gan, A. Gong, T. Li, J. Xie and L. Hu, *Chem*, 2018, **4**, 544–554.
- 58 L. Yuhe, K. Steven-Friso, V. den B. Gil, V. A. Joost, V. den B. Sander, R. Tom, N. Kranti, N. Thomas, V. A. Korneel, M. Maarten, M. Hironori, T. J. M., V. A. Karel, L. Bert, V. Danny and S. B. F., *Science (80-.)*, 2020, **367**, 1385–1390.
- 59 Z. Tao, *Science (80-.)*, 2020, **367**, 1305–1306.
- 60 H. M. E., D. Shi-You, J. D. K., A. W. S., N. M. R., B. J. W. and F. T. D., *Science (80-.)*, 2007, **315**, 804–807.
- 61 P. Pallinti, H. Ruoya and Z. Jochen, *Science (80-.)*, 2020, **369**, 1089–1094.
- 62 R. A. J., B. G. T., B. M. J., C. Richard, C. Fang, D. M. F., D. B. H., D. R. A., G. Paul, K. Martin, L. Paul, N. A. K., S. J. N., T. T. J., T. G. A. and W. C. E., *Science (80-.)*, 2014, **344**, 1246843.
- 63 S. Sadjadi, M. Akbari, B. Léger, E. Monflier and M. M. Heravi, *ACS Sustain. Chem. Eng.*, 2019, **7**, 6720–6731.
- 64 X. Lu, J. He, R. Jing, P. Tao, R. Nie, D. Zhou and Q. Xia, *Sci. Rep.*, 2017, **7**, 2676.
- 65 L. Ceatra, O. C. Pârvulescu, I. Rodríguez Ramos and T. Dobre, *Ind. Eng. Chem. Res.*, 2016, **55**, 1491–1502.
- 66 S. Gryglewicz, A. Śliwak, J. Ćwikła and G. Gryglewicz, *Catal. Letters*, 2014, **144**, 62–69.
- 67 R. Bardestani, R. Biriaei and S. Kaliaguine, *Catalysts*, 2020, **10**, 934.
- 68 Y. Niu, X. Huang, Y. Wang, M. Xu, J. Chen, S. Xu, M.-G. Willinger, W. Zhang, M. Wei and B. Zhang, *Nat. Commun.*, 2020, **11**, 3324.
- 69 R. W. Coughlin, *Ind. Eng. Chem. Prod. Res. Dev.*, 1969, **8**, 12–23.
- 70 J. Wang, J. Kim, S. Choi, H. Wang and J. Lim, *Small Methods*, 2020, **4**, 2000621.
- 71 M. Sevilla and R. Mokaya, *Energy Environ. Sci.*, 2014, **7**, 1250–1280.
- 72 X. Liu, J. Liu, Y. Yang, Y.-W. Li and X. Wen, *ACS Catal.*, 2021, **11**, 2156–

- 2181.
- 73 E. Auer, A. Freund, J. Pietsch and T. Tacke, *Appl. Catal. A Gen.*, 1998, **173**, 259–271.
- 74 V. Arunajatesan, B. Chen, K. Möbus, D. J. Ostgard, T. Tacke and D. Wolf, 2008.
- 75 I. C. Gerber and P. Serp, *Chem. Rev.*, 2020, **120**, 1250–1349.
- 76 F. J. Derbyshire, V. H. J. De Beer, G. M. K. Abotsi, A. W. Scaroni, J. M. Solar and D. J. Skrovanek, *Appl. Catal.*, 1986, **27**, 117–131.
- 77 C. Prado-Burguete, A. Linares-Solano, F. Rodriguez-Reinoso and C. S.-M. De Lecea, *J. Catal.*, 1989, **115**, 98–106.
- 78 H. Jüntgen, *Fuel*, 1986, **65**, 1436–1446.
- 79 D. S. Park, D. Yun, T. Y. Kim, J. Baek, Y. S. Yun and J. Yi, *ChemSusChem*, 2013, **6**, 2281–2289.
- 80 A. Y. Stakheev and L. M. Kustov, *Appl. Catal. A Gen.*, 1999, **188**, 3–35.
- 81 R. Gutzler, S. Stepanow, D. Grumelli, M. Lingenfelder and K. Kern, *Acc. Chem. Res.*, 2015, **48**, 2132–2139.
- 82 G. Wan, G. Zhang and X.-M. Lin, *Adv. Mater.*, 2020, **32**, 1905548.
- 83 C. S. Diercks, Y. Liu, K. E. Cordova and O. M. Yaghi, *Nat. Mater.*, 2018, **17**, 301–307.
- 84 X. Cui, W. Li, P. Ryabchuk, K. Junge and M. Beller, *Nat. Catal.*, 2018, **1**, 385–397.
- 85 P. McKeown, M. Kamran, M. G. Davidson, M. D. Jones, L. A. Román-Ramírez and J. Wood, *Green Chem.*, 2020, **22**, 3721–3726.
- 86 B. H. Lipshutz, *Adv. Synth. Catal.*, 2001, **343**, 313–326.
- 87 Y. Xue, P. Johnston and X. Bai, *Energy Convers. Manag.*, 2017, **142**, 441–451.
- 88 W. Buss, C. Wurzer, D. A. C. Manning, E. J. Rohling, J. Borevitz and O. Mašek, *Commun. Earth Environ.*, 2022, **3**, 67.
- 89 L. Zhang, Y. Tan, D. Cai, J. Sun, Y. Zhang, L. Li, Q. Zhang, G. Zou, Z. Song and Y. Bai, *Energy*, 2022, **249**, 123667.
- 90 M. D. Adsuar-García, J. X. Flores-Lasluisa, F. Z. Azar and M. C. Román-Martínez, *Catalysts*, 2018, **8**, 572.
- 91 K. Hu, T. Ohto, Y. Nagata, M. Wakisaka, Y. Aoki, J. Fujita and Y. Ito, *Nat. Commun.*, 2021, **12**, 203.
- 92 P. K. W. Likun, H. Zhang and Y. Fan, *Chinese J. Chem. Eng.*, 2022, **42**, 196–

- 209.
- 93 Z. Yao, X. Ma and Z. Xiao, *Renew. Energy*, 2020, **151**, 514–527.
- 94 S. Gupta, P. Patel and P. Mondal, *ACS Sustain. Chem. Eng.*, 2022, **10**, 5770–5780.
- 95 J. Sun, W. Wang, Q. Yue, C. Ma, J. Zhang, X. Zhao and Z. Song, *Appl. Energy*, 2016, **175**, 141–157.
- 96 D. Voiry, J. Yang, J. Kupferberg, R. Fullon, C. Lee, H. Y. Jeong, H. S. Shin and M. Chhowalla, *Science (80-.)*, 2016, **353**, 1413–1416.
- 97 D.-H. Kang, W. B. Han, H. Il Ryu, N. H. Kim, T. Y. Kim, N. Choi, J. Y. Kang, Y. G. Yu and T. S. Kim, *Nat. Commun.*, 2022, **13**, 1261.
- 98 A. K. Mohanty, S. Vivekanandhan, J.-M. Pin and M. Misra, *Science (80-.)*, 2018, **362**, 536–542.
- 99 Z. Chen, X. Zeng, S. Wang, A. Cheng and Y. Zhang, *ChemSusChem*, 2022, **15**, e202200411.
- 100 R. Paul, C. Sarkar, Y. Yan, Q. T. Trinh, B. S. Rao, C.-W. Pao, J.-F. Lee, W. Liu and J. Mondal, *ChemCatChem*, 2020, **12**, 3687–3704.
- 101 G. T. M. Kadja, M. M. Ilmi, N. J. Azhari, M. Khalil, A. T. N. Fajar, Subagjo, I. G. B. N. Makertihartha, M. L. Gunawan, C. B. Rasrendra and I. G. Wenten, *J. Mater. Res. Technol.*, 2022, **17**, 3277–3336.
- 102 F.-F. Wang, R. Guo, C. Jian, W. Zhang, R. Xue, D.-L. Chen, F. Zhang and W. Zhu, *Inorg. Chem.*, 2022, **61**, 9138–9146.
- 103 J. Mazarío, M. P. Romero, P. Concepción, M. Chávez-Sifontes, R. A. Spanevello, M. B. Comba, A. G. Suárez and M. E. Domine, *Green Chem.*, 2019, **21**, 4769–4785.
- 104 H. Xin, W. Zhang, X. Xiao, L. Chen, P. Wu and X. Li, *J. Catal.*, 2021, **393**, 126–139.
- 105 L. Zhang, M. Zhou, A. Wang and T. Zhang, *Chem. Rev.*, 2020, **120**, 683–733.
- 106 X. Wang, X. Liang, P. Geng and Q. Li, *ACS Catal.*, 2020, **10**, 2395–2412.
- 107 M. G. Prakash, R. Mahalakshmy, K. R. Krishnamurthy and B. Viswanathan, *Catal. Today*, 2016, **263**, 105–111.
- 108 D. Verma, R. Insyani, H. S. Cahyadi, J. Park, S. M. Kim, J. M. Cho, J. W. Bae and J. Kim, *Green Chem.*, 2018, **20**, 3253–3270.
- 109 X. Huang, T. Liu, J. Wang, F. Wei, J. Ran and S. Kudo, *J. Energy Inst.*, 2020, **93**, 2505–2510.

- 110 P. Sabatier, *La catalyse en chimie organique*, 1920.
- 111 A. J. Medford, A. Vojvodic, J. S. Hummelshøj, J. Voss, F. Abild-Pedersen, F. Studt, T. Bligaard, A. Nilsson and J. K. Nørskov, *J. Catal.*, 2015, **328**, 36–42.
- 112 P. Gallezot and D. Richard, *Catal. Rev.*, 1998, **40**, 81–126.
- 113 M. G. Prakash, R. Mahalakshmy, K. R. Krishnamurthy and B. Viswanathan, *Catal. Sci. Technol.*, 2015, **5**, 3313–3321.
- 114 L. J. Malobela, J. Heveling, W. G. Augustyn and L. M. Cele, *Ind. Eng. Chem. Res.*, 2014, **53**, 13910–13919.
- 115 W. S. Putro, T. Hara, N. Ichikuni and S. Shimazu, *Chem. Lett.*, 2017, **46**, 149–151.
- 116 G. Vilé, D. Albani, N. Almora-Barrios, N. López and J. Pérez-Ramírez, *ChemCatChem*, 2016, **8**, 21–33.
- 117 F. Delbecq and P. Sautet, *J. Catal.*, 1995, **152**, 217–236.
- 118 G. Gómez Millán, S. Hellsten, J. Llorca, R. Luque, H. Sixta and A. M. Balu, *ChemCatChem*, 2019, **11**, 2022–2042.
- 119 J. Park, U. Mushtaq, J. R. Sugiarto, D. Verma and J. Kim, *Appl. Catal. B Environ.*, 2022, **310**, 121280.
- 120 S. H. Krishna, D. J. McClelland, Q. A. Rashke, J. A. Dumesic and G. W. Huber, *Green Chem.*, 2017, **19**, 1278–1285.
- 121 J. Sherwood, M. De bruyn, A. Constantinou, L. Moity, C. R. McElroy, T. J. Farmer, T. Duncan, W. Raverty, A. J. Hunt and J. H. Clark, *Chem. Commun.*, 2014, **50**, 9650–9652.
- 122 R. Geyer, J. R. Jambeck and K. L. Law, *Sci. Adv.*, 2022, **3**, e1700782.
- 123 M. Raoul, K. Arne, B. Marvin, W. Benedikt, Z. Christian, S. Sangwon and B. André, *Science (80-.)*, 2021, **374**, 71–76.
- 124 B. S. B., R. Jeremy, L. K. Lavender, M. C. C., L. Laurent, M. Alexis, M. Erin, J. Jenna, L. G. H., H. M. A., E. Marcus, P. H. P., D. F. Hannah, G. L. R., P. Beth, T. Akbar, B. Miranda, M. Nicholas, B. Megan and R. C. M., *Science (80-.)*, 2020, **369**, 1515–1518.
- 125 X. Zhao, B. Boruah, K. F. Chin, M. Đokić, J. M. Modak and H. Sen Soo, *Adv. Mater.*, 2021, **n/a**, 2100843.
- 126 J. Huang, A. Veksha, W. P. Chan, A. Giannis and G. Lisak, *Renew. Sustain. Energy Rev.*, 2022, **154**, 111866.
- 127 C. Jehanno, J. W. Alty, M. Roosen, S. De Meester, A. P. Dove, E. Y.-X. Chen,

- F. A. Leibfarth and H. Sardon, *Nature*, 2022, **603**, 803–814.
- 128 I. Vollmer, M. J. F. Jenks, M. C. P. Roelands, R. J. White, T. van Harmelen, P. de Wild, G. P. van Der Laan, F. Meirer, J. T. F. Keurentjes and B. M. Weckhuysen, *Angew. Chemie Int. Ed.*, 2020, **59**, 15402–15423.
- 129 M. Chu, Y. Liu, X. Lou, Q. Zhang and J. Chen, *ACS Catal.*, 2022, 4659–4679.
- 130 O. Dogu, M. Pelucchi, R. Van de Vijver, P. H. M. Van Steenberge, D. R. D’hooge, A. Cuoci, M. Mehl, A. Frassoldati, T. Faravelli and K. M. Van Geem, *Prog. Energy Combust. Sci.*, 2021, **84**, 100901.
- 131 L. S. Lens-Pechakova, *Adv. Ind. Eng. Polym. Res.*, 2021, **4**, 151–158.
- 132 K. Hu, Y. Yang, Y. Wang, X. Duan and S. Wang, *Chem Catal.*, , DOI:https://doi.org/10.1016/j.checat.2022.02.003.
- 133 J.-G. Rosenboom, R. Langer and G. Traverso, *Nat. Rev. Mater.*, , DOI:10.1038/s41578-021-00407-8.
- 134 B. Zhu, D. Wang and N. Wei, *Trends Biotechnol.*, 2022, **40**, 22–37.
- 135 H. Inderthal, S. L. Tai and S. T. L. Harrison, *Trends Biotechnol.*, 2021, **39**, 12–23.
- 136 R. J. Wright, G. Erni-Cassola, V. Zadjelovic, M. Latva and J. A. Christie-Oleza, *Environ. Sci. Technol.*, 2020, **54**, 11657–11672.
- 137 C. W. S. Yeung, J. Y. Q. Teo, X. J. Loh and J. Y. C. Lim, *ACS Mater. Lett.*, 2021, **3**, 1660–1676.
- 138 E. Yakushev, A. Gebruk, A. Osadchiev, S. Pakhomova, A. Lusher, A. Berezina, B. van Bavel, E. Vorozheikina, D. Chernykh, G. Kolbasova, I. Razgon and I. Semiletov, *Commun. Earth Environ.*, 2021, **2**, 23.
- 139 V. Fauvelle, M. Garel, C. Tamburini, D. Nerini, J. Castro-Jiménez, N. Schmidt, A. Paluselli, A. Fahs, L. Papillon, A. M. Booth and R. Sempéré, *Nat. Commun.*, 2021, **12**, 4426.
- 140 L. Lebreton and A. Andrady, *Palgrave Commun.*, 2019, **5**, 6.
- 141 A. Cózar, F. Echevarría, J. I. González-Gordillo, X. Irigoien, B. Úbeda, S. Hernández-León, Á. T. Palma, S. Navarro, J. García-de-Lomas and A. Ruiz, *Proc. Natl. Acad. Sci.*, 2014, **111**, 10239–10244.
- 142 J. R. Jambeck, R. Geyer, C. Wilcox, T. R. Siegler, M. Perryman, A. Andrady, R. Narayan and K. L. Law, *Science (80-.)*, 2015, **347**, 768–771.
- 143 K. Amamiya, K. Saido, S.-Y. Chung, T. Hiaki, D. S. Lee and B. G. Kwon, *Sci. Total Environ.*, 2019, **667**, 57–63.

- 144 H. Kimukai, K. Koizumi, H. Taguchi, A. Okabe, K. Takatama, S. Y. Chung, B. G. Kwon, M. Nishimura, S. Mentese and K. Saido, *ACS ES&T Water*.
- 145 B. C. Vance, P. A. Kots, C. Wang, Z. R. Hinton, C. M. Quinn, T. H. Epps, L. T. J. Korley and D. G. Vlachos, *Appl. Catal. B Environ.*, 2021, **299**, 120483.
- 146 C. DelRe, Y. Jiang, P. Kang, J. Kwon, A. Hall, I. Jayapurna, Z. Ruan, L. Ma, K. Zolkin, T. Li, C. D. Scown, R. O. Ritchie, T. P. Russell and T. Xu, *Nature*, 2021, **592**, 558–563.
- 147 C. Wang, H. Han, Y. Wu and D. Astruc, *Coord. Chem. Rev.*, 2022, **458**, 214422.
- 148 B. Whajah, N. da Silva Moura, J. Blanchard, S. Wicker, K. Gandar, J. A. Dorman and K. M. Dooley, *Ind. Eng. Chem. Res.*, 2021, **60**, 15141–15150.
- 149 A. Zayoud, H. D. Thi, M. Kusenberg, A. Eschenbacher, U. Kresovic, N. Alderweireldt, M. Djokic and K. M. Van Geem, *Waste Manag.*, 2022, **139**, 85–95.
- 150 U.-S. Amjad, A. Tajjamal, A. Ul-Hamid, A. Faisal, S. A. H. Zaidi, L. Sherin, A. Mir, M. Mustafa, N. Ahmad, M. Hussain and Y.-K. Park, *Waste Manag.*, 2022, **141**, 240–250.
- 151 L. Dai, N. Zhou, H. Li, Y. Wang, Y. Liu, K. Cobb, Y. Cheng, H. Lei, P. Chen and R. Ruan, *Sci. Total Environ.*, 2021, **771**, 144995.
- 152 P. Rex, I. P. Masilamani and L. R. Miranda, *J. Energy Inst.*, 2020, **93**, 1819–1832.
- 153 J. Jiang, K. Shi, X. Zhang, K. Yu, H. Zhang, J. He, Y. Ju and J. Liu, *J. Environ. Chem. Eng.*, 2022, **10**, 106867.
- 154 S. N., *Sci. Total Environ.*, 2022, **809**, 151160.
- 155 S. Madorsky and S. Straus, *J. Res. Natl. Bur. Stand. (1934)*, 1948, **40**, 417–425.
- 156 Y. S. Kim, G. C. Hwang, S. Y. Bae, S. C. Yi, S. K. Moon and H. Kumazawa, *Korean J. Chem. Eng.*, 1999, **16**, 161–165.
- 157 A. Undri, L. Rosi, M. Frediani and P. Frediani, *Fuel*, 2014, **116**, 662–671.
- 158 M. Bartoli, L. Rosi, M. Frediani, A. Undri and P. Frediani, *J. Anal. Appl. Pyrolysis*, 2015, **113**, 281–287.
- 159 S. Hann and T. Connock, 2020.
- 160 P. Leclerc, J. Doucet and J. Chaouki, *J. Anal. Appl. Pyrolysis*, 2018, **130**, 209–215.

- 161 J. Chaouki, S. Farag, M. Attia and J. Doucet, *Can. J. Chem. Eng.*, 2020, **98**, 832–847.
- 162 M. S. Qureshi, A. Oasmaa and C. Lindfords, *VTT-beyond the obvious. Pyroliq.*
- 163 S. Aron, L. K. Lavender, M. S. E., B. T. S. and Z. Lixin, *Science (80-.)*, 2021, **373**, 51–55.
- 164 M. Häußler, M. Eck, D. Rothauer and S. Mecking, *Nature*, 2021, **590**, 423–427.
- 165 T. M. Adyel, *Science (80-.)*, 2020, **369**, 1314–1315.
- 166 K. Sarah and R. Gloria, *Science (80-.)*, 2021, **373**, 49–50.
- 167 D. Yao, H. Yang, Q. Hu, Y. Chen, H. Chen and P. T. Williams, *Appl. Catal. B Environ.*, 2021, **280**, 119413.
- 168 L. Sibao, K. P. A., V. B. C., D. Andrew and V. D. G., *Sci. Adv.*, 2022, **7**, eabf8283.
- 169 X. Jie, W. Li, D. Slocombe, Y. Gao, I. Banerjee, S. Gonzalez-Cortes, B. Yao, H. AlMegren, S. Alshihri, J. Dilworth, J. Thomas, T. Xiao and P. Edwards, *Nat. Catal.*, 2020, **3**, 902–912.
- 170 P. Johar, E. L. Rylott, C. R. McElroy, A. S. Matharu and J. H. Clark, *Green Chem.*, 2021, **23**, 808–814.
- 171 J. Antonkiewicz, C. Jasiewicz, M. Koncewicz-Baran and R. Sendor, *Acta Physiol. Plant.*, 2016, **38**, 40.
- 172 J. C. Acomb, C. Wu and P. T. Williams, *Appl. Catal. B Environ.*, 2016, **180**, 497–510.
- 173 F. Wilson, P. Tremain and B. Moghtaderi, *Energy & Fuels*, 2018, **32**, 4167–4177.
- 174 C. Liu, X. Liu, X. T. Bi, Y. Liu and C. Wang, *Energy & fuels*, 2011, **25**, 1996–2003.
- 175 A. Khelfa, A. Bensakhria and J. V Weber, *J. Anal. Appl. Pyrolysis*, 2013, **101**, 111–121.
- 176 K. Zeng, B. Wang, S. Xia, C. Cui, C. Wang, A. Zheng, K. Zhao, Z. Zhao, H. Li and M. D. Isobaev, *Energy*, 2022, **254**, 124245.
- 177 P. Giudicianni, V. Gargiulo, C. M. Grottole, M. Alfè, A. I. Ferreira, M. A. A. Mendes, M. Fagnano and R. Ragucci, *Energy & Fuels*, 2021, **35**, 5407–5478.
- 178 X. Cui, Y. Shen, Q. Yang, S. Kawi, Z. He, X. Yang and C.-H. Wang, *Chem. Eng. J.*, 2018, **347**, 543–551.

- 179 S. Maduskar, V. Maliekkal, M. Neurock and P. J. Dauenhauer, *ACS Sustain. Chem. Eng.*, 2018, **6**, 7017–7025.
- 180 X. Yang, Y. Zhao, W. Li, R. Li and Y. Wu, *Energy & Fuels*, 2019, **33**, 4352–4360.
- 181 T. A. Milne and R. J. Evans, *Energy and Fuels*, 1987, **1**, 123–138.
- 182 X. Zhu, F. Qian, C. Zhou, L. Li, Q. Shi, S. Zhang and J. Chen, *Environ. Sci. Technol.*, 2019, **53**, 6580–6586.
- 183 W. Wang, M. Wang, J. Huang, N. Tang, Z. Dang, Y. Shi and M. Zhaohe, *J. Energy Inst.*, 2019, **92**, 1997–2003.
- 184 I. Delidovich, P. J. C. Hausoul, L. Deng, R. Pfützenreuter, M. Rose and R. Palkovits, *Chem. Rev.*, 2016, **116**, 1540–1599.
- 185 K. Ding, S. Liu, Y. Huang, S. Liu, N. Zhou, P. Peng, Y. Wang, P. Chen and R. Ruan, *Energy Convers. Manag.*, 2019, **196**, 1316–1325.
- 186 K. Mette, S. Kühn, A. Tarasov, M. G. Willinger, J. Kröhnert, S. Wrabetz, A. Trunschke, M. Scherzer, F. Girgsdies, H. Düdder, K. Kähler, K. F. Ortega, M. Muhler, R. Schlögl, M. Behrens and T. Lunkenbein, *ACS Catal.*, 2016, **6**, 7238–7248.
- 187 J. M. Escola, J. Aguado, D. P. Serrano, A. García, A. Peral, L. Briones, R. Calvo and E. Fernandez, *Appl. Catal. B Environ.*, 2011, **106**, 405–415.
- 188 C. Wu, V. L. Budarin, M. Wang, V. Sharifi, M. J. Gronnow, Y. Wu, J. Swithenbank, J. H. Clark and P. T. Williams, *Appl. Energy*, 2015, **157**, 533–539.
- 189 I. van Zandvoort, Y. Wang, C. B. Rasrendra, E. R. H. van Eck, P. C. A. Bruijninx, H. J. Heeres and B. M. Weckhuysen, *ChemSusChem*, 2013, **6**, 1745–1758.
- 190 D. J. Nevins, *Am. J. Clin. Nutr.*, 1995, **61**, 915S–921S.
- 191 I. Ziegler-Devin, Z. Menana, L. Chrusciel, M. Chalot, V. Bert and N. Brosse, *Ind. Crops Prod.*, 2019, **140**, 111722.
- 192 S. Suganuma, K. Nakajima, M. Kitano, D. Yamaguchi, H. Kato, S. Hayashi and M. Hara, *J. Am. Chem. Soc.*, 2008, **130**, 12787–12793.
- 193 S. Van de Vyver, J. Geboers, W. Schutyser, M. Dusselier, P. Eloy, E. Dornez, J. W. Seo, C. M. Cortin, E. M. Gaigneaux and P. A. Jacobs, *ChemSusChem*, 2012, **5**, 1549–1558.
- 194 M. Yabushita, H. Kobayashi and A. Fukuoka, *Appl. Catal. B Environ.*, 2014,

- 145**, 1–9.
- 195 N. Sweygers, M. Kamali, T. M. Aminabhavi, R. Dewil and L. Appels, *Biomass Convers. Biorefinery*, 2022, **12**, 173–181.
- 196 F. S. Asghari and H. Yoshida, *Ind. Eng. Chem. Res.*, 2007, **46**, 7703–7710.
- 197 R. W. Thomas and H. A. Schuette, *J. Am. Chem. Soc.*, 1931, **53**, 2324–2328.
- 198 P. Wang, S. H. Zhan and H. B. Yu, in *Advanced Materials Research*, Trans Tech Publ, 2010, vol. 96, pp. 183–187.
- 199 F. D. Pileidis and M. Titirici, *ChemSusChem*, 2016, **9**, 562–582.
- 200 N. Baccile, C. Falco and M.-M. Titirici, *Green Chem.*, 2014, **16**, 4839–4869.
- 201 J. A. Baldock and R. J. Smernik, *Org. Geochem.*, 2002, **33**, 1093–1109.
- 202 C. J. Powell, *Appl. Surf. Sci.*, 1995, **89**, 141–149.
- 203 W. ~H. Qi and M. ~P. Wang, *J. Nanoparticle Res.*, 2005, **7**, 51–57.
- 204 H. Yang, Q. Lin, C. Zhang, X. Yu, Z. Cheng, G. Li, Q. Hu, X. Ren, Q. Zhang and J. Liu, *Nat. Commun.*, 2020, **11**, 1–8.
- 205 J. Lin, S. Sun, D. Xu, C. Cui, R. Ma, J. Luo, L. Fang and H. Li, *Chem. Eng. J.*, 2021, 132195.
- 206 M. Zhao, K. Yuan, Y. Wang, G. Li, J. Guo, L. Gu, W. Hu, H. Zhao and Z. Tang, *Nature*, 2016, **539**, 76–80.
- 207 D. Pybus and C. Sell, *The Chemistry of Fragrances*, The Royal Society of Chemistry, 2006.
- 208 A. M. C. F. Castelijns, J. M. Hogeweg and S. P. J. M. Van Nispen, 1998.
- 209 D. T. Payne, Y. Zhao and J. S. Fossey, *Sci. Rep.*, 2017, **7**, 1720.
- 210 C. G. Frost and B. C. Hartley, *Org. Lett.*, 2007, **9**, 4259–4261.
- 211 C. G. Frost and B. C. Hartley, *J. Org. Chem.*, 2009, **74**, 3599–3602.
- 212 H. Wang, Y. Shi, Z. Wang, Y. Song, M. Shen, B. Guo and L. Wu, *J. Catal.*, 2021, **396**, 374–386.
- 213 S. S. Mohire and G. D. Yadav, *Ind. Eng. Chem. Res.*, 2018, **57**, 9083–9093.
- 214 S. Padmanaban, G. H. Gunasekar and S. Yoon, *Inorg. Chem.*
- 215 B. Bachiller-Baeza, I. Rodriguez-Ramos and A. Guerrero-Ruiz, *Appl. Catal. A Gen.*, 2001, **205**, 227–237.
- 216 B. Li and H. C. Zeng, *ACS Appl. Mater. Interfaces*, 2018, **10**, 29435–29447.
- 217 M. Imran Din and A. Rani, *Int. J. Anal. Chem.*, 2016, **2016**, 1–14.
- 218 A. Zhou, Y. Dou, J. Zhou and J.-R. Li, *ChemSusChem*, 2020, **13**, 205–211.
- 219 M. Y. Miao, J. T. Feng, Q. Jin, Y. F. He, Y. N. Liu, Y. Y. Du, N. Zhang and D.

- Q. Li, *RSC Adv.*, 2015, **5**, 36066–36074.
- 220 R. G. Nuzzo, L. H. Dubois, N. E. Bowles and M. A. Trecocke, *J. Catal.*, 1984, **85**, 267–271.
- 221 J. S. Yadav, P. A. N. Reddy, A. S. Kumar, A. R. Prasad, B. V. S. Reddy and A. A. Al Ghamdi, *Tetrahedron Lett.*, 2014, **55**, 1395–1397.
- 222 W. Chen, S. A. Elfeky, Y. Nonne, L. Male, K. Ahmed, C. Amiable, P. Axe, S. Yamada, T. D. James, S. D. Bull and J. S. Fossey, *Chem. Commun.*, 2011, **47**, 253–255.
- 223 L. L. GASNER, A. O. DENLOYE and T. M. REGAN, *Chem. Eng. Commun.*, 1986, **48**, 349–354.
- 224 M. Marczewski, E. Kamińska, H. Marczewska, M. Godek, G. Rokicki and J. Sokołowski, *Appl. Catal. B Environ.*, 2013, **129**, 236–246.
- 225 M. Artetxe, G. Lopez, M. Amutio, I. Barbarias, A. Arregi, R. Aguado, J. Bilbao and M. Olazar, *Waste Manag.*, 2015, **45**, 126–133.
- 226 Z. Hussain, K. M. Khan, S. Perveen, K. Hussain and W. Voelter, *Fuel Process. Technol.*, 2012, **94**, 145–150.
- 227 K. I. Dement'ev, T. A. Palankoev, O. A. Alekseeva, I. A. Babkin and A. L. Maksimov, *J. Anal. Appl. Pyrolysis*, 2019, **142**, 104612.
- 228 S. Fan, Y. Zhang, T. Liu, W. Fu and B. Li, *J. Anal. Appl. Pyrolysis*, 2022, **162**, 105425.
- 229 R. Prathiba, M. Shruthi and L. R. Miranda, *Waste Manag.*, 2018, **76**, 528–536.
- 230 P. B. Dewangga and C. W. Purnomo, in *IOP Conference Series: Earth and Environmental Science*, IOP Publishing, 2019, vol. 399, p. 12110.
- 231 Z. Hussain, K. M. Khan, N. Basheer and K. Hussain, *J. Anal. Appl. Pyrolysis*, 2011, **90**, 53–55.
- 232 Y. X. Zeng, L. Wang, C. F. Wu, J. Q. Wang, B. X. Shen and X. Tu, *Appl. Catal. B Environ.*, 2018, **224**, 469–478.
- 233 J. Jia, A. Veksha, T.-T. Lim and G. Lisak, *J. Clean. Prod.*, 2020, **258**, 120633.
- 234 M. Sevilla and A. B. Fuertes, *Chem. Phys. Lett.*, 2010, **490**, 63–68.
- 235 L. Fan, Y. Zhang, S. Liu, N. Zhou, P. Chen, Y. Liu, Y. Wang, P. Peng, Y. Cheng and M. Addy, *Energy Convers. Manag.*, 2017, **149**, 432–441.
- 236 K. Hernadi, A. Fonseca, J. B. Nagy, A. Siska and I. Kiricsi, *Appl. Catal. A Gen.*, 2000, **199**, 245–255.
- 237 N. Zhou, L. Dai, Y. Lv, H. Li, W. Deng, F. Guo, P. Chen, H. Lei and R. Ruan,

- Chem. Eng. J.*, 2021, **418**, 129412.
- 238 T. Ueno, E. Nakashima and K. Takeda, *Polym. Degrad. Stab.*, 2010, **95**, 1862–1869.
- 239 E. F. Kukovitskii, L. A. Chernozatonskii, S. G. L’vov and N. N. Mel’Nik, *Chem. Phys. Lett.*, 1997, **266**, 323–328.
- 240 Y. Uemichi, Y. Makino and T. Kanazuka, *J. Anal. Appl. Pyrolysis*, 1989, **14**, 331–344.
- 241 A. D. Russell, E. I. Antreou, S. S. Lam, C. Ludlow-Palafox and H. A. Chase, *RSC Adv.*, 2012, **2**, 6756–6760.
- 242 Y. Uemichi, Y. Kashiwaya, A. Ayame and H. Kanoh, *Chem. Lett.*, 1984, **13**, 41–44.
- 243 EMD Millipore, 2009, Extractables Testing Report: PureFlex™ and SureFlex™ Disposable Process Container Films.
- 244 I. Corazzari, F. Turci and R. Nisticò, *Mater. Lett.*, 2021, **284**, 129030.
- 245 S. I. Senkevich, T. V. Druzhinina, I. M. Kharchenko and Y. G. Kryazhev, *Solid Fuel Chem.*, 2007, **41**, 45–51.
- 246 A. Marcilla, A. Gómez and S. Menargues, *Polym. Degrad. Stab.*, 2005, **89**, 454–460.
- 247 J. A. Reyes-Labarta and A. Marcilla, *Ind. Eng. Chem. Res.*, 2012, **51**, 9515–9530.
- 248 S.-S. Choi and E. Kim, *J. Anal. Appl. Pyrolysis*, 2017, **127**, 1–7.
- 249 P. Johar, C. R. McElroy, E. L. Rylott, A. S. Matharu and J. H. Clark, *Appl. Catal. B Environ.*, 2022, **306**, 121105.
- 250 R. Xie, G. Fan, Q. Ma, L. Yang and F. Li, *J. Mater. Chem. A*, 2014, **2**, 7880–7889.
- 251 F. Wang, Y. Bi, N. Chen, K. Hu and X. Wei, *Chem. Phys. Lett.*, 2018, **711**, 152–155.
- 252 X. Zhang, H. Lei, G. Yadavalli, L. Zhu, Y. Wei and Y. Liu, *Fuel*, 2015, **144**, 33–42.
- 253 X. Zhang and H. Lei, *RSC Adv.*, 2016, **6**, 6154–6163.

